Dissertation

submitted to the
Combined Faculty of Mathematics, Engineering and Natural Sciences
of Heidelberg University, Germany
for the degree of
Doctor of Natural Sciences

Put forward by

Raya Roshana Gallas
born in: Tübingen, Germany

Oral examination: January 29, 2024

Experimental characterisation of the alanine dosimeter in the presence of magnetic fields for applications in magnetic resonance guided radiotherapy

Referees:

Prof. Dr. Jürgen Debus
Prof. Dr. Oliver Jäkel

Experimentelle Charakterisierung des Alanindosimeters in Magnetfeldern für Anwendungen in der MR-geführten Strahlentherapie

In der MR-geführten Strahlentherapie werden MR Linacs verwendet, die einen MR-Scanner mit einem Linearbeschleuniger kombinieren. Ziel dieser Arbeit war die Charakterisierung des Alanindosimeters in Magnetfeldern, wie sie in der MR-geführten Strahlentherapie auftreten, also im dauerhaft am MR Linac vorhandenen statischen Hauptmagnetfeld sowie in Radiofrequenzpulsen und Gradientenfeldern, wie sie zusätzlich während der MR-Bildgebung auftreten.

Alaninpellets wurden in statischen Magnetfeldern am Elekta Unity™ MR Linac und an einem konventionellen Linearbeschleuniger, vor welchem ein Elektromagnet positioniert wurde, bestrahlt. Alaninpellets wurden außerdem am MR Linac und an einem konventionellen MR-Scanner MR-Bildgebung ausgesetzt. Die Dosisinformation wurde mit einem EPR-Spektrometer ausgelesen.

Die für Dosisbestimmungen mit dem Alanindosimeter am Elekta Unity™ und am ViewRay MRIdian™ MR Linac benötigten Magnetfeld-Korrektionsfaktoren wurden bestimmt. Es konnte keine messbare Beeinträchtigung des Alanindosimeters durch die statischen Magnetfelder festgestellt werden, da die ermittelten Korrektionsfaktoren innerhalb der Standardunsicherheit mit Eins übereinstimmen. Weiterhin zeigte sich keine messbare Beeinträchtigung durch MR-Bildgebung.

Das Alanindosimeter ist daher eine ausgezeichnete Wahl für Dosisbestimmungen an MR Linacs. Es ist des Weiteren für End-zu-End-Tests in der MR-geführten Strahlentherapie geeignet, bei welchen MR-Bildgebung nach oder während Bestrahlungen zum Einsatz kommen kann.

Experimental characterisation of the alanine dosimeter in the presence of magnetic fields for applications in magnetic resonance guided radiotherapy

Magnetic resonance guided radiotherapy (MRgRT) uses MR Linacs combining an MR scanner with a linac. This thesis aimed at the characterisation of the alanine dosimeter in the magnetic fields of MRgRT, i.e. the static magnetic main field continuously present at an MR Linac and radiofrequency pulses and gradient fields occuring in addition during MRI.

Alanine pellets were irradiated in static magnetic fields at an Elekta Unity™ MR Linac and at a conventional linac with an electromagnet positioned in front of it. Alanine pellets were also exposed to MRI at the MR Linac and at a conventional MR scanner. The dose information was read out using an EPR spectrometer.

The magnetic field correction factors to be applied for dose assessments with the alanine dosimeter at the Elekta Unity™ and at the ViewRay MRIdian™ MR Linac were determined. Their agreement with unity within the standard uncertainty indicates no measurable effect of the static magnetic fields on the alanine dosimeter. Furthermore, no measurable impact of MRI was found.

The alanine dosimeter is, hence, an excellent choice for dose assessments at MR Linacs. It is further suited for end-to-end tests in MRgRT involving MRI after or during irradiations.

Contents

Abbreviations and acronyms

ART adaptive radiotherapy 17

ACR American College of Radiology 129

CT computed tomography 16

ddc depth dose curve 42

DNA deoxyribonucleic acid 33

EGS Electron Gamma Shower 64

EPR electron paramagnetic resonance 15

ERE electron return effect 40

ESR electron spin resonance 50

FID free induction decay 27

FFF flattening-filter-free 34

GUM Guide to the Expression of Uncertainty in Measurement 18

IC ionisation chamber 10

IGRT image guided radiotherapy 33

1 Introduction

Ionising radiation affects many aspects of daily human life. There is the exposure to natural sources of radiation e.g. to radon by breathing or to Kalium-40 by food intake as well as to cosmic and to terrestrial radiation. In addition, there is the exposure due to medical and technical applications. Medical applications of ionising radiation are found in diagnosis and treatment – from x-ray images at the orthopaedist to radiotherapy (RT), which is the treatment of cancer by use of ionising radiation. Technical applications are found in diverse fields reaching from security controls at airports to sterilisation of medical devices. Studying ionising radiation for research, radiation protection, or control of medical or technical applications necessitates methods of measurement. In RT, the measurand is the absorbed dose, which is the mean energy imparted to a mass element by ionising radiation. Its unit in the Système International (SI) is Gray (Gy), defined as the absorbed energy in Joule (J) per mass of matter in kilogramme (kg). The field of physics dealing with the assessment of absorbed doses is called dosimetry; the radiation detectors used for the assessment are called dosimeters. There is a wide range of different types of dosimeters – from ionisation chambers (ICs) that utilise the ionisation of air to gels that utilise the radiation induced polimerisation in the gel – with each dosimeter offering specific advantages for specific questions in different fields of dosimetry.
This thesis is about the alanine dosimeter. Its measurement principle is based on chemical reactions to the impact of ionising radiation. Alanine is an amino acid which is highly sensitive to radiation damage; radicals are formed in the organic substance under the impact of ionising radiation. The concentration of the radicals is proportional to the absorbed dose. The concentration of the unpaired electrons of the radicals and, thus, the absorbed dose can be read out after the irradiation by electron paramagnetic resonance (EPR) spectroscopy[1] [Bradshaw et al., 1962]. Most commonly, alanine powder is pressed into pellets for the use in dosimetry, see Figure 2.20. Advantages of the alanine dosimeter are e.g. the small detector size, the near water-equivalence of the alanine[2], the non-destructive readout, the high stability of the radiation induced radicals, and the low cost and non-toxicity of the alanine pellets [Regulla and Deffner, 1982]. Alanine dosimetry was initially applied in industry e.g. for the preparation of drinking water [Regulla and Deffner, 1982; Schneider et al., 1985; Regulla, 1999], where the alanine dosimeter was used for absorbed doses in the range of some kGy. The potential of the alanine dosimeter for dosimetry in RT, not least because of the water-equivalence mentioned above, was noted early.

[1] The name "electron spin resonance" (ESR) is used likewise.

[2] Water-equivalence is an important aspect in medical dosimetry, as body tissue is – in the broadest sense – water-equivalent.

The alanine dosimeter seemed especially suited as a reference and transfer dosimeter, e.g. due to its small detector size, its non-destructive readout, and the stability of the radicals [Regulla and Deffner, 1982; Regulla, 1999]. The range of absorbed doses accessible with the alanine dosimeter was, hence, extended to the therapeutically relevant low absorbed doses of a few gray at the end of the last century [Sharpe et al., 1996; Sharpe and Sephton, 1998] allowing for the application of alanine dosimetry in RT. The alanine dosimeter has been used e.g. at the UK's National Physical Laboratory (NPL) [Sharpe et al., 1996; Sharpe and Sephton, 1998], at the USA's National Institute of Standards and Technology (NIST) [Sleptchonok et al., 2000; Nagy et al., 2000a,b, 2002], at Italy's Istituto Superiore di Sanità (ISS) [Bartolotta et al., 1993; De Angelis et al., 2000], and in Denmark [Hansen et al., 1987; Olsen et al., 1990]. The alanine dosimeter has been applied in several specialised fields of RT: for auditing the implementation of intensity modulated radiotherapy (IMRT) in the UK [Budgell et al., 2011], for the validation of the absorbed dose in helical tomotherapy [Perichon et al., 2011; Panzeca et al., 2018], and at the Cyberknife RT device [Garcia et al., 2011], exploiting e.g. the suitability of the alanine dosimeter for dose assessments in small irradiation fields. Latest developments of alanine dosimetry in RT are e.g. the addition of gadolinium in order to enhance the sensitivity of the dosimeter [Marrale et al., 2011] or the determination of the absorbed dose in therapeutical proton beams [Marrale et al., 2016]. At the PTB, the alanine dosimetry system was set up and had been maintained for about a decade by Mathias Anton [Anton, 2005, 2006; Anton et al., 2008, 2009, 2013; Anton and Büermann, 2015].

This work focuses on the application of alanine dosimetry in RT. RT is one of the standard methods for cancer treatment besides surgery and chemotherapy. The aim of RT is briefly speaking to damage tumour cells whilst sparing the healthy tissue [Baskar et al., 2012]. In conventional RT, tumours are irradiated with photon beams produced by linear accelerators (linacs) for electrons[3]. Conventional RT with linacs enables considerable success in cancer treatment but it suffers from the fact, that the target, i.e. the tumour, cannot be "seen" during the treatment. Conventional RT is based on computed tomography (CT) acquisitions taken prior to the treatment, but the situation during the treatment might differ due to inter- and intrafractional changes especially in thorax, abdomen, and pelvis [Chin et al., 2020]. Examples are weight loss or gain, different filling levels of the patient's bladder, or the respiratory motion. In order to avoid missing parts of the tumour and, hence, risk a relapse of the disease, a margin around the tumour is also included into the target volume defined for the irradiation; target and margin together are called planning target volume (PTV) [Bangert and Ziegenhein, 2018]. The smaller the margins needed, the more healthy tissue can be spared, resulting in less side effects of RT. Magnetic resonance guided radiotherapy (MRgRT) has developed within the last two decades, with the first feasibility study published in 2005 [Raaijmakers

[3] The photons are produced by directing the electrons onto a target in order to create bremsstrahlung.

et al., 2005] and patient treatments since 2014 [Acharya et al., 2016]. MRgRT addresses the weak point of conventional RT which is the lack of target visualisation during the treatment [Pollard et al., 2017; Chin et al., 2020]. MRgRT uses devices called "MR Linacs" combining an MR scanner for imaging and a linac for dose delivery [Raaijmakers et al., 2005; Lagendijk et al., 2008; Fallone et al., 2009; Lagendijk et al., 2014]. The MR image guidance enables the visualisation of the target (i.e. the tumour) and of organs at risk (OAR) in real time during the RT treatment leading up to smaller margins included in the PTV and, thus, less radiation exposure of healthy surrounding tissue [Zou et al., 2018; Chin et al., 2020]. This makes MRgRT especially promising for paediatric RT [Chin et al., 2020]. The MR image guidance is connected with adaptive radiotherapy (ART) with offline or online replanning based on the variations found by imaging and with motion management techniques such as gating [Chin et al., 2020]. It is beneficial that MRI offers a supreme soft tissue contrast, entails no additional exposure to ionising radiation, and does not only provide morphological information but also functional information[4]. These are aspects that image guidance with e.g. cone beam CT cannot offer [Jäkel, 2018]. The high soft tissue contrast and the functional information provided by MRI ease the discrimination between tumour and surrounding tissue. This facilitates the tumour delineation as well as the OAR delineation. Functional MRI during the RT treatment has, in addition, the potential to indicate the treatment response by imaging biomarkers during the treatment [Pollard et al., 2017; Chin et al., 2020] which is an important step towards individualised and biologically adaptive RT [Chin et al., 2020].

The aim of this work is the characterisation of the alanine dosimeter in magnetic fields as they occur in MRgRT. These fields include the static magnetic base field continuously present at an MR Linac with magnetic flux densities between 0.35 T to 1.5 T, and radiofrequency (RF) pulses and gradient fields occuring at an MR Linac during MRI. The characterisation of the alanine dosimeter in the static magnetic main field is of relevance for the quality assurance (QA) in MRgRT, which includes the assessment of absorbed doses at the MR Linac. Attention has to be paid here to the impact of the Lorentz force on the secondary electrons. This characterisation was the focus of the first part of this thesis. Data on the characterisation of the alanine dosimeter in static magnetic fields has already been presented by [Billas et al., 2020, 2021], however with the alanine system applied at the NPL. It is, hence, beneficial to provide the data obtained with the alanine system at the PTB for comparison. To my knowledge, there is no literature data on the impact of the RF pulses and the gradient fields of MRI on the alanine dosimeter. The results of the second part of this thesis addressing the impact of MRI on the alanine dosimeter are, hence, important for assessing the suitability of the alanine dosimeter for end-to-end tests in MRgRT which include the exposure of the alanine detectors to MRI [Gallas et al.,

[4] A possibility for functional MRI is e.g. diffusion weighted MRI generating contrast from the diffusion of water molecules. It allows, hence, to observe changes in the water mobility which can be connected with pathological findings [Chin et al., 2020]. Diffusion weighted MRI is discussed as a predictor for RT response e.g. in lung cancer [Weiss et al., 2016].

2015; Niebuhr et al., 2019]. Since the impairment of the alanine dosimeter by the magnetic fields was expected to be – if at all – minor, special emphasis was placed on the uncertainty determination in this thesis which was performed according to the Guide to the Expression of Uncertainty in Measurement (GUM).
Chapter 2 provides the background knowledge required for this thesis. The materials and methods for the performed investigations are described in Chapter 3. That Chapter is divided into the investigations in static magnetic fields (Section 3.1) and in MRI (Section 3.2). The results obtained in the investigations are presented in Chapter 4, with the structure of the sections arranged in parallel to Chapter 3. Chapter 4 also contains a summary of the results in Section 4.3. The obtained results are discussed in Chapter 5, again providing the same structure of sections and including a summarising discussion in Section 5.3. Conclusion and outlook in Chapter 6 close the thesis.

2 Background

2.1 Magnetic Resonance Imaging

During magnetic resonance imaging (MRI), the patient is situated in a static magnetic main field several ten thousand times stronger than the terrestrial magnetic field[1]. The magnetic moments of the hydrogen nuclei within the patient align parallel and antiparallel to this magnetic field.[2] A macroscopic magnetisation in the direction of the magnetic field results from the difference in the population of these two orientations. This state of equilibrium can be distorted by a radiofrequency (RF) pulse. The distortion is followed by a relaxation back to the equilibrium state. The excited nuclei emit an RF signal during this relaxation which is detected as the MR signal. Imaging with MR requires spatial encoding of this MR signal. This is accomplished by additional magnetic gradient fields. The MRI system is basically composed of three elements: superconducting magnet, gradient system, and RF system. Since these three components consist of coils, and since the RF system is placed within the gradient system which is itself placed within the bore or the cylindric superconducting magnet, the MRI system can be shortishly described as a "coil in a coil in a coil" [Ladd et al., 2018], see Figure 2.1. In the following, these three components are described with a technical focus before their functional interaction for MRI is addressed.

2.1.1 Components of an MRI system

Superconducting magnet

The superconducting magnet generates the static magnetic main field $\vec{B}_0$ in which the magnetic moments of the hydrogen nuclei align, see Figure 2.2. The magnet has to be cooled in order to sustain its superconductivity. This is usually done with liquid helium (temperatures of about 4 K) [Ladd et al., 2018]. The static magnetic main field $\vec{B}_0$ is continuously present and cannot be switched off easily. A loss of superconductivity ("quench") can, however, result e.g. from defects in the superconductor or a shortage of helium. A quench can also be induced by an emergency stop switch in case of danger. Independent of the cause, a quench is followed by the vaporisation of a vast amount of the helium. The vaporised helium has to be led outside in order to prevent damage to the building due to the high

[1] The terrestrial magnetic field in Central Europe has a flux density of almost 50 µT [PTB, 2022], typical clinically applied flux densities for MRI are 1.5 T or 3.0 T.

[2] Other nuclei can be used for MRI, too. Hydrogen nuclei are, however, most commonly used.

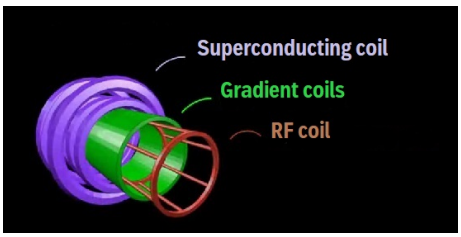

Figure 2.1: Schematic setup of an MRI system. Illustration taken and modified from a talk that Christina Stengl gave about her Master thesis [Stengl, 2020].

pressures involved and in order to prevent danger of suffocation due to displacement of oxygen in the air. A quench is accompanied by an evacuation of the surrounding of the MRI system [Ladd et al., 2018]. High requirements are imposed on the static magnetic main field $\vec{B}_0$ in terms of homogeneity in the area used for imaging [Cosmus and Parizh, 2010]. A shimming system (active via local coils or passive via local metal or synthetic plates) is used for further homogenisation [Ladd et al., 2018]. The direction of the magnetic field is along the patient couch in the bore of the superconducting magnet, which is commonly labeled as z-axis, see Figure 2.3. The static magnetic main field can, thus, be written as $\vec{B}_0 = (0, 0, B_0)$.

Gradient fields

The temporally and spacially modified gradient magnetic fields (G_x, G_y, G_z) are used for spatial encoding of the MR signal. This is accomplished by superimposing the static magnetic main field $\vec{B}_0$ with the three gradient fields G_x, G_y, and G_z which are linear in the three spatial directions [Hidalgo-Tobon, 2010] (see Figure 2.3 and see Section 2.1.4 for further details). Gradient fields are specified by the amplitude in units of $\mathrm{mT/m}$ and the slew rate in units of $\mathrm{T/m/s}$. The amplitude characterises the slope of the respective gradient field, while the slew rate characterises how fast the respective gradient field can be switched. Fast MRI requires high amplitudes and fast slew rates. Typical amplitudes are in the range of $20\,\mathrm{mT/m}$ to $80\,\mathrm{mT/m}$, typical slew rates are in the range of $100\,\mathrm{T/m/s}$ to $200\,\mathrm{T/m/s}$ [Ladd et al., 2018]. High requirements are imposed on the gradient fields G_x, G_y, and G_z in terms of linearity in order to prevent geometric distortions in the resulting image. The gradient system is composed of three independent pairs of electric coils. It is placed as a tube inside the cylindric opening of the superconducting magnet ("coil in a coil"), see Figure 2.4. In order to enable the above mentioned typical amplitudes and slew rates, currents of several hundred ampere are required. Thus, strong Lorentz forces (see Section 2.3.3) affect the gradient coils within the static magnetic main field $\vec{B}_0$. As the direction of the gradient fields changes in the range of microseconds, the direction of the Lorentz forces changes within the same time range. The resulting strong dragging at the mounting of the gradient tube causes noisy sounds during MRI.

RF system

The RF system accounts for the excitation of the hydrogen nuclei and the subsequent detection of the MR signal from the sample. It is, thus, composed of a transmitting and a receiving unit. The transmitting coil is located within the gradient tube behind the casing of the MRI system ("coil in a coil in a coil"), see Figure 2.5.[3] The purpose of the transmitting unit is to homogeneously excite the hydrogen nuclei in the entire imaging region via the transmitted time-limited oscillating magnetic field $\vec{B}_1(t)$.[4] The resonance condition for the excitation is

$$\omega_0 = \gamma \cdot B_0 \tag{2.1}$$

with the Larmor frequency ω_0, the gyromagnetic ratio γ of the excited nuclei (here: hydrogen nuclei) and the magnetic flux density of the static magnetic main field $\vec{B}_0$ (see Section 2.1.2 and Equation 2.8). The frequency required for the excitation (i.e. the required oscillating rate of the transmitted oscillating magnetic field $\vec{B}_1(t)$) is, therefore, linked to the magnetic flux density of the main field and the magnetic properties of the nuclei to be excited. The oscillating rates of the applied time-limited magnetic fields $\vec{B}_1(t)$ range from some 10 MHz to some 100 MHz [Ladd et al., 2018], which is within the RF range of the electromagnetic spectrum. The time-limited oscillating magnetic field $\vec{B}_1(t)$ is, thus, also refered to as "RF pulse". The resonance frequency for the excitation of hydrogen nuclei in a 3 T MRI system is at about 128 MHz; RF pulses of about 64 MHz are used for 1.5 T [Ladd et al., 2018]. Traditional MRI systems relied on one-channel transmitting systems. Recently, multi-channel systems are becoming increasingly common [Ladd, 2007] as they allow further homogenisation of the transmitted oscillating magnetic field $\vec{B}_1(t)$. Inhomogeneities in the field $\vec{B}_1(t)$ are problematic e.g. as they can lead to local exceedance of tolerable heating of tissue [Ladd et al., 2018].
The receiving unit is needed for detection and amplification of the weak RF signals from the sample [Fujita, 2007]. It is tuned to the Larmor frequency ω_0 just as the transmitting unit. The receiving unit is, thus, inactivated while the high-powered transmitting unit is active. The receiving unit is crucial for the signal to noise ratio (SNR) and, hence, the image quality of the resulting acquisition. The receiving unit is placed close to the respective imaging region (see Figure 2.6). Small receiving coils enable a high SNR in their immediate surrounding. Imaging of larger objects or deeper regions within the sample requires coils of larger dimensions which is unfortunately limiting the SNR. A recent tendency of development is, thus, the application of a combined system of smaller receiving RF coils called "multi-channel array coils". Their arrangement can be optimised for the respective imaging task allowing for both high SNR and a large imaging region.

[3] It is, however, also possible to use local transmitting coils.

[4] The electric component is not further mentioned here, as it has no relevance for the excitation of the hydrogen nuclei.

Figure 2.2: The superconducting coil required for generating the magnetic main field for MRI is shown on the left; the right shows the cryogenic vessel containing helium for cooling. Illustration from [Ladd et al., 2018].

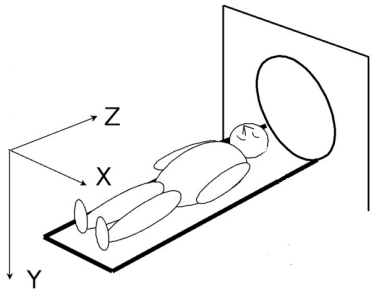

Figure 2.3: Schematic illustration of the conventional orientations in an MRI system. Illustration modified from [VTK].

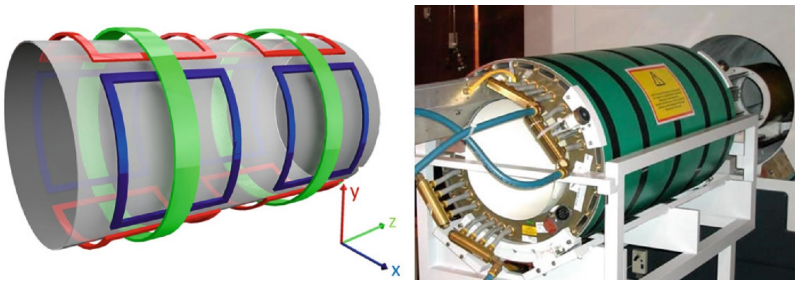

Figure 2.4: The gradient system of an MRI system. The left shows a schematic illustration of the gradient coils. The toroidal coil pair (green) generates the gradient field G_z in z-direction; the two saddle coil pairs (blue and red) generate the gradient fields G_x andG_y in x- and y-direction, respectively. (The coordinate system shown here is left-handed. I therefore assume, that it is only used for illustrating the generation of the gradient fields, while the right-handed coordinate system shown in Figure 2.3 is the general convention for orientations in an MRI system.) The right shows a gradient system prior to its installation in the bore of the superconducting magnet of an MRI system. Illustration taken from [Ladd et al., 2018].

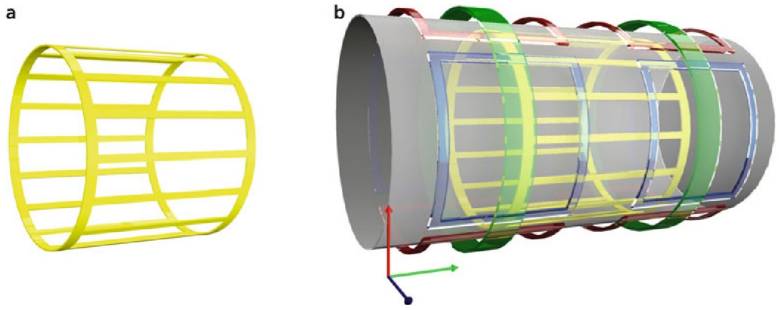

Figure 2.5: The transmitting unit of the RF system. (a) is a schematic illustration of an one-channel RF transmitting coil. This coil is firmly installed within the MRI system. (b) shows the position of the transmitting coil relative to the gradient system (see Figure 2.4). Illustration taken from [Ladd et al., 2018].

Figure 2.6: A receiving coil destined for MR images of the head. Illustration taken from [Siemens].

2.1.2 Function principle of MRI

MRI is based on a magroscopic magnetisation $\vec{M}$ in the sample. In the following, the origin of this magnetisation $\vec{M}$ is described. Nuclei with an uneven number of neutrons and/or protons (these are about two-thirds of the stable nuclei) own a non-vanishing intrinsic angular momentum called nuclear spin $\vec{I}$ and are, hence, potential sources for MR signals [Ladd et al., 2018]. Linked with this nuclear spin $\vec{I}$ is a magnetic moment $\vec{\mu}$:

$$\vec{\mu} = \gamma \cdot \vec{I} \tag{2.2}$$

The proportionality factor γ is called gyromagnetic ratio. The gyromagnetic ratio for hydrogen nuclei is $\gamma = 2.675 \times 10^8 \frac{\text{rad}}{\text{s}\cdot\text{T}}$ [NIST, a] (or $\frac{\gamma}{2\pi} = 42.58 \frac{\text{MHz}}{\text{T}}$ [NIST, b] if frequencies instead of angular frequencies are used). This gyromagnetic ratio is the highest value among stable nuclei [Bachert, 2014], which is – together with the vast abundance of hydrogen nuclei in tissue – the reason for the focus of MRI on hydrogen nuclei. All orientations of the magnetic moment $\vec{\mu}$ are energetically equal in the absence of an external magnetic field. The quantisation of the nuclear spin $\vec{I}$ is manifested in the presence of an external magnetic field. The interaction of a magnetic moment $\vec{\mu}$ with an external magnetic field $\vec{B}$ is described by the Hamiltonian operator $\hat{H}$:[5]

$$\hat{H} = -\vec{\mu} \cdot \vec{B} \tag{2.3}$$

For an external static magnetic field in z-direction ($\vec{B} = (0, 0, B_0)$, see Figure 2.3), the previous equation becomes:

$$\hat{H} = -\gamma \cdot \hbar \cdot I_z \cdot B_0 \tag{2.4}$$

with $\hbar$, Planck's constant divided by 2π, and I_z, the absolute value of the nuclear spin projected onto the z-axis. The eigenvalues E_m of the Hamilton operator which are the stationary energy states are

$$E_m = -\gamma \cdot \hbar \cdot m \cdot B_0 \tag{2.5}$$

where m is the quantum number of the z-component of the nuclear spin I_z.[6] The energy difference between adjacent energy levels is, thus,

$$\Delta E = E_m - E_{m-1} = \gamma \cdot \hbar \cdot B_0 \tag{2.6}$$

[5] The Hamiltonian is the operator in quantum mechanics which provides possible energy observables and the time evolution. It is, thus, the "energy operator".

[6] The absolute value $|\vec{I}|$ of the nuclear spin is constrained by $|\vec{I}| = \hbar \cdot \sqrt{I(I+1)}$ with the quantum number I. The projection I_z of the nuclear spin vector onto the z-axis is constrained for a given quantum number I by $I_z = \hbar \cdot m$ with the quantum number $m = \{-I, -I+1, ..., I-1, I\}$, which corresponds to $2I+1$ possible orientations or spin states. For hydrogen nuclei, it is $I = \frac{1}{2}$ and consequently $m = \{-\frac{1}{2}, +\frac{1}{2}\}$. Thus, there are two orientations or spin states of different energy level ("spin up/down", or also called "parallel/antiparallel orientation") in an external magnetic field.

According to De Broglie's wave equation, an energy difference corresponds to a frequency multiplied with Planck's constant: $\Delta E = h \cdot \nu = \hbar \cdot \omega$. Adding this to Equation 2.6 results in

$$\Delta E = E_m - E_{m-1} = \gamma \cdot \hbar \cdot B_0 = \hbar \cdot \omega_0 \tag{2.7}$$

Equation 2.7 provides the definition of the Larmor frequency ω_0 and the resonance condition (see Equation 2.24 in Section 2.1.1):

$$\omega_0 = \gamma \cdot B_0 \tag{2.8}$$

Hydrogen nuclei have a nuclear spin with $I = \frac{1}{2}$, and there are, thus, two orientations or spin states with different energy levels ("spin up/down", or also called "parallel/antiparallel orientation") in an external magnetic field.
The magnetic moments $\vec{\mu}$ of the hydrogen nuclei in the external magnetic main field $\vec{B}_0$ – connected to the nuclear spin vector $\vec{I}$ via Equation 2.2 – give rise to the macroscopic magnetisation $\vec{M}$. The pictorial representation in Figure 2.7 is an attempt to make it easier to imagine how the macroscopic magnetisation $\vec{M}$ occurs in terms of the quantum mechanical description. The spin state $m = -\frac{1}{2}$ corresponds to a higher energy than the spin state $m = +\frac{1}{2}$ (see Equation 2.5). The two possible spin states are symbolised in Figure 2.7 by the two cones. The length of the nuclear spin ($|\vec{I}|^2$) and its projection onto the z-axis (I_z) are known, but not the direction of the nuclear spin vector $\vec{I}$. This is symbolised by the large amount of tips on each cone. Please note that the amount of tips on one cone in Figure 2.7 does not represent an amount of nulcear spins $\vec{I}$, but the fact, that the orientation of the nuclear spin $\vec{I}$ is unknown for an individual hydrogen nucleus. Each hydrogen nucleus has to be imagined as one cone. Figure 2.7 represents, thus, two hydrogen nuclei, one in spin down and one in spin up state. The amount of all hydrogen nuclei in the sample – corresponding to many cones as shown in Figure 2.7 – has to be considered. The population of the two spin states is given by the Boltzmann distribution. The population of the lower energetic spin state $m = +\frac{1}{2}$ is slightly higher according to that. The sample contains, thus, slightly more "$m = +\frac{1}{2}$ cones". In addition, the positions of the tip on the cone (i.e. the orientations of individual nuclear spin vectors $\vec{I}$) are evenly distributed among all cones in equilibrium. The sum of all cones – up and down state and each with unknown, yet evenly distributed position of the tip – gives rise to the macroscopic magnetisation $\vec{M}$ oriented in z-direction, i.e. parallel to the direction of the external magnetic field $\vec{B}_0$ [Bachert, 2014]. The excess population of the lower energetic spin state is only of the order of 10^{-6} at room temperature according to the Boltzmann distribution. The MR signal is therefore produced by a minor amount of the hydrogen nuclei in the sample. The macroscopic magnetisation $\vec{M}$ is only measurable due to the vast total amount of hydrogen nuclei in the sample which is in the order of the Avogadro constant.

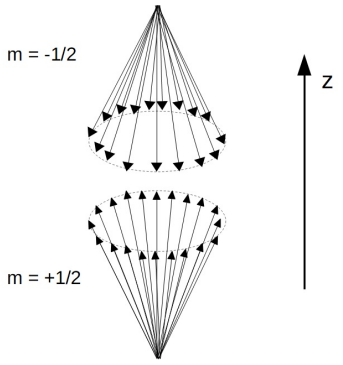

Figure 2.7: Schematic drawing illustrating the occurrence of the macroscopic magnetisation $\vec{M}$ following notes from [Bachert, 2014]. Please see the text for further description.

2.1.3 Excitation and relaxation in MRI

The net magnetisation $\vec{M}$ is in the order of µT [McRobbie et al., 2017] which is six orders of magnitude smaller than the static magnetic main field $\vec{B}_0$. It is therefore impossible to measure the magnetisation $\vec{M}$ when it is oriented parallel to the static magnetic main field $\vec{B}_0$. If the macroscopic magnetisation $\vec{M}$ is, however, deflected to the transversal plane (xy-plane, see Figure 2.3) it can be measured by a detector which is only sensitive to this plane [McRobbie et al., 2017].
The macroscopic magnetisation $\vec{M}$ in the state of equilibrium (i.e. the orientation parallel to the direction of the static magnetic main field $\vec{B}_0$) is named $\vec{M}_0$ in the following. The term "excitation" in MRI refers to the process of deflecting the magnetisation $\vec{M}_0$ from its equilibium position. The deflection of the magnetisation $\vec{M}_0$ can be accomplished by superimposing the static magnetic main field $\vec{B}_0$ with a time-limited oscillating magnetic field $\vec{B}_1(t)$ with amplitude B_1 and oscillating rate ω_{RF} in the RF range, which is polarised perpendicular to the direction of the main field $\vec{B}_0$. The angular frequency ω_{RF} has to equal the Larmor frequency ω_0.[7] The time-limited transmission of the RF field $\vec{B}_1(t)$ ("RF pulse") does not only deflect the magnetisation $\vec{M}$ out of its equilibrium orientation, it also brings all magnetic moments $\vec{\mu}$ of the sample into phase coherence [McRobbie et al., 2017]. The flip angle by which the macroscopic magnetisation $\vec{M}$ is deflected from its equilibrium orientation depends on the amplitude B_1 of the RF pulse and the exposure time to the RF pulse.[8]

[7] The electric component of the RF field is irrelevant for the excitation. Thus, only the magnetic component is mentioned here and hereafter. The electric component plays, however, a role for energy deposition in tissue [Ladd et al., 2018].

[8] The macroscopic magnetisation $\vec{M}$ can take any direction in contrast to the nuclear magnetic moments $\vec{\mu}$ which are constrained to $2I + 1$ discrete orientations relative to the external magnetic field $\vec{B}_0$.

In summary, the equilibrium magnetisation $\vec{M}_0$ oriented parallel to the direction of the static magnetic main field $\vec{B}_0$ in z-direction can be deflected to the transversal xy-plane under the temporary influence of an appropriate resonant RF pulse, also called 90° pulse. The resulting transversal magnetisation $\vec{M}_{xy}$ precesses around the direction of the static magnetic main field $\vec{B}_0$ and induces a voltage in the receiving unit of the RF system.
The amplitude of the signal received in the RF system shows an exponential decay to zero within milliseconds, which is called "free induction decay (FID)".[9] The magnetisation $\vec{M}$ reverts from the deflected state to the equilibrium state due to relaxation processes [Bloch, 1946].
Two relaxation processes can be distinguished. The longitudinal spin-lattice relaxation with time constant $T1$ is due to fluctuating magnetic fields produced by diverse rotational and translational movements of electric and magnetic moments in tissue. These movements result in a broad frequency spectrum of magnetic fields. The part of the spectrum in the range of the resonance frequency ω_0 induces transitions between the spin states leading to the recovery of the equilibrium magnetisation $\vec{M}_0$.
The transversal spin-spin relaxation with time constant $T2$ is due to the fact that the coherence of the spin phases drops away irreversibly due to mutual interactions of the spins. This leads to an exponential decay of the transversal magnetisation $\vec{M}_{xy}$.
In reality, there is a superposition of the $T2$ relaxation with the dephasing due to local inhomogeneities of the magnetic field, resulting in the time constant $T2^*$.[10]
The relaxation times $T1$ and $T2$ are characteristic for the respective tissue, which enables various contrasts for MRI. The resulting image contrast is always a mixture of proton density weighting, $T1$-weighting and $T2$-weighting. The predominant contrast depends on the echo time (TE) (the time between excitation and measurement of the signal) and the repetition time (TR) (the time between two excitation pulses) chosen and in general on the order of RF pulses, gradients and waiting times applied to the sample [Ladd et al., 2018].

2.1.4 Spatial encoding of the MR signal

Spatial encoding is required in order to know from which position in a body the MRI signal comes from. The spatial encoding of the MR signal is addressed in the following.

Slice selection

The equilibrium magnetisation $\vec{M}_0$ (in z-direction) is deflected to the transversal plane by the RF pulse of the transmitting coil. A "slice selection gradient" is needed

[9] In applied MRI, it is not the FID which is measured, but intentionally created echoes of the signal, so called "spin echoes" or "gradient echoes". This will, however, not be further discussed here.

[10] The dephasing due to local inhomogeneities is reversibel e.g. by a 180° refocussation pulse, which is exploited in the spin echo technique.

in order to not excite the entire volume within the transmitting coil but only the slice of interest. It is assumed – without loss of generality – that the normal on the slice of interest is in z-direction. The appropriate slice selection gradient is, then, the linear gradient field G_z in z-direction. This gradient field G_z superimposes the static main magnetic field $\vec{B}_0$ and, thus, the Larmor frequency becomes a function of position in z-direction according to Equation 2.8:

$$\omega(z) = \gamma \cdot (B_0 + G_z \cdot z) \tag{2.9}$$

The frequency width of the RF excitation pulse Δf together with the amplitude (slope) of the gradient field G_z results in the excitation of a slice with thickness Δz, as illustrated in Figure 2.8. The slice position is determined by the carrier frequency of the RF pulse, and the slice thickness is determined by the gradient field amplitude and the bandwidth of the RF pulse[11]. An undesired effect of the slice selection gradient is the imprint of a phase along the gradient field resulting in a distortion of the signal due to interference phenomena. The problem is solved by a refocussing gradient with a polarity inverse to the slice selection gradient applied for a certain time interval prior to data acquisition (see Figure 2.9). The slice selection gradient reduces the 3D problem of spatial encoding to a 2D problem.

Frequency encoding

The spatial encoding in x-direction (without loss of generality) can be accomplished by a gradient field G_x in x-direction which superimposes the static magnetic main field $\vec{B}_0$ during data acquisition. The Larmor frequency of the received signal becomes, thus, according to Equation 2.8, a function of the position in x-direction:

$$\omega(x) = \gamma \cdot (B_0 + G_x \cdot x) \tag{2.10}$$

All magnetic moments $\vec{\mu}$ in a stripe orthogonal to the gradient field G_x "experience" the same total magnetic flux density – composed of the main field $\vec{B}_0$ and the gradient field G_x – and contribute with the same frequency to the readout signal of the excited slice. The Fourier transform of the signal reveals the different frequency components $C(\omega)$. An individual frequency component $C(\omega_i)$ is proportional to the amount of magnetic moments $\vec{\mu}$ precessing with ω_i, and ω_i again contains the spatial information in x-direction. The Fourier transform of the readout signal corresponds eventually to the projection of the density of magnetic moments $\vec{\mu}$ within the object slice onto the direction of the gradient field G_x. The gradient field G_x is called "readout gradient", as it is applied during signal detection. The process of spatial encoding in its direction is called "frequency encoding".

[11] The RF pulse is shaped such that the envelope in the time domain is a sinc function, since this results in a rectangular shape in the frequency domain.

Phase encoding

Slice selection gradient and readout gradient reduce spatial encoding to a 1D problem which is solved by a third gradient field G_y in y-direction (without loss of generality). The gradient field G_y is switched on for a certain time interval t_y between excitation and signal detection. During the exposure to this gradient field G_y, the Larmor frequency of the magnetic moments $\vec{\mu}$ is a function of position in y-direction. As soon as the gradient field G_y is switched off, all magnetic moments $\vec{\mu}$ in the excited slice precess with the same frequency again, but the difference in the phase angle ϕ, which is a function of the position in y-direction, remains:

$$\phi(y) = \gamma \cdot G_y \cdot t_y \cdot y \tag{2.11}$$

All components contribute to the readout signal with the same frequency but with a different phase angle. This process is called phase encoding, the respective gradient field is called phase encoding gradient. The aim of phase encoding is, as for frequency encoding, a "spin density projection" onto the direction of the phase encoding gradient.

k-space

In order to understand how frequency encoding, phase encoding, and two dimensional Fourier transform result in an MR image, the concept of the "k-space" is introduced, see also Figure 2.9. The k-space is an array of numbers representing the measured values from signal detection; the two dimensional Fourier transform of the k-space provides the resulting MR image. For frequency encoding, the signal is measured at M points in time (Δt), each for the same gradient strength G_x, which provides M data points along the k_x-axis in the k-space. In order to fill the k-space also in k_y-direction, the process of slice selective excitation, exposure to phase encoding gradient and signal detection during exposure to the readout gradient has to be repeated N times, each time with a different strength of the phase encoding gradient. The signal is measured for N different gradient strengths (ΔG_y), each at only one point of time t. Eventually, the k-space is filled with $M \times N$ values, whose two dimensional Fourier transform reveals the MR image (see Figure 2.9). A whole volume instead of a certain slice only can be measured by repeating the described procedure for different slice selections.

2.1.5 MR sequences

The general procedure in MRI is "RF excitation of a slice to be measured" – "spatial encoding using the gradient fields" – "acquisition of the MR signal induced in the receiving coil". This order is termed "MR sequence". The MR sequence is repeated until enough information has been acquired for image reconstruction. There is a vast amount of different MR sequences. They differ in the order and type of RF pulses, gradients and waiting times in order to provide special image properties. MR

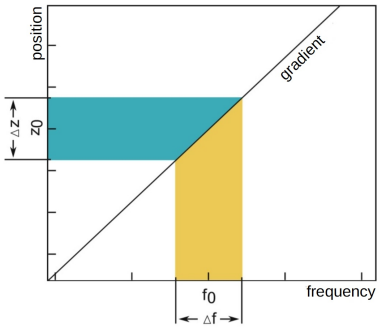

Figure 2.8: Visualisation of slice selection. The linear gradient field results in a Larmor frequency linearly varying in z-direction. The thickness Δz of the selected slice is determined by the amplitude of the gradient field and the bandwidth Δf of the RF pulse. Illustration modified from [Ladd et al., 2018].

sequences are a science in themselves and are not covered in detail here. Important for the present thesis is that MRI is equivalent to the exposure to a static magnetic main field, a large number of RF pulses, and fast changing gradient fields.

2.1.6 RF pulses in MRI

The MR sequence used for imaging can be modified to either enhance or suppress the RF pulses, i.e. to increase or decrease the RF power emitted from the transmitting coil.

Enhancement of RF pulses

Enhancement of the RF pulses is possible by the following adjustments. Several slices can be excited simultaneously. In order to do so, the multiband factor has to be set to an integer N higher than one. The MR scanner then provides N frequency bands of the same shape with different mean frequencies.[12] The transmitted power is then N times as high as for excitation of one slice at a time. Another important parameter for producing enhanced RF pulses is the reference voltage Tx. The reference voltage Tx is the voltage with which an RF pulse has to be transmitted in order to cause a deflection of the magnetisation of 90° in the target volume. In general, the reference voltage Tx has to be determined in a calibration measurement, as it cannot be set universally due to the influence of shape and load of the coil. If Tx is not determined in a calibration measurement, but set to an arbitrary high value without regard to the image quality, increased RF power is emitted from the transmitting coil. The flip angle can also be used in order to generate enhanced RF pulses. The flip angle is the deflection of the magnetisation in the target volume after

[12] A frequency band corresponds to a slice to be excited because of the linear slice selection gradient, see Section 2.1.4.

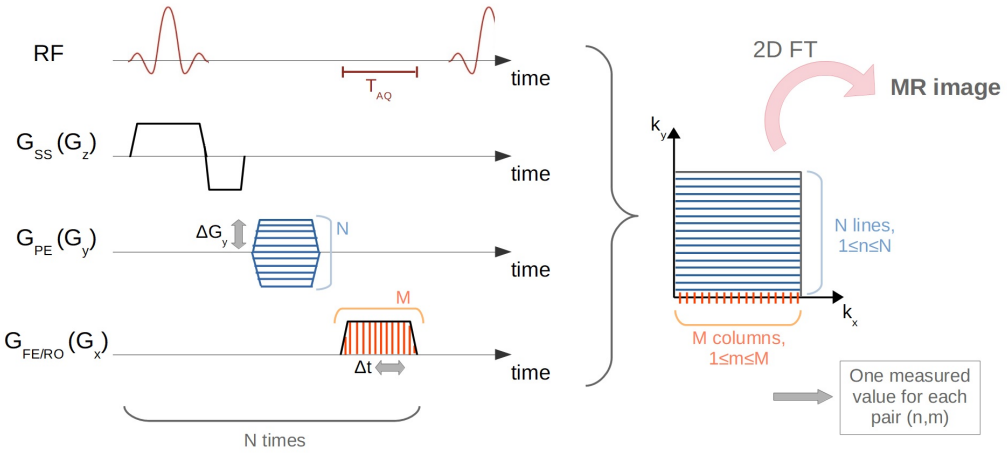

Figure 2.9: Schematic illustration of spatial encoding and k-space following notes from [Bachert, 2014]. The time axis labeled with "RF" represents the RF pulses. A sinc shaped RF pulse is used for the excitation, the area labeled "T_{AQ}" represents the time of the signal acquisition. The time axis labeled with "G_{SS}" represents the slice selection (SS) gradient in z-direction. It is active during the RF pulse. The negative part is the refocussing gradient preventing signal distortion due to interference phenomena (see Section 2.1.4). The time axis labeled with "G_{PE}" represents the phase encoding (PE) gradient in y-direction. It is switched on with a certain strength for a time interval between excitation and signal detection. The time axis labeled with "$G_{FE/RO}$" represents the frequency encoding (FE) or readout (RO) gradient in x-direction. It is active during data acquisition. The process of slice selective excitation, phase encoding, and signal detection during frequency encoding is repeated N times, each time with a different strength of the phase encoding gradient G_{PE} (G_y). For each strength of the phase encoding gradient, another line at another k_y-position in the k-space, which is vizualised on the right, is filled with measured values. During data acquisition, M data points are taken, which fill the k-space in k_x-direction. Finally, the k-space is filled with $M \times N$ measured values and the two dimensional Fourier transform ("2D FT") reveals the resulting MR image.

the excitation. It can be varied since many imaging sequences do not necessarily require a deflection of 90° in order to achieve a satisfying image quality. A small flip angle provides two advantages: the subsequent excitation can ensue sooner since the relaxation back to the equilibrium requires less time and it is easier to comply with the specific absorption rate (SAR) limits (see below in Section 2.1.7) since the transmitted RF power is reduced. However, setting the flip angle to values higher than 90° results in enhanced RF pulses. Finally, the fat saturation is another option for involving additional RF pulses. The signal of fat in the sample is often undesired as it can outshine lesions due to its high signal intensity. In order to suppress the fat signal, a fat suppression modul can be applied prior to the actual imaging sequence. This modul provides an RF pulse exciting the fat signal, which is followed by a so called "spoiler gradient", which results in the de-phasing of the transversal fat magnetisation. The fat signal can therefore not deliver a signal contribution in the subsequent acquisition [Berger and Breithaupt, 2018].

Suppression of RF pulses

Suppression of the RF pulses on the contrary is possible by the following adjustments. The reference voltage Tx can be set to an arbitrary low value without regard to the image quality. The flip angle can be set to a value lower than 90°. Reference voltage Tx and flip angle can actually be set so low that image acquisition is no longer possible. The suppression of the fat signal should be switched off for suppressing RF pulses, as this suppression involves additional RF pulses prior to the actual imaging sequence (see Section 2.1.6).

2.1.7 The specific absorption rate

The RF field $\vec{B}_1(t)$ used for excitation is a potential danger for patients in terms of heating of tissue due to the energy absorbed. Excessive heating can result in damage to the tissue. In order to avoid such scenarios, regulatory thresholds have to be met e.g. for the specific absorption rate (SAR) [International Electrotechnical Commission IEC, 2015]. The SAR is a measure for the energy absorbed per unit mass (units of W/kg). The thresholds are technically implemented by constraints on the transmitting power, which are based on measurements and on simulation models for the SAR in dependence on the RF transmitting power. The SAR depends on several parameters of the MR sequences, e.g. on the flip angle, i.e. the angle by which the longitudinal magnetisation is deflected during excitation, or the repetition time TR, i.e. the time between two subsequent excitations. The run of an MR measurement is, thus, proceeded by a check if the SAR thresholds are met with the chosen parameters. During imaging, the actual transmitting power is monitored, allowing for an automatic termination in case of doubt.

The possible effect of MRI on the alanine dosimeter is addressed in Section 2.4.3.

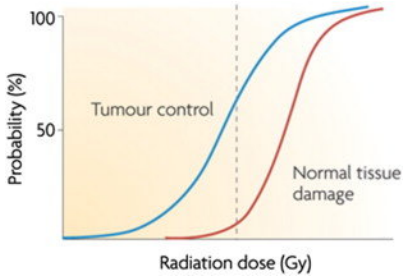

Figure 2.10: Probability curves for tumour control (blue) and normal tissue complication (red). The dashed line indicates the radiation dose resulting in a tumour control probablity of 60 % and a normal tissue complication probablity of 5 %. The figure is taken from [Ray et al., 2015].

2.2 Radiotherapy

2.2.1 Principles of radiotherapy

Radiotherapy (RT) is an important treatment modality for cancer exploiting that ionising radiation induced deoxyribonucleic acid (DNA) damage can lead to cell death. In external beam RT (also called teletherapy) the patient's tumour is irradiated with ionising radiation originating from a source outside the patient. Most common is the generation of photon beams with nominal accelerating potentials between 4 MV and 15 MV by linacs [Schlegel et al., 2018].
Cell death arising from the exposure to ionising radiation does not only occur in the malicious tumour tissue but also in the surrounding healthy tissue. The challenge in RT is, thus, to balance the probablity of tumour control and the risk of side effects due to the damage of healthy normal tissue, see Figure 2.10. Modern radiation techniques improved the risk-to-benefit ratio greatly, aiming at the delivery of the highest possible dose to the tumour while minimising the risk for healthy tissue. Intensity modulated radiotherapy (IMRT) for example allows for the local modulation of the beam intensity. High doses can be delivered to the targeted tumour while the healthy tissue is spared. The superposition of several intensity modulated radiation fields enables even the sparing of healthy tissue located in a concavity of the target volume [Schlegel et al., 2018]. In fractionated treatment schemes, the total dose is not delivered in a single irradiation but in daily irradiations over a period of some weeks exploiting the generally more pronounced repair capability of healthy tissue compared to tumour tissue [Karger, 2018a]. Image guided radiotherapy (IGRT) allows to deliver the radiation doses more precisly by visualising the tumour directly prior or during the treatment. The agreement between treatment planning and actual treatment can be ensured allowing for higher doses to the targeted tumor, especially when organs at risk (OAR) are located in immediate proximity of the high dose region [Schlegel et al., 2018].

2.2.2 Accuracy in radiotherapy dose delivery

The outcome of RT depends on various aspects such as patient or tumour specifics. Another aspect is the accurate delivery of the treatment dose which is assured by dosimetry. Accuracy in general is the closeness of a value to a "true value" [Thwaites, 2013]. Accuracy in RT dose delivery is the closeness of the planned absorbed dose value to the actually absorbed dose value [de Prez, 2019]. [Thwaites, 2013] states that the currently recommended accuracy in RT dose delivery is 3 % ($k = 1$), what should be understood as the relative standard deviation of the delivered dose at the dose specification point defined in the treatment planning. Besides dosimetry, there are more contributions affecting the dose delivery, e.g. patient positioning or treatment delivery. As a consequence, all contributions should be kept as small as possible to ensure the compliance with the 3 % limit.

2.2.3 Developments in external beam radiotherapy

There are current developments in external beam RT further improving the risk-to-benefit ratio (see Section 2.2.1) such as IGRT or the adaptation of external beam RT to the current capabilities of computer calculation e.g. the usage flattening-filter-free (FFF) beams. The developments relevant for this thesis are described in the following.

Image guided radiotherapy

Image guided radiotherapy (IGRT) was already addressed in Chapter 1. Conventional RT relies on CT acquisitions taken prior to the treatment. IGRT provides images of the tumuor and the surrounding tissue just before or during the treatment and allows, hence, to detect inter- or intrafractional changes that could lead to sparing of parts of the tumour or unnecessary radiation exposure of the surrounding tissue. Linacs in clinical application feature flat panels, i.e. two dimensional semi-conducting detectors, for imaging with the therapeutic MV photon beam. The resulting images feature relatively low contrasts due to the high energy of the therapeutic beam. Hence, modern linacs are also equipped with an additional flat panel and a diagnostic kV photon beam. Three dimensional imaging is also possible by aquisition of several projections (cone beam CT) [Karger, 2018b]. Imaging with these techniques comes, however, with an additional dose to the patient, especially when applying cone beam computed tomography, whilst providing moderate soft tissue contrast. MRgRT (see Section 2.2.3) allows to overcome these disadvantages. Inter- as well as intra-factional changes can be detected by the application of MRI prior to and during the treatment. Further modalities used for image guidance are ultrasound and optical methods [Schlegel et al., 2018].

MRI in radiotherapy

Magnetic resonance imaging (MRI) (see Section 2.1) is a valuable imaging modality for diagnosis prior to RT. In addition, the usage of MRI in treatment planning for RT can improve the tumour delineation compared to the usage of CT only and, thus, contribute to a reduction of side effects in RT, see Chapter 1. This is due to the fact that the soft tissue contrast of MRI is superior to the soft tissue contrast provided by CT. Further advantage are, that MRI does no imply further exposure to ionising radiation for the patients and that MRI allows for functional imaging in addition to morphological imaging, as it was already mentioned in Chapter 1. Due to these advantages, MRI is increasingly applied in RT [Metcalfe et al., 2013; Liney and Moerland, 2014; Rai et al., 2017]. Compared to CT, the use of MRI only for treatment planning comes, however, with the disadvantage, that MRI does not provide information about the electron density of the tissue. CT acquisitions provide the tissue specific absorption values in Hounsfield Units (HU), which can be converted into electron densities by usage of a so called Hounsfield look up table, and this electron density information is required in treatment planning for RT. Efforts are, however, made to obtain pseudo-CT values from MR acquisitions [Rank et al., 2013; Leu et al., 2020]. Another disadvantage of treatment planning based on MRI are geometric distortions of the images resulting mainly from inhomogeneities in the static magnetic main field $\vec{B}_0$ and non-linearities in the gradient magnetic fields (G_x, G_y, G_z). Local changes in the magnetic susceptibility of the tissue can also contribute. These geometric distortions are handled by characterisation and correction [Shan et al., 2020]. MRI plays an important role in IGRT, too, in terms of MRgRT, which is addressed in the following paragraph.

Magnetic resonance guided radiotherapy

As mentioned in Section 2.2.3, MRI is an advantageous imaging modality for IGRT. In magnetic resonance guided radiotherapy (MRgRT), devices combining a linac and an MR scanner, so called MR Linacs, are applied [Raaijmakers et al., 2005; Lagendijk et al., 2008; Fallone et al., 2009; Lagendijk et al., 2014]. The advantages were already outlined in Chapter 1: Morphological imaging of the patient during the treatment with high soft tissue contrast and without additional exposure to ionising radiation allows for gating and tracking, i.e. a moving tumour is only irradiated in a certain position in order to spare healthy tissue. It also allows for adaptive radiotherapy (ART), i.e. the treatment is adapted to the current patient anatomy. Both measures enable dose escalation to the tumour and reduction of side effects by sparing of healthy tissue [Zou et al., 2018; Chin et al., 2020]. Functional imaging with MRI provides additional information valuable for tumour delineation and enables the evaluation of the treatment response [Pollard et al., 2017; Chin et al., 2020].

One of the currently clinically available MR Linac devices is the Elekta Unity™ machine. It was developed in a cooperation between the Universitair Medisch Cen-

trum (UMC) Utrecht, the Elekta Instrument AB Stockholm, Sweden, and Koninklijke Philips N.V., The Netherlands [Raaijmakers et al., 2005; Raaymakers et al., 2017]. This MR Linac combines a 1.5 T MR scanner by Philips and a linac featuring a 7 MV FFF photon beam (see Section 2.2.3) [de Pooter et al., 2020]. The static magnetic main field inside the bore of the scanner is directed perpendicular to the photon beam. The photon beam passes the cryostat of the MR scanner in a region without superconducting coils. The other clinically applied MR Linac device is the ViewRay MRIdian™ machine (ViewRay Inc., Oakwood, USA). It combines a 0.35 T MR scanner with a linac featuring a 6 MV FFF photon beam [Mutic and Dempsey, 2014; de Pooter et al., 2020]. The photon beam is oriented perpendicular to the static magnetic main field as in the Elekta Unity™ device. However, the photon beam does not pass through the MR scanner due to the split bore design of this MR Linac. There are further MR Linac devices in development with a parallel orientation of magnetic field and photon beam. One is the Australian MR Linac with a 1.5 T MR scanner and a linac featuring a 6 MV photon beam parallel to the magnetic field [Liney et al., 2016]. The MR Linac developed at the University of Alberta (Edmonton, Canada) features a 0.6 T magnetic field oriented parallel or perpendicular to a 6 MV photon beam [Fallone, 2014]. In addition, there is the concept of offline MRgRT, where a shuttle system is used for transporting the patient in treatment position from a conventional MR scanner to a conventional linac. The disadvantages of the offline approach are the need to transport the patient also implying additional sources of uncertainty and that intrafractional changes are not detectable. The advantages of the offline approach are, however, that neither special devices nor special efforts regarding dosimetry are required [Bostel et al., 2018; Zhou et al., 2018].

Dosimetry at MR Linacs, however, requires special attention since the static magnetic main field cannot be switched off easily. The secondary electron trajecories and, thus, the energy deposition (compare Section 2.3) are affected in a static magnetic field due to the Lorentz force. The static magnetic field can affect both, the dose deposition and the detector response. A magnetic field correction factor k_{mag} is, hence, required for dosimetry in static magnetic fields. This issue is discussed in more detail below.

FFF beams

The usage of flattening-filter-free (FFF) beams is becoming increasingly common in external beam RT [Arslan and Sengul, 2020]. An FFF beam is obtained if no flattening filter is positioned in the beam path resulting in an irregular lateral dose profile where the central dose is higher than the dose in the periphery (see e.g. Figure 5 in [Billas et al., 2021]). Beams passing a flattening filter feature, in contrast, a nearly contstant lateral dose profile over the radiation field. The main advantage of FFF beams is the reduced treatment time due to the increased dose rate [Xiao et al., 2015]. Furthermore, the reduced scattering in the radiation head due to the missing

flattening filter allows for improved beam modelling [Xiao et al., 2015; Arslan and Sengul, 2020] and leads to a lower out-of-field dose for the patient [Spruijt et al., 2013]. The usage of FFF beams is now possible since modern treatment planning connected with present computing capacity allows to take the shape of the beam profile into account.
An additional correction factor is required for dosimetry in FFF beams. The quantity absorbed dose-to-water (compare Section 2.4.1) is defined at one point but the measurement of absorbed dose-to-water has to be performed in the extended sensitive volume of a detector. If the lateral dose profile is not constant over the sensitive volume, as it is the case e.g. for measurements with alanine detectors at the Elekta Unity™ MR Linac, a correction factor k_{vol} is required considering the change of the lateral dose profile over the sensitive volume of the respective detector. This issue is further discussed in Section 2.4.2.

2.3 Physics of ionising radiation

Radiotherapy (RT) is based on the deposition of energy in tissue by charged particles. In RT with photons, these charged particles are secondary electrons. The following sections address the generation of the secondary electrons in interactions of photons with matter (see Section 2.3.1) and the interaction of the secondary electrons with matter (see Section 2.3.2).

2.3.1 Interaction of photons with matter

The interaction types of photons with matter relevant in the energy range applied in RT are photoelectric effect, Compton scattering, and pair production. The probablity for these interaction types depends on the energy of the incident photon and the atomic number of the absober material (see Figure 2.11). The photoelectric effect is dominant for low-energetic photons. It is an interaction between a photon and an electron in an inner atomic shell of an absorber atom. The photon is totally absorbed and its complete energy is transferred to the electron. The electron is released as a secondary electron with a kinetic energy equal to the energy of the incident photon minus the binding energy of the electron [Greilich and Osinga-Blättermann, 2018]. Compton scattering is dominant at intermediate energies roughly between 0.1 MeV and 10 MeV (see Figure 2.11). It is, thus, the most important interaction type in MV photon RT. It is an interaction between a photon and an electron that can be assumed as free. Photon and electron are scattered and at this, energy is transferred from the photon to the electron. The electron continues as a secondary electron with increased kinetic energy [Greilich and Osinga-Blättermann, 2018]. Pair production is dominant for high-energetic photons. It is an interaction between a photon with a minimum energy of $2 \times 511\,\mathrm{keV}$[13] and an electron-positron pair. The photon is totally absorbed and the electron-positron pair is generated. This interaction takes

[13] $2 \times 511\,\mathrm{keV}$ are the rest energy for an electron-positron pair.

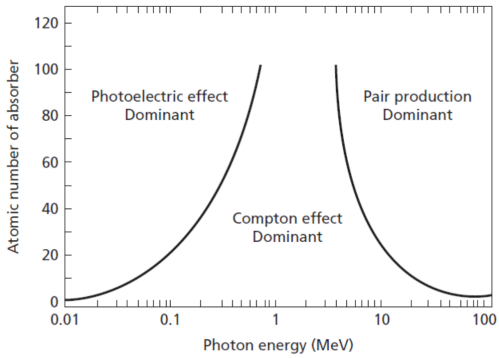

Figure 2.11: Relative importance of the interaction types photoelectric effect, Compton scattering, and pair production for photons in matter in dependence of the photon energy and the atomic number of the absorber. Illustration taken from [Pawlicki et al., 2016].

place near an atomic nucleus required for the conservation of momentum. The electron passes through the medium as a secondary electron; the positron forms another electron-positron pair decaying into mostly two photons (both 511 keV) [Greilich and Osinga-Blättermann, 2018]. Photons can, hence, pass through matter undergoing no, a single, or multiple interactions. In one interaction of a photon with matter the photon can transfer its total energy (photoelectric effect, pair production) or a part of its energy (Compton scattering). Each interaction results in the transfer of energy from a photon to an electron which continues as a secondary electron with increased kinetic energy.

2.3.2 Interaction of electrons with matter

As described in the previous section, interactions of photons with matter result in secondary electrons with increased kinetic energy. These electrons move through matter experiencing multiple interactions along their path. Only small amounts of their energy are transferred to the medium in each interaction. The mean energy loss per length $\frac{d\bar{E}}{dx}$ is called stopping power S (in units of Joule per metre) [Greilich and Osinga-Blättermann, 2018]; the mass stopping power $\frac{S}{\rho}$ is related to the density ρ of the absorber material: $\frac{S}{\rho} = \frac{d\bar{E}}{\rho \cdot dx}$ (in units of J m^2 kg^{-1}, or usually MeV cm^2 g^{-1}) [Reich and Burmester, 1990].
There are two different types of energy transfer: collision losses and radiation losses. In the case of collision losses, the electron interacts with the electrons of an absorber atom resulting in the excitation (i.e. transfer of one electron to a higher electron shell of the atom) or ionisation (i.e. ejection of an electron from the atom) of the atom [Podgorsak et al., 2005]. Electrons ejected from the absorber atoms can be energetic enough to produce further excitation of ionisation along their paths themselves. If an electron is ejected from an inner shell of the absorber atom, the vacancy is filled by an electron from an outer shell. The excess energy is re-

leased by photon emission (characteristic x-ray) or the excess energy is transferred to another electron of the atom which, then, leaves the atom as an Auger-Meitner electron [Schlegel, 2018; Greilich and Osinga-Blättermann, 2018]. In the case of radiation losses, Coulomb interactions occur between the initial electron and a nucleus of the absorber medium. The electron is scattered and loses energy by photon emission (bremsstrahlung) [Podgorsak et al., 2005]. The probability for bremsstrahlung decreases with the atomic number of the absorber medium. It is, thus, of minor importance in RT due to the relatively low atomic numbers occuring in human tissue. Collision losses are dominant in RT. They occur until the initial electron and the further released electrons transferred all their energy to the medium. The energy transferred to the medium by the secondary electrons is the absorbed dose.

2.3.3 Photon beams and secondary electrons in magnetic fields

The interaction between particles and a magnetic field is determined by the Lorentz force defined as

$$\vec{F}_L = q \cdot \vec{v} \times \vec{B} \tag{2.12}$$

in the absence of an electric field. Incident photons are, hence, unaffected by the magnetic field due to their missing charge, and their interactions with matter (see Section 2.3.1) are also not significantly affected in the presence of a magnetic field with flux densities used in MRgRT [Szymanowski et al., 2015]. The secondary electrons with charge $q = -e$ (with the elementary charge e) that are set in motion in these interactions of photons with matter are, however, affected by the magnetic field: The magnetic field affects the trajectories of the electrons between the single interaction points depending on the angle θ between the velocity $\vec{v}$ of the electron and the magnetic field $\vec{B}$. The absolute value of the Lorentz force is

$$F_L = q \cdot v \cdot B \cdot sin(\theta) \tag{2.13}$$

For $\theta = 0°$, i.e. (anti-)parallel alignment of electron velocity and magnetic field, the Lorentz force vanishes and the trajectories of the electrons are the same with and without magnetic field. For $\theta = 90°$, i.e. perpendicular orientation between electron velocity and magnetic field, the electrons experience the maximum Lorentz force perpendicular to their velocity and to the magnetic field resulting in circular paths (see Figure 2.12). All other angles θ result in helical paths since only the velocity component perpendicular to the magnetic field contributes to the Lorentz force (see Equation 2.12). The curved trajectories of the secondary electrons in the magnetic field are the reason for the changes in the dose dostribution in a medium in the presence of a magnetic field. Despite energy losses due to synchrotron radiation, the path length of electrons is the same with and without a magnetic field [de Pooter et al., 2020], but the curvature of the trajectories results e.g. in a shift of the depth dose profile (see Figure 2.13) for MR Linacs with perpendicular orientation of

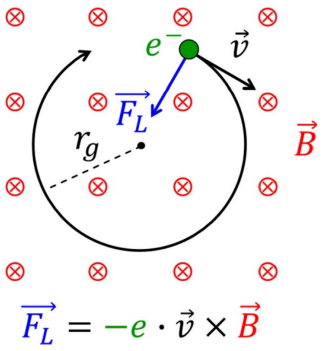

Figure 2.12: Circular path of an electron with velocity $\vec{v}$ in a magnetic field $\vec{B}$ for an angle of $\theta = 90°$ between $\vec{v}$ and $\vec{B}$. Illustration taken from [de Pooter et al., 2020].

photon beam and magnetic field (see Section 2.2.3). The electrons are "swept aside" in perpendicular direction to the magnetic field [de Pooter et al., 2020]. The region in which the dose is deposited is, thus, tilted and closer to the point of interaction in the presence of a magnetic field; the build-up distance is reduced and the lateral profile is asymmetric [Raaijmakers et al., 2007a, 2008; de Pooter et al., 2020]. Pronounced effects occur also at interfaces of media with different densities, e.g. water and air. In the lower density medium, where the distances between the interaction points are larger, the curvature of the electron trajectories is more pronounced resulting in a return of the electrons to the medium with higher density and, hence, an increase in the absorbed dose in the medium with higher density (electron return effect (ERE), [Raaijmakers et al., 2005]).

2.4 Radiation dosimetry

2.4.1 Dosimetric principles

Dosimetry is the metrology of the interaction of ionising radiation with matter [Reich and Burmester, 1990]. The quantity absorbed dose defined in a single point ("Punktgröße") is used to describe the energy transferred to matter in these interactions. The absorbed dose D is defined via the mean energy $\mathrm{d}\bar{E}$ imparted to the mass element $\mathrm{d}m$:

$$D = \frac{\mathrm{d}\bar{E}}{\mathrm{d}m} \tag{2.14}$$

The unit of the absorbed dose is Joule per kilogramme, which is also referred to as Gray (Gy).
Direct measurements of the impact of ionising radiation on matter are not possible. Only the effects of the impact of ionising radiation can be measured, e.g. ionisation, light emission, or chemical changes [Podgorsak et al., 2005]. The absorbed dose is

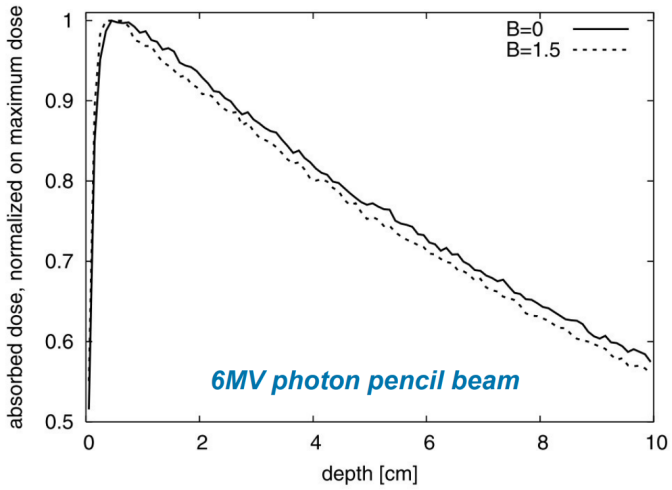

Figure 2.13: Monte Carlo (MC) simulations for depth dose profiles of a 6 MV photon beam without magnetic field and in the presence of a magnetic field with 1.5 T flux density perpendicular to the photon beam. The abscissa shows the depth in water, the ordinate shows the relative dose. The profile in the presence of the magnetic field is shifted to lower depths. Illustration modified from [Raaymakers et al., 2004].

mostly determined via the probe method ("Sondenmethode") in RT, i.e. a detector as a probe ("dosimeter") is placed in or on the medium for which the absorbed dose is to be determined and the absorbed dose is obtained from the indication of the probe together with additional quantities ("Hilfsgrößen") [Hartmann, 2018]. This method does not allow to obtain the absorbed dose D defined in one point but the mean absorbed dose $\bar{D}$ due to the finite extent of the sensitive volume of the detectors. The mean absorbed dose $\bar{D}$ is

$$\bar{D} = \frac{\bar{E}}{m} \tag{2.15}$$

i.e. the mean energy $\bar{E}$ absorbed in a mass m due to the impact of ionising radiation. There is a wide variety of dosimeters. The dosimetry with ICs (see Section 2.4.2) is very common. Of central interest in the present thesis is the dosimetry with alanine (see Section 2.4.3).
The target quantity ("Zielgröße") of dosimetry in RT is generally the absorbed dose-to-water D_W where the mass m consists of water. This absorbed dose-to-water serves as a measure for the effect of ionising radiation in human tissue. The short term "dose" usually refers to this absorbed dose-to-water. Water is chosen as it is easily available and unproblematic to handle while it is similar to human tissue (which consists of water to a great extent) in terms of its radiation transport properties [Hartmann, 2018]. Hence, the determination of absorbed dose in RT usually takes place in a water phantom, i.e. a tank of water [Hartmann, 2018].
The PTB has the legal duty to realise the physical quantity of absorbed dose-to-

water. The institute is operating a water calorimeter[14] as a primary standard to this aim [Krauss, 2006] (absolute dosimetry). Other dosimeter types can be calibrated via the primary standard, i.e. a relation is established between the indication of the respective detector and the true value of the absorbed dose-to-water (reference dosimetry). These calibrations can be performed directly to the primary standard or indirectly by application of one or several transfer standards.
An important task in clinical radiation dosimetry is the calibration of the linac output in terms of reference dosimetry. Transmission ICs (see Section 2.4.2), where the beam passes through thin entry and exit windows, are often applied to this aim. Transmission ICs are usually included in the accelator heads of clinical linacs providing a reading in arbitrary monitor units (MU). By calibration, this reading in MU is related to the absorbed dose-to-water D_W.
For ensuring consistency in the dose determination among different RT sites, there are Codes of Practice, e.g. DIN 6801-1 [DIN-Normenausschuss Radiologie (NAR), 2016] or TRS 398 [Andreo et al., 2000], describing the general procedures to be used in clinical dosimetry and defining the reference conditions for such calibrations, e.g. a radiation field size of 10 cm×10 cm, a measurement depth in water of 10 cm for MV photons and of 5 cm for Cobalt-60 gamma radiation, or a source to surface distance (SSD)[15] of 100 cm. Dosimeters utilized according to these standards have to feature a calibration traceable to a primary standard. Further, correction factors have to be applied for the quantities influencing the determined absorbed dose-to-water (see Section 2.4.2).
Current Codes of Practice do not include dosimetry in MRgRT. A formalism was, however, proposed by [van Asselen et al., 2018] including a correction factor for the magnetic field (see Sections 2.2.3 and 2.4.2).
Besides reference dosimetry aiming at the determination of the absolute value for the absorbed dose-to-water D_W, there is also relative dosimetry determining absorbed doses-to-water normalised to a certain value, e.g. the maximum absorbed dose-to-water. Valuable outputs for clinical dosimetry are depth dose curves (ddcs) showing the relative absorbed dose-to-water with increasing water depth (see Figure 2.13) or lateral profiles of the radiation field showing the absorbed dose-to-water in lateral direction, i.e. perpendicular to the radiation beam.

2.4.2 Reference dosimetry with ionisation chambers

Air-filled ionisation chambers (ICs) are commonly used in clinical radiation dosimetry since they are easy to handle while they provide a reproducible reading without

[14] Water calorimetry allows for the most fundamental determination of absorbed dose-to-water. The quantity is determined directly in water and not in another detector material like air or alanine [Greilich and Osinga-Blättermann, 2018]. Water calorimetry is based on the measurement of the temperature rise ΔT due to the energy transfer by ionising radiation, which is about 0.24 mK per Gray [Greilich and Osinga-Blättermann, 2018].

[15] The SSD is the distance between the target for the generation of bremsstrahlung inside the accelerator head of the linac ("source") and the front window of the water phantom ("surface").

any waiting time. Their function principle, which is illustrated in Figure 2.14, is based on the detection of radiation induced charge carriers. An air-filled IC consists of an air cavity between two electrodes of opposite polarity. The energy transfer in the interactions of secondary electrons with air molecules (see Section 2.3.2) results in the generation of pairs of positive and negative charge carriers (ion pairs) in the air cavity. Since the air cavity is located between an anode and a cathode, the pairs of charge carriers are separated if an electric field is applied and they are collected by the anode and the cathode, respectively. This results in a current or – if integrated over time – in a charge proportional to the amount of generated charge carriers. Current or charge are measured and indicated by an electrometer connected to the IC. The quotient of this indication M and the causative absorbed dose D is called response R:

$$R = \frac{M}{D} \tag{2.16}$$

In principle, the absorbed dose-to-water can be determined absolutely with ICs via the energy W_{air} required for the generation of one pair of charge carriers in air and the application of cavity theory since the absorbed dose-to-air has to be converted into the absorbed dose-to-water [Podgorsak et al., 2005]. This approach is, however, inconvenient in clinical dosimetry since e.g. the exact measures of the air cavity are required which vary due to manufacturing. In clinical routine, the absorbed dose-to-water is determined with ICs via calibration against a primary standard as described in codes of practice like [Andreo et al., 2000] or [DIN-Normenausschuss Radiologie (NAR), 2016], see Section 2.4.1.
If an IC is applied under reference conditions, i.e. the conditions stated in the code of practice under which its calibration has been performed, the absorbed dose-to-water D_W is obtained as

$$D_W = M \cdot N_{D_W,Q_0} \tag{2.17}$$

with the reading M of the IC, i.e. the current or charge indicated by the electrometer, and the calibration coefficient N_{D_W,Q_0} for the absorbed dose-to-water in the reference radiation quality Q_0, which is usually Cobalt-60 gamma radiation. There are, however, several influence quantities that affect the indication of ICs and usually, the conditions in clinical radiation dosimetry differ from the reference conditions applied during the calibration of the ICs. It is, then, necessary to include a product of correction factors k_i in Equation 2.17 in order to correct the raw reading M_{raw} of the IC for the various influence quantities differing from the reference conditions:

$$D_W = M_{raw} \cdot N_{D_W,Q_0} \cdot \prod_i k_i \tag{2.18}$$

The correction factors k_i relevant in this thesis are described in the following paragraphs.

Radiation quality correction factor k_Q

If the radiation quality Q in the application of the IC differs from the reference radiation quality Q_0 in the calibration of the IC, a radiation quality correction factor k_Q has to be included in Equation 2.18 which is defined as

$$k_Q = \frac{N_{D_W,Q}}{N_{D_W,Q_0}} \tag{2.19}$$

The calibration factor $N_{D_W,Q}$ and, hence, the radiation quality correction factor k_Q can be determined experimentally e.g. by measurements with a water calorimeter and an IC in the radiation quality Q [Krauss and Kapsch, 2014]. For photon beams, the radiation quality can be quantified by the tissue phantom ratio (TPR). The $\mathrm{TPR}_{20,10}$ is obtained from the indications of a dosimeter irradiated in 20 cm and 10 cm depth within a water phantom under reference conditions [Deutsches Institut für Normung e.V., 2008]. At that, the dosimeter stays in the same position; the front of the water phantom is closer to the radiation source for the irradiation in 20 cm water depth.

Temperature and air pressure correction factor k_{TP}

The indication of an IC depends on the air mass in the cavity. The ICs used in this thesis are air-vented. Thus, the air mass is affected by variations in the temperature and the air pressure. If the temperature T and the air pressure p in the application of the IC deviate from the reference conditions ($T_0 = 293.15\,\mathrm{K}$, $p_0 = 1013.25\,\mathrm{mbar}$), a temperature and air pressure correction factor k_{TP} has to be applied which is defined as

$$k_{TP} = \frac{p_0 \cdot T}{p \cdot T_0} \tag{2.20}$$

Humidity correction factor k_{hum}

The humidity influences several parameters that have an impact of the indication of ICs, e.g. the air density, the energy W_{air} required for the generation of one pair of charge carriers in air (see above), or the mass stopping power for electrons (see Section 2.3.2) [IAEA, 2008]. However, these effects usually compensate each other and if the relative humidity is between 20 % and 70 % throughout the application of the IC (the reference condition for the calibration is a relative humidity of 50 %), no humidity correction factor k_{hum} is required [Bichsel et al., 1979; McEwen and Taank, 2017].

Polarity correction factor k_{pol}

The response of an IC can change significantly when the polarity of the voltage U applied to the electrodes of the IC is changed. This polarity effect depends among

others on the radiation quality, the field size, and the measurement depth [Derikum, 1992]. No correction for the polarity effect is required if the magnitude and the polarity of the voltage as well as the radiation quality are the same in the calibration and in the application of the respective IC. Otherwise, the correction factor k_{pol}, that can be calculated via the indications of the respective IC for positive and negative polarity, has to be considered.

Recombination correction factor k_{ion}

The charge collected by the electrodes of the IC can be incomplete due to the recombination of the radiation induced charge carriers (ions). The respective correction factor for the ion recombination k_{ion} can be determined experimentally via a so called "Jaffé plot" as it is described in the appendix of [Deutsches Institut für Normung e.V., 2008]: The voltage U applied to the electrodes of the IC has to be varied within the maximum limits according to the manufacturer and the indications M_U of the IC for these voltages U have to be recorded. The reciprocal of the indications $\frac{1}{M_U}$ is then plotted as a function of the reciprocal of the voltages $\frac{1}{U}$. There should be a linear part in the resulting graph which allows to extrapolate the reciprocal of the indication M_S for the experimentally not accessible case of an infinitely high voltage U. The recombination correction factor k_{ion} is then obtained as

$$k_{ion} = \frac{M_S}{(M - M_0) \cdot k_{TP} \cdot k_{pol}} \tag{2.21}$$

with the indication M_S for an infinitely high voltage U, the indication M for the usually applied voltage U, the zero indication M_0 of the IC, and the correction factors for temperature and air pressure k_{TP} and for the polarity effect k_{pol}.

Leakage current correction factor $k_{leakage}$

The leakage current is the current registered by an electrometer connected to an IC in the absence of ionising radiation [IAEA, 2008]. No correction factor $k_{leakage}$ is required if the electrometer is warmed up and zeroed prior to a measurement.

Electrometer correction factor k_{elec}

The correction factor k_{elec} addresses a possible effect due to the electrometer applied.

Linac output correction factor k_{output}

The correction factor k_{output} accounts for drifts in the output of the linac applied for the irradiation of the IC.

Volume correction factor k_{vol}

As described in Section 2.2.3, the absorbed dose decreases from the center of the radiation field to the exterior in case of FFF beams. The quantity absorbed dose-to-water D_W is defined in one point but the experimental determination of the absorbed dose-to-water D_W has to be performed in the extended sensitive volume of a detector (see Section 2.4.1). If the lateral dose profile in the application cannot be assumed as constant over the sensitive volume of the detector, a volume correction factor k_{vol} is required considering the variation of the lateral dose profile over the sensitive volume of the respective detector.
There are two possibilities for determining the correction factor k_{vol}: (1) by using Equation (54) from [Palmans et al., 2017] as it is for example done in [Billas et al., 2021], and (2) dividing the integral of a constant function with the value of the central axis dose over the length of the detector by the integral of the lateral dose profile over the length of the detector, see Figure 2.15, as it is for example done in [de Prez et al., 2019] (Sec. 2.4).

Magnetic field correction factor k_B

A magnetic field correction factor k_B (or denoted k_{mag} for the alanine dosimeter in this thesis, see Section 2.4.3) has to be included if an IC calibrated in the absence of a magnetic field is applied in the presence of a magnetic field[16] due to the changes in the dose deposition in the presence of a static magnetic field (see Sections 2.2.3 and 2.3.3).
Instead of using the calibration factor N_{D_W,Q_0} for a calibration in the reference radiation quality Q_0, the correction factor for the radiation quality k_Q, and the magnetic field correction factor k_B (see Equation 2.18), it is also possible to use the magnetic field calibration factor $N_{D_W,Q,B}$ since it is

$$N_{D_W,Q,B} = N_{D_W,Q_0} \cdot k_Q \cdot k_B \tag{2.22}$$

The magnetic field calibration factor can be obtained experimentally by using a water calorimeter that can be applied in the presence of a static magnetic field [de Prez et al., 2019]. Please note that the radiation quality during the calibration and during the application has to be the same in this case. The absorbed dose-to-water D_W can than be obtained as

$$D_W = M_{raw} \cdot N_{D_W,Q,B} \cdot \prod_i k_i \tag{2.23}$$

with the correction factors k_i as described in the preceding paragraphs but without the correction factors k_Q for the radiation quality and k_B for the magnetic field since they are already included in the calibration factor $N_{D_W,Q,B}$.

[16] A correction is also required if the magnetic flux density of the field during calibration and application is not the same.

Types of ICs

There are many different types of ICs. Relevant for this thesis are air-filled transmission ICs and Farmer-type ICs. Transmission ICs are commonly mounted within the accelerator heads of a clinical linacs. Their profile has dimensions in the size of the radiation beam while their extent in beam direction is preferably thin. Figure 2.16 shows an example for a transmission IC. Farmer-type ICs are very versatile not least due to their small size. They are constructed cylindrically with one central electrode wire and a surrounding electrode wall, see Figure 2.17. The transmission and Farmer-type ICs used in this thesis are described in detail in Chapter 3.

Air gaps around ICs in magnetic fields

Non-waterproof ICs are placed in a waterproof sleeve for measurements in water phantoms. Measurements with ICs in reference dosimetry are also often taken in solid phantoms. Both situations include small air gaps between the IC and the sleeve or between the IC and the phantom. These air gaps require attention for dosimetry in the presence of magnetic fields.
The first study on the effect of sub-millimetre air gaps for dosimetry with ICs in static magnetic fields was conducted by [Hackett et al., 2016]. [Hackett et al., 2016] investigated air gaps of 0.1 mm to 0.3 mm between ICs and waterproof sleeves in water phantoms (among others). For irradiations in the presence of a magnetic field with flux density 1.5 T accomplished with an MR Linac, it was found that filling the small air gaps between the (waterproof) ICs and the sleeve with water resulted in an increase of the ICs' responses of 0.7 % to 1.2 %. The same experiment performed at a conventional linac in the absence of a magnetic field resulted in changes of the ICs' responses below 0.3 %.
[O'Brien et al., 2017] rotated ICs inserted into plastic phantoms around their long axis, which resulted in varying sub-millimetre air gaps. In the absence of a magnetic field, these varying air gaps resulted in a response variation below 0.1 %. In the presence of a magnetic field with flux density 1.5 T, the variation was larger than 1 %.
An early MC study of air gaps around ICs was provided by [Malkov and Rogers, 2016]. [Malkov and Rogers, 2016] simulated air gaps of 0.5 mm and 1.0 mm size around an IC in magnetic fields with flux densities up to 2 T using the EGSnrc code (see Section 2.5). Variations in the response of around 1 % were found.
[Agnew et al., 2017] presented a detailed study on asymmetric air gaps around ICs. Irradiations were performed with a Cobalt-60 beam while the ICs were placed in a solid phantom between the pole shoes of an electromagnet. The study focussed on magnetic flux densities around 1.5 T. The custom-made solid phantom allowed to rotate an asymmetric air gap around the ICs. The maximum variation found due to this air gap was (8.5 ± 0.2) %, the minimum variation was (1.1 ± 0.1) %. Filling the asymmetric gap with water reduced the changes due to rotation to negligible values.
[O'Brien and Sawakuchi, 2017] aimed at studying sub-millimetre air gaps around

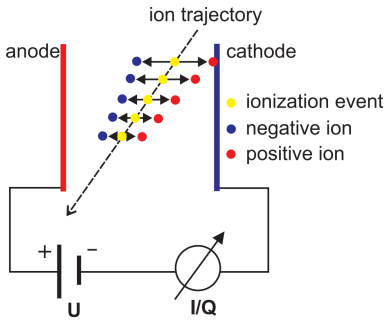

Figure 2.14: Function principle of an IC. Illustration taken from [Osinga-Blättermann, 2017].

ICs in solid phantoms in the presence of a static magnetic field by means of Geant4 MC simulations. The response was investigated for symmetric and asymmetric air gaps modeled around ICs for magnetic flux densities up to 1.5 T. In order to better understand the resulting effects, the gyroradii of the electrons were scored and the total energy deposited within the IC was divided according to its origin from (1) inside the IC, (2) the immediate vicinity around the IC, and (3) outside the IC. A variation of 1.6 % in the IC response was found for an asymmetric air gap with 0.2 mm width, while symmetric air gaps up to 1.4 mm led to effects smaller than 0.5 %. The information on the gyroradii and on the origin of the deposited dose allowed the conclusion that the changes found in the IC response are not due to the ERE ([Raaijmakers et al., 2007b, 2005, 2008]) since the gyroradii observed (4 mm) are too large for that. It was, however, found that the air gaps around the IC reduce the energy contribution of electrons released in the immediate vicinity of the IC. In the presence of a magnetic field, this loss cannot be completely compensated by electrons released in more distant regions due to the reduced electron range in the magnetic field caused by the bent trajectories.
The overall recommendation from the publications mentioned above is to use only waterproof ICs completely immersed into water for dosimetry in the presence of magnetic fields.

2.4.3 Reference dosimetry with alanine

Principle of alanine dosimetry

The measurement principle of alanine dosimetry is based on the chemical reaction of alanine to ionising radiation. L-α-alanine[17] is an amino acid; its structural formula is shown in Figure 2.18. Different stable radicals are formed in alanine due to the impact of ionising radiation, see Figure 2.19 [Malinen et al., 2003a].[18] Radicals

[17] The term “alanine” refers to L-α-alanine in the following.

[18] It is usually assumed that three radicals are formed if an energy of 100 eV is absorbed [Anton et al., 2009].

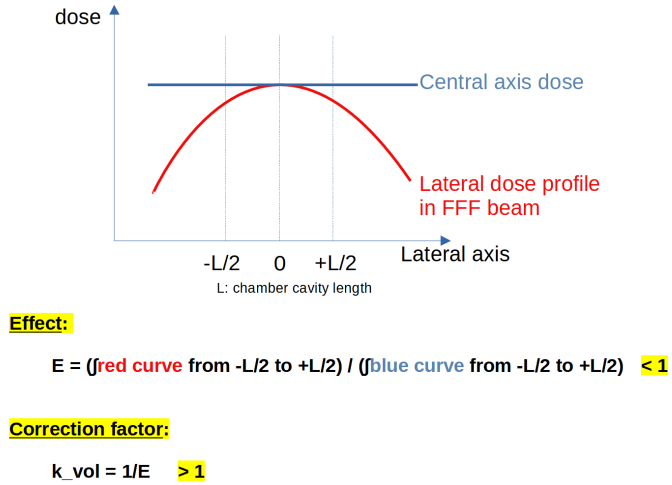

Figure 2.15: Illustration of the determination of the correction factor k_{vol}.

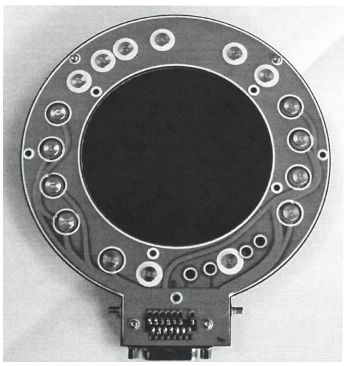

Figure 2.16: The transmission IC installed within the accelerator head of the Elekta Precise Treatment System™ linac at the PTB. The photo is taken from the Elekta manual for this linac.

Figure 2.17: A typical Farmer-type IC (PTW 30013) for dosimetry in RT together with a suitable build-up cap (build-up caps can be used for measurements with ICs in air in order to generate more secondary electrons) [PTW-Freiburg].

feature unpaired electrons and behave, thus, paramagnetic[19]. The total concentration of radicals formed is proportional to the absorbed dose-to-alanine and, hence, also to the absorbed dose-to-water. The concentration of the radicals and, thus, the absorbed dose-to-water can be determined by EPR spectroscopy[20] of the alanine pellets due to the paramagnetic behaviour of the radicals (see below) [Bradshaw et al., 1962]. It was first assumed that there is only one radical species (R1 in Figure 2.19), which is formed by deamination, i.e. the removal of the amino group. Now, it is, however, known that there are at least two further radical species [Sagstuen et al., 1997; Heydari et al., 2002; Malinen et al., 2003a]: One is formed by hydrogen abstraction from the central carbon atom (R2 in Figure 2.19); the other with its suggested structures labeled as R3 in Figure 2.19 is a minority species (5-10 % compared to 55-60 % and 30-35 % for R1 and R2, respectively) [Malinen et al., 2003a].[21] Most commonly, alanine powder is pressed into small cylindrical pellets for the use in dosimetry. An alanine pellet as applied in this work is shown in Figure 2.20 on the left. Advantages of the alanine dosimeter are e.g. the small detector size, the close similarity of alanine to water[22] and human soft tissue with respect to the absorption of radiation energy [Ciesielski et al., 2003], the minor dependence of the response on the radiation quality for MV x-rays [Sharpe et al., 1996; Bergstrand et al., 2003; Zeng et al., 2004; Anton et al., 2008][23], the linearity in the dose response up to 10 kGy [Olsson et al., 2002; Malinen et al., 2003a], the non-destructive readout, the high stability of the radiation induced radicals, the independence of the dose rate, and the low cost and non-toxicity of the alanine pellets [Regulla and Deffner, 1982]. Alanine dosimetry is a well-established method for the determination of absorbed doses in industry since decades e.g. for food preservation, the sterilisation of medical devices, or the preparation of drinking water [Regulla and Deffner, 1982; Schneider et al., 1985; Regulla, 1999]. The typical absorbed doses in industrial applications are in the range of some kGy. The potential of the alanine dosimeter for dosimetry in RT, not least because of the water-equivalence mentioned above, was noted early. The alanine dosimeter seemed especially suited as a reference and transfer dosimeter, e.g. due to its small detector size, its non-destructive readout, and the stability of the

[19] Stable molecules feature electron bonds by pairs of electrons whose spins are oriented in opposite direction. Their magnetic moments cancel, thus, and there is no interaction with an external magnetic field.

[20] The term electron spin resonance (ESR) spectroscopy is also commonly used for the same technique.

[21] All radical species contribute to the alanine EPR spectrum. The behaviour of the three components regarding the absorbed dose is very similar, but their behaviour regarding fading (see below) and spectrometer microwave power differs significantly [Malinen et al., 2003a]. Since the alanine test and base pellets are stored and read out under identical conditions in this work, these differences do not impair the applied alanine dosimetry procedure.

[22] Water-equivalence is an important aspect in dosimetry for RT since human soft tissue can be assumed to be water-equivalent for many issues.

[23] The relative response, i.e. the ratio r of the determined absorbed dose-to-water D^c and the known value of the delivered absorbed dose-to-water D ($r = \frac{D^c}{D}$) [Anton et al., 2013], varies less than 1 % between Cobalt-60 (average photon energy 1.25 MeV) and 25 MV x-rays [Anton et al., 2013].

radicals [Regulla and Deffner, 1982; Regulla, 1999]. From the mid nineties on, the range of absorbed doses-to-water accessible with the alanine dosimeter was extended to the therapeutically relevant low absorbed doses-to-water of a few gray [Sharpe et al., 1996; Sharpe and Sephton, 1998] allowing for the application of alanine dosimetry in RT. The alanine dosimeter has been used at the UK's NPL [Sharpe et al., 1996; Sharpe and Sephton, 1998], at the USA's NIST [Sleptchonok et al., 2000; Nagy et al., 2000a,b, 2002], at Italy's ISS [Bartolotta et al., 1993; De Angelis et al., 2000], and in Denmark [Hansen et al., 1987; Olsen et al., 1990]. The alanine dosimeter has been applied in several specialised fields of RT: for auditing the implementation of IMRT in the UK [Budgell et al., 2011], for the validation of the absorbed dose in helical tomotherapy [Perichon et al., 2011; Panzeca et al., 2018], and at the Cyberknife RT device [Garcia et al., 2011], exploiting e.g. the suitability of the alanine dosimeter for dose determinations in small irradiation fields. Latest developments of alanine dosimetry in RT are e.g. the addition of gadolinium in order to enhance the sensitivity of the dosimeter [Marrale et al., 2011] or the determination of the absorbed dose-to-water in therapeutical proton beams [Marrale et al., 2016]. At the PTB, the alanine dosimetry system was set up by Mathias Anton; he maintained the system for about a decade [Anton, 2005, 2006; Anton et al., 2008, 2009, 2013; Anton and Büermann, 2015].

Implementation for the present work

The alanine detectors applied in this thesis are composed of a stack of four alanine pellets, each with a diameter of 4.85 mm and a height of approximately 2.8 mm (see Figure 2.20 on the left). The pellets are made of about 90 % polycrystalline L-α-alanine powder together with about 10 % paraffin as a binder (Harwell dosimeters, UK). Four alanine pellets per detector were chosen as a trade-off between obtaining a favourable mean signal of the pellets and the time required for the readout of all alanine pellets.[24] In addition, the use of several alanine pellets per detector ensures that results are obtainable even if one pellet should get damaged. These alanine detectors are stored in microtiter plates with one hole per alanine pellet. The pellets composing one detector are stored in the same column.[25] This ordered storage is of importance since the alanine pellets themselves cannot be labeled. For irradiations, the alanine pellets are placed in a holder made of polymethyl methacrylate (PMMA) (see Figure 2.20 on the right) in this work. This allows on the one hand to hold the stack of the four alanine pellets of one alanine detector in place; on the other hand, it allows to prevent direct contact of the alanine pellets with water during irradiations in water phantoms since the alanine pellets are not waterproof. The PMMA holder applied has the outer shape of a typical Farmer-type IC – the model was a PTW 30013 IC, see Figure 2.17 – which allows to use the same setups as for

[24] This optimum was found by Mathias Anton during his years of working on alanine dosimetry.

[25] The lines in this microtiter plates are labelled with letters, the columns with numbers. The labelling of the detectors composed of four pellets is, accordingly, e.g. hm27-a5...d5, with hm27 the label of the respetive microtiter plate.

ICs. The holder can be screwed open at the position discernible due to the black O-ring (see Figure 2.20) in order to exchange the alanine detector inside.

Readout using EPR spectroscopy

The essential components of a spectrometer are a source for electromagnetic radiation, a sample to be investigated, and a detector for observing the absorption. The general layout of the EPR spectrometer used in this work for the readout of the alanine detectors is shown in Figure 2.21. The microwave bridge top left serves as the source for the electromagnetic radiation (microwaves are used) and as the detector. The microwave cavity contains the sample inside a resonator, which helps to amplify the weak signal of the sample. The surrounding electromagnet is needed in order to provide the magnetic field in which the magnetic moments of the unpaired electrons align (see below), and the console on the right is used for signal processing and control electronics; it is connected to a computer for analysing the data [Weber et al., 1998]. The spectrometer used in this thesis is a "reflection spectrometer", as it measures the changes in the amount of radiation which is reflected back from the sample. The microwave bridge contains a so called circulator ensuring that the microwaves from the source reach only the cavity with the sample and not the detector, and that the reflected microwaves from the sample reach only the detector and not the source [Weber et al., 1998]. The cavity can be understood as a metal box resonating with microwaves like an organ pipe resonating with sound waves [Weber et al., 1998]. At the resonance frequency of the cavity with the sample, no microwaves are reflected back due to standing waves inside the cavity [Weber et al., 1998]. The system is tuned such, that the cavity with the sample is in resonance. The transfer of microwaves to the cavity is changed ("coupling") when the sample absorbes the microwave energy (see below) resulting in the fact that then, microwaves are reflected back to the microwave bridge. The detector converts this reflected microwave signal into a current that results in the EPR signal [Weber et al., 1998].
For the readout of the dose information of an irradiated alanine pellet via EPR spectroscopy, the alanine pellet is placed inside the cavity within the homogeneous static magnetic field generated between the pole shoes of the electromagnet of the EPR spectrometer, see Figures 2.22 and 2.23, and the system is tuned such, that the cavity with the sample is in resonance, i.e. no microwaves are reflected back to the microwave bridge. The energy of the two possible spin states ($m_s = \pm\frac{1}{2}$) of the unpaired electrons at the radicals in the alanine sample differs by the energy ΔE within this magnetic field, corresponding to parallel or antiparallel alignment of the magnetic moment of the electron with the magnetic field. The populations of these two states are determined by the Boltzmann distribution in case of thermal equilibrium. Transitions between the two states can be induced by the absorption of electromagnetic radiation with a frequency ν matching the resonance condition

$$\Delta E = h \cdot \nu = \mu_B \cdot g \cdot B \tag{2.24}$$

with the energy difference ΔE in a magnetic field with flux density B, Planck's constant h, the frequency of the electromagnetic radiation ν, the Landé factor g (≈ 2 for the radicals) and the Bohr magneton μ_B (see Equation 2.8). Microwaves with frequencies ν of about 10 GHz (X-band) are typically applied in alanine dosimetry. For these frequencies, the magnetic flux density B has to be around 0.35 T in order to fulfil the resonance condition for an alanine sample. The cavity with the sample is, then, due to the absorption no longer in resonance and microwaves are reflected back to the bridge, resulting in the EPR signal. The absorption of the alanine sample is proportional to the amount of spins and, thus, radicals involved. Due to technical advantages, it is not the frequency ν which is varied to fulfil the resonance condition (see Equation 2.24), but the magnetic flux density B of the electromagnet. In the EPR spectrometer used in this work (see Chapter 3), a range of 30 mT around the centered value of 348.096 mT is scanned. Since the signal to be measured is comparatively small, the lock-in technique is applied, resulting in the fact that the first derivative of the absorption signal is detected. An example for a resulting alanine EPR spectrum is shown in Figure 2.22 on the right. The abscissa shows the scanned range of the magnetic flux density in Millitesla while the ordinate shows the measured signal, i.e. the derivative of the absorption signal. The EPR spectrum of alanine features several peaks due to the hyperfine interaction of the spin of the unpaired electron with the surrounding nuclear spins.

Determination of the absorbed dose-to-water

The peak-to-peak amplitude of the central feature of the alanine EPR spectrum divided by the mass of the respective alanine pellet can be used as the measure for the absorbed dose-to-alanine [Bradshaw et al., 1962]. Amplitude and mass are, thus, essential quantities in alanine dosimetry. The determination of the absorbed dose-to-water D[26] with the alanine dosimeter requires a calibration with alanine pellets irradiated to a known absorbed dose-to-water, e.g. in the Cobalt-60 reference field at the PTB, linking the intensity of the alanine EPR signal to a value of absorbed dose-to-water [Kuntz et al., 1996].[27] The analysis method using the peak-to-peak amplitudes is applied by several groups working on alanine dosimetry. It was described here since it is quite intuitive, although the analysis method applied in this work uses a slightly different approach: an EPR spectrum of a "base" alanine pellet irradiated to a known absorbed dose-to-water ("base function") is fitted to the EPR spectrum of a "test" alanine pellet by means of least squares. This method first mentioned by [Sharpe et al., 1996] is based on the assumption that only the amplitude of the alanine EPR spectrum is affected by the absorbed dose and not the shape of the signal. This assumption is valid in the dose range relevant for this

[26] In order to simplify the equations, D instead of D_W is used for the absorbed dose-to-water from now on.

[27] The usage of a complete calibration curve is described in [Anton, 2005, 2006]. In this work, the calibration is established by comparison with one high dose value (here 25 Gy) as described in [Anton et al., 2013].

work [Anton, 2006]. The factor by which the base function has to be multiplied for the best fit to the EPR spectrum of the alanine "test" pellet is used as amplitude[28]. The method using the least squares fit is advantageous for the elimination of underground signals, which can distort the peak-to-peak amplitude.[29]
The absorbed dose-to-water D in alanine dosimetry can be determined as

$$D = \frac{A}{m} \cdot m^b \cdot D^b \tag{2.25}$$

A is the amplitude of an irradiated alanine "test" pellet, m is its mass, m^b is the mass of an alanine pellet irradiated to a known absorbed dose-to-water ("base pellet"), and D^b is this known absorbed dose-to-water. In order to remind of the fact, that the value of the absorbed dose-to-water originates from an amplitude in an alanine EPR spectrum, the dose-normalised amplitude A_D with the dimension of an absorbed dose is used instead of D:

$$A_D = \frac{A}{m} \cdot m^b \cdot D^b \tag{2.26}$$

Further modifications of this equation are required in order to correctly represent the experimental situation. As mentioned above, alanine detectors composed of four alanine pellets are used in this work. Thus, the mean masses $\bar{m}^{(b)}$ and the mass-related mean amplitude A_m are used:

$$A_D = \frac{A_m}{\bar{m}} \cdot \bar{m}^b \cdot D^b \tag{2.27}$$

The mass-related mean amplitude A_m is defined as

$$A_m = \bar{m} \cdot \frac{1}{n} \sum_{i=1}^{n} \frac{A_i}{m_i} \tag{2.28}$$

with the individual amplitude values A_i, the individual pellet masses m_i and the mean $\bar{m}$ of n masses.
Furthermore, several correction factors K_i (see Section 2.4.2) have to be included in Equation 2.27 for all relevant influencing quantities differing between the irradiation and storage conditions of the alanine test and base pellets. Since all corrections refer to a certain base, the correction factors for the alanine test pellets k_i are given in relation to the correction factors k_i^b for the respective base pellets:

$$K_i := \frac{k_i}{k_i^b} \tag{2.29}$$

[28] The term "amplitude" is used in both approaches alike, i.e. for the peak-to-peak amplitude and the factor obtained from the least squares fit.

[29] The Matlab routines performing these fits were developed by Mathias Anton. More information regarding the fitting procedure can be found in [Anton, 2006].

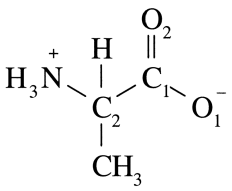

L-α-alanine

Figure 2.18: Structural formula of L-α-alanine reproduced from [Malinen et al., 2003a].

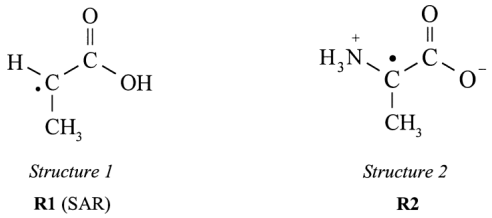

Structure 1
R1 (SAR)

Structure 2
R2

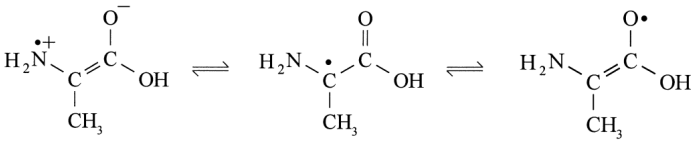

Structure 3
R3

Figure 2.19: Structural formulae of radiation induced radicals in L-α-alanine reproduced from [Malinen et al., 2003a]. The abbreviation SAR stands for "stable alanine radical" in this case, a label often used for radical R1.

The corrected dose-normalised amplitude A_D^{corr} obtained by averaging the results of several alanine pellets irradiated together as one alanine detector is, thus, given as

$$A_D^{corr} = \frac{A_m}{\bar{m}} \cdot \bar{m}^b \cdot D^b \cdot \prod K_i \tag{2.30}$$

The correction factors K_i relevant in this thesis are described in the following.

Volume and sensitivity correction factor $K_{V,s}$. It has to be considered, that the quantity absorbed dose-to-water D is defined in one point while the experimental determination of the absorbed dose-to-water D has to be performed in the extended sensitive volume of the alanine detector (see Section 2.4.2). Furthermore, the sensitivity of the used EPR spectrometer decreases parabolically with increasing distance from the alanine pellet center. These effects can be considered in the combined volume and sensitivity correction factor $K_{V,s}$, which has to be calculated

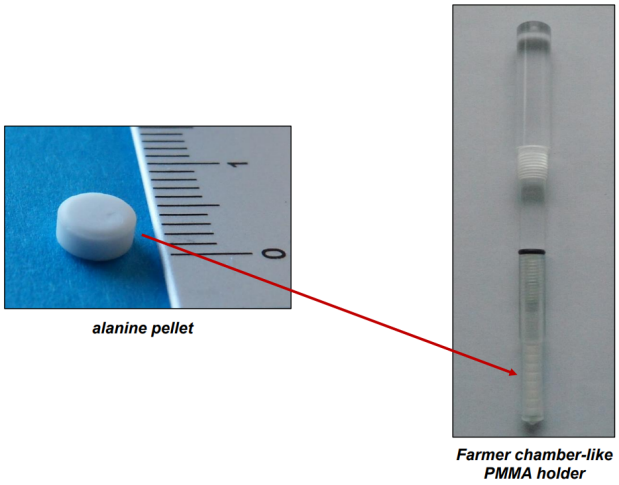

Figure 2.20: A single alanine pellet (left) and a Farmer IC-like PMMA holder containing several alanine pellets (right).

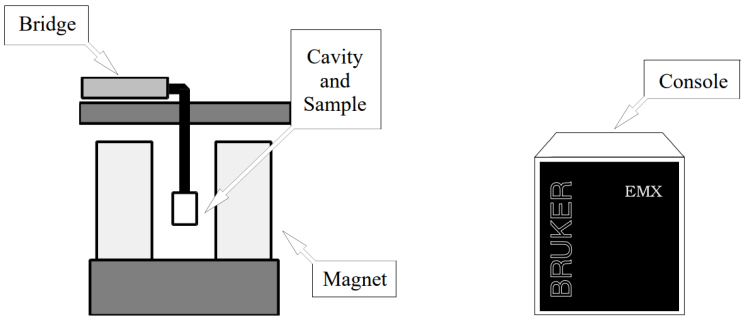

Figure 2.21: Sketch of a typical EPR spectrometer, taken from [Weber et al., 1998]. Please see the text for further explanations.

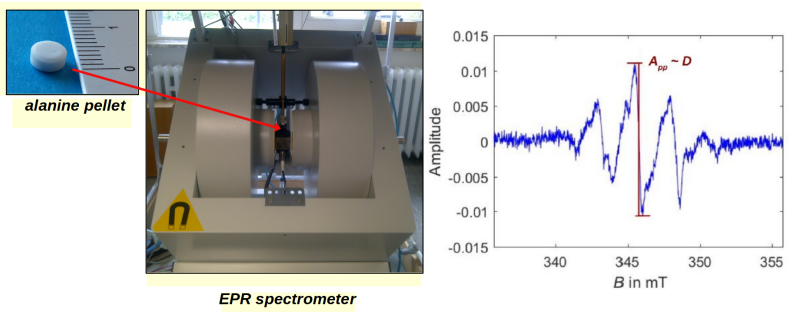

Figure 2.22: Principle of the readout via EPR spectroscopy. The picture in the middle shows the electromagnet of the EPR spectrometer at the PTB with the microwave cavity in between its pole shoes.

numerically. There are, however, exceptions allowing for analytical solutions, especially the case of constant gradients: The correction factor $K_{V,s}$ equals unity if the dose distribution within the alanine test and base pellets can be described by constant gradients irrespective of their slope.[30]

Irradiation temperature correction factor K_T. The recombination probablity of the radiation induced radicals in the alanine depends on the irradiation temperature. Thus, the irradiation temperature correction factor K_T has to be considered if the irradiation temperature for the alanine test and base pellets is not identical. It is obtained as

$$K_T = \frac{k_T}{k_T^b} \tag{2.31}$$

with the correction factors $k_T^{(b)}$

$$k_T^{(b)} = 1 - c_T \cdot (T^{(b)} - T_0) \tag{2.32}$$

with $c_T = 1.82 \times 10^{-3}\,\frac{1}{\mathrm{K}}$ and $T_0 = 20°\mathrm{C} = 293.15\,\mathrm{K}$. The uncertainty associated with the correction factors $k_T^{(b)}$ can be calculated using

$$u_r(k_T^{(b)}) = \sqrt{\left(\frac{c_T \cdot \Delta T^{(b)}}{1 - c_T \cdot \Delta T^{(b)}}\right)^2 \cdot (u_r(c_T)^2 + u_r(\Delta T^{(b)})^2)} \tag{2.33}$$

with $\Delta T^{(b)} = T^{(b)} - T_0$, $u(\Delta T^{(b)}) = u(T^{(b)})$ and $u_r(\Delta T^{(b)}) = \frac{u(T^{(b)})}{\Delta T^{(b)}}$, and $u(c_T) = 8 \times 10^{-5}\,\frac{1}{\mathrm{K}}$ and $u_r(c_T) = \frac{u(c_T)}{c_T}$.
The uncertainty $u_r(K_T)$ associated with K_T follows from error propagation as:

$$u_r(K_T) = \sqrt{u_r(k_T)^2 + u_r(k_T^b)^2} \tag{2.34}$$

The Equations 2.31 to 2.34 and the constants were derived by Mathias Anton, see also [Krystek and Anton, 2011].

Radiation quality correction factor K_Q. A radiation quality correction factor K_Q has to be considered, if the alanine test pellets are not irradiated with the same radiation quality as the alanine base pellets, which are irradiated in the Cobalt-60 reference field at the PTB in this work. Radiation quality correction factors were experimentally determined by Mathias Anton for a wide variety of radiation qualities [Anton et al., 2013]. The correction factors for the radiation qualities required within this thesis are listed in Table 2.1. These correction factors were determined by Mathias Anton in radiation fields with 10 cm×10 cm size and with an SSD of 100 cm. The field size and the SSD in the experimental setups in this work deviate from these reference conditions. However, the effects of these deviations regarding the radiation quality correction factors K_Q can be assumed to be negligible.

[30] This was derived by Mathias Anton.

Table 2.1: Radiation quality correction factors K_Q and their associated absolute uncertainties $u(K_Q)$ for base irradiations in the Cobalt-60 reference field at the PTB ($k_Q^b = 1$) for the radiation qualities relevant in this thesis. The correction factors and uncertainties were determined by Mathias Anton.

Nominal accelerating potential	$TPR_{20,10}$	K_Q	$u(K_Q)$
6 MV	0.683	1.0030	0.0035
8 MV	0.714	1.0042	0.0041
10 MV	0.733	1.0061	0.0036
15 MV	0.760	1.0111	0.0037

Environment correction factor K_{env}. The correction required for the impact of the material surrounding the alanine pellets has to be determined by a combination of MC simulations and measurements. If alanine test and base detectors are, however, irradiated in the same environment as it is the case for all experiments in this thesis, the environment correction factor equals unity and no uncertainty component has to be considered.

Fading correction factor K_F. The radiation induced radicals in the alanine are not completely stable but show a slow recombination called "fading" of a few percent per year [Anton, 2006]. The fading depends on several influences like temperature [Ettinger, 1989; Regulla and Deffner, 1982; Heydari et al., 2002], humidity [Arber and Sharpe, 1993; Ettinger, 1989; Regulla and Deffner, 1982; Sleptchonok et al., 2000; Dolo and Feaugas, 2005], or illumination [Ciesielski et al., 2004]. The correction factor K_F for the fading is obtained as

$$K_F = \frac{k_F}{k_F^b} \tag{2.35}$$

with the correction factors $k_F^{(b)}$

$$k_F^{(b)} = \exp\left(\lambda \cdot \Delta t^{(b)}\right) \tag{2.36}$$

The fading constant $\lambda = 6.84 \times 10^{-5}$ with its associated uncertainty $u(\lambda) = \frac{\lambda}{\sqrt{3}}$ was determined by Mathias Anton. It is $\Delta t^{(b)} = t_{meas}^{(b)} - t_{irr}^{(b)}$, where $t_{meas}^{(b)}$ is the time of measurement of the respective alanine detector in the EPR spectrometer and $t_{irr}^{(b)}$ is the time of irradiation of the respective alanine detector.
The uncertainty associated with the correction factors $k_F^{(b)}$ can be calculated using

$$u_r(k_F^{(b)}) = \sqrt{(\Delta t^{(b)})^2 \cdot u(\lambda)^2 + \lambda^2 \cdot u(\Delta t^{(b)})^2} \tag{2.37}$$

with $u(\Delta t^{(b)})^2 = u(t^{(b)}_{meas})^2 + u(t^{(b)}_{irr})^2$ with $u(t^{(b)}_{meas}) = u(t^{(b)}_{irr}) = 0.29\,\mathrm{d}$ corresponding to a uniform distribution with 1 d width.
The uncertainty $u_r(K_F)$ associated with K_F follows from error propagation as:

$$u_r(K_F) = \sqrt{u_r(k_F)^2 + u_r(k^b_F)^2} \tag{2.38}$$

The Equations 2.35 to 2.38 and the constants were derived by Mathias Anton.

Magnetic field correction factor K_{mag}. A magnetic field correction factor k_{mag} (or denoted k_B for the ICs used in this thesis, see Section 2.4.2) has to be included if the alanine test detectors are irradiated in the presence of a magnetic field since the irradiation of the base detectors in the Cobalt-60 reference field at the PTB takes place in the absence of a magnetic field. This correction factor accounts for both the changes in the dose deposition in the presence of a static magnetic field (see Sections 2.2.3 and 2.3.3) and the possible changes of the response of the alanine dosimeter in the presence of the magnetic field.
The determination of the correction factor k_{mag} for several clinically relevant situations was the main aim of this thesis.

Air gap correction factor K_{air}. The correction factor K_{air} addresses the changes due to air gaps surrounding alanine detectors which are based on the alteration of the local dose distribution due to the inserted air volume; this correction factor is needed in the presence and in the absence of a magnetic field alike.

Magnetic field and air gap interdependency correction factor $K_{mag,air}$. The correction factor K_{mag} addresses the change of the local dose distribution and the indication of the dosimeter in the presence of a magnetic field without consideration of a possible air gap (see Section 2.4.3). The correction factor K_{air} addresses the changes due to air gaps without consideration of a magnetic field (see Section 2.4.3). The correction factor $K_{mag,air}$, however, addresses the effect of air gaps surrounding the alanine detector originating in the interdependency of the air gap and the magnetic field. This effect, e.g. due to interfaces of materials with different densities in magnetic fields, does not occur in the absence of a magnetic field. The separation of the effect of air gaps in the presence of a magnetic field into K_{air} and $K_{mag,air}$ provides the advantage, that the correction factor K_{air} cancels out if ratios of data obtained in the presence and in the absence of a magnetic field are formed, see Section 3.1.1.

The corrected dose-normalised amplitude A^{corr}_D (Equation 2.30) is used as the indication of the alanine dosimeter in this work, as it was done by Mathias Anton. Since this thesis aimed at the determination of the magnetic field correction factor k_{mag},

comparisons of the situation with and without magnetic field are of importance. The corrected dose-normalised amplitude A_D^{corr} without a magnetic field correction factor is referred to as "standard indication".

In order to ensure clarity, it has not been mentioned so far, that in the actually applied measurement procedure at the PTB, it is not the amplitude obtained from the alanine test and base pellets which is used, but these alanine amplitudes divided by the amplitude obtained from a reference sample[31] permanently positioned[32] within the resonator of the EPR spectrometer (see Figure 2.23), i.e. the absorption signals of the alanine pellet and of the reference substance are measured simultaneously [Anton, 2005]. Relating the alanine amplitude A^{ala} to the reference amplitude A^{ref} allows for smaller measurement uncertainties since the impact of variations in the spectrometer sensitivity is diminished [Nagy, 2000; Nagy et al., 2000b, 2002; Bergstrand et al., 2003; Zeng et al., 2004; Anton, 2005, 2006]. As a consequence, it is not only one base function which is fitted to the obtained EPR spectrum by means of least squares, but the base function for the alanine component and the base function for the reference sample component, see Figure 2.24. The base function for the reference component is obtained from the EPR spectra of unirradiated alanine pellets and contains the EPR signal of the reference sample as well as underground signals of the resonator, the positioning device inside the resonator, and the unirradiated alanine pellets; the base function for the alanine component is obtained from the EPR spectra of alanine pellets irradiated to a known absorbed dose-to-water D (in this work 25 Gy in the Cobalt-60 reference field at the PTB) after subtraction of the base function for the reference component, i.e. this base function contains the pure alanine signal (see Figure 2.25). The amplitudes A and A_i, respectively, given in the Equations 2.25, 2.26, and 2.28 have, thus, to be interpreted as

$$A_{(i)} = \frac{A_{(i)}^{ala}}{A_{(i)}^{ref}} \tag{2.39}$$

Details on the fitting procedures can be found in Anton [2005, 2006]. The alanine/EPR system at the PTB can be used for measurements of absorbed doses-to-water in the range of 5 Gy to 25 Gy. The uncertainty for absorbed doses-to-water under reference conditions determined with this system is about 0.5 %.

Possible impact of an MRI system on the alanine dosimeter

The following addresses how the three components of an MRI system described in Section 2.1.1 could affect the alanine dosimeter. The possible effect of MRI on the alanine dosimeter is investigated by the experiments described in Section 3.2.

[31] The composition of the sample is not publicised by Bruker due to patent issues. Considerations regarding suitable reference substances can be found in [Anton, 2005].

[32] More information regarding the positioning device can be found in [Anton, 2006; Hackel, 2006].

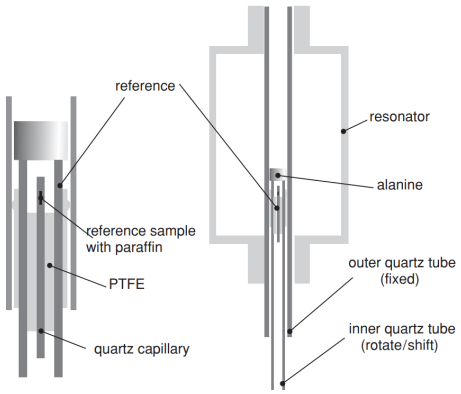

Figure 2.23: Schematic drawing of the positioning device for the alanine sample and the reference substance in the EPR spectrometer at the PTB. Left: detail (to scale). Right: positioning of the device in the resonator. The illustration is taken from [Anton, 2006].

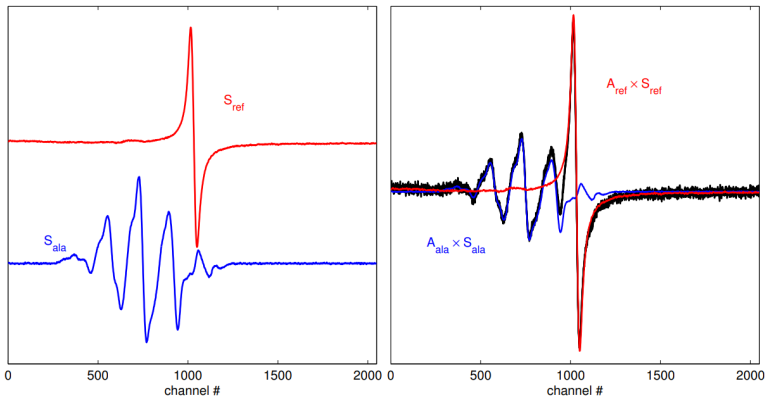

Figure 2.24: Illustration of the fitting of base functions to the EPR spectrum. Left: The base function of the reference sample is shown in red, the base function of the alanine sample is shown in blue. Right: Both base functions are fitted to the measured EPR spectrum (black) by means of least squares. Please note the favourable spectrum of the reference substance: the signal is located close to the alanine signal but not in its center [Anton, 2005]. Reproduced with thanks to Mathias Anton.

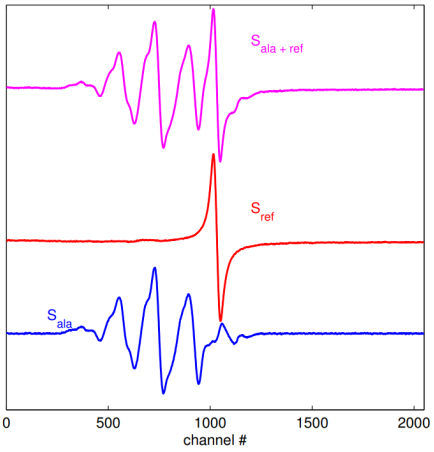

Figure 2.25: Illustration how the pure alanine signal S_{ala} (blue) is obtained by subtracting the reference signal S_{ref} (red) from the signal $S_{ala+ref}$ (pink), which is obtained by the simultaneous EPR measurement of the alanine and the reference substance. Reproduced with thanks to Mathias Anton.

Possible effect of the superconducting magnet on the alanine dosimeter. The superconducting magnet generates the static magnetic main field $\vec{B}_0$, see Section 2.1.1. An important quantity determining the interaction of a probe with a static magnetic field is the magnetic susceptibility χ. Almost all tissues are diamagnetic (magnetic susceptibility $\chi < 0$) with susceptibilities close to water (molar magnetic susceptibility $\chi_{m,water} = -1.631 \times 10^{-10}\,\mathrm{m}^3/\mathrm{mol}$ [Arrighini et al., 1968]). Due to these very small susceptibilities, magnetic forces on stationary tissue are negligible [Ladd et al., 2018]. The molar magnetic susceptiblity of alanine is approximately $-5 \times 10^{-11}\,\mathrm{m}^3/\mathrm{mol}$ [Swift et al., 2008], it can thus be assumed that the same applies to the alanine pellets. Electric fields $\vec{E} = \vec{v} \times \vec{B}$ are induced if tissues move with the velocity $\vec{v}$ in the magnetic field $\vec{B}$. This is relevant in MRI e.g. with respect to moving the patient in and out of the magnet bore, to patients moving their head, or to the blood flow [Schenck, 2005]. Currents induced to the retina and the optic nerve can lead to so called magnetophosphenes which are sense impressions like flashes or colourful areas [Schenck, 2005]. Moving particles with charge q e.g. in the blood or in the saliva are deflected according to the Lorentz force $\vec{F} = q \cdot (\vec{v} \times \vec{B})$ (see Section 2.3.3). This serves as an explanation for vertigo[33] and metallic taste[34], which are increasingly reported by patients with increasing magnetic flux density. The radicals induced in the alanine pellet due to ionising radiation have an odd amount of electrons in their outer shell, but their amount of

[33] Vertigo is explained with the Lorentz force on the potassium-rich liquid in the vestibular system in the inner ear [Schenck, 2005].

[34] The metallic taste is explained with the generation of ions due to voltages induced in the mouth [Cavin et al., 2007].

protons equals the amount of electrons, what leaves them electrically neutral. Furthermore, the radicals are trapped in the crystal alanine lattice. It is, thus, not to be expected that they are moved due to the Lorentz force e.g. if the patient bench on which they are placed is moved within the static magnetic main field $\vec{B}_0$.

Possible effect of the gradient fields on the alanine dosimeter. The gradient fields used for spatial encoding are changed fast during MRI, see Section 2.1.1. According to the Maxwell equation

$$\frac{\partial \vec{B}}{\partial t} = -\vec{\nabla} \times \vec{E} \tag{2.40}$$

a temporal change in the magnetic flux density leads to an electric vortex field, which induces a current in conductive material. This is relevant for patients undergoing MRI in terms of the stimulation of the peripheral nerves. In order to prevent this undesired effect, only 80 % of the stimulation threshold are allowed in the general operating mode of an MRI system. It is not expected that the electric vortex fields induced by the temporal changes of the gradient fields have any effect on the amount of radicals in the alanine pellets.

Possible effect of the RF pulses on the alanine dosimeter. As described in Section 2.1.7 the RF field used for exciting the nuclear spins can potentially heat the patient tissue. The SAR is introduced in order to assess the potential danger. The SAR is a measure for the energy absorbed per unit mass, see Section 2.1.7. Temperature is an important influence quantity in alanine dosimetry. The temperature during the irradiation has an impact on the final amount of radicals, and the temperature during storage after the irradiation (together with e.g. humidity and light irradiation) affects the process of recombination of the radicals ("fading")[35]. The exposure of the alanine pellets to MR sequences could, thus, potentially augment the fading. However, the energy involved in MRI is insufficient for breaking down chemical bonds or for exciting vibrational degrees of freedom or electronic levels in molecules [Ladd et al., 2018]. An effect on the radicals in the alanine pellets in that respect can, thus, be excluded.

2.5 Monte Carlo radiation transport simulations

Monte Carlo (MC) simulations can be used for investigating complex situations in the transport of ionising radiation through matter. They allow for numerical solutions in cases that are not solvable in an analytical manner, and they allow for gaining information that is not accessible by experiment.
The main goal of this work is the determination of the correction factors k_{mag}, see

[35] The alanine pellets used in this work are stored in a locker in a temperature-controlled laboratory at a relative humidity below 55 % and at room temperatures of 21-22°C.

Section 2.4.3, converting the standard indication of the alanine dosimeter in the presence of a static magnetic field into the actual absorbed dose-to-water at the point of measurement in the presence of the magnetic field. The determination of these correction factors requires on the one hand the experimental assessment of the indication of the alanine dosimeter in the presence and in the absence of a static magnetic field. On the other hand, it requires MC simulations. This is, because a static magnetic field has a twofold impact in terms of dosimetry which cannot be separated in the experimental investigation: the potential impairment of the dosimeter and the change of the dose distribution. The change of the dose distribution due to a static magnetic field at a point of interest can be expressed by the $c_{\vec{B}}$ factor, which converts the absorbed dose-to-water D at a point of interest in the absence of a magnetic field into the absorbed dose-to-water $D^{\vec{B}}$ in the presence of a magnetic field $\vec{B}$ at the same point of interest [van Asselen et al., 2018]:

$$D^{\vec{B}} = c_{\vec{B}} \cdot D \tag{2.41}$$

This $c_{\vec{B}}$ factor can be determined by MC simulations as described in Chapter 3.2 in [van Asselen et al., 2018], see Chapter 3.
Different software for MC simulations is available, e.g. Geant4 [Agostinelli et al., 2003] or PENELOPE [Salvat et al., 2008]. The simulations of the ddcs required for the determination of the $c_{\vec{B}}$ factors in the experimental setups applied in this work were performed using the EGSnrc software toolkit [Kawrakow et al., 2000].
The EGSnrc software toolkit is intended for the simulations of radiation transport through media. It originates from the Electron Gamma Shower (EGS) software package used at the Stanford Linear Accelerator Center (SLAC) in the 1970s [Bielajew et al., 1994; Rogers, 2006].[36] One feature of this toolkit is the availability of different applications (previously referred to as "user codes").
Details on the performed simulations, the used application and the implementation of the magnetic field are given in Chapter 3.

2.6 Determination of uncertainties according to the GUM

A measured value is in general not identical with the "true" value of a measurand; they differ by the measurement error. However, the true value and the measurement error are never known precisely [IAEA, 2008]. This is why the measurement uncertainty is such an important concept. An entire measurement result is composed of the measured value of a quantity and its associated uncertainty [Sommer and Siebert, 2004], e.g. $Y = y \pm u(y)$ with the true value Y, the measured value y, and the range $\pm u(y)$ as the measurement uncertainty. This equation expresses that the

[36] The "nrc" in today's name stands for National Research Council Canada, since it is contributing "to the development and application of the MC method in the modelling of radiation transport since the early 1980s." [Canada].

true value propably lies between $y-u(y)$ and $y+u(y)$ [IAEA, 2008]. "Probably" has of course to be defined; the concept of confidence limits is explained below. Comparisons of results are only reasonable if the uncertainties are taken into account. The associated uncertainties in this work are determined according to the Guide to the Expression of Uncertainty in Measurement (GUM) [Joint Committee for Guides in Metrology (JCGM), 2008].

The model equation $Y = f(X_i)$ which describes the relation between the measurand Y and its relevant input quantities X_i is of central importance according to the GUM [Sommer and Siebert, 2004]. Since the true values of the quantities Y and X_i, respectively, are generally unknown, estimated values y and x_i, respectively, are used and the model equation becomes

$$y = f(x_i) \tag{2.42}$$

The combined standard uncertainty $u(y)$ which is the measurement uncertainty associated with the estimated value y can be determined from the standard uncertainties $u(x_i)$ associated with the input quantities x_i with the aid of the model equation 2.42 according to the GUM. It is

$$u(y) = \sqrt{\sum_{i=1}^{N} \left(\frac{\partial f}{\partial x_i}\right)^2 \cdot u^2(x_i)} \tag{2.43}$$

in case of N uncorrelated input quantities x_i.

Two types of uncertainties have to be distinguished for the determination of the standard uncertainties $u(x_i)$ associated with the input quantities according to the GUM: type A and type B estimates.
Type A estimates are determined via statistical analyses. If there are n values for an input quantity X_i obtained under the same conditions, the best estimate of the input quantity X_i is the arithmetic mean

$$x_i = \bar{X}_i = \frac{1}{n} \cdot \sum_{k=1}^{n} X_{i,k} \tag{2.44}$$

The standard deviation of each value $X_{i,k}$ is

$$s(X_{i,k}) = \sqrt{\frac{1}{n-1} \cdot \sum_{k=1}^{n} (X_{i,k} - \bar{X}_i)^2} \tag{2.45}$$

and the standard deviation of the mean $\bar{X}_i$ is

$$\begin{aligned} s(\bar{X}_i) &= \sqrt{\frac{1}{n(n-1)} \cdot \sum_{k=1}^{n} (X_{i,k} - \bar{X}_i)^2} \\ &= \frac{s(X_{i,k})}{\sqrt{n}} \end{aligned} \tag{2.46}$$

This standard deviation of the mean is the standard uncertainty for type A estimates: $u(x_i) = s(\bar{X}_i)$.
Type B estimates are determined for an input quantity X_i by any method except for statistical analysis. This can e.g. be knowledge from previous measurements, information given by the manufacturer, or data from calibration certificates. An appropriate probability distribution has to be chosen according to the available information. Frequently applied probability distributions are the rectangular distribution and the Gaussian distribution.
The rectangular distribution describes the situation if the possible values of an input quantity lie within the interval $[a_+; a_-]$ with the same probability, see Figure 2.26 on the left. The best estimate for the value of a quantity described by a rectangular distribution is the midpoint of the interval $[a_+; a_-]$:

$$x_i = \frac{a_+ - a_-}{2} \tag{2.47}$$

The standard uncertainty in this case is given by:

$$u(x_i) = \frac{\Delta a}{\sqrt{3}} \tag{2.48}$$

with Δa the half-value width of the interval. An example for the application of the rectangular distribution is the determination of the standard uncertainty for a digital meter where the last indicated digit is in question.
The Gaussian distribution (see Figure 2.26 on the right) describes the situation if an estimated value μ and a standard deviation σ are given. Examples are values provided in calibration certificates or results of statistical analyses (see the explanations regarding type A estimates above) [Sommer and Siebert, 2004]. The best estimate of a quantity described by a Gaussian distribution is the mean value:

$$x_i = \mu \tag{2.49}$$

The standard uncertainty in this case equals the standard deviation:

$$u(x_i) = \sigma \tag{2.50}$$

As mentioned above the combined standard uncertainty $u(y)$ for the estimated value y is obtained from the standard uncertainties $u(x_i)$ of the input quantities x_i according to Equation 2.43. It was also mentioned above that the meaning of "the true value *probably* lies between $y - u(y)$ and $y + u(y)$" has to be defined. The standard uncertainty corresponds to a confidence probability of 68 %, i.e. the probability to find the true value between $y - u(y)$ and $y + u(y)$ is 68 % [IAEA, 2008]. The GUM comprises the concept of expanded uncertainty [Joint Committee for Guides in Metrology (JCGM), 2008]. The expanded uncertainty U is obtained from the combined standard uncertainty $u(y)$ via the coverage factor k:

$$U = k \cdot u(y) \tag{2.51}$$

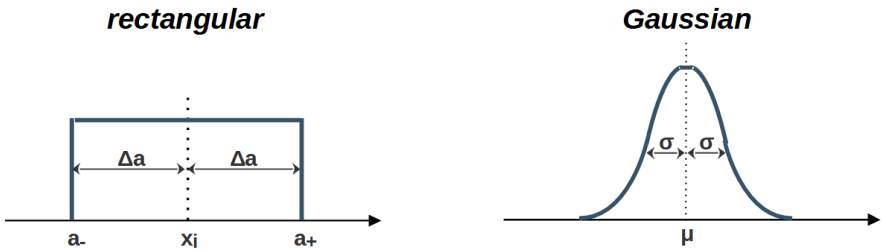

Figure 2.26: Illustrations of a rectangular distribution on the left and a Gaussian distribution on the right following the depiction in [Sommer and Siebert, 2004].

An indication of a measurement result that excludes any ambiguity is, hence, "$Y = y \pm U$ with the coverage factor k", expressing that the measurand Y lies in the interval $[y - U; y + U]$ with a probability depending on the chosen coverage factor k. For $k = 1$, there is no difference between the expanded uncertainty U and the combined standard uncertainty $u(y)$. If a higher level of confidence is required, a coverage factor $k > 1$ has to be used. In the case of a Gaussian distribution for the measurand Y, a 95 % confidence interval is obtained when a coverage factor $k = 1.96$ is applied, which is usually rounded to $k = 2$.
The probability distribution for the measurand Y is generally unknown. The indication of the desired coverage interval $[y-U; y+U]$ is, nevertheless, possible following the approach of effective degrees of freedom and the t-distribution as described in the appendix of the GUM or in the appendix of [IAEA, 2008]. For the common usage it can be noted that a coverage factor $k = 1$ results in a coverage interval with 68 % coverage probability, and that a coverage factor $k = 2$ results in a coverage interval with about 95 % coverage probability. In this work, it is assumed that deviations of values with coverage intervals obtained with coverage factors $k \geq 3$ are significant.

3 Materials and methods

3.1 Characterisation of the alanine dosimeter in static magnetic fields

3.1.1 Preparatory experiment regarding sub-millimetre air gaps

The aim of this preparatory experiment was to investigate the possible effect of sub-millimetre air gaps around alanine detectors. The reason for this investigation were studies observing significant effects of sub-millimetre air gaps around ICs in the presence of static magnetic fields (see Section 2.4.2). This preparatory experiment is of relevance for the subsequent work in this thesis, since air gaps around the alanine pellets cannot be avoided completely in the experimental situation.

Experiment and applied devices

Detector holders. As mentioned in Section 2.4.3, stacks of four alanine pellets placed in a holder made of PMMA are used as alanine detectors in this work (see Figure 2.20). A set of five special PMMA holders was manufactured for this preparatory experiment. These PMMA holders provide – different than the holder shown in Figure 2.20 – defined air gaps of (0.0, 0.1, 0.2, 0.5, 1.0) mm around the alanine detectors.[1] Typical air gaps occuring in alanine dosimetry have a size of 0.05 mm. The situation in this range is investigated using the holders providing air gaps of (0.0, 0.1, 0.2) mm. Air gap sizes of 0.5 mm and 1.0 mm do not play a realstic role in alanine dosimetry. These air gap sizes were chosen in order to provoce an effect which would be easier to measure. The holders are designed such, that they are waterproof for quite some time allowing for irradiations of several minutes in water phantoms without the use of an additional waterproof sleeve. A construction sketch is exemplarily shown for the holder providing the 0.5 mm air gap around the alanine detector in Figure 3.1. Pictures of the same holder (0.5 mm air gap) are shown in Figure 3.2.

Alanine pellets. Ten alanine detectors were used as alanine test pellets in this preparatory experiment: one per PMMA air gap holder in two irradiation series.

[1] 0.0 mm air gap means "air gap as small as possible; the alanine pellet can just be put in and removed again". It is certainly below 0.03 mm, which is the uncertainty of the air gap width for all five holders.

Two additional alanine detectors were used as alanine base pellets. One was irradiated to a nominal absorbed dose-to-water of 25 Gy in the Cobalt-60 reference field at the PTB, the other one remained unirradiated. All these detectors were composed of four alanine pellets from Harwell Batch AM603.

Weighting. The alanine pellet mass is an important entity in alanine dosimetry, see Section 2.4.3. All alanine pellets were weighed with the micro balance Mettler-Toledo MX5 prior to the irradiations.

Irradiation of the base pellets at the Cobalt-60 facility at the PTB. The Cobalt-60 facility at the PTB, which was used for the irradiation of the alanine base detector to a nominal absorbed dose-to-water of 25 Gy, is dedicated to metrological purposes and, thus, features high reproducibility, i.e. the dose rate varies less then 0.01 % when the radiation is repeatedly switched on and off. This stability is possible since the source is not moved between a shielded position and an open position for switching on and off (as it is done in conventional facilities where the dose rate differences are in the order of several 0.1 %). At the PTB, switching on and off is achieved via a shutter which blocks or unblocks the radiation. The shutter moves with such a high speed that the maximum dose rate is reached in less than 50 ms after switching on. The radiation field of the source is determined by a collimator integrated in the shutter system. Different collimators are available. The referece field size for the calibration of secondary standards e.g. according to [Deutsches Institut für Normung e.V., 2008] is a 10 cm×10 cm square. The standard collimator made of a tungsten-copper alloy generates, hence, a radiation field with field size 10 cm×10 cm in 100 cm distance from the radiation source. This standard collimator was applied for all Cobalt-60 irradiations in this work. The absorbed dose-to-water for irradiations at the Cobalt-60 reference field is well known due to the knowledge of the dose rate and the registration of the irradiation time.
The alanine base detector was placed in the standard Farmer-IC-like PMMA holder (see Figure 2.20), i.e. not in one of the air gap holders which were only used for the alanine test detectors in this experiment.[2] The Farmer-IC-like PMMA holder was placed in a water phantom (30 cm×30 cm×30 cm), see Figure 3.3, such that the symmetry axis of the pellets was perpendicular to the beam axis. The center of the alanine pellets was in 5 cm depth measured from the outside of the water phantom. (The measures of the entrance window and the PMMA holder are not scaled from PMMA to water.) The SSD, which is the distance from the source to the front of the water phantom, was 95 cm. The use of the standard collimator resulted, thus, in a field size of 10 cm×10 cm at the center plane of the alanine pellets. This setup is in accordance with reference protocols like [Deutsches Institut für Normung e.V., 2008]. The irradiation temperature, which is an important entity in alanine dosimetry, see

[2] Please note, that eight alanine pellets fit into the Farmer-IC-like PMMA holder (position A-H). However, only the four inner pellets (position C-F) were used in this work. Dummy pellets were placed on the positions A, B, G, and H.

Section 2.4.3, was registered.

Irradiation of the test pellets at the Elekta precise treatment system™ linac at the PTB. The irradiation of the alanine test pellets was performed on two subsequent days. On each day, five alanine detectors were irradiated in the five PMMA holders providing different air gap sizes. The irradiation series on the first day was performed in the absence of a magnetic field; it allows to study the effect of submillimetre air gaps in the absence of a magnetic field and serves as a "background" for studying the effect in the presence of a magnetic field. The irradiation series on the second day was performed in the presence of a static magnetic field with flux density 1 T since this is in the typical range of magnetic flux densities available at MR Linacs (see Section 2.2.3).
The alanine test pellets were irradiated at the Elekta precise treatment system™ linac at the PTB. A photon beam with nominal accelerating potential of 6 MV generated by this clinical linac was applied (corresponding to a $TPR_{20,10}$ of 0.683) since this is an accelerating potential in the typical range of MR Linacs (see Section 2.2.3). The pulse rate frequency was 200 Hz. The dose rate was 267 monitor units (MU)[3] per minute on the first and 265 MU per minute on the second irradiation day, respectively. The magnetic field was generated by an electromagnet. The electromagnet ER073W (Bruker) was placed in front of the accelerator head of the linac in order to allow for irradiations in the presence of a static magnetic field, see Figure 3.4.[4] The electromagnet is positioned in such a way that the photon beam axis – indicated by room lasers – is running centrally through the space between its pole shoes. The electromagnet was located in this position for both irradiation series, in the absence and in the presence of the magnetic field in order to ensure comparability of the setup. The distance from the bremsstrahlung target in the accelerator head to the center of the pole shoes of the electromagnet was 120 cm. The alanine detectors were irradiated in a water phantom (7 cm × 20 cm × 20 cm) fitting between the pole shoes of the electromagnet, see Figure 3.5. The SSD, i.e. the distance from the bremsstrahlung target to the front of the water phantom was 110 cm. This is slightly larger than for reference conditions (SSD= 100 cm, see reference protocols like [Deutsches Institut für Normung e.V., 2008]) in order to reduce the impact of the stray magnetic field on the monitor IC at the accelerator head (see below). The changes due to the deviation in the SSD from the reference conditions are negligible according to the experience in the working group. The field size of the photon field was collimated such that it was 5 cm in the horizontal direction and 10 cm in the vertical direction at a plane in 100 cm distance from the bremsstrahlung target. This field size deviating from the 10 cm×10 cm field required for reference conditions was chosen in order to spare the pole shoes of the electromagnet and, hence, avoid

[3] Monitor units are the units of radiation dose used by clinical linacs.
[4] Please note that this electromagnet is different from the electromagnet applied in the EPR spectrometer used for the readout of the irradiated alanine pellets.

scattered radiation.[5]
For the irradiations, the alanine test detectors were placed in the PMMA holders with different air gap sizes. No additional sleeve was used around the PMMA holders due to their sufficient waterproofness. The PMMA holders were positioned in the water phantom using a frame such that the symmetry axis of the pellets was perpendicular to the beam axis and such that the center of the alanine pellets was in 10 cm depth measured from the outside of the water phantom. The measures of the entrance window were scaled from PMMA to water (factor 1.15) while the measures of the PMMA holders were not scaled. The PMMA holders were positioned such that an air gap (i.e. not one of the supports) faced the accelerator head. The frame fixing the PMMA holders in the water phantom was positioned at the beginning of the first irradiation day. It was not moved until the end of the second irradiation day ensuring the same position for all alanine detectors.
The indication of the alanine dosimeter is sensitive to the irradiation temperature, which, thus, has to be determined reliably. The water temperature was measured with a sensor positioned within the water phantom; the sensor can be seen for example in Figure 3.10. The alanine detectors within the PMMA holder were placed in the water phantom at least ten minutes prior to their irradiation in order to ensure the acclimatisation of the alanine pellets to the water temperature by the time the irradiation starts.
Each alanine test detector was irradiated to a nominal absorbed dose-to-water of 15 Gy.
The irradiations were monitored by a transmission IC in front of the accelerator head.[6] This PTB-built large-area transmission IC is mounted on the "shadow tray" in front of the accelerator head, see Figure 3.6. It is composed of two independent compartments. A schematic illustration of the two compartments of this transmission IC is shown in Figure 3.7. On each irradiation day, the compartment showing higher stabilty is chosen. The general experience in the group is, that the signal of compartment "a" is more stable than the signal of compartment "b". A possible explanation is, that the compartment "b" is closer to various sources of heat in the accelerator head. The distance between the transmission IC and the outside of the accelerator head is approximately 13 cm. The external transmission IC is generally recommended for monitoring the output of the linac at the PTB – instead of the internal transmission IC installed in the accelerator head of the linac by default. This recommendation is based on the experience of the group that the PTB-built

[5] It was confirmed with data taken during the commissioning of the linac that this reduced field size is sufficiently homogeneous in the lateral direction such that possible lateral displacements of the alanine detectors of ±0.2 mm can be neglected, as it is the case in a reference field with field size 10 cm×10 cm.

[6] The output of the applied linac (as for any clinical linac) shows a pronounced drift throughout an irradiation day, since no effort is made in the design of clinical linacs in terms of stability of the output against e.g. temperature or air pressure variations. This is due to the fact, that it is only of importance to measure if the output was sufficient in the clinical application, together with the fact, that missing stabilisation measures come along with reduced effort for maintenance and service.

external transmission IC provides signals of higher stability.
As mentioned above, the series on the first irradiation day was performed in the absence of a magnetic field. The electromagnet was switched on subsequently and set to 1 T for warming up over night in order to exclude temperature effects for the irradiation series in the presence of the magnetic field on the second irradiation day.

Readout with the Bruker EMX 1327 EPR spectrometer at the PTB. After the irradiation, the alanine detectors were read out with the Bruker EMX 1327 EPR spectrometer at the PTB. This EPR spectroneter uses an 8" water-cooled electromagnet [Anton, 2005][7]. 2048 channels are used for the data acquisition. For each alanine pellet, nine spectra are measured and the alanine pellet is rotated by 40° in between the nine measurements. The nine spectra are then averaged. The magnetic flux density B_0 in the center of the spectrum is 348.096 mT. An intervall of 30 mT is paced around this center. The modulation amplitude and the frequency were set to 0,5 mT and 100 kHz, respectively. The microwave power was 2 mW with 20 dB attenuation. The microwave frequency was approx. 9.68 GHz (X-band). Conversion time and time constant were set to 15 ms and 41 ms, respectively. These settings were determined by Mathias Anton in order to obtain optimum EPR signals. The resulting measurement time per alanine pellet is approximately five minutes. The readout in this investigation was performed on one measurement day.

Analysis and uncertainties

The aim of this preparatory experiment was to find out whether sub-millimetre air gaps around alanine detectors have a measurable effect. The irradiation series in the absence of a magnetic field was analysed separately in a first step. This part of the analysis is described in Section A in the Appendix. In a second step, the ratios $\frac{k_{mag,air,X}}{k_{mag,air,0.0mm}}$ were determined using the irradiation series in the absence and in the presence of the magnetic field. These correction factors address the effect of the interdependency of magnetic field and air gap in the case of an air gap size X and an air gap with 0.0 mm size (see Section 2.4.3). The ratio was formed since this allows for a smaller overall uncertainty since several components cancel out in the ratio. The derivation of the model equation for $\frac{k_{mag,air,X}}{k_{mag,air,0.0mm}}$ is outlined in the following.

Derivation of the model equation. With the corrected dose-normalised amplitude A_D^{corr} as the indication of the alanine detectors and the applied dose-to-water D_{appl} the response R of the alanine detectors is

$$R = \frac{A_D^{corr}}{D_{appl}} \tag{3.1}$$

[7] Please note, that this electromagnet is not the same as the electromagnet used for generating the magnetic field during the irradiation.

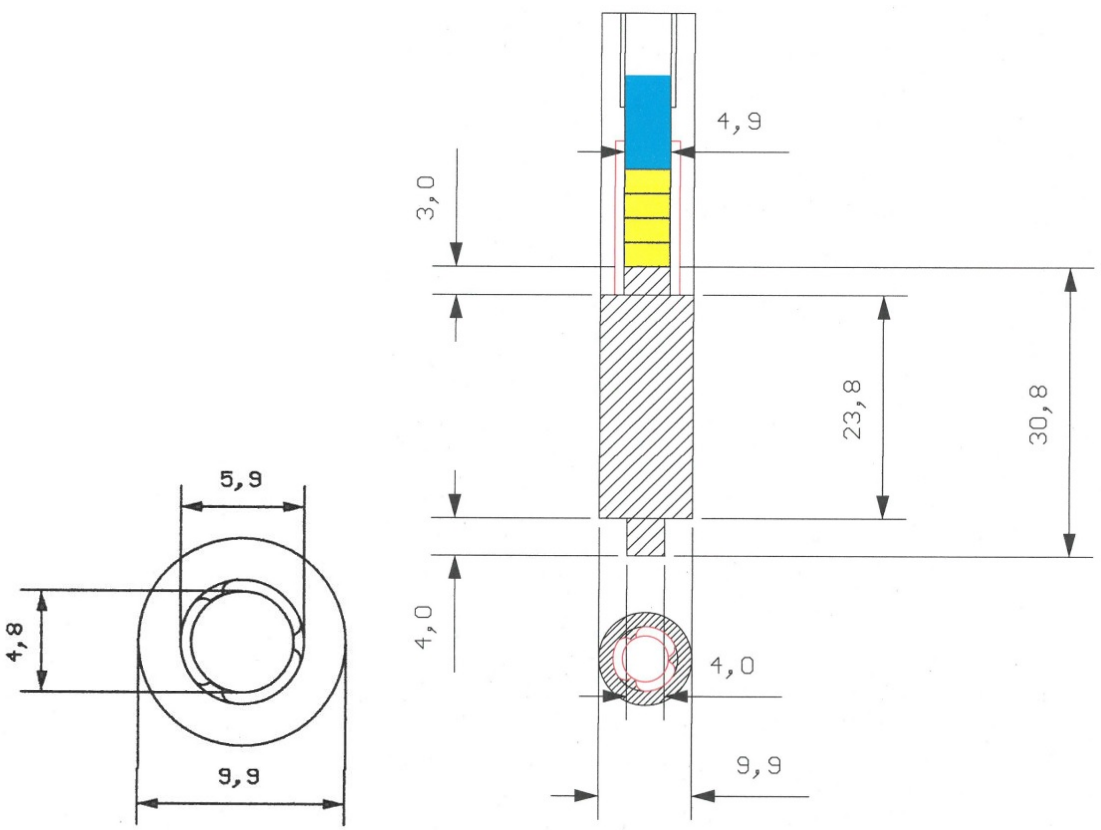

(a) (b)

Figure 3.1: Construction sketch of the PMMA holder providing an air gap of 0.5 mm around the alanine detector. (a) Profile of the PMMA holder with 0.5 mm air gap. The outer diameter is 9.9 mm. The thickness of the PMMA wall is 2.0 mm in the case of the 0.5 mm air gap. The outer diameter is the same for all built holders, thus, the PMMA wall thickness varies depending on the air gap thickness (it is e.g. 2.5 mm in the case of the vanishing air gap). The air gap is not continuous, but intermitted by small PMMA supports, which ensure a centered position of the alanine pellets. (b) Construction sketch of the PMMA holder with 0.5 mm air gap in lateral view. The upper part shows the section depicted in the profil in (a). The alanine pellets inside the holder are shown in yellow. They are fixated by a small cylinder made of PMMA, which is shown in blue. The shaded part is made of PMMA as well. It is glued to the upper piece. It allows to position the alanine detector at the same location as the sensitive volume of an IC of NE2571 type.

(a)

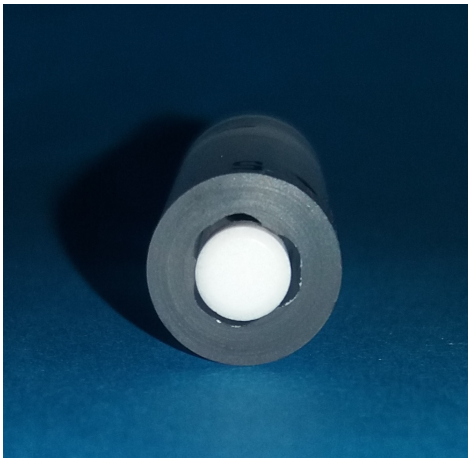

(b)

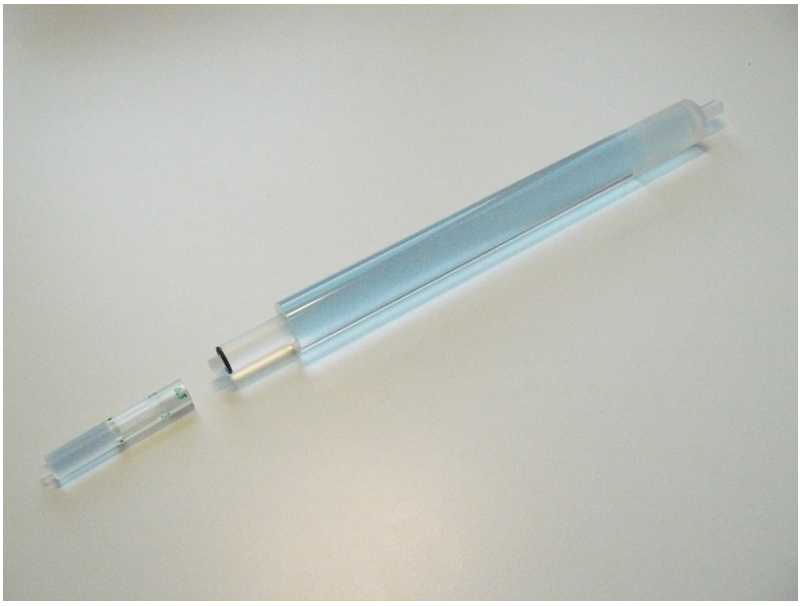

(c)

Figure 3.2: Pictures of the PMMA holder providing an air gap of 0.5 mm around the alanine detector. (a) Picture of the PMMA holder with 0.5 mm air gap following the construction sketch in Figure 3.1(b). (b) Picture of the PMMA holder with 0.5 mm air gap during manufacturing. The terminating piece (shaded part in Figure 3.1(b)) is not yet glued to the holder. Thus, it can be seen how the alanine pellet is fixed in a central position by the PMMA supports (see Figure 3.1(a)). (c) The PMMA holder shown in (a) is screwed to a PMMA rod for the irradiations in the water phantom. The same PMMA rod can be used for all five holders with different air gap sizes.

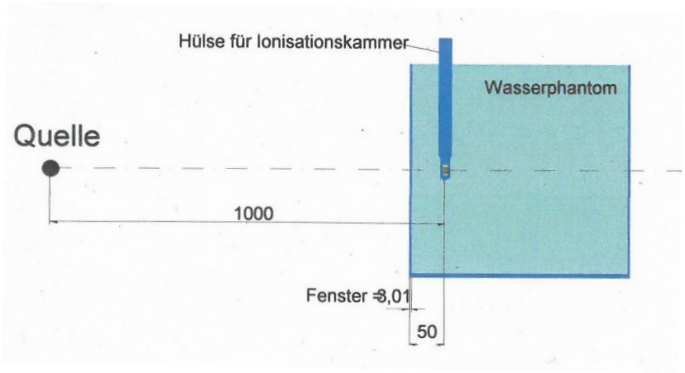

Figure 3.3: Setup for the irradiations of the alanine pellets in the Cobalt-60 reference field at the PTB. The sleeve for an IC ("Hülse für Ionisationskammer") or in this case the alanine detector in the PMMA holder is located within a water phantom ("Wasserphantom") in a distance of 1000 mm from the source ("Quelle").

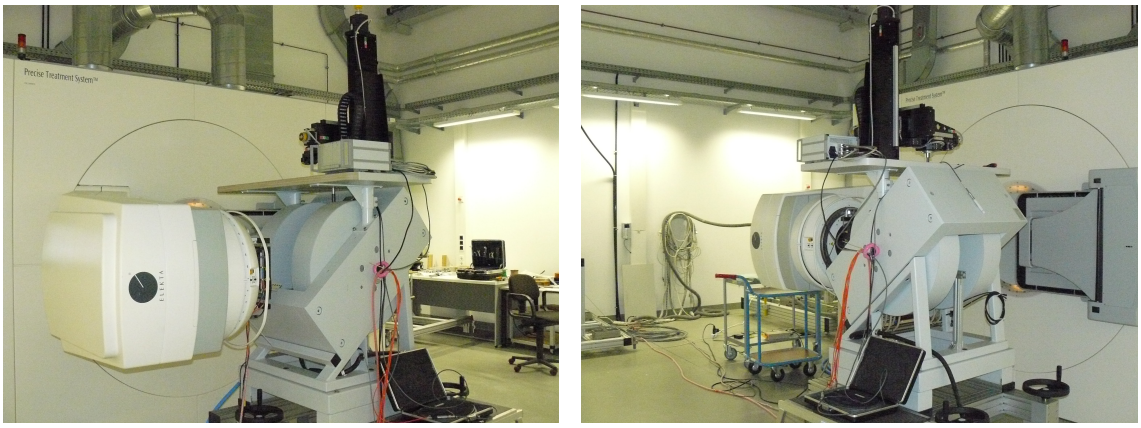

(a) (b)

Figure 3.4: The Elekta Precise Treatment System™ linac with the Bruker electromagnet ER073W positioned to the right in front of it. The black device on top of the electromagnet is used for positioning the detectors.

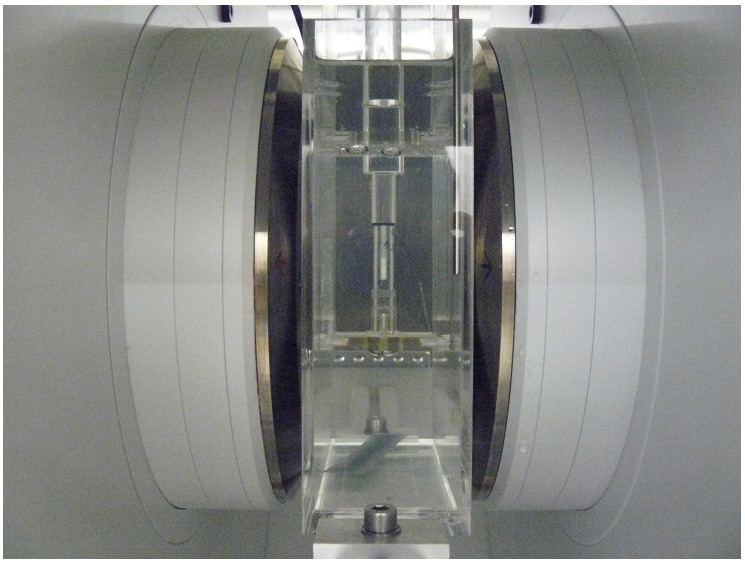

Figure 3.5: An alanine detector within one of the air gap PMMA holders in the water phantom between the pole shoes of the electromagnet. The four alanine pellets can be seen in white. The PMMA frame fixating the PMMA holder can also be seen.

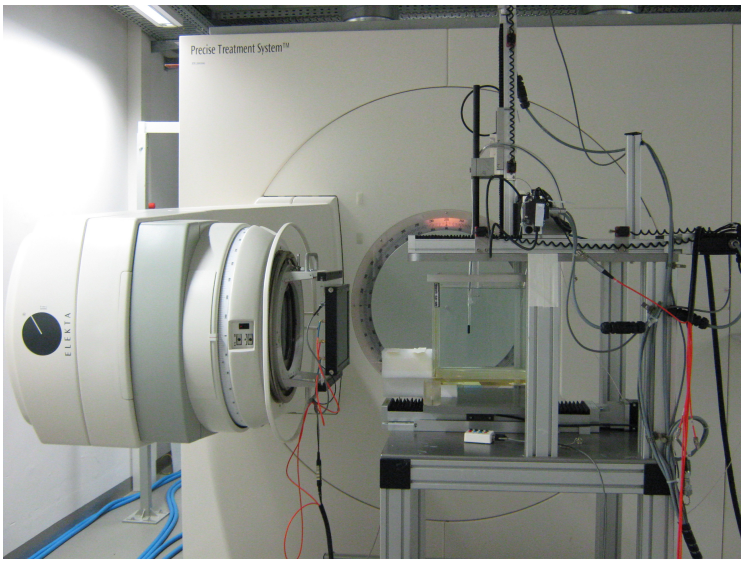

Figure 3.6: Head of the linac eqipped with the external transmission IC in a setup for an irradiation of an IC in a water phantom under reference conditions, i.e. this picture does not depict the setup in the present experiment. This picture is only shown since the position of the external transmission IC (black) at the shadow tray in front of the accelerator head can be seen clearly.

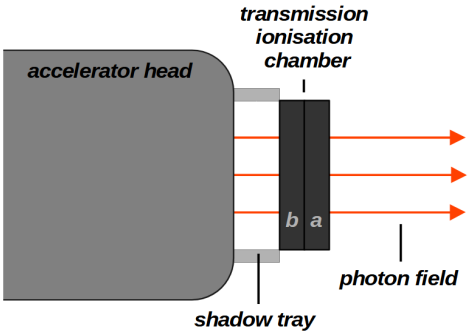

Figure 3.7: Scheme of the position of the external transmission IC in front of the accelerator head.

The corrected dose-normalised amplitude A_D^{corr} is given by Equation 2.30. No volume and sensitivity correction is required here due to constant gradients in all irradiations (see Section 2.4.3), and no environment correction is required since all irradiations are performed within water phantoms (see Section 2.4.3). The expression for A_D^{corr} in the present situation is, hence:

$$A_D^{corr} = \frac{A_m}{\bar{m}} \cdot \bar{m}^b \cdot D^b \cdot K_T \cdot K_Q \cdot K_F \cdot K_{air} \cdot K_{mag,air} \cdot K_{mag} \tag{3.2}$$

In order to mitigate confusion, the correction factors K_{air}, $K_{mag,air}$, and K_{mag} are shortly described again (see Sections 2.4.3 to 2.4.3): K_{air} addresses the changes due to air gaps surrounding alanine detectors which are based on the alteration of the local dose distribution due to the inserted air volume; this correction factor is required in the presence and the absence of a magnetic field alike. K_{mag} addresses the change of the local dose distribution and the indication of the dosimeter in the presence of a magnetic field without consideration of possible air gaps. And $K_{mag,air}$ addresses the effect of air gaps surrounding the alanine detector originating in the interdependency of the air gap and the magnetic field. This effect, e.g. due to interfaces of materials with different densities in magnetic fields, does not occur in the absence of a magnetic field. The separation of the effect of air gaps in the presence of a magnetic field into K_{air} and $K_{mag,air}$ provides the advantage, that the correction factor K_{air} cancels out if ratios of data obtained in the presence and in the absence of a magnetic field are formed.
The ratio of two alanine response values R equals unity in the case of entirely corrected response values. The ratio of two response ratios – in the presence and in the absence of the magnetic field – is used, which provides the advantage that the effect of air gaps in the absence of a magnetic field cancels out as mentioned in the previous paragraph. The values from the irradiation series in the absence of a magnetic field are labeled with “0T”, the values from the irradiation series in the

presence of a magnetic field with flux density 1 T are labeled with "1T":

$$1 = \frac{\frac{R_{X,1T}}{R_{0.0mm,1T}}}{\frac{R_{X,0T}}{R_{0.0mm,0T}}} \tag{3.3}$$

Combining the Equations 3.1, 3.2, and 3.3 eventually results in the model equation

$$\begin{aligned}\frac{k_{mag,air,X}}{k_{mag,air,0.0mm}} =& \frac{Q_{X,1T}}{\frac{A_{m,X,1T}}{\bar{m}_{X,1T}} \cdot k_{T,X,1T}} \cdot \frac{\frac{A_{m,0.0mm,1T}}{\bar{m}_{0.0mm,1T}} \cdot k_{T,0.0mm,1T}}{Q_{0.0mm,1T}} \\ & \cdot \frac{\frac{A_{m,X,0T}}{\bar{m}_{X,0T}} \cdot k_{T,X,0T}}{Q_{X,0T}} \cdot \frac{Q_{0.0mm,0T}}{\frac{A_{m,0.0mm,0T}}{\bar{m}_{0.0mm,0T}} \cdot k_{T,0.0mm,0T}}\end{aligned} \tag{3.4}$$

The masses of the base pellets and the absorbed doses-to-water applied to the base pellets cancel out in the ratio ($\bar{m}^b_{X,1T} = \bar{m}^b_{X,0T} = \bar{m}^b_{0.0mm,1T} = \bar{m}^b_{0.0mm,0T}$ and $D^b_{X,1T} = D^b_{X,0T} = D^b_{0.0mm,1T} = D^b_{0.0mm,0T}$) since the same base pellets are used throughout the experiment. The radiation quality correction cancels out since the same radiation quality was used for all test detectors and since the same base was used for all test detectors ($K_{Q,X,1T} = K_{Q,X,0T} = K_{Q,0.0mm,1T} = K_{Q,0.0mm,0T}$). The magnetic field correction is only required for the series in the presence of the magnetic field where it cancels out since the magnetic field and its orientation to the photon beam are the same for the irradiations of all the alanine detectors in the different PMMA holders ($K_{mag,X,1T} = K_{mag,0.0mm,1T}$). The air gap correction in the absence of a magnetic field cancels out since the effect described by this correction is the same in the absence and in the presence of a magnetic field ($K_{air,X,0T} = K_{air,X,1T}$ and $K_{air,0.0mm,0T} = K_{air,0.0mm,1T}$). Instead of $K_{T,i}$, $k_{T,i}$ can be used for the irradiation temperature correction due to Equation 2.29 and due to the same base pellets used for all test detectors ($k^b_{T,X,1T} = k^b_{T,X,0T} = k^b_{T,0.0mm,1T} = k^b_{T,0.0mm,0T}$). Likewise, $k_{mag,air}$ can be used instead of $K_{mag,air}$ since the same base pellets are used for all test detectors. Since $k_{mag,air,X,1T}$ and $k_{mag,air,0.0mm,1T}$ do not occur in the absence of a magnetic field, they can be denoted as $k_{mag,air,X}$ and $k_{mag,air,0.0mm}$. The fading correction cancels out since the correction factor is the same for all alanine test detectors within the series in the absence of the magnetic field and for all alanine test detectors within the series in the presence of the magnetic field ($K_{F,X,1T} = K_{F,0.0mm,1T}$ and $K_{F,X,0T} = K_{F,0.0mm,0T}$).

Quantities in the model equation and uncertainty budget. The following describes how the ratio $\frac{k_{mag,air,X}}{k_{mag,air,0.0mm}}$ was obtained from the experimental data. The basis for this procedure is the model equation 3.4.

Alanine pellet mass. The masses of the alanine pellets were obtained from the weighting process (see Section 3.1.1) and the mean masses $\bar{m}_{X,1T/0T}$ and $\bar{m}_{0.0mm,1T/0T}$ were obtained by averaging the masses of the alanine pellets composing the respective detectors.

The alanine pellets are handled with vacuum tweezers; nevertheless a material loss of about 3 µg to 5 µg per handling is possible (determined by Mathias Anton). The uncertainty due to the weighing is negligible. A contribution of 50 µg (based on the realistic assumption of less than ten handlings per pellet) is, thus, considered for a single pellet. The uncertainty contribution due to the mass of the alanine pellets in the test detectors $u_r(\bar{m})$ composed of n alanine pellets is, hence, given by

$$u_r(\bar{m}) = \frac{0.05\,\mathrm{mg}}{\sqrt{n} \cdot \bar{m}} \tag{3.5}$$

($u(m_i) = 0.05\,\mathrm{mg}$, $u(\bar{m}) = \frac{u(m_i)}{\sqrt{n}}$, and $u_r(\bar{m}) = \frac{u(\bar{m})}{\bar{m}}$). The component $u_r(\bar{m})$ has to be considered four times in the present investigation: for the test detector surrounded by the air gap with size X irradiated in the absence of the magnetic field, for the test detector surrounded by the air gap with size X irradiated in the presence of the static magnetic field with flux density 1 T, for the test detector surrounded by the gap with 0.0 mm size irradiated in the absence of the magnetic field, and for the test detector surrounded by the gap with 0.0 mm size irradiated in the presence of the 1 T magnetic field. The component has to be considered only twice, however, for the value $\frac{k_{mag,air,0.0mm}}{k_{mag,air,0.0mm}}$. No contribution due to the mass of the base pellets is needed, since all values were obtained on the same EPR measurement day, ruling out a contribution due to changes in the mass by additional handling.

Alanine amplitude. The values of $A_{m,X,1T/0T}$ and $A_{m,0.0mm,1T/0T}$ were obtained from the EPR measurements of the alanine detectors irradiated in the absence of a static magnetic field and of the alanine detectors irradiated in the presence of a static magnetic field with flux density 1 T. The uncertainty associated with the amplitude values $A_{m,X/0.0mm,1T/0T}$ has two contributions. One is due to the reproducibility of the amplitude measurement and the other one is due to the homogeneity of the detector material. These contributions have to be considered for the alanine test and the alanine base detectors. The contribution due to reproducibility of the test pellets $u_r(A_{test}^{repro})$ has to be considered four times: for the test detector surrounded by the air gap with size X irradiated in the absence of the magnetic field, for the test detector surrounded by the air gap with size X irradiated in the presence of the static magnetic field with flux density 1 T, for the test detector surrounded by the gap with 0.0 mm size irradiated in the absence of the magnetic field, and for the test detector surrounded by the gap with 0.0 mm size irradiated in the presence of the 1 T magnetic field. The contribution due to homogeneity of the test pellets $u_r(A_{test}^{hom})$ has to be considered four times as well, again for the origins listed above. Both components $u_r(A_{test}^{repro})$ and $u_r(A_{test}^{hom})$ have, however, to be considered only twice for the value $\frac{k_{mag,air,0.0mm}}{k_{mag,air,0.0mm}}$. The contributions due to reproducibility and homogeneity for the base pellets ($u_r(A_{base}^{repro})$ and $u_r(A_{base}^{hom})$) cancel out since the quantity of interest is a ratio of values which were obtained on the same EPR measurement day using the same base.

The uncertainty components $u_r(A_{test}^{repro})$ are calculated as follows:

$$u_r(A_{test}^{repro}) = \sqrt{\frac{{u_{repro}}^2}{n \cdot A_D^{corr2}} \cdot \left(1 + \frac{1}{f^2} \cdot \frac{A_D^{corr2}}{D^{b2}}\right)} \tag{3.6}$$

with $u_{repro} = 0.05\,\mathrm{Gy}$ and $f = 1.42$ for the reference probe holder used (both values determined by Mathias Anton). The corrected dose-normalised amplitude A_D^{corr} used in Equation 3.6 was calculated using Equation 3.2 without the correction factors K_{air}, $K_{mag,air}$, and K_{mag} since they were unknown beforehand[8]. The correction factors were used as follows: $K_{V,s} = 1$ due to constant gradients, K_T was calculated as described in Section 2.4.3, $K_Q = 1.0030$ for the radiation quality used (determined by Mathias Anton), $K_{env} = 1$ since all irradiations took place in water phantoms, and K_F was calculated as described in Section 2.4.3. The values for A_m were obtained from the EPR measurement. The values for $\bar{m}^{(b)}$ were determined by weighting the alanine pellets (test and base (b) pellets) and averaging the masses of the alanine pellets composing one alanine detector. The value for D^b was obtained by multiplying the dose rate of the source of the Cobalt-60 reference field with the irradiation time.
The uncertainty components $u_r(A_{test}^{hom})$ are calculated as follows:

$$u_r(A_{test}^{hom}) = \frac{0.003}{\sqrt{n}} \tag{3.7}$$

with the number of pellets n in the detector, since the uncertainty for a single pellet is 0.3 % (determined by Mathias Anton).

Irradiation temperature correction. The correction factors $k_{T,i}$ for the irradiation temperature were obtained as follows. The temperature of the water in the phantom, which equals the temperature of the alanine detectors due to a waiting time of ten minutes prior to each irradiation, was measured by a calibrated thermometer in the water phantom. The absolute uncertainty associated with the measured irradiation temperature T at the linac at the PTB is $u(T) = 0.1\,\mathrm{K}$. The correction factor $k_{T,i}$ and the associated uncertainty were calculated as described in Section 2.4.3.
The component $u_r(k_T)$ has to be considered four times: for the test detector surrounded by the air gap with size X irradiated in the absence of the magnetic field, for the test detector surrounded by the air gap with size X irradiated in the presence of the static magnetic field with flux density 1 T, for the test detector surrounded by the gap with 0.0 mm size irradiated in the absence of the magnetic field, and for the test detector surrounded by the gap with 0.0 mm size irradiated in the presence of the 1 T magnetic field. The component has to be considered only twice for the value $\frac{k_{mag,air,0.0mm}}{k_{mag,air,0.0mm}}$.

[8] The exact value of A_D^{corr} used is not that relevant for determining the uncertainty contribution.

Charge indicated by the monitor. The applied dose-to-water $D_{appl,i}$ was determined by the external transmission IC, see Section 3.1.1 and Figures 3.6 and 3.7. The charge indicated by the external transmission IC is already corrected for the air pressure and the temperature (see Section 2.4.2). It is assumed, that other correction factors (e.g. $k_{leakage}, k_{ion}, k_{pol}$, see Section 2.4.2) do not change over the irradiation day. Thus, the charge Q indicated by the external transmission IC can be used directly, i.e. without being converted into an absorbed dose-to-water.
The uncertainty contribution due to the applied dose D_{appl} or rather due to the charges Q indicated by the external transmission IC is composed of the following components (the values in brackets give the relative standard deviation): current measurement (0.05%), random variation drift ($\frac{0.1\%}{\sqrt{3}}$)[9], non-consideration of leakage current ($\frac{0.01\%}{\sqrt{3}}$), deviation of measured temperature and temperature in the IC ($\frac{0.1\%}{\sqrt{3}}$), and influence of temperature variation on the measurement system (0.1%). Contributions for the calibration of the barometer and the thermometer are not required, since all measured values are affected in the same manner. Contributions for the change of the air pressure and the change of the temperature are not required since both are measured and used for correcting the monitor signal continuously. A contribution for the deviation of the measured pressure from the pressure in the IC is negligible. Taken together, this results in a relative uncertainty $u_r(Q_i)$ for a single charge indication of $u_r(Q_i) = 0.16\,\%$. The irradiations of the alanine detectors have been performed as three times 5 Gy irradiations in a row.[10] The contribution $u_r(Q)$ for the sum of these three charge indications summing up to a nominal dose of 15 Gy is, hence, obtained from error propagation as $u_r(Q) = 0.09\,\%$. The component $u_r(Q)$ has to be considered four times: for the test detector surrounded by the air gap with size X irradiated in the absence of the magnetic field, for the test detector surrounded by the air gap with size X irradiated in the presence of the static magnetic field with flux density 1 T, for the test detector surrounded by the gap with 0.0 mm size irradiated in the absence of the magnetic field, and for the test detector surrounded by the gap with 0.0 mm size irradiated in the presence of the 1 T magnetic field. The component has to be considered only twice for the value $\frac{k_{mag,air,0.0mm}}{k_{mag,air,0.0mm}}$.

Summary of the uncertainty budget. In the following, it is discussed how the uncertainty budget for $\frac{k_{mag,air,X}}{k_{mag,air,0.0mm}}$ is set up. The symbol u is used for absolute uncertainties, u_r for relative uncertainties. All uncertainties are given for a coverage factor $k = 1$ and are, thus, corresponding to a confidence probability of approximately 68 % (see Section 2.6). The uncertainty associated with $\frac{k_{mag,air,X}}{k_{mag,air,0.0mm}}$ results from the uncertainty budget containing the following contributions: The rela-

[9] The division by $\sqrt{3}$ here and below is due to the underlying uniform probablity density function, see Section 2.6.

[10] This was done, since – in the backsight – unnecessary checks with a Farmer-type IC were performed in between the alanine irradiations, and these checks are three times faster if an irradiation to 5 Gy is performed instead of 15 Gy.

tive uncertainties $u_r(\bar{m}_X, 1T)$, $u_r(\bar{m}_X, 0T)$, $u_r(\bar{m}_{0.0mm,1T})$, and $u_r(\bar{m}_{0.0mm,0T})$ associated with the mean alanine detector masses; the relative uncertainties $u_r(A^{repro}_{test,X,1T})$, $u_r(A^{repro}_{test,X,0T})$, $u_r(A^{repro}_{test,0.0mm,1T})$, and $u_r(A^{repro}_{test,0.0mm,0T})$ and the relative uncertainties $u_r(A^{hom}_{test,X,1T})$, $u_r(A^{hom}_{test,X,0T})$, $u_r(A^{hom}_{test,0.0mm,1T})$, and $u_r(A^{hom}_{test,0.0mm,0T})$ for the amplitude of the alanine test pellets; the relative uncertainties $u_r(k_{T,X,0T})$, $u_r(k_{T,X,0T})$, $u_r(k_{T,0.0mm,0T})$, and $u_r(k_{T,0.0mm,0T})$ for the irradiation temperature correction; and the relative uncertainties $u_r(Q_{X,1T})$, $u_r(Q_{0.0mm,1T})$, $u_r(Q_{0.0mm,1T})$, and $u_r(Q_{0.0mm,0T})$ associated with the applied dose (i.e. in this case the charges indicated by the monitoring IC). These components are added in quadrature in order to obtain the combined standard uncertainty associated with the ratio $\frac{k_{mag,air,X}}{k_{mag,air,0.0mm}}$. This budget is also listed in Table 3.1. The single components and the total uncertainty are rounded according to the rules stated in [Beringer et al., 2012]. The dominant uncertainty contribution is due to the amplitude determination.

3.1.2 Characterisation at the Elekta Unity™ MR Linac device

The aim of this experiment was to determine the magnetic field correction factor k_{mag}, which has to be applied to the indication of the alanine dosimeter for irradiations at the Elekta Unity™ MR Linac (1.5 T, 7 MV) in order to obtain the actual absorbed dose-to-water. The results of this experiments are, hence, required for the application of the alanine dosimeter in MRgRT with the Elekta Unity™ MR Linac.

Experiment and applied devices

Detector holders. Stacks of four alanine pellets were placed within the Farmer IC-like PMMA holder as shown in Figure 2.20 to be used as detectors throughout this experiment.[11] This holder is waterproof and can be positioned within water phantoms without an additional sleeve.

Alanine pellets. Five alanine detectors were used as alanine test pellets in this exeriment and eventually the mean of the five correction factors k_{mag} determined with these five detectors was taken. Four additional alanine detectors were used as alanine base pellets. Two of them were irradiated to a nominal absorbed dose-to-water of 25 Gy in the Cobalt-60 reference field at the PTB, two remained unirradiated. All these detectors were composed of four alanine pellets from Harwell Batch AM603.

Weighting. The weighting was performed as described in Section 3.1.1.

[11] The alanine holder can contain eight pellets, and it was filled with pellets a...h accordingly. However, only the four inner pellets (c...f) were used for the analysis. The pellets a, b. g, h were "dummy pellets".

Table 3.1: Uncertainty budget for the ratio $\frac{k_{mag,air,X}}{k_{mag,air,0.0mm}}$. The total uncertainty was calculated using the non-rounded single components. All uncertainties are given for a coverage factor $k = 1$. The values in brackets are for the data point at 0.0 mm, where several components cancel out (see text).

Contribution	due to ...	u_r in %
$u_r(\bar{m}_X, 1T)$	mass of test pellets (air gap X, irradiation at 1 T)	0.04 (–)
$u_r(\bar{m}_X, 0T)$	mass of test pellets (air gap X, irradiation at 0 T)	0.04 (–)
$u_r(\bar{m}_{0.0mm,1T})$	mass of test pellets (0.0 mm air gap, irradiation at 1 T)	0.04 (0.04)
$u_r(\bar{m}_{0.0mm,0T})$	mass of test pellets (0.0 mm air gap, irradiation at 0 T)	0.04 (0.04)
$u_r(A^{repro}_{test,X,1T})$	reproducibility of the amplitude determination (test pellets, air gap X, irradiation at 1 T)	0.18 (–)
$u_r(A^{repro}_{test,X,0T})$	reproducibility of the amplitude determination (test pellets, air gap X, irradiation at 0 T)	0.18 (–)
$u_r(A^{repro}_{test,0.0mm,1T})$	reproducibility of the amplitude determination (test pellets, 0.0 mm air gap, irradiation at 1 T)	0.18 (0.18)
$u_r(A^{repro}_{test,0.0mm,0T})$	reproducibility of the amplitude determination (test pellets, 0.0 mm air gap, irradiation at 0 T)	0.18 (0.18)
$u_r(A^{hom}_{test,X,1T})$	homogeneity of the alanine pellet composition (test pellets, air gap X, irradiation at 1 T)	0.15 (–)
$u_r(A^{hom}_{test,X,0T})$	homogeneity of the alanine pellet composition (test pellets, air gap X, irradiation at 0 T)	0.15 (–)
$u_r(A^{hom}_{test,0.0mm,1T})$	homogeneity of the alanine pellet composition (test pellets, 0.0 mm air gap, irradiation at 1 T)	0.15 (0.15)
$u_r(A^{hom}_{test,0.0mm,0T})$	homogeneity of the alanine pellet composition (test pellets, 0.0 mm air gap, irradiation at 0 T)	0.15 (0.15)
$u_r(k_{T,X,1T})$	correction for irradiation temperature (test pellets, air gap X, irradiation at 1 T)	0.022 (–)
$u_r(k_{T,X,0T})$	correction for irradiation temperature (test pellets, air gap X, irradiation at 0 T)	0.020 (–)
$u_r(k_{T,0.0mm,1T})$	correction for irradiation temperature (test pellets, air gap X, irradiation at 1 T)	0.022 (0.022)
$u_r(k_{T,0.0mm,0T})$	correction for irradiation temperature (test pellets, air gap X, irradiation at 0 T)	0.020 (0.020)
$u_r(Q_{X,1T})$	sum of charge readings of the external transmission chamber (monitor 2) for test pellets (air gap X, irradiation at 1 T)	0.09 (–)
$u_r(Q_{X,0T})$	sum of charge readings of the external transmission chamber (monitor 2) for test pellets (air gap X, irradiation at 0 T)	0.09 (–)
$u_r(Q_{0.0mm,1T})$	sum of charge readings of the external transmission chamber (monitor 2) for test pellets (0.0 mm air gap, irradiation at 1 T)	0.09 (0.09)
$u_r(Q_{0.0mm,0T})$	sum of charge readings of the external transmission chamber (monitor 2) for test pellets (0.0 mm air gap, irradiation at 0 T)	0.09 (0.09)
Total:	$u_r\left(\frac{k_{mag,air,X}}{k_{mag,air,0.0mm}}\right) = 0.5\ (0.4)$	

Irradiation of the base pellets at the Cobalt-60 facility at the PTB. The Cobalt-60 facility at the PTB was used for the irradiation of two alanine base detectors as described in Section 3.1.1.

Irradiation of the test pellets at the Elekta Unity™ MR Linac. The alanine test detectors were irradiated at the Elekta Unity™ MR Linac device at The Christie hospital in Manchester, UK, which features a static magnetic field with flux density 1.5 T and an FFF beam with a nominal accelerating potential of 7 MV (see Section 2.2.3). A picture of this MR Linac is shown in Figure 3.8.
The irradiation of the alanine detectors was performed within a water phantom positioned on the patient couch inside the bore of the MR Linac. A schematic illustration indicating the orientations of the alanine detectors, the photon beam, and the magnetic field is shown in Figure 3.9. The alanine detectors were positioned such that the tip of the PMMA holder pointed to the floor. The water phantom used was built at the NPL, the UK's metrology institute. This water phantom has a width and a length of 33.0 cm and a height of 21.5 cm. The walls are made of PMMA and the phantom includes a square frame made of PMMA for reproducible positioning of the detectors. This frame is fixated in the phantom via "rails" at the walls of the water phantom.
During the experiment, alanine detectors and Farmer-type ICs which had been calibrated directly in the magnetic field [de Prez et al., 2019] were irradiated in alternation. This allowed to refer the alanine indications to the absorbed doses-to-water measured with the Farmer-type IC transfer standards. The three Farmer-type IC transfer standards applied in the present experiment were PTW 30013-8377, PTW 30013-7120, and IBA FC65G-3213. These three transfer standards were provided by Van Swinden Laboratory (VSL), the Dutch metrology institute [de Prez et al., 2019]. Both, the alanine detectors and the Farmer-type IC transfer standards were mounted on the PMMA frame of the water phantom (see Figure 3.9). This frame was positioned such, that the Farmer-type IC transfer standards were located in the isocenter of the MR Linac in a water equivalent depth of 10 cm (the front wall of the phantom was scaled from PMMA to water). The distance between the source and the isocenter of the Elekta Unity™ MR Linac is 143.5 cm. Due to a problem in mounting the PMMA holder of the alanine detectors on this PMMA frame, the alanine detectors could unfortunately not be irradiated in exactly the same position as the Farmer-type IC transfer standards. The larger water depth for the alanine detectors was, however, considered in the analysis by the application of a correction factor (see Section 3.1.2). The size of the radiation field was 10 cm×10 cm at the measurement plane.
For the irradiations of the Farmer-type IC transfer standards, these ICs were connected to an electrometer. Negative charge was collected. The electrometer was warmed up and zeroed prior to each measurement in order to exclude background signals. The irradiation temperature, which is required for the dose assessment with the alanine dosimeter and with the ICs, was measured with a thermometer placed

Figure 3.8: The Elekta Unity™ MR Linac device at The Christie hospital in Manchester, UK. The water phantom applied in the present investigation can be seen on the patient couch.

within the water phantom. The relative humidity in the measurement room, which is relevant for the dose assessment with the ICs was monitored to be between 20 % and 70 %, and the air pressure in the measurement room was monitored with a calibrated barometer. Air pressure and temperature were used for correcting the signal of the Farmer-type IC transfer standards to standard environmental conditions (see Section 3.1.2). All irradiations were monitored with a Farmer-type IC that was placed in the water phantom close to the front wall.
The exact order of irradiations used in this experiment is listed in Table 3.2. Please note that these irradiations were performed within a measurement week with several participants. The time between the listed irradiations was filled with irradiations performed by other participants.

Readout with the Bruker EMX 1327 EPR spectrometer at the PTB. The alanine detectors were read out with the Bruker EMX 1327 EPR spectrometer at the PTB as described in Section 3.1.1. The readout was performed on two measurement days. Three alanine test detectors were read out with the base detectors on the first day, the remaining two alanine test detectors were read out with the same base pellets on the second measurement day.[12]

Analysis and uncertainties

The aim of this analysis was to determine the magnetic field correction factor k_{mag} that has to be applied to the indication of the alanine dosimeter for measurements at the Elekta Unity™ MR Linac in order to obtain the absorbed dose-to-water in

[12] Please note, that the fact that the alanine detectors were read out on two different days does not increase the uncertainty associated with the resulting correction factor k_{mag} since the model equations 3.13 and 3.14 compare one alanine signal with one Farmer-type IC transfer standard signal each time and not different alanine signals (see Section 3.1.2).

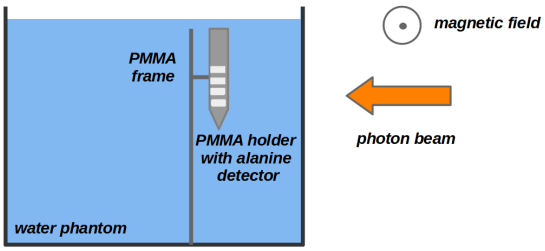

Figure 3.9: Schematic illustration of the setup at the Elekta Unity™ MR Linac device indicating the orientation of the alanine detectors, the photon beam, and the magnetic field.

Table 3.2: Order of irradiations of alanine detectors and Farmer-type IC transfer standards analysed in the present investigation. The alanine detectors and transfer standard irradiations which were referred to each other in the analysis are grouped between horizontal lines.

Date	Time	Run	Alanine detector/transfer standard	Monitor units
2017-09-19	12:18	12	Alanine detector hm35-c1...f1	2×750 MU
2017-09-19	12:31	13	PTW 30013-8377	5×200 MU
2017-09-19	14:04	17	PTW 30013-7120	5×200 MU
2017-09-19	14:39	19	Alanine detector hm35-c2...f2	2×750 MU
2017-09-20	14:06	15	Alanine detector hm35-c3...f3	2×750 MU
2017-09-20	14:14	16	IBA FC65G-3213	5×200 MU
2017-09-21	11:47	14	Alanine detector hm35-c4...f4	2×750 MU
2017-09-21	11:55	15	IBA FC65G-3213	5×200 MU
2017-09-21	15:44	33	Alanine detector hm35-c5...f5	2×750 MU
2017-09-21	15:51	34	IBA FC65G-3213	5×200 MU

the presence of the static magnetic field with flux density 1.5 T. This is achieved by comparing each of the indications A_D^{corr} of the five alanine detectors irradiated at the Elekta Unity™ MR Linac in the presence of the static magnetic field with the absorbed dose-to-water D_{appl} measured closest in time with on of the Farmer-type IC transfer standards in the same setup.

Derivation of the model equation. Assuming completely corrected values results in

$$1 = \frac{A_D^{corr}}{D_{appl}} \tag{3.8}$$

which is the starting point for the derivation of the model equation. The corrected dose-normalised amplitude A_D^{corr} is given by Equation 2.30. At this, the correction factor $K_{V,s}$ for volume and sensitivity (see Section 2.4.3) equals unity due to constant gradients in beam direction and can, hence, be omitted without consideration of an uncertainty contribution. The non-constant gradient in the lateral direction due to the FFF beam of the Elekta Unity™ MR Linac is considered by the correction factor k_{vol}^{ala} (see Section 2.4.2) which was applied in analogy to [Billas et al., 2021] and [de Prez et al., 2019] not only for the Farmer-type IC transfer standards but also for the alanine detectors in order to correct for the resulting volume effect, see Section 3.1.2. The correction factor K_{env} for the environment surrounding the alanine detectors can be omitted without considering an uncertainty component ($K_{env} = 1$) since both the irradiation of the base detectors in the Cobalt-60 reference field at the PTB and the irradiation of the test detectors at the MR Linac were performed with the alanine detectors in the PMMA holder positioned within a water phantom. The correction factors K_{air} and $K_{mag,air}$ are not required according to the results of the previously described preparatory experiment (see Section 4.1.1). The expression for A_D^{corr} in the present situation is hence:

$$A_D^{corr} = \frac{A_m}{\bar{m}} \cdot \bar{m}^b \cdot D^b \cdot K_T \cdot K_Q \cdot K_F \cdot K_{vol}^{ala} \cdot K_{mag} \tag{3.9}$$

The absorbed dose-to-water D_{IC} obtained with the Farmer-type IC transfer standard is

$$D_{IC} = M_{raw} \cdot k_{TP} \cdot k_{ion} \cdot k_{elec} \cdot N_{D_W,Q,B} \cdot k_{vol}^{IC} \cdot k_{output} \cdot k_{depth} \tag{3.10}$$

following Equation 2.23. In addition to the correction factors listed in Section 2.4.2, the correction factor k_{depth} is used correcting for the slightly different water equivalent depth of the transfer standards and the alanine detectors in the setup (see Section 3.1.2).
The absorbed dose-to-water D_{IC} obtained with the Farmer-type IC transfer standard is, however, not equal to the absorbed dose-to-water D_{appl} applied to the alanine detector. The alanine detectors were irradiated to 1500 MU while the transfer standards were irradiated to 1000 MU (see Table 3.2). The absorbed dose-to-water D_{IC}

received by the Farmer-type IC transfer standard has, thus, to be scaled to the absorbed dose-to-water D_{appl} applied to the alanine detector. This is done using the signal of the monitoring Farmer-type IC. The absorbed dose-to-water D_{appl} applied to the alanine detector is the absorbed dose-to-water D_{IC} received by the Farmer-type IC transfer standard divided by the reading $M_{mon,IC}$ of the monitoring Farmer-type IC during the irradiation of the transfer standard and multiplied with the reading $M_{mon,ala}$ of the monitoring Farmer-type IC during the irradiation of the alanine detector:

$$D_{appl} = \frac{D_{IC}}{M_{mon,IC}} \cdot M_{mon,ala} \tag{3.11}$$

Please note, that both $M_{mon,IC}$ and $M_{mon,ala}$ are corrected to standard environmental conditions:

$$M_{mon,IC/ala} = M^{raw}_{mon,IC/ala} \cdot k_{TP,mon,IC/ala} \tag{3.12}$$

As mentioned above, the aim of this analysis is to determine the magnetic field correction factor k_{mag}. The determination of this correction factors k_{mag} is, however, based on an assumption about the radiation quality correction factor K_Q (see Section 3.1.2). In the practical application, both the correction factor k_{mag} and the correction factor K_Q have to be applied. Since the product $(K_Q \cdot k_{mag})$ is experimentally accessible without any assumption about the radiation quality correction factor K_Q which implies a smaller associated uncertainty, the product of correction factors $(K_Q \cdot k_{mag})$ was determined in addition in this analysis ("Analysis A") in order to provide this product for the application. The determination of the mere correction factor k_{mag} ("Analysis B") is, however, important for the comparison with results from literature and results from the other experiments within this thesis.

Combining the Equations 3.8 to 3.12 results in the model equations. The model equation for Analysis A results from the equations above as:

$$(K_Q{\cdot}k_{mag}) = \frac{M_{raw} \cdot k_{TP} \cdot k_{ion} \cdot k_{elec} \cdot N_{D_W,Q,B} \cdot k^{IC}_{vol} \cdot k_{output} \cdot k_{depth} \cdot \frac{M^{raw}_{mon,ala} \cdot k_{TP,mon,ala}}{M^{raw}_{mon,IC} \cdot k_{TP,mon,IC}}}{\frac{A_m}{\bar{m}} \cdot \bar{m}^b \cdot D^b_W \cdot K_T \cdot K_F \cdot K^{ala}_{vol}} \tag{3.13}$$

Please note, that k_{mag} can be used instead of K_{mag} since the correction factor k^b_{mag} for the alanine base detector irradiated in the absence of a magnetic field equals unity (see Equation 2.29).

The model equation for Analysis B results analogously as:

$$k_{mag} = \frac{M_{raw} \cdot k_{TP} \cdot k_{ion} \cdot k_{elec} \cdot N_{D_W,Q,B} \cdot k^{IC}_{vol} \cdot k_{output} \cdot k_{depth} \cdot \frac{M^{raw}_{mon,ala} \cdot k_{TP,mon,ala}}{M^{raw}_{mon,IC} \cdot k_{TP,mon,IC}}}{\frac{A_m}{\bar{m}} \cdot \bar{m}^b \cdot D^b_W \cdot K_T \cdot K_Q \cdot K_F \cdot K^{ala}_{vol}} \tag{3.14}$$

Quantities in the model equation and uncertainty budget. The following describes how k_{mag} and $(K_Q \cdot k_{mag})$ were obtained from the experimental data. The basis for this procedure are the model equations 3.13 and 3.14.

Reading of the ICs, correction to standard conditions, and scaling to the alanine irradiation. The raw readings M_{raw} of the Farmer-type IC transfer standards and $M^{raw}_{mon,IC/ala}$ of the monitoring Farmer-type IC were denoted during the experiment. Five irradiation to 200 MU were performed each time. The signals of these five irradiations were summed up. The charges collected for the Farmer-type IC transfer standard irradiations and the monitoring Farmer-type IC were corrected to standard conditions (i.e. 20°C and 1013.25 mbar) by applying the correction factor $k_{TP(,mon,IC/ala)}$ for temperature and air pressure. The correction factor $k_{TP(,mon,IC/ala)}$ was calculated according to the description in Section 2.4.2. The associated relative uncertainty was calculated as

$$u_r(k_{TP(,mon,IC/ala)}) = \sqrt{\frac{u(p)^2}{p^2} + \frac{u(T)^2}{(273.15+T)^2}} \tag{3.15}$$

with $u(T) = 0.3$°C (composed of the uncertainties for the calibration factor of the thermometer, the difference between measured water temperature and the temperature of the IC and the alanine detector, respectively, and the imprecision of reading) and $u(p) = 0.20$ mbar.

Correction for the recombination. The correction factor k_{ion} was applied to the signal of the Farmer-type IC transfer standards in order to consider the incomplete charge collection due to recombination. The correction factor k_{ion} was determined by Illias Billas (NPL), who also participated in the measurement week, based on measurements for a "Jaffé plot" taken during the measurement week with voltages between +300 V and +100 V, which is the lowest voltage the used electrometer allows for. The correction factor for the transfer standards PTW 30013-8377 and PTW 30013-7120 is $k^{PTW}_{ion} = 1.0041$ and for IBA FC65G-3213 $k^{IBA}_{ion} = 1.0048$ with a relative uncertainty of $u_r(k_{ion}) = 0.04\,\%$ in each case.

Correction for the electrometer. The electrometer used during the measurement week was provided by the NPL and, thus, the correction factor for the electrometer k_{elec} was applied according to NPL's recommendations as $k_{elec} = 1.000$ with a relative uncertainty of $u_r(k_{elec}) = 0.10\,\%$.

Calibration factors for the Farmer-type IC transfer standards. The calibration factors $N_{D_W,Q,B}$ converting the signal of the Farmer-type IC transfer standards in the presence of the static magnetic field at the Elekta Unity™ MR Linac into the actual absorbed dose-to-water are taken from [de Prez et al., 2019], Table

4[13]. The values applied here are:

$$\begin{aligned} N_{D_W,Q,B}^{PTW30013-7120} &= 50.65\,\mathrm{mGynC^{-1}} \\ N_{D_W,Q,B}^{PTW30013-8377} &= 50.66\,\mathrm{mGynC^{-1}} \\ N_{D_W,Q,B}^{IBAFC65G-3213} &= 45.29\,\mathrm{mGynC^{-1}} \end{aligned} \tag{3.16}$$

with $u_r(N_{D_W,Q,B}^{PTW}) = 0.35\,\%$ for the transfer standards PTW 30013-8377 and PTW 30013-7120 and $u_r(N_{D_W,Q,B}^{IBA}) = 0.10\,\%$ for the transfer standard IBA FC65G-3213. An uncertainty component of 0.05 % was included in the analysis in addition considering the fact that the calibration factors $N_{D_W,Q,B}$ were determined at another Elekta Unity™ machine (UMC Utrecht) than the machine which was used for the present experiment (The Christie hospital). This additional uncertainty contribution was estimated based on the tabulated k_Q factors as a function of beam quality $\mathrm{TPR}_{20,10}$ in [Andreo et al., 2000] (Tab. 6III), considering the finding of [Billas et al., 2021] that the $\mathrm{TPR}_{20,10}$ can vary up to 0.5 % between different Elekta Unity™ machines. It is (according to [de Prez et al., 2019])

$$N_{D_W,Q,B} = N_{D_W,Q_0} \cdot k_Q \cdot k_B \tag{3.17}$$

with the usual calibration factor N_{D_W,Q_0} converting the signal of an IC into the absorbed dose-to-water in the absence of a magnetic field, the correction factor for the radiation quality k_Q, and the correction factor for the additional magnetic field k_B; i.e. $N_{D_W,Q,B} \propto k_Q$. Hence, the expected changes in $N_{D_W,Q,B}$ can be estimated from the changes in k_Q.

Volume correction. The volume correction factor k_{vol} is required for the Farmer-type IC and for the alanine detectors due to the FFF beam of the Elekta Unity™ MR Linac, see Section 2.4.2. It is denoted as k_{vol}^{IC} for the Farmer-type IC transfer standard signal and as k_{vol}^{ala} for the alanine signal (see Equations 3.13 and 3.14). Both methods of determination mentioned in Section 2.4.2 were used within this analysis in order to receive more reliability by comparison of the resulting correction factors k_{vol}.

The first method is based on Equation (54) from [Palmans et al., 2017]:

$$k_{vol} = 1 + (6.2 \times 10^{-3} \cdot \mathrm{TPR}_{20,10}(10) - 3.57 \times 10^{-3}) \cdot \left(\frac{100}{\mathrm{SDD}}\right)^2 \cdot L^2 \tag{3.18}$$

L is the nominal cavity length L of the detector. It is $L = 2.3\,\mathrm{cm}$ for the applied Farmer-type IC transfer standards [de Prez et al., 2019] (Sec. 3.2) and $L = 1.12\,\mathrm{cm}$ for the alanine detectors (i.e. four times the height 2.8 mm of a single alanine pellet). The $\mathrm{TPR}_{20,10}$ for a $10\,\mathrm{cm} \times 10\,\mathrm{cm}$ photon field is $\mathrm{TPR}_{20,10} = (0.697 \pm 0.003)$ in this

[13] Please note, that the unit [$\mathrm{mGypC^{-1}}$] given in [de Prez et al., 2019] is a typo, it has to be [$\mathrm{mGynC^{-1}}$]. (Confirmed in personal communication with the author.)

experiment [Billas et al., 2021] (see the comments regarding the correction factor K_Q in Section 3.1.2). The source to detector distance (SDD) is the sum of the SSD and the measurement depth with SDD= 143.5 cm in this experiment. Please note that Equation 3.18 is based on the assumption that the field size is defined in 100 cm distance from the source [Palmans et al., 2017], which is not the case in this experiment (here: 143.5 cm). It can, however, be assumed that this detail has no significant effect on the result since the photon field size 10 cm×10 cm is maintained. The uncertainty associated with the resulting correction factor k_{vol} is $u_r(k_{vol}) = 0.05\,\%$ [Billas et al., 2021]. The results obtained with this method for the Farmer-type IC transfer standards and the alanine detectors are $k_{vol}^{IC} = 1.0019 \pm 0.0005$ and $k_{vol}^{ala} = 1.0005 \pm 0.0005$, respectively. This is in agreement with the correction factors k_{vol} obtained by [Billas et al., 2021] (1.0019 and 1.0005, [Billas et al., 2021], Sec. 3.4).

The second method is based on dividing the integral of a constant function with the value of the central axis dose over the length of the detector by the integral of the lateral dose profile over the length of the detector [de Prez et al., 2019], (Sec. 2.4). The first step for this second method is to perform a fit to a measured lateral dose profile of the applied photon beam. The data used was taken during the commissioning of the Elekta Unity™ MR Linac at The Christie hospital. The fit was performed as a fourth grade polynomial. The fit function was used for determining the central axis dose and it was used for the integral over the nominal cavity length L (as in the first method it is $L = 2.3$ cm for the transfer standards [de Prez et al., 2019], (Sec. 3.2) and $L = 1.12$ cm for the alanine detectors). Furthermore, the integral over the nominal cavity length for a constant function with the value of the central axis dose was determined. The correction factor k_{vol} was eventually obtained by dividing this integral of the function with the value of the central axis dose by the integral over the fourth grade polynomial, see Figure 2.15. The associated uncertainties are $u_r(k_{vol}) = 0.05\,\%$ [de Prez et al., 2019] (Sec. 3.2). The results obtained with this method for the Farmer-type IC transfer standards and the alanine detectors are $k_{vol}^{IC} = 1.0026 \pm 0.0005$ and $k_{vol}^{ala} = 1.0006 \pm 0.0005$, respectively. The factor for the transfer standards is in agreement with the factor determined in [de Prez et al., 2019] (1.0022(5), Sec. 3.2). No factor for alanine detectors was determined in [de Prez et al., 2019].[14]

The results obtained with method (1) and (2) are in agreement with each other which increases the reliability of the results. It was decided to apply the correction factors k_{vol} determined with method (2), since it is assumed that measured data is a more reliable basis than a standard formula, especially since the assumption for Equation 3.18 that the field size is defined in 100 cm distance from the source is not fulfilled in the present setup. The correction factors k_{vol} used in this analysis are,

[14] As an additional consistency check, the determination of the correction factors k_{vol} was also performed for the lateral dose profile in the second direction. No significant difference was found in the correction factors k_{vol} determined for lateral x and y direction. This is in agreement with the results of [de Prez et al., 2019], (Sec. 3.2).

thus:

$$\begin{aligned} k_{vol}^{IC} &= 1.0026 \pm 0.0005 \\ k_{vol}^{ala} &= 1.0006 \pm 0.0005 \end{aligned} \tag{3.19}$$

Correction for the output of the MR Linac. This analysis is based on comparing the signals of alanine detectors and Farmer-type IC transfer standards. The alanine and transfer standard irradiations were performed throughout the measurement week. The transfer standard measurement with the smallest time difference to the respective alanine irradiation was chosen for the comparison each time. The time differences between the pairs of alanine irradiation and transfer standard irradiation are about 10 minutes (see Table 3.2). It is possible, that the output of the MR Linac, which is the dose per MU, changes between the alanine and the transfer standard irradiation. The drift of the MR Linac output was, thus, investigated.
The maximum drift of the MR Linac output in percent per minute was determined using the signals of the three transfer standards before and after each alanine irradiation. The maximum drift was determined in order to obtain a conservative estimation. This was done by using the higher transfer standard signal plus the associated uncertainty (coverage factor $k = 1$) and the lower transfer standard signal minus the associated uncertainty. The obtained output drift in percent per minute was then scaled to the time difference between the alanine and the transfer standard irradiation. In the cases where pairs of values before and after the alanine irradiation were available for more than one of the transfer standards, the drift was averaged. The drift was not corrected in the final analysis, i.e. $k_{output} = 1$, but the determined maximum drift during the time difference between the alanine and the transfer standard irradiation was considered in the uncertainty budget as $u_r(k_{output})$. The resulting uncertainty components $u_r(k_{output})$ due to the MR Linac output drift which were considered in the uncertainty budgets are (0.032, 0.04, 0.020, 0.033, 0.04) % for the alanine detectors hm35-c1...f1, hm35-c2...f2, hm35-c3...f3, hm35-c4...f4, and hm35-c5...f5, respectively.

Depth correction. As mentioned above, the PMMA holder containing the alanine detectors could not be fixated in the water phantom in the same position as the Farmer-type IC transfer standards, which were positioned in 10 cm water equivalent depth (phantom front wall scaled from PMMA to water). The alanine detectors were positioned in a slightly larger water equivalent depth of (10.15 ± 0.05) cm. The associated uncertainty refers to the determination of the depth. A component considering the reproducibility of the positioning can be neglected since the PMMA holder with the alanine detectors was screwed firmly to the distal side of the holding device in each irradiation. A correction factor k_{depth} considering the different position of the alanine detectors and the transfer standards was determined based on the depth dose profile measured during the commissioning of the Elekta Unity™ MR Linac at The Christie hospital. A linear fit was performed through the three data points of this depth dose profile closest to the measurement points of the alanine

dosimeter and the transfer standards (i.e. (9.61, 10.11, 10.61) cm). The correction factor k_{depth} is multiplied with the signal of the transfer standard in the model equations 3.13 and 3.14. The correction factor k_{depth} is, thus, determined by dividing the dose at the position of the alanine detector (10.15 cm) obtained from the fitted line by the dose at the position of the transfer standard (10.00 cm) obtained from the fitted line. The associated uncertainty was estimated by repeating this calculation with a depth of 10.10 cm and 10.20 cm, respectively, for the alanine dosimeter, according to the uncertainty of 0.05 cm associated with the position of the alanine detectors. The correction factor k_{depth} was finally determined to be

$$k_{depth} = 0.9922 \pm 0.0026 \tag{3.20}$$

Alanine pellet mass. The individual masses m_i of the four alanine pellets composing a single alanine test detector are averaged for obtaining the mean mass $\bar{m}$ of the respective detector. An uncertainty contribution $u_r(\bar{m})$ has to be considered for each alanine detector according to the description in Section 3.1.1. Likewise, the individual masses m_i^b of the eight alanine pellets composing the two alanine base detectors are averaged for obtaining the mean mass $\bar{m}^b$ of the base. The uncertainty associated with $\bar{m}^b$ is determined analogously to $u_r(\bar{m})$.

Alanine amplitude. The values for A_m are obtained from the EPR measurements of the alanine detectors. The uncertainty associated with the amplitude values A_m has two contributions. One is due to the reproducibility of the amplitude measurement and the other one is due to the homogeneity of the detector material. These contributions have to be considered for the alanine test and the alanine base detectors.
The uncertainty component $u_r(A_{m,test}^{repro})$ due to the reproducibility for the alanine test detector is calculated using Equation 3.6 as described in Section 3.1.1 and the uncertainty component $u_r(A_{m,base}^{repro})$ due to the reprocucibility for the alanine base detector is calculated as

$$u_r(A_{m,base}^{repro}) = \sqrt{\frac{{u_{repro}}^2}{n_b \cdot {D_W^b}^2} \cdot (1 + \frac{1}{f^2})} \tag{3.21}$$

The uncertainty component $u_r(A_{m,test}^{hom})$ due to the homogeneity for the alanine test detector is calculated with Equation 3.7 as described in Section 3.1.1 and the component $u_r(A_{m,base}^{hom})$ due to the homogeneity for the alanine base detector is determined analogously.

Irradiation temperature correction. The correction factor K_T for the irradiation temperature required in the model equations 3.13 and 3.14 is obtained via the same principle as described in Section 3.1.1. The absolute uncertainty associated with the measured irradiation temperature T at the Elekta Unity™ is $u(T) = 0.3\,\mathrm{K}$

(see Section 3.1.2); the absolute uncertainty associated with the measured irradiation temperature T^b in the Cobalt-60 reference field at the PTB is $u(T^b) = 0.1\,\mathrm{K}$. The correction factor K_T and the associated uncertainty are obtained as described in Section 2.4.3.

Radiation quality correction. This analysis requires a correction factor K_Q considering the difference in the radiation quality between the alanine base detectors irradiated in the Cobalt-60 reference field at the PTB and the alanine test detectors irradiated in the 7 MV photon field of the Elekta Unity™ MR Linac at The Christie hospital. This correction factor K_Q has to be multiplied with the alanine indication in the model equation (see Equation 3.14). The first step in determining the correction factor K_Q is to consider the $\mathrm{TPR}_{20,10}$ at the Elekta Unity™ device. The tissue phantom ratio $\mathrm{TPR}_{20,10}$ can be used to quantify the radiation quality. The $\mathrm{TPR}_{20,10}$ is obtained from the indications of a dosimeter irradiated in 20 cm and 10 cm depth within a water phantom under reference conditions [Deutsches Institut für Normung e.V., 2008], see Section 2.4.2. [de Prez et al., 2019] determined the $\mathrm{TPR}_{20,10}$ of the Elekta Unity™ device in the presence of 1.5 T at UMC Utrecht to $\mathrm{TPR}_{20,10} = 0.701(2)$. [Billas et al., 2021] determined the average $\mathrm{TPR}_{20,10}$ of the Elekta Unity™ devices at The Christie hospital in Manchester, UK, at the Odense University Hospital, Denmark, at the Netherlands Cancer Institute, The Netherlands, and at the Royal Marsden Hospital, UK in the presence of 1.5 T to $\mathrm{TPR}_{20,10} = 0.697 \pm 0.003$. [Billas et al., 2021] states in addition that the $\mathrm{TPR}_{20,10}$ can vary up to 0.5 % between different Elekta Unity™ machines at 1.5 T. It was decided to consider the value $\mathrm{TPR}_{20,10} = 0.697 \pm 0.003$ in the present investigation. It is considered to be more reliable for the present investigation than the value from [de Prez et al., 2019] as it is based on measurements at four different Elekta Unity™ MR Linacs with one of them being the MR Linac the present experiment was performed at. No measured value of the correction factor K_Q for the alanine dosimeter was available for this $\mathrm{TPR}_{20,10} = 0.697 \pm 0.003$. However, this $\mathrm{TPR}_{20,10}$ is in the region for which the correction factor K_Q of the alanine dosimeter is nearly constant [Anton et al., 2013]. The correction factor K_Q for the present investigation at $\mathrm{TPR}_{20,10} = 0.697 \pm 0.003$ was, thus, determined as the mean of the closest available measured correction factors K_Q, which are $K_Q = 1.0030 \pm 0.0035$ for $\mathrm{TPR}_{20,10} = 0.683$ and $K_Q = 1.0042 \pm 0.0041$ for $\mathrm{TPR}_{20,10} = 0.714$ (determined by Mathias Anton). The uncertainty associated with the resulting correction factor K_Q was determined such, that it covers the complete confidence interval with coverage factor $k = 1$ of the measured values $K_Q = 1.0030 \pm 0.0035$ and $K_Q = 1.0042 \pm 0.0041$. The resulting correction factor K_Q for $\mathrm{TPR}_{20,10} = 0.697 \pm 0.003$ for the alanine dosimeter applied in the present investigation results as

$$K_Q = 1.004 \pm 0.005 \tag{3.22}$$

This is in agreement with the value $K_Q = 1.004 \pm 0.006$ based on [Thomas et al., 2014], which is applied in [Billas et al., 2021]. Nevertheless, it has to be considered, that the applied correction factor K_Q is based on an assumption and not on

a measurement. The analysis was, thus, performed in two ways. Once, the correction factor k_{mag} was determined using the correction factor K_Q (Equation 3.22) for comparison with results from previous experiments and from literature (see Equation 3.14), and once, the product of correction factors ($K_Q \cdot k_{mag}$) was determined for application (see Equation 3.13). This product is not based on any assumptions about the factor K_Q but on pure measurement; the associated uncertainty is, hence, smaller.

Fading correction. The correction factor K_F for the fading which is the slow recombination of radicals in the alanine material required in the model equations 3.13 and 3.14 and the associated uncertainty are obtained as described in Section 2.4.3.

Polarity correction. A correction factor for the polarity of the Farmer-type IC transfer standards is not required (or else: $k_{polarity} = 1$) since these transfer standards collected negative charge during their calibration in the magnetic field performed by VSL at the (at that time pre-clinical) Elekta Unity™ device of the UMC Utrecht and negative charge was also collected during the measurement week at the MR Linac at The Christie hospital.

Leakage current correction. A correction factor for the leakage current of the Farmer-type IC transfer standards is not required (or else: $k_{leakage} = 1$) since the electrometer applied was warmed up and zeroed prior to each measurement.

Humidity correction. A correction factor for the humidity is not required (or else: $k_{humidity} = 1$) since the relative humidity was between 20 % and 70 % throughout the measurement week [Bichsel et al., 1979; McEwen and Taank, 2017].

Summary of the uncertainty budget. The uncertainty associated with the correction factor k_{mag} obtained from Equation 3.14 for one alanine signal and the corresponding transfer standard signal results from the uncertainty budget containing the following contributions: The relative uncertainties $u_r(k_{TP})$ for the correction to standard environmental conditions for the signal of the Farmer-type IC transfer standard, for the signal of the monitoring IC during the transfer standard irradiation, and for the signal of the monitoring IC during the alanine detector irradiation; the relative uncertainty $u_r(k_{ion})$ for the correction of incomplete charge collection due to recombination; the relative uncertainty $u_r(k_{elec})$ for the electrometer; the relative uncertainty $u_r(N_{D_W,Q,B})$ for the calibration factor and the additional component $u_r(N_{D_W,Q,B,add})$ due to the fact that the calibration was performed with another Elekta Unity™ machine than the present experiment was performed with; the relative uncertainty $u_r(k_{ion}^{IC})$ for the volume correction for the Farmer-type IC transfer standard; the relative uncertainty $u_r(k_{output})$ for possible drifts in the output of the MR Linac; the relative uncertainty $u_r(k_{depth})$ for the

correction due to the slightly different water depths of alanine detectors and transfer standards; the relative uncertainties $u_r(A^{repro}_{m,test})$ and $u_r(A^{repro}_{m,base})$ and the relative uncertainties $u_r(A^{hom}_{m,test})$ and $u_r(A^{hom}_{m,base})$ associated with the amplitudes of the alanine test and base pellets; the relative uncertainties $u_r(\bar{m})$ and $u_r(\bar{m}^b)$ associated with the mean masses $\bar{m}$ and $\bar{m}^b$ of the alanine test pellets and the alanine base pellets, respectively; the relative uncertainty $u_r(K_T)$ for the irradiation temperature correction for the alanine detector; the relative uncertainty $u_r(K_F)$ for the fading correction for the alanine detector; the relative uncertainty $u_r(k^{ala}_{ion})$ for the volume correction for the alanine detector; and the relative uncertainty $u_r(K_Q)$ for the radiation quality correction for the alanine dosimeter. These components are added in quadrature in order to obtain the combined standard uncertainty associated with the correction factor k_{mag} (with coverage factor $k = 1$). This budget is also listed in Table 3.3. The single components and the total uncertainty are rounded according to the rules stated in [Beringer et al., 2012]. Please note that the smaller total uncertainty for the alanine detectors hm35-c3...f3, hm35-c4...f4, and hm35-c5...f5 results from the fact that the IBA FC65G-3213 transfer standard was used for comparison in these cases, resulting in a smaller component for the calibration factor.

The uncertainty associated with the product of correction factors $(K_Q \cdot k_{mag})$ obtained from Equation 3.13 for one alanine signal and the corresponding transfer standard signal results from the same uncertainty budget as described for the correction factor k_{mag} in the previous paragraph with the only difference, that there is no component $u_r(K_Q)$ for the radiation quality correction for the alanine dosimeter. The remaining components are added in quadrature in order to obtain the combined standard uncertainty associated with the product of correction factors $(K_Q \cdot k_{mag})$ (with coverage factor $k = 1$), see Table 3.3.

Uncertainty after averaging. As mentioned above, there were five pairs of alanine and transfer standard signals in this analysis. This allows to reduce the final uncertainties by averaging the results. The mean was taken ($M = \frac{1}{5} \cdot (M_1 + M_2 + M_3 + M_4 + M_5)$) with $M_{(i)} = k_{mag,(i)}$ and $M_{(i)} = (K_{Q,(i)} \cdot k_{mag,(i)})$, respectively. The associated uncertainty was determined using error propagation ($u(M) = \frac{1}{5} \cdot \sqrt{u(M_1)^2 + u(M_2)^2 + u(M_3)^2 + u(M_4)^2 + u(M_5)^2}$ and $u_r(M) = \frac{u(M)}{M}$). The resulting final values for k_{mag} and $(K_Q \cdot k_{mag})$ are shown in Section 4.1.2.

3.1.3 Characterisation in magnetic fields up to 1.4 T for 6 MV photons

Experiment, MC simulations, and applied devices

The aim of this investigation was, as in the previously described experiment (see Section 3.1.2), the determination of the correction factor k_{mag} converting the standard indication of the alanine dosimeter (see Section 2.4.3) in the presence of a

Table 3.3: Uncertainty budget for the correction factor k_{mag} (Equation 3.14) and for the product of correction factors $(K_Q \cdot k_{mag})$ (Equation 3.13), respectively, for one alanine signal and the corresponding transfer standard signal. The total uncertainty was calculated using the non-rounded single components. All uncertainties are given for a coverage factor $k = 1$. Please note, that this is not the uncertainty of the final result for the correction factor k_{mag} and for $(K_Q \cdot k_{mag})$, respectively. Due to the averaging over the results for the five alanine detectors used, the final uncertainties, as presented in Chapter 4.1.2, are obtained from the values shown in this table according to error propagation as described in the text. The uncertainty budget for the product of correction factors $(K_Q \cdot k_{mag})$ differs from the uncertainty budget for the correction factor k_{mag} only in omitting the contribution $u_r(K_Q)$, which is hence enclosed in brackets.

Contribution	due to ...	u_r in %
$u_r(k_{TP,transferstandard})$	correction to standard environmental conditions for the transfer standard signal	0.104 (hm35-c1...f1, hm35-c3...f3, hm35-c4...f4); 0.105 (hm35-c2...f2, hm35-c5...f5)
$u_r(k_{TP,mon,IC})$	correction to standard environmental conditions for the monitor signal during the transfer standard irradiation	0.104 (hm35-c1...f1, hm35-c3...f3, hm35-c4...f4); 0.105 (hm35-c2...f2, hm35-c5...f5)
$u_r(k_{TP,mon,ala})$	correction to standard environmental conditions for the monitor signal during the alanine irradiation	0.104 (hm35-c1...f1, hm35-c3...f3, hm35-c4...f4); 0.105 (hm35-c2...f2, hm35-c5...f5)
$u_r(k_{ion})$	correction for incomplete charge collection	0.04
$u_r(k_{elec})$	the electrometer	0.1
$u_r(N_{D_W,Q,B})$	the calibration factor	0.35 (PTW 30013-7120 and -8377); 0.1 (IBA FC65G-3213)
$u_r(N_{D_W,Q,B,add})$	determination of the calibration factor in a different machine	0.05
$u_r(k_{vol}^{IC})$	volume correction for the transfer standard	0.05
$u_r(k_{output})$	drifts in the output	0.032 (hm35-c1...f1); 0.04 (hm35-c2...f2); 0.02 (hm35-c3...f3); 0.033 (hm35-c4...f4); 0.04 (hm35-c5...f5)
$u_r(k_{depth})$	due to a slightly different position of alanine detectors and transfer standards	0.26
$u_r(A_{m,test}^{repro})$	reproducibility of the amplitude determination for test pellets	0.18
$u_r(A_{m,base}^{repro})$	reproducibility of the amplitude determination for base pellets	0.12
$u_r(A_{m,test}^{hom})$	homogeneity of the alanine pellet composition for test pellets	0.15
$u_r(A_{m,base}^{hom})$	homogeneity of the alanine pellet composition for base pellets	0.15
$u_r(\bar{m})$	mass of test pellets	0.04
$u_r(\bar{m}^b)$	mass of base pellets	0.04
$u_r(K_T)$	correction for the irradiation temperature for the alanine detectors	0.06
$u_r(k_F)$	correction for the fading for the alanine detectors	0.1 (hm35-c1...f1, hm35-c2...f2, hm35-c3...f3); 0.14 (hm35-c4...f4, hm35-c5...f5)
$u_r(k_{vol}^{ala})$	volume correction for the alanine detector	0.05
$(u_r(K_Q))$	(correction for the radiation quality for the alanine detectors)	(0.5)
Total for k_{mag}:		0.8 (hm35-c1...f1, hm35-c2...f2); 0.7 (hm35-c3...f3, hm35-c4...f4, hm35-c5...f5)
Total for $(K_Q \cdot k_{mag})$:		0.6 (hm35-c1...f1, hm35-c2...f2); 0.5 (hm35-c3...f3, hm35-c4...f4, hm35-c5...f5)

static magnetic field into the actual absorbed dose-to-water at the point of measurement in the presence of the magnetic field. In this experiment, the correction factor k_{mag} was, however, determined for several magnetic flux densities up to 1.4 T[15] and photons with a nominal accelerating potential of 6 MV. Since there are no IC transfer standards available that are directly calibrated in these magnetic fields for this radiation quality, MC simulations were required in addition to the experimental determination of alanine indications in the presence and in the absence of the static magnetic fields. The static magnetic fields for this purpose were – as in the preparatory experiment described in Section 3.1.1 – provided by the electromagnet ER073W (Bruker) at the PTB, which was positioned in front of the Elekta precise treatment system™ linac at the PTB (see Section 3.1.1). Figure 3.4 shows pictures of the electromagnet in front of the linac. In this study, alanine detectors were irradiated with 6 MV photons while they were placed in the static magnetic field of the electromagnet with (0, 0.3, 0.6, 0.9, 1.2, 1.4) T flux density, respectively. This allowed to determine the correction factors k_{mag} for (0.3, 0.6, 0.9, 1.2, 1.4) T and 6 MV photons.

Detector holders. The detectors in this experiment were formed by stacks of four alanine pellets placed within the Farmer IC-like PMMA holder (see Section 2.4.3 and Figure 2.20).[16,17] This holder is waterproof and can be positioned within water phantoms without an additional sleeve.

Alanine pellets. Seven alanine detectors were used as test pellets in each of the three irradiation runs, i.e. 21 alanine test detectors were used in total. These seven alanine detectors of each run were irradiated to nominal absorbed doses-to-water of 18 Gy in the presence of magnetic fields with flux densities of (0, 0, 0.3, 0.6, 0.9, 1.2, 1.4) T, respectively, see Section 3.1.3.[18] Six additional alanine detectors were used as alanine base pellets. Four of them (4×4 pellets) were irradiated to a nominal absorbed dose-to-water of 25 Gy in the Cobalt-60 reference field at the PTB, see Section 3.1.3, two of them (2×8 pellets) remained unirradiated. All these detectors were composed of four alanine pellets (eight in case of the unirradiated base detectors) from Harwell Batch AM603.

Weighting. The weighting was performed as described in Section 3.1.1.

[15] 1.4 T is the maximum flux density achievable with the applied electromagnet.

[16] This is the standard holder for alanine pellets in this work. The holders providing different air gap sizes were only used in the preparatory experiment described in Section 3.1.1.

[17] This Farmer IC-like PMMA holder can contain eight pellets, and it was filled with pellets a...h accordingly. However, only the four inner pellets (c...f) were used for the analysis. The pellets a, b. g, h were "dummy pellets".

[18] Two alanine detectors per irradiation run were irradiated in the absence of a magnetic field.

Irradiation of the base pellets at the Cobalt-60 facility at the PTB. The Cobalt-60 facility at the PTB was used for the irradiation of the four alanine base detectors as described in Section 3.1.1.

Irradiation of the test pellets at the Elekta precise treatment system™ linac at the PTB. Alanine detectors were irradiated in the presence of static magnetic fields with flux densities of (0, 0, 0.3, 0.6, 0.9, 1.2, 1.4) T in order to cover the range of flux densities available with the applied electromagnet which is also the range of interest in MRgRT. Three runs of this procedure were performed in order to obtain more reliable data. The photon beams for this experiment were generated by the Elekta Precise Treatment System™ linac at the PTB. Pictures of this linac are shown in Figure 3.4. A photon beam with a nominal accelerating potential of 6 MV was used. The $TPR_{20,10}$ (see Section 2.4.2) for this photon beam is 0.683, which is in the typical range of the nominal accelerating potentials applied in MR Linacs, see Section 2.2.3.[19] For being able to irradiate alanine detectors in the presence of the static magnetic field, the electromagnet ER073W (Bruker) was placed in front of the Elekta precise treatment system™ linac (see Section 3.1.1 and see Figure 3.4). The distances in this setup were the same as described in Section 3.1.1, and the field size was set as described in Section 3.1.1.
The alanine detectors were irradiated in the same water phantom as desribed in Section 3.1.1, which was again positioned between the pole shoes of the electromagnet (see Figure 3.10). All alanine detectors were irradiated within the same PMMA holder shown in Figure 2.20, see Section 3.1.3. Special effort was made in order to ensure the reliable positioning of the alanine detectors. Each alanine detector was placed in the PMMA holder. The PMMA holder was, then, fixed in a PMMA frame using a ring screw, such that the black O-ring of the PMMA holder was directly above the screw (see Figure 3.11). This PMMA frame, again, containing the PMMA holder with the alanine detectors was pushed into a holding device ("Käfighalter"), which is used at the PTB for reference irradiations of ICs (see Figure 3.10). This holding device was positioned prior to the first irradiation such that the center of the sensitive volume of the alanine detectors, i.e. the pellet center, was positioned in 10 cm water depth; the front wall of the water phantom was scaled from PMMA to water using a factor of 1.15.[20] Afterwards, the holding device was not moved until the end of the third irradiation run. For exchanging the alanine detectors in the PMMA holder, only the PMMA frame with the PMMA holder was taken out of the water phantom. Then, the PMMA holder was extracted from the frame, and the alanine detector inside the PMMA holder was exchanged. The PMMA holder containing the next alanine detector was then again screwed into the frame, which was then re-fixated in the holding device within the water phantom. In order to

[19] The ViewRay MRIdian™ device uses a 6 MV FFF beam ($TPR_{20,10}$ = 0.648, according to a talk of Achim Krauss from May 2019 at the PTB) and the Elekta Unity™ device uses a 7 MV FFF beam, which has to pass through the MR scanner component [de Pooter et al., 2020]. A $TPR_{20,10}$ of 0.701(2) is reported in [de Prez et al., 2019].

[20] The PMMA of the holder around the pellets was not scaled from PMMA to water.

ensure the same inclination of the PMMA frame in all irradiations, the frame was strained to the back (i.e. in beam direction) using a rubber band (see Figure 3.10). As visible in Figures 3.11 and 3.10, eight alanine pellets (referred to as pellet "a" to "h" fit into the PMMA holder. However, only the four inner pellets, i.e. pellet "c" to "f" were used in the analysis, see Section 3.1.3. The positioning was set such that the vertical line of the room lasers was between the alanine pellets "e" and "d", i.e. in the middle of the sensitive volume (see Figure 3.13).
The indication of the alanine dosimeter is sensitive to the irradiation temperature, which, thus, has to be determined reliably. The water temperature was measured as described in Section 3.1.1.
Two different transmission ICs are available for monitoring the output of the linac: the internal transmission IC defaultly installed within the accelerator head of the linac and the PTB-built external transmission IC mounted directly in front of the accelerator head. The external transmission IC was used for monitoring in the preparatory experiment regarding the air gaps around alanine detectors and was, hence, described in Section 3.1.1. In the present experiment, the external transmission IC was only used for determining the point of time to stop the irradiation.[21] Besides that, it was decided to use the internal transmission IC in the present study. The internal transmission IC is located in the collimator assembly in the path of the radiation beam within the accelerator head of the linac. The chamber is open to the atmosphere for air density correction. A picture is shown in Figure 2.16. This internal transmission IC is generally not used for monitoring in irradiations performed by the respective group at the PTB, since the external PTB-built transmission IC was found to provide signals of higher stability. For monitoring irradiations in the presence of static magnetic fields performed in a setup with the electromagnet in front of the linac, the signal of the internal transmission IC is, however, of higher interest: Installed within the accelerator head, it is positioned in a larger distance from the electromagnet than the external transmission IC. This is of relevance since the static magnetic field generated between the pole shoes of the electromagnet is accompanied by a stray magnetic field which decreases rapidly with increasing distance from the center of the electromagnet. The study presented in Chapter B in the appendix showed that there is no measurable effect of the stray magnetic field of the electromagnet on the internal transmission IC, whereas correction factors have to be applied for the external transmission IC. The uncertainty associated with this additional correction factor enters into the analysis. It is larger than the uncertainty

[21] This monitor was calibrated using the Farmer-type IC FC65G-771 as a transfer standard. For doing so, the transfer standard Farmer-type IC was positioned such, that its sensitive volume was in the same position as the sensitive volume of the alanine detectors. The same PMMA frame was used for the IC and for the PMMA holder with outer shape of an IC containing the alanine detectors. In order to ensure for the same vertical position, the position on the IC corresponding to the black O-ring of the PMMA holder was marked with a yellow piece of tape (see Figure 3.12). This calibration has, however, no relevance for the present analysis since the ratio of the alanine indication in the presence and in the absence of a magnetic field was used.

contribution due to the lower signal stability of the internal transmission IC, leading to a larger overall uncertainty of the final results for the correction factors k_{mag} determined when using the external transmission IC for dose monitoring. In the present experiment, it was, thus, of advantage to use the monitoring information from the internal transmission IC despite its inferior signal stability compared to the external transmission IC.
Each alanine test detector was irradiated to a nominal absorbed dose-to-water of 18 Gy, since the alanine/EPR system at the PTB offers the smallest uncertainties in this range of absorbed doses-to-water.
For the first run, the dose rate was 264 MU/min and the pulse rate frequency was 200 Hz. The order of flux densities was (0, 0, 0.3, 0.6, 0.9, 1.2, 1.4) T. For the flux density of 1.4 T, the beam guidance in the accelerator head had to be corrected for the impact of the stray magnetic field as described in Section B.1.4 in the appendix ("2T error"). The procedure for the second and third run was the same with a dose rate of 265 MU/min and 262 MU/min, respectively.

Readout with the Bruker EMX 1327 EPR spectrometer at the PTB. All alanine test pellets irradiated in one irradiation run were read out with the EPR spectrometer on one measurement day. The same base pellets were used for the test detectors on each measurement day. The settings of the spectrometer were set as described in Section 3.1.1.

MC simulations with EGSnrc. In the previously described experiment at the Elekta Unity™ MR Linac, see Section 3.1.2, the correction factor k_{mag} could be determined by measurements with the alanine dosimeter in comparison to measurements with IC transfer standards calibrated directly in the magnetic field applied. Such transfer standards are not available for the present setup. The determination of the correction factors k_{mag} in the present experiment requires, hence, not only experimental data of the indication of the alanine dosimeter in the presence and in the absence of the static magnetic fields, but also MC simulations as it was described in Section 2.5.
The principle of the approach is to simulate ddcs in the experimentally applied setup, one time in the presence of a magnetic field with the flux density of interest and one time in the absence of a static magnetic field. The $c_{\vec{B}}$ factors (see Section 2.5) can then be obtained by forming the ratio of these ddcs in the presence and in the absence of the magnetic field. The simulations of the ddcs were performed using the "egs_chamber" application of the EGSnrc software toolkit [Kawrakow et al., 2000] (see Section 2.5). The magnetic field was employed in this application as described in [Malkov and Rogers]. Prior to the accomplishment of the MC simulations, the experimentally applied setup had to be modelled as a virtual geometry and the radiation source had to be defined.
The reproduction of the experimental setup in the simulation geometry is of impor-

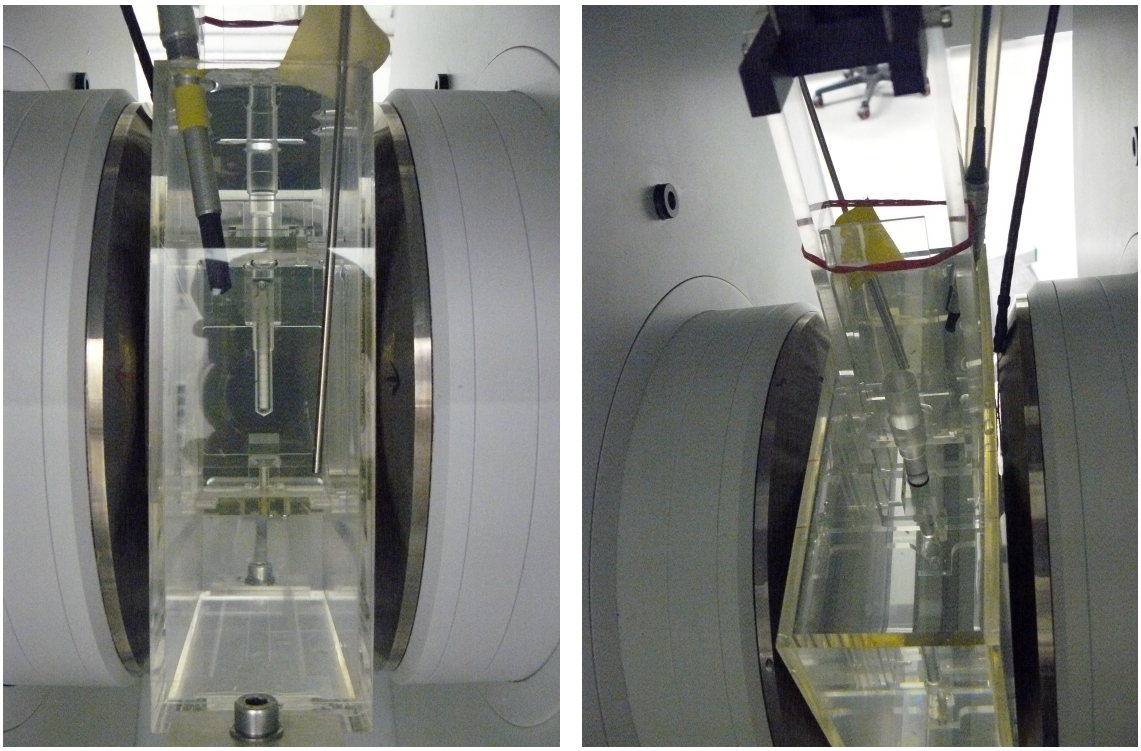

(a) (b)

Figure 3.10: An alanine detector in the water phantom positioned between the pole shoes of the electromagnet. The alanine detector is contained in the PMMA holder which is screwed into the PMMA frame which is, again, pushed into the holding device (see the text). (a) is the view opposing to the beam direction, i.e. the back side of the phantom is shown. (b) is the view from above in beam direction, i.e. the front side of the phantom is shown. The rubber band at the top of the PMMA frame ensures identical inclinations (see text). The transfer standard IC can be seen in the back part of the phantom (on the left in (a) with a yellow tape; on the right in (b), the sleeve around the cable is visible on the right). This IC is placed in the back part of the water phantom in order to keep the temperature of the water in the phantom. In addition, the temperature sensor measuring the water temperature can be seen. It is the thin rod on the right side of the water phantom in (a) and on the left side of the water phantom in (b), respectively.

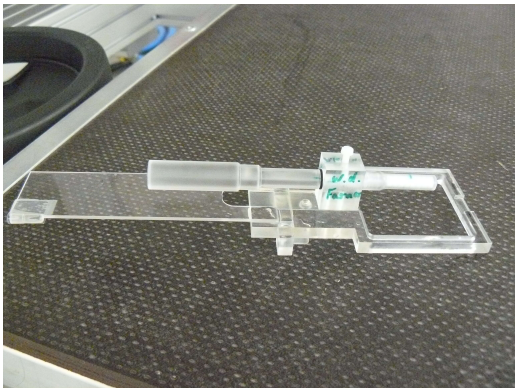

Figure 3.11: The PMMA frame with the PMMA holder containing an alanine detector positioned in its ring screw. This PMMA frame is put into a holding device for the irradiations within the water phantom.

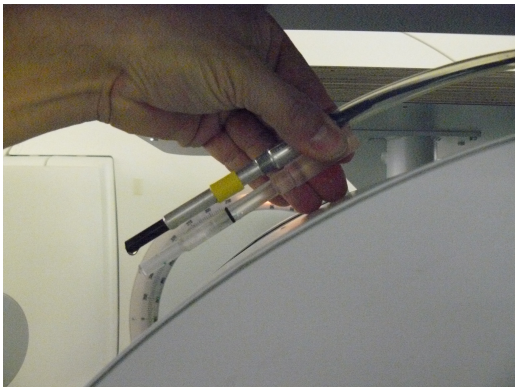

Figure 3.12: The transfer standard IC and the PMMA holder containing an alanine detector. The position on the IC corresponding to the black O-ring on the PMMA holder is marked with the yellow tape.

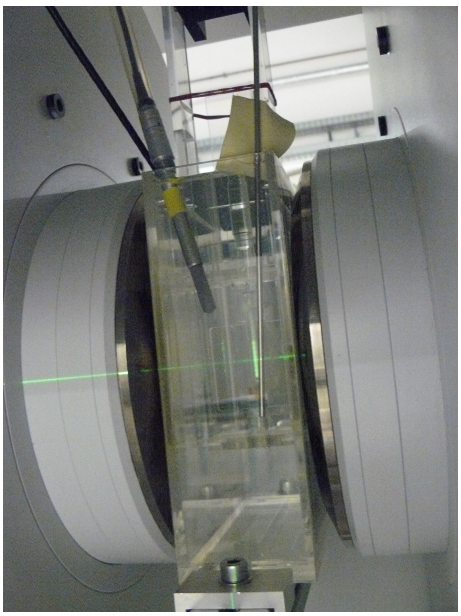

Figure 3.13: The green line of the room laser was used for vertical positioning of the alanine detectors.

tance since the $c_{\vec{B}}$ factors are specific for the respective experimental setup.[22] The applied simulation geometry consisted of the water phantom with 7 cm width, 20 cm length, and 20 cm height, which was built using "EGS_XYZGeometry", and the pole shoes of the electromagnet, which were built using "EGS_ConeStack". The water phantom and the pole shoes were both inserted into an air box, see Figure 3.14. The inner parts of the pole shoes (i.e. the metallic parts visible e.g. in Figure 3.13) were defined as iron, the outer parts (i.e. the white/greyish parts visible e.g. in Figure 3.13) were defined as stainless steel (type302), according to the realities. Dose scoring for obtaining the ddcs was accomplished by dividing the water inside the water phantom into slices of 1 mm thickness perpendicular to the beam direction. The radiation source was defined using the phase space file for the respective radiation quality at the linac. A cutout resulting in the experimentally used field size with 5 cm width and 10 cm height was applied. Global ECUT and global PCUT were set to 0.521 MeV and 0.01 MeV, respectively: ECUT and PCUT define the cut off energy below which electrons and photons, respectively, are no longer transported. For the calculation of ddcs in the presence of a magnetic field, EM ESTEPE, which is the maximum fractional energy loss per step, was set to 0.2 MeV, as suggested in [Malkov and Rogers]. Otherwise, default settings were used. In the simulations for the individual ddcs, the number of histories was set to 5×10^6 in order to obtain uncertainties below one percent associated with the data points for the absorbed dose-to-water referring to the suggestion in [van Asselen et al., 2018].

[22] Please note, that no detector geometry is needed in the virtual geometry, since only ddcs are required.

According to [van Asselen et al., 2018], the ddc for each magnetic flux density of interest was simulated 13 times with 1 mm grid size (accomplished by the 1 mm thick slices in the virtual geometry) and the 13 ddcs were averaged.[23] The ratio "mean ddc with magnetic field" over "mean ddc without magnetic field" was formed. Finally, the mean of this ratio using the data points from 5.5 cm water depth behind 0.5 cm PMMA to 14.4 cm water depth behind 0.5 cm PMMA (measures in accordance with [van Asselen et al., 2018], see below) was used as $c_{\vec{B}}$ factor at the point of measurement for the respective magnetic flux density in the experimentally applied setup.
The following describes in more detail how the $c_{\vec{B}}$ factors and the associated uncertainties were obtained. The mean ddcs of the 13 ddcs with and the 13 ddcs without magnetic field were calculated. The uncertainties for the data points of the mean ddcs were obtained from the uncertainties indicated in the simulation output via error propagation. In the next step, each data point of the mean ddc in the presence of a magnetic field was divided by the respective data point of the mean ddc in the absence of a magnetic field. The uncertainty of this ratio was obtained via error propagation from the uncertainties associated with the data points of the individual mean ddcs. According to [van Asselen et al., 2018] who refers to [O'Brien et al., 2016], this ratio is "nearly constant" in "depths ranging from 6 to 15 cm". Thus, the mean of this ratio was taken in the range from 5.5 cm water depth behind 0.5 cm PMMA to 14.4 cm water depth behind 0.5 cm PMMA (the 0.5 cm PMMA are due to the front wall of the phantom). The resulting value was used as the $c_{\vec{B}}$ factor in the respective setup for the respective magnetic flux density at the point of the alanine measurement, which is in 10 cm water equivalent depth. The uncertainty associated with this $c_{\vec{B}}$ factor was obtained via error propagation from the uncertainties associated with the values that were averaged.
Figure 3.15 shows exemplarily the calculated mean ddcs for 1.2 T and 0 T, respectively. The abscissa shows the depth in water behind 0.5 cm PMMA in Centimetre, and the ordinate shows the simulated data points for the absorbed dose-to-water normalised to the fluence. The resulting $c_{\vec{B}}$ factors for the experimental setup are presented in Chapter D.1 in the appendix (Table D.2 and Figure D.2).
Since the resulting $c_{\vec{B}}$ factors showed an unexpected behaviour (see Chapter D.1 in the appendix and Chapter 5), additional simulations were performed with modified simulation geometries in order to better understand the reasons for the behaviour of the $c_{\vec{B}}$ factors in the experimentally used setup. These simulations and their results are also described in the appendix (see Chapter D.2).

Analysis and uncertainties

The aim of this analysis was – as in the previously described experiment, see Section 3.1.2 – the determination of the correction factors k_{mag} required in Equation 2.30 for converting the standard indication of the alanine dosimeter in the presence of a

[23] For each of the 13 calculations, the initial seeds were varied using "ranmar".

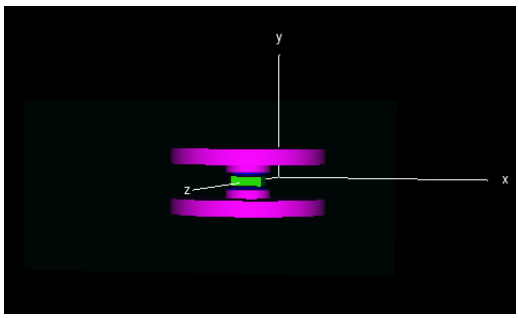

Figure 3.14: Simulation geometry consisting of the water phantom (water in green, PMMA walls in red) and the pole shoes of the electromagnet (pink and blue). The air box surrounding these components is hardly discernable in cyan since it was set transparent for this picture.

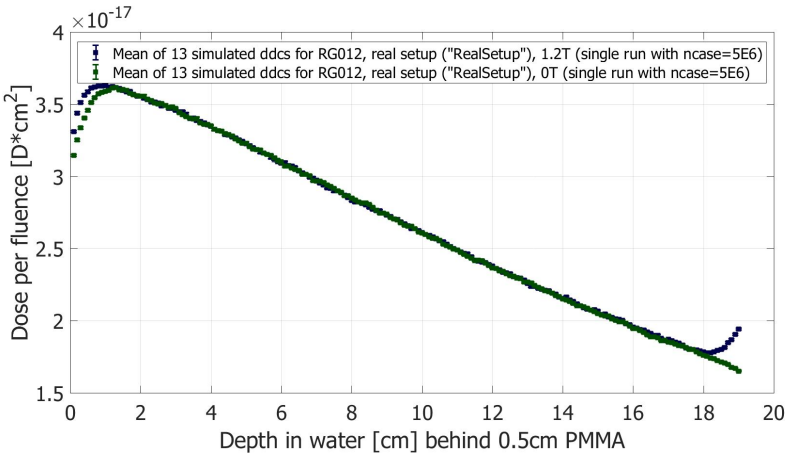

Figure 3.15: Simulated mean ddcs in the presence of a magnetic field with flux density 1.2 T (blue) and in the absence of a magnetic field (green). Prominent are the shift of the ddc in the presence of the magnetic field in the build-up region (below 2 cm water depth behind 0.5 cm PMMA) and the rise in the dose at the backside of the water phantom (behind 18 cm water depth behind 0.5 cm PMMA), which is probably due to the ERE, see Section 2.3.3.

static magnetic field into the absorbed dose-to-water at the point of measurement in the presence of a magnetic field. However, here not for the conditions at the Elekta Unity™ MR Linac (1.5 T, 7 MV), but for a series of magnetic flux densities at 6 MV. Due to the lack of transfer standards directly calibrated under these conditions, the determination of the correction factors k_{mag} had to be performed in two steps. In a first step, the correction factors k^*_{mag} were determined from the experimental data. These correction factors k^*_{mag} convert the indication of the alanine dosimeter in the presence of a static magnetic field into the hypothetic absorbed dose-to-water at the point of measurement in the absence of a magnetic field. They were obtained from the irradiations of the alanine detectors in the presence of magnetic fields with flux densities of (0, 0, 0.3, 0.6, 0.9, 1.2, 1.4) T repeated in three runs. The correction factors k^*_{mag} were determined for each individual magnetic flux density in each irradiation run, then the results for the same flux densities were averaged. In a second step, the correction factors k_{mag} aimed for were calculated from these correction factors k^*_{mag} and the $c_{\vec{B}}$ factors determined by the MC simulations (see Section 3.1.3). In the following, the derivation of the model equations is described, followed by a more detailed description of the two steps for determining the correction factors k_{mag}. Please take note of the general comments regarding the uncertainties in Section 3.1.1.

Derivation of the model equations. In the following, the model equations for the correction factors k_{mag} and k^*_{mag} are derived and the relationship between these correction factors is addressed.

Model equation for the correction factor k_{mag}. The corrected dose-normalised amplitude A_D^{corr} is given by Equation 2.30. The basic correction factors K_i, which were introduced by Mathias Anton, are described in Sections 2.4.3 to 2.4.3 ($K_{V,s}$ to K_F). A_D^{corr} obtained with these correction factors is the standard indication of the alanine dosimeter (see Section 2.4.3). For irradiations in the presence of a static magnetic field, the additional correction factor K_{mag} is required, see Section 2.4.3.[24] The corrected dose-normalised amplitude A_D^{corr} obtained with the correction factor K_{mag} in addition is referred to as "particular indication" of the alanine dosimeter in order to distinguish it from the standard indication obtained without the correction factor K_{mag}. The response of the alanine dosimeter in a static magnetic field with flux density X is the particular indication $A_{D,X}^{corr}$ divided by the actually applied absorbed dose-to-water $D_{appl,X}$:

$$R_X = \frac{A_{D,X}^{corr}}{D_{appl,X}} \tag{3.23}$$

The model equation for the correction factors k_{mag} and k^*_{mag}, respectively, is obtained by forming the ratio of the response of the alanine dosimeter in a magnetic field with

[24] The correction factors described in the Sections 2.4.3 to 2.4.3 (K_{air} to $K_{mag,air}$) are not required according to the results of the preparatory experiment, see Section 4.1.1.

flux density X and 0 T. Forming this ratio is advantageous since several components cancel out in the final model equation, resulting in a smaller overall uncertainty. The ratio of the two response values is unity in case of entirely corrected response values. This is used as the starting point for the derivation of the model equation for the correction factor k_{mag}:

$$\begin{aligned} 1 &= \frac{R_X}{R_{0T}} \\ &= \frac{\frac{A_{D,X}^{corr}}{D_{appl,X}}}{\frac{A_{D,0T}^{corr}}{D_{appl,0T}}} \end{aligned} \tag{3.24}$$

$A_{D,X}^{corr}$ is the particular indication of the alanine dosimeter in the presence of the static magnetic field with flux density X, and $A_{D,0T}^{corr}$ is the standard indication of the alanine dosimeter in the absence of a static magnetic field (0 T). $D_{appl,0T}$ is the absorbed dose-to-water applied to the alanine detector in the absence of a magnetic field; it can be obtained from the monitoring transmission IC as it does not experience the magnetic field. Due to the ratio, it is sufficient to use the charge Q_{0T} indicated by the monitor without converting it into an absorbed dose-to-water. $D_{appl,X}$ is the absorbed dose-to-water applied to the alanine detector in the presence of a magnetic field with flux density X. $D_{appl,X}$ can be obtained by multiplying the charge Q_X indicated by the monitoring transmission IC with the $c_{\vec{B}}$ factor obtained by the MC simulations (see Section 3.1.3) for the respective setup:

$$D_{appl,X} = Q_X \cdot c_{\vec{B}} \tag{3.25}$$

Combining the Equations 2.30, 3.23, 3.24, and 3.25 eventually results in the model equation for the correction factor $k_{mag,X}$ for a magnetic field with flux density X:

$$k_{mag,X} = \frac{c_{\vec{B},X} \cdot Q_X}{\frac{A_{m,X}}{\bar{m}_X} \cdot k_{T,X}} \cdot \frac{\frac{A_{m,0T}}{\bar{m}_{0T}} \cdot k_{T,0T}}{Q_{0T}} \tag{3.26}$$

This compact expression for the model equation results from the following facts: The same base pellets were used in all EPR measurements of the present investigation; hence, the masses of the base pellets and the absorbed doses-to-water applied to the base pellets cancel out in the ratio ($\bar{m}_X^b = \bar{m}_0^b T$ and $D_X^b = D_0^b T$). The radiation field at the point of the measurement featured constant gradients; hence, no volume and sensitivity correction factor $K_{V,s}$ is required ($K_{V,s,X} = K_{V,s,0T} = 1$, see Section 2.4.3). The same radiation quality was used in the presence and in the absence of the magnetic field (and the same base pellets were used for all test detectors); hence, the radiation quality correction factor cancels out in the ratio ($K_{Q,X} = K_{Q,0T}$). The environment of the alanine pellets was the same during irradiations in the presence and in the absence of the magnetic field; hence, no environment correction factor K_{env} is required ($K_{env,X} = K_{env,0T} = 1$, see Section 2.4.3). The fading correction factor is the same for the alanine pellets irradiated in the presence and in

the absence of the magnetic field, since the time differences between irradiation and EPR measurement were the same ($K_{F,X} = K_{F,0T}$). The correction factor k^b_{mag} for the base pellets equals unity as they were irradiated in the absence of a magnetic field. And K_{mag} and $c_{\vec{B}}$ do not occur in the parts of the equation referring to the irradiation in the absence of a magnetic field. Due to the same base pellets, correction factors k_i instead of correction factors K_i can be used (see Equation 2.29). No corrections for air gaps are required according to the results of the preparatory experiment (see Section 4.1.1).

Relationship between the correction factors k_{mag} and k^*_{mag}. The correction factor k_{mag} converts the standard indication of the alanine dosimeter into the particular indication (see Section 3.1.3 above). The particular indication corresponds to the actual absorbed dose-to-water $D^{\vec{B}}$ at the point of measurement in the presence of a magnetic field $\vec{B}$. In order to convert this actual absorbed dose-to-water $D^{\vec{B}}$ into the hypothetic absorbed dose-to-water D at the point of measurement in the absence of a magnetic field, $D^{\vec{B}}$ has to be divided by the respective $c_{\vec{B}}$ factor (see Equation 2.41). This is tantamount to the application of the correction factor k^*_{mag}, which converts the standard indication of the alanine dosimeter into the hypothetic absorbed dose-to-water D at the point of measurement in the absence of a magnetic field. The correction factors k_{mag} and k^*_{mag} are related according to

$$k^*_{mag} = \frac{k_{mag}}{c_{\vec{B}}} \tag{3.27}$$

Model equation for the correction factor k^*_{mag}. The model equation for k^*_{mag} can be derived analogously as above for k_{mag} (see Section 3.1.3). It is obtained by forming the ratio of the "hypothetic response" R^*_X (see below) of the alanine dosimeter in a magnetic field with flux density X and the response R_{0T} of the alanine dosimeter in the absence of a magnetic field:

$$\begin{aligned} 1 &= \frac{R^*_X}{R_{0T}} \\ &= \frac{\frac{A^{*,corr}_{D,X}}{D^*_{appl,X}}}{\frac{A^{corr}_{D,0T}}{D_{appl,0T}}} \end{aligned} \tag{3.28}$$

The hypothetic response R^*_X is obtained by dividing $A^{*,corr}_{D,X}$ by $D^*_{appl,X}$; $A^{*,corr}_{D,X}$ is the standard indication of the alanine dosimeter multiplied with the correction factor k^*_{mag}, and $D^*_{appl,X}$ is the hypothetic absorbed dose-to-water at the point of measurement in the absence of a magnetic field. $D^*_{appl,X}$ is directly accessible via the indication of the monitoring IC, since the measurement point of the monitoring IC is outside the magnetic field; likewise, it is $D^*_{appl,X} = \frac{D_{appl,X}}{c_{\vec{B}}}$ (see Equation 2.41). The response R_{0T} is obtained as above (see Equation 3.24 and the description above

in Section 3.1.3). Analogously to the derivation above (see Section 3.1.3), the model equation for the correction factor k^*_{mag} follows as

$$k^*_{mag,X} = \frac{Q_X}{\frac{A_{m,X}}{\bar{m}_X} \cdot k_{T,X}} \cdot \frac{\frac{A_{m,0T}}{\bar{m}_{0T}} \cdot k_{T,0T}}{Q_{0T}} \tag{3.29}$$

The only difference to the model equation for the correction factor k_{mag} (see Equation 3.26) is the missing $c_{\vec{B}}$ factor, see Equation 3.27.

As mentioned above, the correction factors k_{mag} aimed for were determined in two steps. First, the correction factors k^*_{mag} were determined from the experimental data. Then, the correction factors k_{mag} were calculated from these correction factors k^*_{mag} and the $c_{\vec{B}}$ factors determined by the MC simulations (see Section 3.1.3). These steps are described in the following.

Quantities in the model equation for k^*_{mag} and uncertainty budget. The following describes how the correction factor k^*_{mag} was obtained from the experimental data. The basis for this procedure is the model equation 3.29.

Alanine pellet mass. The individual masses m_i of the four alanine pellets composing the single alanine detectors were averaged for obtaining the mean masses $\bar{m}_{X/0T}$ of the respective detectors. The uncertainty contributions $u_r(\bar{m}_{X/0T})$ have to be considered according to the description in Section 3.1.1.

Alanine amplitude. The values for the mass-related mean amplitude $A_{m,X/0T}$ were obtained from the EPR measurements of the alanine detectors. The uncertainty associated with the amplitude values $A_{m,X/0T}$ has two contributions. One is due to the reproducibility of the amplitude measurement and the other one is due to the homogeneity of the detector material.
The uncertainty component $u_r(A^{repro}_{m,test,X/0T})$ due to the reproducibility is calculated using Equation 3.6 as described in Section 3.1.1. The uncertainty component $u_r(A^{hom}_{m,test,X/0T})$ is calculated with Equation 3.7 as described in Section 3.1.1.[25]

Irradiation temperature correction. The correction factors $k_{T,X/0T}$ for the irradiation temperature required in the model equation 3.29 and the associated uncertainties $u(k_{T,X/0T})$ were obtained via the same principle as described in Section 3.1.1. The absolute unertainty of each irradiation temperature T was $u(T) = 0.1\,\mathrm{K}$ ($u(T) = 0.2\,\mathrm{K}$ for the irradiations in the presence of a magnetic field with flux density $1.4\,\mathrm{T}$ due to the stronger dynamic in the temperature development).

[25] In general, these two components have to be considered for the test and for the base pellets. Here, however, the contributions of the base cancel out since only the ratio of values obtained on one measurement day using the same base is of interest.

Charge indicated by the monitor. As discussed in Section 3.1.3 (see also Chapter B in the appendix), the internal transmission IC was used for the dose monitoring. As mentioned above (see Section 3.1.3), only the indicated charges, which are already corrected to the reference conditions of air temperature and air density (correction factor k_{TP}, see Section 2.4.2), are required (i.e. not the absorbed doses-to-water). These corrected charges $Q_{X/0T}$ were obtained from the log-files of the linac. The relative uncertainty $u_r(Q_{X/0T,i})$ for a single charge indication is $u_r(Q_{X/0T,i}) = 0.22\,\%$, which ensues from the uncertainty budget presented in Section B.2.1 in the appendix. Since the alanine irradiations were performed in three parts (three times 6 Gy for 18 Gy in total, see the explanation given in Section 3.1.1), the contribution $u_r(Q_{X/0T})$ for the sum of the three charge indications during one alanine irradiation ($Q_{X/0T} = Q_{X/0T,1} + Q_{X/0T,2} + Q_{X/0T,3}$) is obtained from error propagation.

Summary of the uncertainty budget. The uncertainty associated with the correction factor k^*_{mag} obtained from Equation 3.29 for a single alanine detector irradiated in the presence of a magnetic field with flux density X and a single alanine detector irradiated in the absence of a static magnetic field (0 T) results from the uncertainty budget containing the following contributions: The relative uncertainties $u_r(\bar{m}_X)$ and $u_r(\bar{m}_{0T})$ associated with the mean masses; the relative uncertainties $u_r(A^{repro}_{m,test,X})$ and $u_r(A^{repro}_{m,test,0T})$ and the relative uncertainties $u_r(A^{hom}_{m,test,X})$ and $u_r(A^{hom}_{m,test,0T})$ for the amplitudes of the alanine test pellets; the relative uncertainties $u_r(k_{T,X})$ and $u_r(k_{T,0T})$ associated with the irradiation temperature correction; and the relative uncertainties $u_r(Q_X)$ and $u_r(Q_{0T})$ for the charges indicated by the monitoring IC. This budget is also listed in Table 3.4. The single components and the total uncertainty are rounded according to the rules stated in [Beringer et al., 2012].
As described in Section 3.1.3, one alanine detector was irradiated for each magnetic flux density different from zero in each irradiation run, but two alanine detectors were irradiated in the absence of a magnetic field in each irradiation run. This allows to reduce the final uncertainties by averaging the results. For each irradiation run, the correction factors k^*_{mag} were determined twice according to Equation 3.29: one time using the first alanine detector irradiated in the absence of a magnetic field ($k^*_{mag,a}$) and one time using the second alanine detector irradiated in the absence of a magnetic field ($k^*_{mag,b}$). The mean was taken and the associated uncertainty was determined using error propagation. Results for $k^*_{mag,a}$ and $k^*_{mag,b}$ before averaging are shown in the appendix in Section D.1.
For the final results, these mean values obtained for the three irradiation runs I, II, and III ($k^{*,\mathrm{I}}_{mag}$, $k^{*,\mathrm{II}}_{mag}$, and $k^{*,\mathrm{III}}_{mag}$) were averaged and the associated uncertainty was obtained from error propagation. Results for the individual irradiation runs before averaging are shown in the appendix in Section D.1.
The resulting final values for k^*_{mag} (which are the mean over the three irradiation runs and the two irradiations in the absence of a magnetic field) are also shown in

the appendix in Section D.1.

Determination of the correction factors k_{mag}. In the following it is described how the correction factors k_{mag} were calculated from the experimentally determined correction factors k^*_{mag} (see Section 3.1.3) and the $c_{\vec{B}}$ factors determined by the MC simulations (see Section 3.1.3). According to Equation 3.27, the correction factors k_{mag} were determined as

$$k_{mag} = c_{\vec{B}} \cdot k^*_{mag} \tag{3.30}$$

To this end, the correction factors k^*_{mag} averaged over the two irradiations in the absence of a magnetic field and averaged over the three irradiation runs were used (see Section 3.1.3). The uncertainty associated with the resulting correction factors k_{mag} was obtained from error propagation according to

$$u_r(k_{mag}) = \sqrt{u_r(c_{\vec{B}})^2 + u_r(k^*_{mag})^2} \tag{3.31}$$

The resulting final values for k_{mag} are shown in Section 4.1.3.

3.1.4 Energy dependence in magnetic fields up to 1.4 T

Experiment, MC simulations, and applied devices

The aim of the present experiment was the investigation of the energy dependence of the correction factor k_{mag}. To this end, the correction factor k_{mag}, which was determined for irradiations with a photon beam with nominal accelerating potential of 6 MV for magnetic flux densities of (0.3, 0.6, 0.9, 1.2, 1.4) T in the previously described investigation (see Section 3.1.3), was also determined for irradiations with photon beams with a nominal accelerating potential of 10 MV and 15 MV, respectively. Magnetic flux densities of 0.7 T and 1.4 T were investigated for these additional accelerating potentials. These magnetic flux densities were chosen in order to cover the range accessible with the applied electromagnet (see Section 3.1.3), to cover the range of interest in MRgRT, and to cover the range of magnetic flux densities applied in the previous investigation with the 6 MV beam. The amount of applied flux densities was reduced to two in the investigations using 10 MV and 15 MV photon beams in order to reduce the required beam time.[26]

Detector holders. The detector holder was used as described in Section 3.1.3.

[26] In hindsight, it would have been preferable to apply a magnetic flux density of 0.6 T instead of 0.7 T in the 10 MV and 15 MV series for enabling the direct comparison with the data point from the 6 MV series.

Table 3.4: Uncertainty budget for the correction factor k^*_{mag} obtained from Equation 3.29 for a single alanine detector irradiated in the presence of a magnetic field with flux density X and a single alanine detector irradiated in the absence of a static magnetic field (0 T). The value in brackets is only valid for the data point at 1.4 T. The total uncertainty was calculated using the non-rounded single components. All uncertainties are given for a coverage factor $k = 1$. Please note, that this is not the uncertainty of the final results for the correction factor k^*_{mag}. Due to the averaging over the two irradiations in the absence of a magnetic field and the averaging over the three irradiation runs, the final uncertainties, as presented in Table D.1 and Figure D.1 in Section D.1 in the appendix, are obtained from the value shown in this table according to error propagation as described in Section 3.1.3.

Contribution	due to ...	u_r in %
$u_r(\bar{m}_X)$	mass of test pellets irradiated at X	0.04
$u_r(\bar{m}_{0T})$	mass of test pellets irradiated at 0 T	0.04
$u_r(A^{repro}_{m,test,X})$	reproducibility of the amplitude determination for test pellets irradiated at X	0.16
$u_r(A^{repro}_{m,test,0T})$	reproducibility of the amplitude determination for test pellets irradiated at 0 T	0.16
$u_r(A^{hom}_{m,test,X})$	homogeneity of the alanine pellet composition for test pellets irradiated at X	0.15
$u_r(A^{hom}_{m,test,0T})$	homogeneity of the alanine pellet composition for test pellets irradiated at 0 T	0.15
$u_r(k_{T,X})$	correction for the irradiation temperature for test pellets irradiated at X	0.034 (0.04)
$u_r(k_{T,0T})$	correction for the irradiation temperature for test pellets irradiated at 0 T	0.03
$u_r(Q_X)$	sum of charge readings of the internal transmission IC for test pellets irradiated at X	0.13
$u_r(Q_{0T})$	sum of charge readings of the internal transmission IC for test pellets irradiated at 0 T	0.13
Total:		0.4

Alanine pellets. Four alanine detectors were used as test pellets in each irradiation run. For the irradiation series with 10 MV beams, which was performed in three runs, these are twelve alanine test detectors in total. For the irradiation series with 15 MV beams, which was performed in four runs, these are 16 alanine test detectors in total. These four alanine test detectors of each run were irradiated to nominal absorbed doses-to-water of 18 Gy in the presence of magnetic fields with flux densities of (0, 0, 0.7, 1.4) T, respectively, see Section 3.1.4.[27] Additional alanine detectors were used as alanine base pellets. For the irradiation series with 10 MV beams, these were four detectors (4×4 pellets) irradiated to a nominal absorbed dose-to-water of 25 Gy in the Cobalt-60 reference field at the PTB, see Section 3.1.4, and two detectors (2×8 pellets) that remained unirradiated. For the first three runs in the 15 MV series, these were another four detectors (4×4 pellets) irradiated to a nominal absorbed dose-to-water of 25 Gy in the Cobalt-60 reference field at the PTB and two detectors (2×8 pellets) that remained unirradiated. For the fourth run of th 15 MV series, another two detectors (2×4 pellets) irradiated to a nominal absorbed dose-to-water of 25 Gy were used and another two detectors (2×4 pellets) that remained unirradiated. All of these detectors were composed of four alanine pellets (eight in case of most of the unirradiated base detectors) from Harwell Batch AM603 with exception of the test and base detectors in the fourth run of the 15 MV series, which were from Harwell Batch BF616.

Weighting. The weighting was performed as described in Section 3.1.1.

Irradiation of the base pellets at the Cobalt-60 facility at the PTB. The Cobalt-60 facility at the PTB was used for the irradiation of the alanine base detectors as described in Section 3.1.1.

Irradiation of the test pellets at the Elekta precise treatment system™ linac at the PTB. Alanine detectors were irradiated in the presence of static magnetic fields with flux densities of (0, 0, 0.7, 1.4) T. This procedure was performed in several irradiation runs in order to obtain more reliable data. The photon beams for the irradiations were generated by the Elekta Precise Treatment System™ linac at the PTB. Pictures of this linac are shown in Figure 3.4. Photon beams with nominal accelerating potential of 10 MV were used in the first series, photon beams with a nominal accelerating potential of 15 MV in the second series. The $TPR_{20,10}$ (see Section 2.4.2) for these beams is $TPR_{20,10} = 0.733$ and $TPR_{20,10} = 0.760$, respectively. These nominal accelerating potentials are not in the typical range of potentials applied in MR Linacs (see Section 2.2.3).[28] However, these potentials were chosen in

[27] Two alanine detectors per irradiation run were irradiated in the absence of a magnetic field.

[28] The ViewRay MRIdian™ device uses a 6 MV FFF beam ($TPR_{20,10} = 0.648$, according to a talk of Achim Krauss from May 2019 at the PTB) and the Elekta Unity™ device uses a 7 MV FFF beam, which has to pass through the MR scanner component [de Pooter et al., 2020]. A $TPR_{20,10}$ of 0.701(2) is reported in [de Prez et al., 2019].

order to enable a comparison of the results with the previous results obtained in a 6 MV photon beam (see Section 4.1.3). 10 MV were chosen here in order to provide a higher energy which is still in the therapeutically relevant range and 15 MV were chosen here in order to provide a higher energy which is still at the edge of the therapeutically relevant range. The electromagnet ER073W (Bruker) was placed in front of the Elekta precise treatment system™ linac for being able to irradiate alanine detectors in the presence of static magnetic fields, see Section 3.1.1 and Figure 3.4. The distances in this setup were the same as described in Section 3.1.1, and the field size was set as described in Section 3.1.1. An additional irradiation run was performed with varied field size. This additional run is described in Section E.4 in the appendix.
The alanine detectors were irradiated in the same water phantom as described in Section 3.1.1, which was again positioned between the pole shoes of the electromagnet (see Figure 3.10). All alanine detectors were irradiated within the same PMMA holder shown in Figure 2.20, see Section 3.1.4. Special effort was made in order to ensure reliable positioning of the alanine detectors with a PMMA frame and a holding device as described in Section 3.1.3.
As shown in Figures 3.11 and 3.10 in Section 3.1.3, eight alanine pellets (referred to as pellet "a" to "h" fit into the PMMA holder. However, only the four inner pellets, i.e. pellet "c" to "f", were used in the analysis (see Section 3.1.4). The positioning was, as in the irradiation series with 6 MV, set such that the vertical line of the room lasers was between the alanine pellets "e" and "d", i.e. in the middle of the sensitive volume (see Figure 3.13 in Section 3.1.3).
The indication of the alanine dosimeter is sensitive to the irradiation temperature, which, thus, has to be determined reliably. The water temperature was measured as described in Section 3.1.1.
Each alanine test detector was irradiated to a nominal absorbed dose-to-water of 18 Gy and the irradiations were monitored using the internal transmission IC as described in Section 3.1.3.
The dose rates for the three runs of the 10 MV series were (354, 358, 355) MU/min, respectively, and the pulse rate frequency was 200 Hz. The dose rates for the four runs of the 15 MV series were (465, 453, 453, 227) MU/min, respectively, and the pulse rate frequencies were (196, 196, 196, 98) Hz, respectively.[29] The beam guidance in the accelerator head was corrected for the impact of the stray magnetic field in the irradiations in the presence of a magnetic field with flux density of 1.4 T as described in Section B.1.4 in the appendix ("2T error").
Please note that the order of flux densities was changed from (0, 0, 0.7, 1.4) T in the 10 MV series and Run I to III in the 15 MV series to (0, 0.7, 1.4, 0) T in Run IV of the 15 MV series in order to provide a higher reliability by the 0 T irradiation at the beginning and at the end of the irradiation run.

[29] Dose rate and pulse rate frequency in the last run of the 15 MV series were set differently since this run was performed several months after the first three runs.

Readout with the Bruker EMX 1327 EPR spectrometer at the PTB. All alanine test pellets irradiated in one irradiation run were read out with the EPR spectrometer on one measurement day. The same base pellets were used for the test detectors on each measurement day. The settings of the spectrometer were set as described in Section 3.1.1.

MC simulations with EGSnrc. $c_{\vec{B}}$ factors obtained from MC simulations are required in addition to the data obtained from the experiment described in the previous paragraphs. This issue was described in detail in Section 3.1.3. The procedure for the 10 MV series was the same as described in that section. Figure 3.16 shows exemplarily the calculated mean ddcs for 1.4 T and 0 T, respectively, for 10 MV. The abscissa shows the depth in water behind 0.5 cm PMMA in cm, and the ordinate shows the simulated data points for the absorbed dose-to-water normalised to the fluence.
The procedure for the 15 MV series was also the same as described in Section 3.1.3 with one difference regarding the definition of the radiation source. Phase space files were used for defining the radiation source in the studies with 6 MV and 10 MV photons. There is, however, no phase space file available for the 15 MV photon beam applied in the present investigation. The radiation source for the 15 MV series was, thus, defined using the mohan15.spectrum provided by EGSnrc. It was defined as a collimated source with a field size of 5 cm width and 10 cm height. Due to the use of this mohan spectrum for 15 MV, an additional correction factor k_{mohan} was required. This correction factor k_{mohan} converts the $c_{\vec{B}}$ factors obtained with the mohan spectrum into the $c_{\vec{B}}$ factors for the real setup. The correction factor k_{mohan} and its associated uncertainty were determined based on the comparison of the $c_{\vec{B}}$ factors obtained with mohan spectra and phase space files for the 6 MV and the 10 MV photon beams. Details and results of these comparisons are presented in the appendix in Section E.2. The uncertainty associated with this correction factor k_{mohan} had to be considered in addition for the uncertainties associated with the $c_{\vec{B}}$ factors in the 15 MV series. Figure 3.17 shows exemplarily the calculated mean ddcs for 1.4 T and 0 T, respectively, for 15 MV. The abscissa shows the depth in water behind 0.5 cm PMMA in cm, and the ordinate shows the simulated data points for the absorbed dose-to-water normalised to the fluence.
The eventually applied $c_{\vec{B}}$ factors for the 10 MV and the 15 MV series are presented in Section E.1 in the appendix (Table E.2 and Figure E.2).

Analysis and uncertainties

The determination of the correction factors k_{mag}, which are required in Equation 2.30 for converting the standard indication of the alanine dosimeter in the presence of a static magnetic field into the absorbed dose-to-water at the point of measurement in the presence of a magnetic field, followed the procedure described in detail in Section 3.1.3 for the 6 MV series with the only differences that the flux densities in the 10 MV and 15 MV series were (0, 0, 0.7, 1.4) T and that there were four

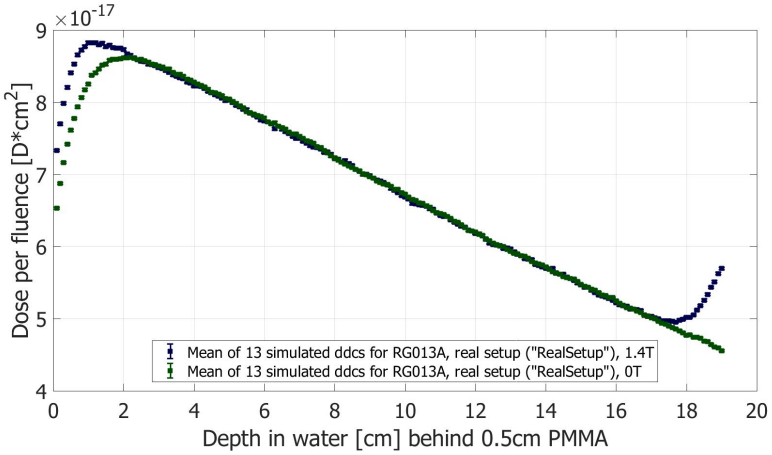

Figure 3.16: Simulated mean ddcs in the presence of a magnetic field with flux density 1.4 T (blue) and in the absence of a magnetic field (green) for 10 MV. Prominent are the shift of the ddc in the presence of the magnetic field in the build-up region (below 2 cm water depth behind 0.5 cm PMMA) and the rise in the dose at the backside of the water phantom (behind 17 cm water depth behind 0.5 cm PMMA), which is probably due to the ERE, see Section 2.3.3.

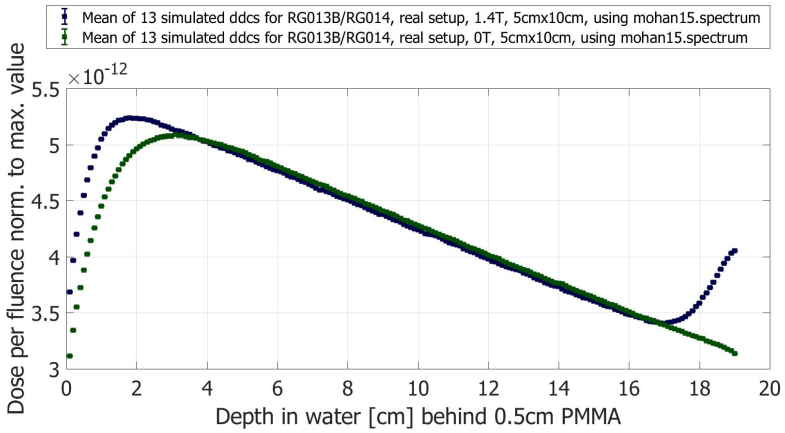

Figure 3.17: Simulated mean ddcs in the presence of a magnetic field with flux density 1.4 T (blue) and in the absence of a magnetic field (green) for 15 MV. Prominent are the shift of the ddc in the presence of the magnetic field in the build-up region (below 4 cm water depth behind 0.5 cm PMMA) and the rise in the dose at the backside of the water phantom (behind 17 cm water depth behind 0.5 cm PMMA), which is probably due to the ERE, see Section 2.3.3.

irradiation runs for averaging in the 15 MV series.
The model equations 3.26 and 3.29 for the correction factors k_{mag} and k^*_{mag} apply here, too, as well as the uncertainty budget given in Table 3.4. The correction factors k_{mag} were eventually obtained from the correction factors k^*_{mag} based on the experimental data and the $c_{\vec{B}}$ factors based on the simulated data as described in Section 3.1.3. The values for k^*_{mag} and $c_{\vec{B}}$ are given in Section E.1 in the appendix. In addition to the values for the correction factors k^*_{mag} (which are the mean over the two irradiations in the absence of a magnetic field and the three 10 MV irradiation runs and four 15 MV irradiation runs, respectively, see Section 3.1.3), the values before averaging over the two irradiations in the absence of a magnetic field and before averaging over the irradiation runs are shown in the appendix in Section E.1. The resulting final values for the correction factors k_{mag} are shown in Section 4.1.4.

3.2 Characterisation of the alanine dosimeter in MRI

3.2.1 Effect of MRI on irradiated alanine detectors

Experiment and applied devices

The aim of this experiment was to find out whether the exposure of already irradiated alanine detectors to the three types of magnetic fields of an MRI system – (1) static magnetic main field, (2) gradient magnetic fields, and (3) oscillating magnetic field of the RF pulses, see Section 2.1.1 – affects the indication of the alanine dosimeter, i.e. if the amount of radicals in the irradiated alanine pellets is altered by the impact of the three MRI components.

Detector holders. The alanine pellets were irradiated in the Farmer-IC-like PMMA holder as described in Section 3.1.1. The irradiated alanine pellets were placed in a PMMA block with four drilled holes for the exposure to the MRI system. A schematic drawing of the block is shown in Figure 3.18. It can also be seen in Figure 3.19. Three drillings in this block are 15 cm apart, which allowed to position one alanine detector in the isocenter of the MR scanner, one 15 cm apart from the isocenter, and one 30 cm apart from the isocenter; a fourth drilling allowed to locate one alanine detector in 27.5 cm from the isocenter, see Section 3.2.1.

Alanine pellets. Twelve alanine test detectors (hm27-a1...d1, hm27-a2...d2, ..., hm27-a12...d12) were irradiated to a nominal absorbed dose-to-water of 25 Gy in the Cobalt-60 reference field at the PTB. Two additional alanine detectors were used as alanine base pellets. One was irradiated to a nominal absorbed dose-to-water of 25 Gy in the same radiation field, too, one remained unirradiated. All of these detectors were composed of four alanine pellets from Harwell Batch AM603.

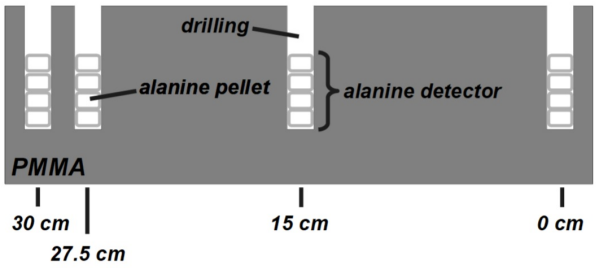

Figure 3.18: Schematic drawing of the PMMA block used for positioning the alanine detectors in the MRI system (see Figure 3.19).

Weighting. The weighting was performed as described in Section 3.1.1.

Irradiation of the base pellets in the Cobalt-60 facility at the PTB. The Cobalt-60 facility at the PTB was used for the irradiation of two alanine base detectors as described in Section 3.1.1.[30]

Irradiation of the test pellets in the Cobalt-60 facility at the PTB. The Cobalt-60 facility at the PTB was also used for the irradiation of the alanine test detectors. The automatic irradiation at the Cobalt-60 reference field was not working during this test pellet irradiation. A possible solution for this problem was a program already existing in the department which closed the shutter after 2085 sec (corresponding to an absorbed dose-to-water of approx. 25 Gy with the activity of the Cobalt-60 source at the time of the experiment). It was, thus, decided to irradiate the alanine test detectors to 25 Gy despite the fact that the alanine system at the PTB is optimised for dose measurements in the range of 5 Gy to 20 Gy. Dose measurements of 25 Gy are critical yet possible due to the calibration of the system with pellets irradiated to 25 Gy. The irradiation to 25 Gy is in this case, however, not as critical as in general since the pellets irradiated to 25 Gy are compared to themselves in the analysis. If the amplitude determination by EPR spectrometry is impaired due to the applied doses around 25 Gy, it can be assumed that the impairment is the same for each EPR measurement of an individual alanine pellet.
The uncertainty associated with the applied dose in case of using the program is slightly higher than in case of the automatic irradiation. However, this does not

[30] However, the base pellets in this experiment (see Section 3.2.1) belong to a set of alanine detectors used for determining a calibration curve, composed of detectors irradiated to (2.5, 5, 7, 10, 12.5, 15, 17.5, 20, 25, 25, 0, 0) Gy. These detectors were not originally irradiated for this experiment, they were only taken from the storage locker in order to provide detectors irradiated to 25 Gy and 0 Gy, respectively. This was due to inexperience in my agreement with the assisting engineer. In retrospect, it would have been preferable to use requisite pellets irradiated at the same time as the test pellets or at least alanine detectors with an irradiation date closer to the performed experiment. Nevertheless, with the analysis method applied, this unfavourable base pellet selection does not affect the results.

affect the final results of this experiment since the applied dose does not occur in the model equation, see Equation 3.34.

Readout with the Bruker EMX 1327 EPR spectrometer at the PTB prior to the exposure to the MRI system. The alanine detectors were read out with the Bruker EMX 1327 EPR spectrometer at the PTB as described in Section 3.1.1. The readout was performed on two measurement days. Six alanine test detectors were read out on each measurement day with the base detectors mentioned in Section 3.2.1.

Exposure to the MRI system. The Siemens Verio MRI system located at the PTB Berlin was applied in this experiment. This MRI system features a main magnetic field with a flux density of 2.89 T, a gradient amplitude of 45 mT/m , a gradient slew rate of 200 T/m/s, and a ^{1}H frequency of 123.2 MHz. The irradiated alanine detectors were exposed to five different conditions in this MRI system, labeled Condition A, B, C, D, and E. These conditions are described in detail in the following paragraphs; Table 3.5 shows the overview. For the exposure, the alanine pellets were placed in the drilled holes in the PMMA block described in Section 3.2.1. This block with the alanine detectors was placed on the patient couch in front of a head coil belonging to the receiving unit of the RF system, see Figure 3.19. A water phantom was placed inside this coil in order to prevent the MRI system from aborting the sequences, which happens if no signal from a water probe is received.

Condition A. The alanine detectors hm27-a11...d11 (A_1) and hm27-a12...d12 (A_2) were used for a consistency check. They were stored in the same microtiter plate as the other detectors and were taken to the PTB Berlin, however, they were not exposed to the MRI system.

Condition B. Condition B aimed at a strong impact of the RF system ("maxRF"). The alanine detectors hm27-a1...d1, hm27-a2...d2, and hm27-a3...d3 were, thus, exposed to a multiband measurement in the MRI system with enhanced RF pulses. The enhancement possibilities described in Section 2.1.6 were applied. The multiband factor was set to three, i.e. three slices were excited simultaneously. The reference voltage Tx was set to the arbitrary high value of 800 V without regard to the (in this case meaningless) image quality. And the flip angle was set to the high value of 130°. The fat saturation modul was included, as this involves additional RF pulses (see Section 2.1.6). The measurement involved 30 slices with slice thickness 5 mm in transversal orientation. The TR was 477 ms. The TE was 18.4 ms. In total, 4000 measurements were taken; the total duration of this MR measurement was 32 min 1 sec. The duration of an excitation pulse was 6000 µs. The SAR (see Section 2.1.7) was at 94 % of the allowed threshold. Alanine detector hm27-a1...d1 was positioned in the isocenter of the MRI system where gradient fields are zero (B_a, "minGrad"), detector hm27-a3...d3 was placed 30 cm left of the isocenter, where the

gradient fields are most pronounced (B_c, "maxGrad"), and detector hm27-a2...d2 was placed in between, 15 cm left of the isocenter, where gradient fields are at medium strength (B_b, "midGrad"), see Figure 3.19. This was accomplished by using the PMMA block described in Section 3.2.1, see Figure 3.18. The static magnetic main field $\vec{B}_0$ with a flux density 2.89 T was experienced by all three alanine detectors hm27-a1...d1, hm27-a2...d2, and hm27-a3...d3.

Condition C. Condition C aimed at a diminishing impact of the RF system ("minRF"). The alanine detectors hm27-a4...d4, hm27-a5...d5, and hm27-a6...d6 were, thus, exposed to a measurement in the MRI system with suppressed RF pulses. The multiband factor was three as in Condition B. The suppression possibilities described in Section 2.1.6 were applied. The value for the reference voltage Tx was set to the arbitrary low value of 10 V, again without regard to the image quality, and the flip angle was set to 10° (see Section 2.1.6). With these settings, the transmitted RF power was that small that image acquisition was no longer possible. As before, the measurement involved 30 slices with slice thickness 5 mm. The TR was 1034 ms (about twice as long as in Condition B). The TE was 53.8 ms (about three times longer than in Condition B). In Condition C, the suppression of the fat signal was switched off, as this fat suppression involves additional RF pulses prior to the actual imaging sequence (see Section 2.1.6). In total, 1870 measurements were taken; the total duration of this MR measurement was 32 min 20 sec. The SAR (see Section 2.1.7) was at 1 % of the threshold, which is in contrast to 94 % for Condition B. The duration of the excitation pulses was 1020 µs (about a factor of six less than in Condition B). Again, the detectors were positioned at different distances from the isocenter in order to vary the impact of the gradient system. Alanine detector hm27-a4...d4 was positioned in the isocenter of the MRI system (C_a, "minGrad"), detector hm27-a5...d5 was placed 15 cm left of the isocenter (C_b, "midGrad"), and detector hm27-a6...d6 was placed 30 cm left of the isocenter (C_c, "maxGrad"), see Figure 3.19. As in Condition B, the static magnetic main field $\vec{B}_0$ with flux density 2.89 T was experienced by all three involed alanine detectors.

Condition D. The purpose of Condition D was to provide a situation as similar as possible to an MR Linac in terms of the MRI. The alanine detectors hm27-a7...d7, hm27-a8...d8, and hm27-a9...d9 were, thus, exposed to a realtime motion MR measurement which was assumed – at that time – to be similar to the sequences that could be applied in MR Linacs ("cine"). The imaging was triggered by a simulated heart beat. The measurement involved 20 slices. The duration of the applied MR measurement was less than four minutes. It was, thus, performed in total six times in order to achieve a total duration similar to Condition B and C (21 min). Again, the detectors were positioned at different lateral distances from the isocenter corresponding to a varyingly strong impact of the gradient system. Alanine detector hm27-a7...d7 was positioned in the isocenter of the MRI system (D_a, "minGrad"), detector hm27-a8...d8 was placed 15 cm left of the isocenter (D_b, "midGrad"), and

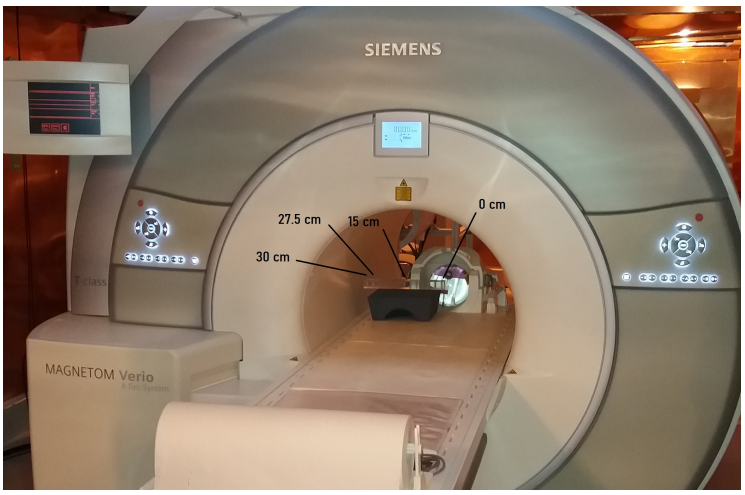

Figure 3.19: The setup during the exposure of the already irradiated alanine detectors to the MRI system Siemens Verio at the PTB Berlin. A PMMA block with drillings for alanine pellets is placed on the patient bench. The drillings are labeled with their respective lateral distance from the isocenter. Behind the PMMA block, the head coil of the receiving unit of the RF system can be seen. It contains a water phantom (see Section 3.2.1).

detector hm27-a9...d9 was placed 30 cm left of the isocenter (D_c, "maxGrad"), see Figure 3.19. As in Condition B and C, the static magnetic main field $\vec{B}_0$ with flux density 2.89 T was experienced by all three alanine detectors involved.

Condition E. Alanine detector hm27-a10...d10 was used as an additional check by summing up the impact of Condition B, C, and D. Detector hm27-a10...d10 was therefore placed in the MRI system all the time during the application of the MR sequences of Condition B, C, and D. It was positioned 27.5 cm left of the isocenter (since the position 30 cm left of the isocenter was occupied by the detectors used for Condition B, C, and D, see Figure 3.19) where gradient fields are almost at maximum strength ("allwithhighGrad"). Alanine detector hm27-a10...d10, experienced the static magnetic main field $\vec{B}_0$ with flux density 2.89 T as well.

Readout with the Bruker EMX 1327 EPR spectrometer at the PTB after the exposure to the MRI system. The alanine detectors were read out a second time with the Bruker EMX 1327 EPR spectrometer at the PTB after the exposure to the MRI system as described in Section 3.1.1. The readout was performed on one measurement day with the base detectors mentioned in Section 3.2.1.

Table 3.5: Overview of the different situations of exposure to the MRI system.

Detector	Condition	Main field	Gradients	RF pulses	Details
hm27-a11...d11	A_1	–	–	–	no MRI exposure
hm27-a12...d12	A_2	–	–	–	no MRI exposure
hm27-a1...d1	B_a	on	min	max	multiband factor: 3 Tx: 800 V flip angle: 130° TR: 477 ms TE: 18.4 ms fat suppression modul: on excitation pulse duration: 6000 µs SAR: 94 %
hm27-a2...d2	B_b	on	mid	see above	see above
hm27-a3...d3	B_c	on	max	see above	see above
hm27-a4...d4	C_a	on	min	min	multiband factor: 3 Tx: 10 V flip angle: 10° TR: 1034 ms TE: 53.8 ms fat suppression modul: off excitation pulse duration: 1020 µs SAR: 1 %
hm27-a5...d5	C_b	on	mid	see above	see above
hm27-a6...d6	C_c	on	max	see above	see above
hm27-a7...d7	D_a	on	min	cine	cine measurement
hm27-a8...d8	D_b	on	mid	see above	see above
hm27-a9...d9	D_c	on	max	see above	see above
hm27-a10...d10	E	on	high	all	exposure to Condition B, C, and D

Analysis and uncertainties

The aim of this analysis was to determine the correction factor $k_{subsMRI}$ which corrects the indication of the alanine dosimeter in the case of the exposure of an alanine detector to an MRI system subsequent to its irradiation.

Derivation of the model equation. The response R of the alanine detector is given by Equation 3.1.1 as described in Section 3.1.1. The ratio of two alanine response values is unity in the case of entirely corrected response values. This is the starting point for the derivation of the model equation for $k_{subsMRI}$. The two response values in the ratio in this case are R_{before} with the indication $A^{corr}_{D,before}$ obtained from the EPR readout prior to the exposure to the MRI system and R_{after} with the indication $A^{corr}_{D,after}$ obtained from the EPR readout after the exposure to the MRI system, see Sections 3.2.1 and 3.2.1:

$$\begin{aligned} 1 &= \frac{R_{after}}{R_{before}} \\ &= \frac{\frac{A^{corr}_{D,after}}{D_{appl,after}}}{\frac{A^{corr}_{D,before}}{D_{appl,before}}} \end{aligned} \tag{3.32}$$

The applied doses-to-water $D_{appl,after}$ and $D_{appl,before}$ equal each other and, hence, cancel out since the very same alanine pellets, which are of course irradiated to the same dose, are used in this experiment. The corrected dose-normalised amplitude A^{corr}_{D} is given by Equation 2.30. The correction factor $K_{V,s,after/before}$ is equal to unity due to constant gradients in the dose distribution during the irradiation of all alanine detectors used (see Section 2.4.3). The correction factor $K_{env,after/before}$ is equal to unity since all alanine detectors were irradiated within the same water phantom (see Section 2.4.3). The expressions for $A^{corr}_{D,before/after}$ in the present situation are, hence:

$$\begin{aligned} A^{corr}_{D,before} &= \frac{A_{m,before}}{\bar{m}} \cdot \bar{m}^b \cdot D^b \cdot K_T \cdot K_Q \cdot K_{F,before} \\ A^{corr}_{D,after} &= \frac{A_{m,after}}{\bar{m}} \cdot \bar{m}^b \cdot D^b \cdot K_T \cdot K_Q \cdot K_{F,after} \cdot K_{subsMRI} \end{aligned} \tag{3.33}$$

It is $\bar{m}_{after} = \bar{m}_{before} = \bar{m}$ as they are the same pellets, as well as $\bar{m}^b_{after} = \bar{m}^b_{before} = \bar{m}^b$ and $D^b_{after} = D^b_{before} = D^b$. Further, it is $K_{T,after} = K_{T,before} = K_T$ and $K_{Q,after} = K_{Q,before} = K_Q$ since these correction factors refer to the same alanine pellets irradiated in the same irradiation. The fading correction factors $K_{F,after}$ and $K_{F,before}$ equal each other, too, since the difference d of the time intervals $\Delta t^{(b)}_{after/before}$ between the irradiation and the EPR measurement between the test pellets and the base pellets (i.e. $\Delta t_{after/before} - \Delta t^b_{after/before}$) is the same for all test detectors (see Section 2.4.3). It is $k^b_{subsMRI} = 1$, since the base pellets were not

exposed to the MRI system. Combining Equations 3.32 and 3.33, hence, eventually results in the model equation

$$k_{subsMRI} = \frac{A_{m,before}}{A_{m,after}} \tag{3.34}$$

Quantities in the model equation and uncertainty budget. The following describes how the correction factor $k_{subsMRI}$ was obtained from the experimental data according to the model equation 3.34.

Alanine pellet mass. The alanine pellet mass cancels out in the model equation, see Section 3.2.1. Nevertheless, contributions for the alanine test pellet mass and the alanine base pellet mass have to be considered in the uncertainty budget due to the fact that $\bar{m}_{after}$ and $\bar{m}^b_{after}$, respectively, can slightly differ from $\bar{m}_{before}$ and $\bar{m}^b_{before}$, respectively, due to a material loss during the handling for the exposure to the MRI system (only test pellets) and the additional EPR readout (test and base pellets). Both situations account for two additional handlings. Hence, there are four additional handlings for the test pellets and two for the base pellets. The uncertainty components to be considered are:

$$u_r(\bar{m}^{(b)}) = \frac{u(m_i^{(b)})}{\sqrt{n} \cdot \bar{m}^{(b)}} \tag{3.35}$$

with the absolute uncertainty of the mass of an individual alanine pellet $u(m_i^{(b)})$, the mean mass of n pellets $\bar{m}^{(b)}$, the absolute uncertainty of the mean mass of an alanine detector composed of n pellets $u(\bar{m}^{(b)})$, and the relative uncertainty of the mean mass of an alanine detector composed of n pellets $u_r(\bar{m}^{(b)})$. For the test pellets, it is $u(m_i) = 4 \cdot 4\,\mu g$ ($u(m_i) = 2 \cdot 4\,\mu g$ for the test detectors hm27-a11...d11 and hm27-a12...d12, which were not exposed to the MRI system, see Section 3.2.1); for the base pellets, it is $u(m_i^b) = 2 \cdot 4\,\mu g$. The averaged masses are obtained from weighting the alanine pellets prior to the experiment as described in Section 3.1.1. The possible material loss of about $4\,\mu g$ per handling was determined by Mathias Anton, see Section 3.1.1.

Alanine amplitude. The uncertainty associated with the amplitude values $A_{m,before}$ and $A_{m,after}$ has two contributions. One is due to the reproducibility of the amplitude measurement and the other one is due to the homogeneity of the detector material. Both contributions affect the test and the base pellets. In this analysis, the components due to the homogeneity cancel out for test and base pellets since the twelve test detectors hm27-a1...d1 to hm27-a12...d12 are compared to themselves and the same base detectors (hm16-a10...d10 and hm27-e12...h12) are used in all EPR measurements. Only the contributions due to the reproducibility of the amplitude determination for test and base detectors ($u_r(A^{repro}_{test})$ and $u_r(A^{repro}_{base})$) have to be considered in this analysis. The uncertainty component $u_r(A^{repro}_{m,test})$ due

to the reproducibility for the alanine test detector is calculated using Equation 3.6 as described in Section 3.1.1 and the uncertainty component $u_r(A^{repro}_{m,base})$ due to the reproducibility for the alanine base detector is calculated using Equation 3.21 as described in Section 3.1.2. The model equation 3.34 contains two amplitude values. Nevertheless, the uncertainty components due to reproducibility of the amplitude for test and base pellets have to be considered only for one amplitude value in the uncertainty budget: The result of one EPR measurement based on given amplitude values for test and base pellets is as it is. The result of the other EPR measurement might differ due to the restricted reproducibility, which is accounted for by the uncertainty contribution for the reproducibility of the amplitude for test and base pellets. The corrected dose-normalised amplitude from the EPR measurement prior to the exposure to the MRI system was used for A^{corr}_D here.[31] It can be calculated as described in Section 3.1.1.[32] The values of $A_{m,before}$ and $A_{m,after}$ are obtained from the respective EPR measurement.

Summary of the uncertainty budget. The uncertainty budget for the correction factor $k_{subsMRI}$ contains the contributions due to the amplitude determination and due to the masses. It is summarised in Table 3.6. The total relative uncertainty associated with $k_{subsMRI}$, $u_r(k_{subsMRI})$, is obtained from the uncertainty contributions according to:

$$u_r(k_{subsMRI}) = \sqrt{u_r(A^{repro}_{test})^2 + u_r(A^{repro}_{base})^2 + u_r(\bar{m})^2 + u_r(\bar{m}^b)^2} \tag{3.36}$$

The uncertainty components due to the possible material loss are negligible compared to the uncertainty components due to the reproducibility of the amplitude determination. Please note that the single components and the total uncertainty are rounded according to the rules stated in [Beringer et al., 2012]. The total uncertainty is calculated using the non-rounded values for the single components.

3.2.2 Effect of MRI during irradiation

Experiment and applied devices

The aim of this experiment was to determine the correction factor k_{RF}[33] which corrects the indication of the alanine dosimeter for the effect of an MR sequence applied in addition to the static magnetic base field of the Elekta Unity™ MR Linac. The effect of the static magnetic field is separately addressed by the magnetic field correction factor k_{mag} determined in Section 3.1.2.

[31] It was decided to use the value from the EPR measurement prior to the exposure to the MRI system, as the effect of the exposure was not known beforehand. In any case, the exact value used is not that relevant for determining the uncertainty contribution.

[32] However, the correction factors $K_{V,s,before}$, $K_{Q,before}$, and $K_{env,before}$ equal unity in this case, and the deviation of $K_{T,before}$ from unity is negligible at this point.

[33] The index "RF" refers to the RF pulses applied during MRI.

Table 3.6: Uncertainty budget for the correction factor $k_{subsMRI}$. The total uncertainty was calculated using the non-rounded single components. All uncertainties are given for a coverage factor $k = 1$.

Contribution	due to ...	u_r in %
$u_r(A_{test}^{repro})$	reproducibility of the amplitude determination (test pellets)	0.12
$u_r(A_{base}^{repro})$	reproducibility of the amplitude determination (base pellets)	0.12
$u_r(\bar{m})$	mass of test pellets (potential material loss due to additional handling); for detector hm27-a11...d11 and hm27-a12...d12 only 0.007 %	0.013 (0.007)
$u_r(\bar{m}^b)$	mass of base pellets (potential material loss due to additional handling)	0.007
Total:	$u_r(k_{subsMRI}) = 0.17$	

Detector holders. Detector holders were used as described in Section 3.1.2.

Alanine pellets. Two alanine detectors were irradiated with concurring MRI in this experiment. In addition, the information of the five alanine detectors irradiated without concurring MRI from the experiment described in Section 3.1.2 was used in the analysis. The same base detectors as for the experiment described in Section 3.1.2 were used. All these detectors were composed of four alanine pellets from Harwell Batch AM603.

Weighting. The weighting was performed as described in Section 3.1.1.

Irradiation of the base pellets in the Cobalt-60 facility at the PTB. The same base detectors as in the experiment described in Section 3.1.2 were used. Their irradiation is described in Section 3.1.2.

Irradiation of the test pellets at the Elekta Unity™ MR Linac. The alanine test detectors for determining the correction factor k_{RF} were irradiated in the same setup at the MR Linac at The Christie hospital in Manchester, UK during the same measurement week as the alanine test detectors used for determining the correction factor k_{mag}, see Section 3.1.2, with only two differences:

A spin echo sequence for American College of Radiology (ACR) phantoms (typically used for QA) with two echoes at 20 ms (proton weighted) and 80 ms (T2 weighted) and a TR of 2000 ms was applied during the irradiations of the two alanine test detectors. An illustration of this MR sequence is shown in Figure 3.20.
The second difference is, that no measurements of the monitoring Farmer-type IC are available for this experiment since this IC could not be applied during the MR sequences. A comparison of the alanine signals with the signals of the Farmer-type IC transfer standards was, thus, not possible. The signals of the alanine test detectors were, hence, compared to the signals of the alanine test detectors irradiated for the determination of the correction factor k_{mag} instead, see Section 3.2.2.
An overview of the irradiations is listed in Table 3.7.

Readout with the Bruker EMX 1327 EPR spectrometer at the PTB. The alanine detectors were read out with the Bruker EMX 1327 EPR spectrometer at the PTB as described in Section 3.1.1. The readout was performed on two measurement days. The two alanine test detectors irradiated with concurring MRI were readout on one measurement day together with two alanine test detectors irradiated without MRI (hm35-c4...f4 and hm35-c5...f5) for comparison and the base detectors. The other three alanine test detectors irradiated without MRI (hm35-c1...f1, hm35-c2...f2, and hm35-c3...f3) were readout on another measurement day using the same base detectors.
It has been mentioned in Section 3.1.2 that the splitting into two measurement days at the EPR spectrometer does not increase the uncertainty associated with the resulting correction factor k_{mag} since the model equations 3.13 and 3.14 compare one alanine signal with one Farmer-type IC transfer standard signal each time and not different alanine signals. For this experiment aiming at the determination of the correction factor k_{RF}, it is, however, unfavourable that the alanine detectors irradiated without MRI were not all readout on the same measurement day as the alanine detectors irradiated with concurring MRI, since the model equation (see Section 3.2.2) compares the signals of two alanine detectors. The uncertainty in the comparisons of the alanine test detectors irradiated with concurring MRI (hm35-c10...f10 and hm35-c11...f11) with the alanine detectors hm35-c1...f1, hm35-c2...f2, and hm35-c3...f3 is, thus, higher than in the comparisons with the alanine detectors hm35-c4...f4 and hm35-c5...f5, see Section 3.2.2.

Analysis and uncertainties

The aim of this analysis was to determine the correction factor k_{RF} which corrects the indication of the alanine dosimeter already corrected for the presence of the static magnetic field by correction factor k_{mag} if an MR sequence is applied in addition to the static magnetic base field of the Elekta Unity™ MR Linac. During the MRI, it was not possible to use the Farmer-type IC transfer standards or the monitoring Farmer-type IC, as it was done in the experiment aiming at the determination of the correction factor k_{mag} (see Section 3.1.2). It is only known, that the two alanine

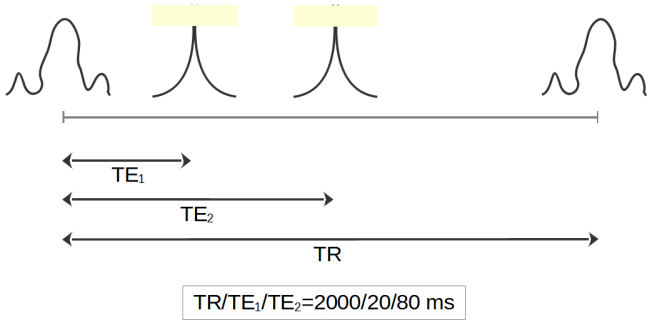

Figure 3.20: The spin echo sequence for ACR phantoms applied during the irradiation of the alanine test detectors hm35-c10...f10 and hm35-c11...f11. The echo after $TE_1 = 20\,ms$ is proton-weighted and the echo after $TE_2 = 80\,ms$ is T2-weighted.

Table 3.7: Order of irradiations of alanine detectors analysed in the present investigation in addition to the alanine irradiations listed in Table 3.2.

Date	Time	Run	Alanine detector	Monitor units
2017-09-20	09:45	01	Alanine detector hm35-c11...f11	$2 \times 750\,MU$
2017-09-20	10:06	02	Alanine detector hm35-c10...f10	$2 \times 750\,MU$

detectors irradiated with simultaneous MRI were irradiated to the same amount of monitor units (i.e. $2 \times 750\,\mathrm{MU}$) as the five alanine detectors irradiated without MRI (see Section 3.1.2).

Derivation of the model equation. The idea for the analysis is, thus, to relate the signal $A^{corr}_{D,RF}$ of the alanine detectors irradiated with simultaneous MRI (see Table 3.7) to the signal $A^{corr}_{D,noRF}$ of the alanine detectors irradiated without MRI (see Table 3.2). Assuming completely corrected values results in

$$1 = \frac{A^{corr}_{D,RF}}{A^{corr}_{D,noRF}} \tag{3.37}$$

The corrected dose-normalised amplitude A^{corr}_{D} is given by Equation 2.30. The correction factors have to be applied as described in Section 3.1.2 – with the additional correction factor k_{RF} in the case of the concurring MRI. This results in

$$A^{corr}_{D,noRF} = \frac{A_{m,noRF}}{\bar{m}_{noRF}} \cdot \bar{m}^b \cdot D^b \cdot K_{V,s} \cdot K_{T,noRF} \cdot K_Q \cdot K_{env} \cdot K_{F,noRF} \cdot K^{ala}_{vol} \cdot K_{mag} \tag{3.38}$$

for alanine detectors irradiated without concurring MRI and

$$A^{corr}_{D,RF} = \frac{A_{m,RF}}{\bar{m}_{RF}} \cdot \bar{m}^b \cdot D^b \cdot K_{V,s} \cdot K_{T,RF} \cdot K_Q \cdot K_{env} \cdot K_{F,RF} \cdot K^{ala}_{vol} \cdot K_{mag} \cdot K_{RF} \tag{3.39}$$

for alanine detectors irradiated with concurring MRI.

Combining the Equations 3.37 to 3.39 results in the model equation:

$$k_{RF} = \frac{\frac{A_{m,noRF}}{\bar{m}_{noRF}} \cdot k_{T,noRF} \cdot k_{F,noRF}}{\frac{A_{m,RF}}{\bar{m}_{RF}} \cdot k_{T,RF} \cdot k_{F,RF}} \tag{3.40}$$

Please note, that $(\bar{m}^b \cdot D^b_W \cdot K_{V,s} \cdot K_Q \cdot K_{env} \cdot K^{ala}_{vol} \cdot K_{mag})$ are the same for the alanine detectors irradiated with and without concurrent MRI, since the same alanine base detectors were used for all alanine test detectors and since the irradiation of all alanine test detectors was performed in the very same manner with the additional MRI as the only exception. Please note, too, that all correction factors are relative to the respective base, see Equation 2.29. This allows for further simplifications. It is sufficient to use k_T and k_F in the model equation since the base components k^b_T and k^b_F are identical in both cases. Furthermore, it is sufficient to use k_{mag} and k_{RF} since k^b_{mag} and k^b_{RF} equal unity due to the irradiation of the alanine base detectors in the absence of any static magnetic field or MRI.

Averaging. There are two alanine detectors irradiated with concurring MRI (hm35-c10...f10 and hm35-c11...f11) and five alanine detectors irradiated without MRI

(hm35-c1...f1, hm35-c2...f2, ..., hm35-c5...f5). The correction factor k_{RF} was calculated five times according to Equation 3.40 for hm35-c10...f10 with the five detectors irradiated without MRI; these five values were averaged. And the correction factor k_{RF} was calculated five times for hm35-c11...f11 with the five detectors irradiated without MRI and these five values were averaged, too. The two resulting mean values were averaged again in order to obtain the final result for the correction factor k_{RF}.

Please note that this comparison of alanine detectors irradiated with and without concurring MRI is based on the assumption that the shape of the EPR spectrum does not differ for the alanine detectors irradiated with and without concurring MRI. The shape of the alanine EPR spectrum depends on the ratio of radicals formed under the impact of the ionising radiation [Malinen et al., 2003a,b]. It could not be excluded beforehand that the impact of the RF pulses during MRI alters the ratio of radicals. A variation in the alanine EPR spectrum due to the applied RF pulses would have required an adaptation of the least squares fit performed for determining the alanine signal (see Section 2.4.3). The alanine EPR spectra for the alanine pellets irradiated with and without concurring MRI were, thus, compared. No significant differences were found. The comparison of alanine detectors irradiated with and without concurring MRI provides, hence, reliable results without the need for an adaptation of the fitting procedure.

Quantities in the model equation and uncertainty budget.

Alanine pellet mass. The individual masses m_i of the four alanine pellets composing a single alanine test detector were averaged for obtaining the mean mass $\bar{m}_{noRF/RF}$ of a respective detector. An uncertainty contribution $u_r(\bar{m}_{noRF/RF})$ has to be considered for each alanine detector according to the description in Section 3.1.1. Likewise, the individual masses m_i^b of the eight alanine pellets composing the two alanine base detectors were averaged for obtaining the mean mass $\bar{m}^b$ of the base. The uncertainty associated with $\bar{m}^b$ is determined analogously to $u_r(\bar{m})$.

Alanine amplitude. The values for the mass-related mean amplitude $A_{m,noRF/RF}$ are obtained from the EPR measurements of the alanine detectors. The uncertainty associated with these amplitude values has two contributions. One is due to the reproducibility of the amplitude measurement and the other one is due to the homogeneity of the detector material. These contributions have to be considered for the alanine test and the alanine base detectors.
The uncertainty component $u_r(A^{repro}_{m,test,noRF/RF})$ due to the reproducibility for the alanine test detectors is determined according to Equation 3.6 as described in Section 3.1.1. The uncertainty component $u_r(A^{repro}_{m,base,noRF/RF})$ due to the reproducibility of the alanine base detectors is determined according to Equation 3.21 as described in Section 3.1.2. The uncertainty component $u_r(A^{hom}_{m,test,noRF/RF})$ due to the ho-

mogeneity for the alanine test detector is calculated according to Equation 3.7 as described in Section 3.1.1 and the component $u_r(A^{hom}_{m,base,noRF/RF})$ due to the homogeneity for the alanine base detector is determined analogously. In general, all these components have to be considered for the test and for the base pellets, i.e. two components for the reproducibility of the two test detectors in this case, two components for the reproducibility of the respective base detectors, two components for the homogeneity of the two test detectors, and two components for the homogeneity of the respective base detectors, see Table 3.8. For the correction factor k_{RF} determined for the two alanine detectors irradiated with concurring MRI with the alanine detectors hm35-c4...f4 and hm35-c5...f5, however, the uncertainty components for the base have to be considered only once since the value of interest is a ratio of values obtained on one single EPR readout day with the same alanine base.[34]

Irradiation temperature correction. The correction factor $k_{T,noRF/RF}$ for the irradiation temperature required in the model equation 3.40 is obtained as described in Section 3.1.1.

Fading correction. The correction factor $k_{F,noRF/RF}$ for the fading required in the model equation 3.40 and the associated uncertainty are obtained as described in Section 3.1.2.

Summary of the uncertainty budget. The uncertainty associated with the correction factor k_{RF} obtained from Equation 3.40 for one alanine signal with concurring MRI and one alanine signal without MRI results from the uncertainty budget containing the following contributions: The relative uncertainties $u_r(A^{repro}_{m,test,RF})$ and $u_r(A^{repro}_{m,base,RF})$ and the relative uncertainties $u_r(A^{hom}_{m,test,RF})$ and $u_r(A^{hom}_{m,base,RF})$ associated with the amplitudes of the alanine test and base pellets for the alanine detector irradiated with concurring MRI, and the relative uncertainties $u_r(A^{repro}_{m,test,noRF})$ and $u_r(A^{repro}_{m,base,noRF})$ and the relative uncertainties $u_r(A^{hom}_{m,test,noRF})$ and $u_r(A^{hom}_{m,base,noRF})$ associated with the amplitudes of the alanine test and base pellets for the alanine detector irradiated without MRI (the uncertainty components $u_r(A^{repro}_{m,base,noRF})$ and $u_r(A^{hom}_{m,base,noRF})$ are not required in the cases in which both the alanine detector irradiated with concurring MRI and the alanine detector irradiated without MRI were readout in the EPR spectrometer on the same measurement day, see Section 3.2.2); the relative uncertainties $u_r(\bar{m}_{RF})$ and $u_r(\bar{m}_{noRF})$ associated with the mean masses of the alanine test pellets irradiated with and without concurring MRI; the relative uncertainty $u_r(\bar{m}^b)$ associated with the mean mass $\bar{m}^b$ of the alanine base pellets; the relative uncertainties $u_r(k_{T,RF})$ and $u_r(k_{T,noRF})$ for the irradiation temperature correction for the alanine detector irradiated with and the alanine detector irradiated without concurring MRI; the relative uncertainties $u_r(k_{F,RF})$

[34] In a repetition of the experiment, it would be favourable to perform the readout of all alanine detectors included in this analysis on the same measurement day in order to minimise the uncertainty associated with the resulting correction factor k_{RF}.

and $u_r(k_{F,noRF})$ for the fading correction for the alanine detector irradiated with and the alanine detector irradiated without concurring MRI; and the relative uncertainty $u_r(k_{output})$ considering possible changes in the output of the MR Linac during the measurements of the alanine detectors with and without concurring MRI. These components are added in quadrature in order to obtain the combined standard uncertainty associated with the correction factor k_{RF} (with coverage factor $k = 1$). This budget is also listed in Table 3.8. The single components and the total uncertainty are rounded according to the rules stated in [Beringer et al., 2012]. Please note that the missing contributions for the base amplitudes in cases when both alanine detectors were readout on the same measurement day do not affect the rounded total uncertainty due to the dominant component for the possible drifts in the output of the MR Linac.

Uncertainty after averaging. As mentioned above, there were two alanine detectors irradiated with concurring MRI and five alanine detectors irradiated without MRI. This allows to reduce the final uncertainties by averaging the results. In a first step, the mean was taken for the five values for k_{RF} obtained with the five alanine detectors irradiated without MRI and the first alanine detector irradiated with concurring MRI ($k_{RF} = \frac{1}{5} \cdot (k_{RF,1} + k_{RF,2} + k_{RF,3} + k_{RF,4} + k_{RF,5})$). The associated uncertainty was determined using error propagation. The same was done for the five values for k_{RF} obtained with the five alanine detectors irradiated without MRI and the second alanine detector irradiated with concurring MRI. In a second step, the two obtained values for k_{RF} were averaged for obtaining the final correction factor k_{RF} ($k_{RF} = \frac{1}{2} \cdot (k_{RF,1} + k_{RF,2})$). The associated uncertainty was again determined using error propagation. The resulting final value for k_{RF} is shown in Chapter 4.2.2.

Table 3.8: Uncertainty budget for the correction factor k_{RF} obtained from Equation 3.40 for one alanine signal with concurring MRI and one alanine signal without MRI. The total uncertainty was calculated using the non-rounded single components. All uncertainties are given for a coverage factor $k = 1$. Please note, that this is not the uncertainty of the final result for the correction factor k_{RF}. Due to the averaging over the results for the two alanine detectors irradiated with MRI and the five alanine detectors irradiated without MRI, the final uncertainties, as presented in Chapter 4.2.2, are obtained from the value shown in this table according to error propagation as described in Section 3.2.2.

Contribution	due to ...	u_r in %
$u_r(A^{repro}_{m,test,RF})$	reproducibility of the amplitude determination for test pellets irradiated with MRI	0.18
$u_r(A^{repro}_{m,base,RF})$	reproducibility of the amplitude determination for base pellets used for the fit to the EPR spectrum of the test pellets irradiated with MRI	0.12
$u_r(A^{hom}_{m,test,RF})$	homogeneity of the alanine pellet composition for test pellets irradiated with MRI	0.15
$u_r(A^{hom}_{m,base,RF})$	homogeneity of the alanine pellet composition for base pellets used for the fit to the EPR spectrum of the test pellets irradiated with MRI	0.15
$u_r(\bar{m}_{RF})$	mass of test pellets irradiated with MRI	0.04
$u_r(A^{repro}_{m,test,noRF})$	reproducibility of the amplitude determination for test pellets irradiated without MRI	0.18
$u_r(A^{repro}_{m,base,noRF})$	reproducibility of the amplitude determination for base pellets used for the fit to the EPR spectrum of the test pellets irradiated without MRI	0.12 (if the alanine detectors compared were readout on different measurement days); – (if the alanine detectors compared were readout on the same measurement day)
$u_r(A^{hom}_{m,test,noRF})$	homogeneity of the alanine pellet composition for test pellets irradiated without MRI	0.15
$u_r(A^{hom}_{m,base,noRF})$	homogeneity of the alanine pellet composition for base pellets used for the fit to the EPR spectrum of the test pellets irradiated without MRI	0.15 (if the alanine detectors compared were readout on different measurement days); – (if the alanine detectors compared were readout on the same measurement day)
$u_r(\bar{m}_{noRF})$	mass of test pellets irradiated without MRI	0.04
$u_r(\bar{m}^b)$	mass of base pellets	0.04
$u_r(k_{T,RF})$	correction for the irradiation temperature for the alanine detector irradiated with MRI	0.05
$u_r(k_{T,noRF})$	correction for the irradiation temperature for the alanine detector irradiated without MRI	0.05 to 0.06
$u_r(k_{F,RF})$	correction for the irradiation temperature for the alanine detector irradiated with MRI	0.11
$u_r(k_{T,noRF})$	correction for the irradiation temperature for the alanine detector irradiated without MRI	0.08 to 0.11
$u_r(k_{output})$	possible drift of the output	0.4
Total:		0.6

4 Results

4.1 Characterisation of the alanine dosimeter in static magnetic fields

4.1.1 Preparatory experiment regarding sub-millimetre air gaps

The aim of this preparatory experiment was to learn whether sub-millimetre air gaps around the alanine detectors have a measurable impact on the indication of the alanine dosimeter in the presence of static magnetic fields. This is of relevance for this work since significant effects of sub-millimetre air gaps around ICs were found in the presence of magnetic fields, see Section 2.4.2, and since air gaps around the alanine detectors cannot be completely prevented in the irradiations in water phantoms performed in the experiments of this thesis due to the non-waterproofness of the alanine pellets.

It was found, that sub-millimetre air gaps around the alanine detectors have no measurable effect on the indication of the alanine dosimeter in the presence of static magnetic fields. Table 4.1 and Figure 4.1 show the experimental results leading to this conclusion, see Section 5.1.1. The ordinate in the graph shows the values for the ratio $\frac{k_{mag,air,X}}{k_{mag,air,0.0mm}}$ while the abscissa shows the size of the air gap surrounding the alanine detector associated with the correction factor $k_{mag,air,X}$ in the numerator of the determined ratio. $\frac{k_{mag,air,X}}{k_{mag,air,0.0mm}}$ is the ratio of correction factors for a possible effect of the surrounding air gaps for an air gap of (0.1, 0.2, 0.5, 1.0) mm size and 0.0 mm size in the presence of a magnetic field. This effect is in addition to the effect that the air gaps would have in the absence of a magnetic field. It was, however, found that sub-millimetre air gaps in the absence of a magnetic field do not have a measurable effect, see Chapter A in the appendix.

4.1.2 Characterisation at the Elekta Unity™ MR Linac device

The aim of this experiment was to determine the magnetic field correction factor k_{mag} for the alanine dosimeter at the clinically applied Elekta Unity™ MR Linac device, which features a static magnetic field with 1.5 T flux density and a photon beam with a nominal accelerating potential of 7 MV.

Table 4.1: Experimentally obtained values for the ratio of correction factors $\frac{k_{mag,air,X}}{k_{mag,air,0.0mm}}$ which correct the indication of the alanine dosimeter for a possible effect of the surrounding air gaps for an air gap of size X and 0.0 mm, respectively, in the presence of a magnetic field. This possible effect is in addition to the effect that the air gaps would have in the absence of a magnetic field. (Coverage factor $k = 1$, the uncertainties given are absolute uncertainties.)

Quantity	experimentally obtained value with absolute uncertainty
$\frac{k_{mag,air,0.1mm}}{k_{mag,air,0.0mm}}$	1.004 ± 0.005
$\frac{k_{mag,air,0.2mm}}{k_{mag,air,0.0mm}}$	1.000 ± 0.005
$\frac{k_{mag,air,0.5mm}}{k_{mag,air,0.0mm}}$	0.998 ± 0.005
$\frac{k_{mag,air,1.0mm}}{k_{mag,air,0.0mm}}$	0.994 ± 0.005
$\frac{k_{mag,air,0.0mm}}{k_{mag,air,0.0mm}}$	1.000 ± 0.004

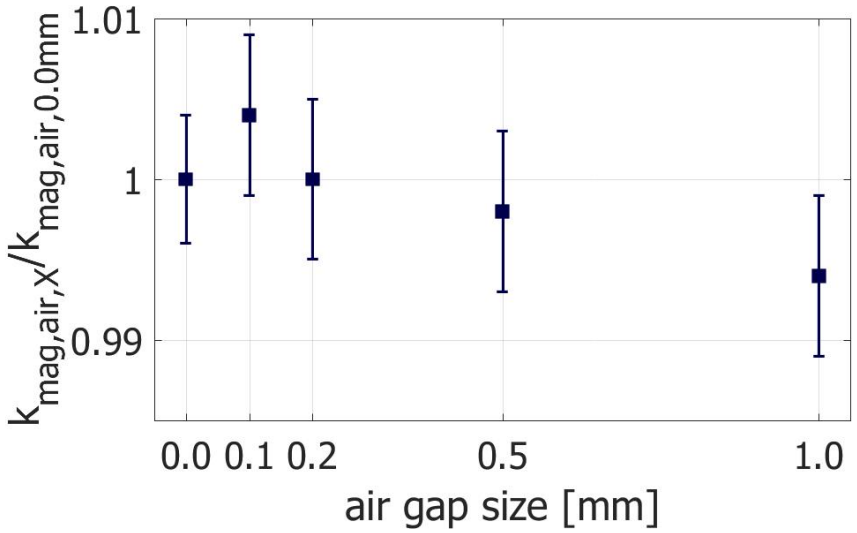

Figure 4.1: Experimentally obtained values for the ratio of correction factors $\frac{k_{mag,air,X}}{k_{\vec{B},air,0.0mm}}$ which correct the indication of the alanine dosimeter for a possible effect of the surrounding air gaps for an air gap of size X and 0.0 mm, respectively, in the presence of a magnetic field. This possible effect is in addition to the effect that the air gaps would have in the absence of a magnetic field. (Coverage factor $k = 1$, $X = (0.0, 0.1, 0.2, 0.5, 1.0)$ mm).

This correction factor k_{mag} was determined to be

$$k_{mag} = 0.9971 \pm 0.0033 \tag{4.1}$$

The product of correction factors $(K_Q \cdot k_{mag})$ was determined in addition in order to provide it for application.[1] It was found to be

$$(K_Q \cdot k_{mag}) = 1.0011 \pm 0.0024 \tag{4.2}$$

Both values, Equation 4.1 and 4.2, are obtained as mean values from five alanine detectors. The single values are presented in Chapter C in the appendix. A discussion of the results is provided in Section 5.1.2.

4.1.3 Characterisation in magnetic fields up to 1.4 T for 6 MV photons

The aim of this experiment was to determine the magnetic field correction factors k_{mag} for the alanine dosimeter for magnetic fields with flux densities of (0.3, 0.6, 0.9, 1.2, 1.4) T in irradiations with a photon beam with a nominal accelerating potential of 6 MV. These results allow e.g. for conclusions regarding the magnetic field correction factor k_{mag} required for dose determinations with the alanine dosimeter at the ViewRay MRIdian™ MR Linac device, which features a magnetic flux density of 0.35 T and a photon beam with a nominal accelerating potential of 6 MV.

The obtained correction factors k_{mag} are shown in Table 4.2 and Figure 4.2. The ordinate in this graph shows the correction factors k_{mag} while the abscissa shows the flux density of the static magnetic field in Tesla.

The correction factors k_{mag} are calculated from correction factors k^*_{mag} obtained directly from the experiment and $c_{\vec{B}}$ factors obtained from MC simulations in the geometry of the experiment. The applied values of the correction factors k^*_{mag} and the applied values of the $c_{\vec{B}}$ factors are presented in Chapter D in the appendix.

4.1.4 Energy dependence in magnetic fields up to 1.4 T

The aim of this experiment was to investigate the energy dependence of the magnetic field correction factors k_{mag}. To this end, the magnetic field correction factors k_{mag} were determined for magnetic fields with flux densities of (0.7, 1.4) T in irradiations with photon beams with nominal accelerating potentials of 10 MV and 15 MV – in

[1] The radiation quality correction factor K_Q has to be applied anyway for practical purposes. The product of correction factors $(K_Q \cdot k_{mag})$ could be determined directly from the experiment with the advantage of a smaller associated uncertainty, while the determination of the pure magnetic field correction factor k_{mag} requires an assumption about the radiation quality correction factor K_Q which is increasing the associated uncertainty, see Section 5.1.2.

Table 4.2: Obtained values for the correction factors k_{mag} (6 MV). This correction factor converts the standard indication of the alanine dosimeter irradiated in the presence of a static magnetic field into the actual absorbed dose-to-water at the point of measurement in the presence of this magnetic field. (Coverage factor $k = 1$, the uncertainties given are absolute uncertainties.)

Magnetic flux density	k_{mag}
0 T	1 ± 0
0.3 T	0.9993 ± 0.0016
0.6 T	0.9994 ± 0.0016
0.9 T	1.0017 ± 0.0016
1.2 T	0.9995 ± 0.0016
1.4 T	1.0058 ± 0.0016

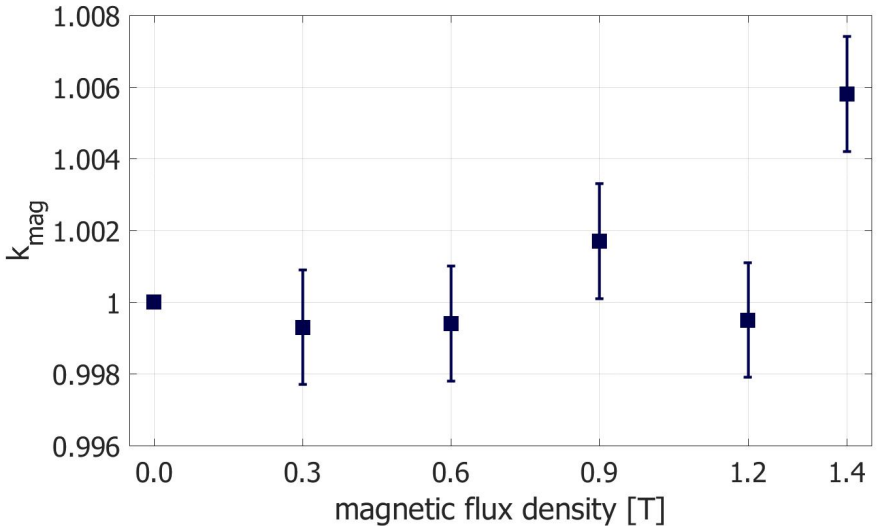

Figure 4.2: Obtained values for the correction factors k_{mag} (6 MV). This correction factor converts the standard indication of the alanine dosimeter irradiated in the presence of a static magnetic field into the actual absorbed dose-to-water at the point of measurement in the presence of this magnetic field. (Coverage factor $k = 1$, the uncertainties given are absolute uncertainties.)

addition to (0.3, 0.6, 0.9, 1.2, 1.4) T with 6 MV as presented in the previous Section 4.1.3.

The obtained correction factors k_{mag} for 10 MV and 15 MV are shown in Table 4.3 and Figure 4.3. Figure 4.4 shows the correction factors k_{mag} obtained with 6 MV (see Section 4.1.3), 10 MV, and 15 MV photon beams and at the Elekta Unity™ MR Linac device (see Section 4.1.2) in comparison. The ordinates in these graphs show the respective correction factors k_{mag}, while the abscissae show the flux density of the static magnetic field in Tesla. No measurable energy dependence of the correction factors k_{mag} could be observed between 6 MV and 15 MV. This is further clarified by the presentation of the results in Figure 4.5, which shows the direct comparisons for magnetic flux densities of 1.4 T and 0.7 T.[2] The ordinates in these graphs show the correction factors k_{mag} while the abscissae show the $TPR_{20,10}$. A detailed discussion of these data will be given in Section 5.1.4.

As mentioned in the previous Section 4.1.3, the correction factors k_{mag} are calculated from correction factors k^*_{mag} obtained directly from the experiment and $c_{\vec{B}}$ factors obtained from MC simulations in the geometry of the experiment. The values of the correction factors k^*_{mag} and the values of the $c_{\vec{B}}$ factors applied for the calculation

[2] No data point with 0.7 T is available for 6 MV photon beams. Thus, the comparison with the data points with the closest available flux densities of 0.6 T and 0.9 T is shown.

Table 4.3: Obtained values for the correction factors k_{mag} (10 MV and 15 MV). This correction factor converts the standard indication of the alanine dosimeter irradiated in the presence of a static magnetic field into the actual absorbed dose-to-water at the point of measurement in the presence of this magnetic field. (Coverage factor $k = 1$, the uncertainties given are absolute uncertainties.)

Magnetic flux density	k_{mag} for 10 MV	k_{mag} for 15 MV
0 T	1 ± 0	1 ± 0
0.7 T	1.0046 ± 0.0015	1.0056 ± 0.0027
1.4 T	1.0073 ± 0.0015	1.0050 ± 0.0027

of the correction factors k_{mag} for 10 MV and 15 MV are presented in Chapter E in the appendix.
The results for the additional irradiation run with varied field size are shown in Section E.4 in the appendix.

4.2 Characterisation of the alanine dosimeter in MRI

4.2.1 Effect of MRI on irradiated alanine detectors

The aim of this experiment was to investigate the impact of MRI on the indication of already irradiated alanine detectors, which is a relevant issue with respect to the usage of the alanine dosimeter for end-to-end tests in MRgRT. To this end, the correction factor $k_{subsMRI}$ correcting for the subsequent exposure of irradiated alanine detectors to MRI was determined for twelve different MRI conditions.

The correction factors $k_{subsMRI}$ obtained for these conditions with varying impact of the RF system and the gradient system (the static magnetic main field was the same in all situations, see Section 3.2.1) are shown in Table 4.4 and Figure 4.6. The results are discussed in Section 5.2.1.

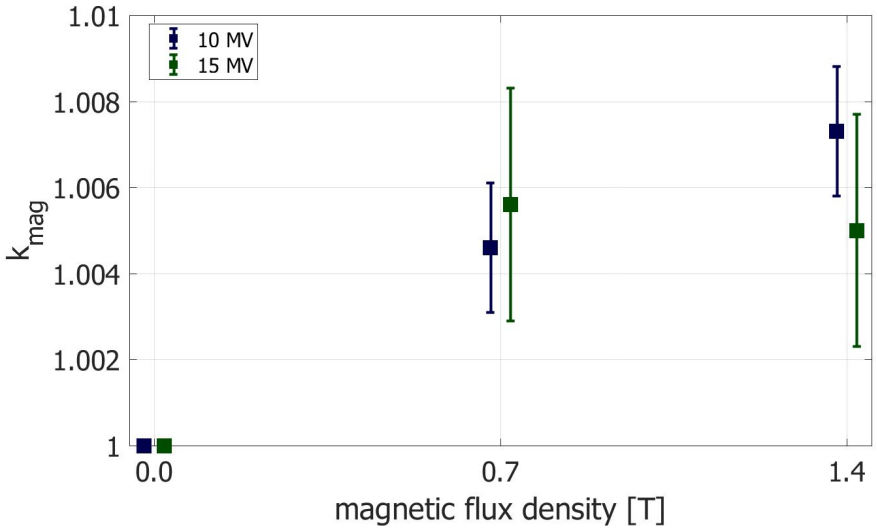

Figure 4.3: Obtained values for the correction factors k_{mag} for 10 MV (blue) and 15 MV (green). This correction factor converts the standard indication of the alanine dosimeter irradiated in the presence of a static magnetic field into the actual absorbed dose-to-water at the point of measurement in the presence of this magnetic field. (Coverage factor $k = 1$, the uncertainties given are absolute uncertainties.)

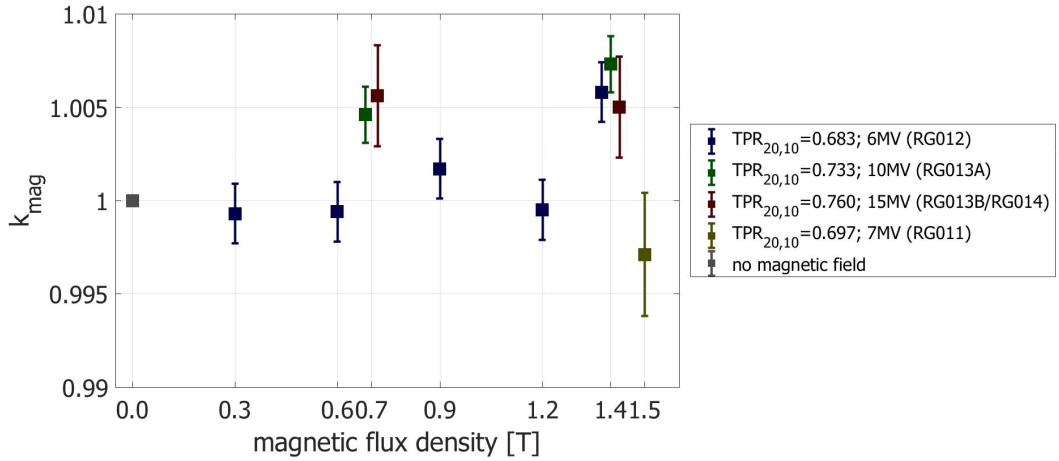

Figure 4.4: Correction factors k_{mag} obtained in the investigations with 6 MV photon beams (blue), 10 MV photons (green), 15 MV photon beams (red), and in the investigation at the Elekta Unity™ MR Linac with 7 MV photon beams (yellow). The situation without magnetic field and, thus, k_{mag} being unity is marked in grey. Please note that the values for k_{mag} at 0.7 T and 1.4 T are plotted in a straightened way in order to improve the distinguishability; nevertheless, they refer to the same magnetic flux density each time. (Coverage factor $k = 1$, the uncertainties given are absolute uncertainties.)

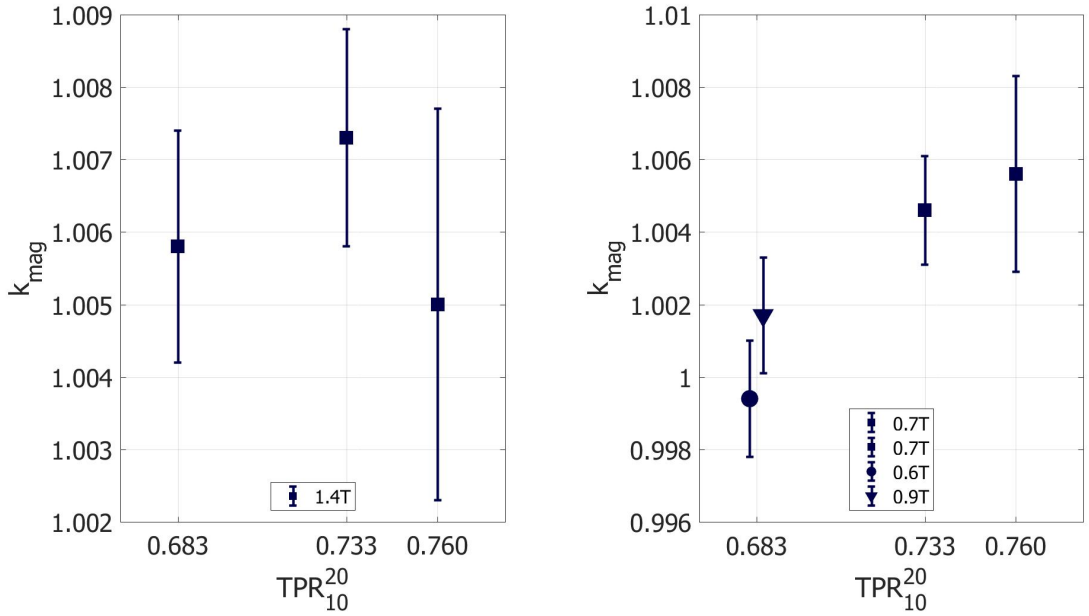

(a) (b)

Figure 4.5: Correction factors k_{mag} obtained with 6 MV photon beams ($TPR_{20,10}$=0.683), 10 MV photon beams ($TPR_{20,10}$=0.733), and 15 MV photon beams ($TPR_{20,10}$=0.760) in comparison. (a) shows the direct comparison for magnetic flux densities of 1.4 T and (b) shows the direct comparison for 0.7 T. Please note, that no data point with 0.7 T is available for 6 MV photon beams. Thus, the comparison with the data points with the closest available flux densities of 0.6 T and 0.9 T is shown. These values are plotted in a straightened way in order to improve the distinguishability; nevertheless, they refer to the same TPR.

Table 4.4: Experimentally obtained values for the correction factor $k_{subsMRI}$ correcting the indication of the alanine dosimeter in the case of the exposure to an MRI system subsequent to irradiation. (Coverage factor $k = 1$.)

Condition	short explanation	$k_{subsMRI}$
A_1	no MRI exposure	0.9998 ± 0.0017
A_2	no MRI exposure	1.0001 ± 0.0017
B_a	main field, max RF, min Grad	0.9992 ± 0.0017
B_b	main field, max RF, mid Grad	0.9997 ± 0.0017
B_c	main field, max RF, max Grad	0.9998 ± 0.0017
C_a	main field, min RF, min Grad	1.0003 ± 0.0017
C_b	main field, min RF, mid Grad	0.9995 ± 0.0017
C_c	main field, min RF, max Grad	0.9978 ± 0.0017
D_a	main field, cine, min Grad	0.9992 ± 0.0017
D_b	main field, cine, mid Grad	0.9986 ± 0.0017
D_c	main field, cine, max Grad	1.0009 ± 0.0017
E	main field, all, high Grad	0.9998 ± 0.0017

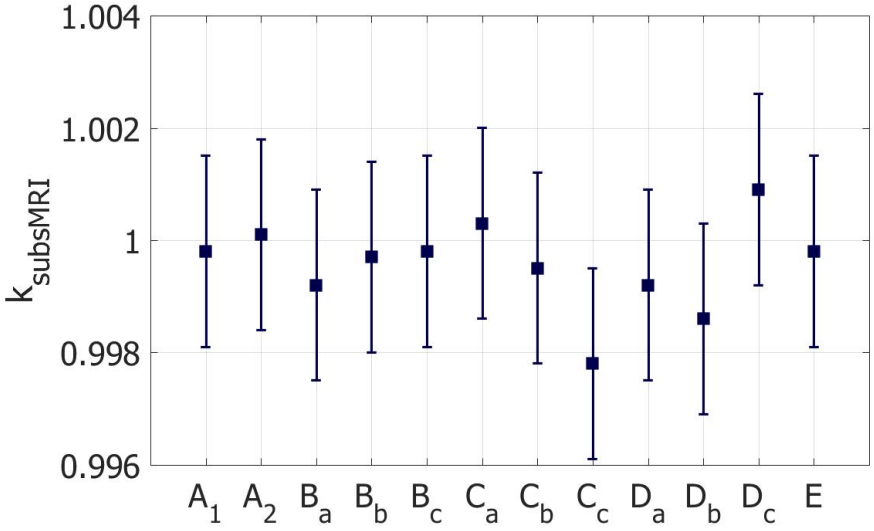

Figure 4.6: Experimentally obtained values for the correction factor $k_{subsMRI}$ correcting the indication of the alanine dosimeter in the case of the exposure to an MRI system subsequent to irradiation. For explanations of the Conditions A_1 to E, please see Section 3.2.1 and Table 4.4. (Coverage factor $k = 1$.)

4.2.2 Effect of MRI during irradiation

The aim of this experiment was to investigate the impact of MRI during the irradiation with a 7 MV photon beam on the indication of the alanine dosimeter. This possible impact is – together with the impact of a subsequent exposure to MRI, see Section 4.2.1 – an important issue for the application of the alanine dosimeter for end-to-end tests in MRgRT.
The impact of an MRI exposure during the irradiation is considered by the correction factor k_{RF}, which was determined to

$$k_{RF} = 0.9999 \pm 0.0019 \tag{4.3}$$

in this experiment. This result is discussed in Section 5.2.2.

4.3 Summary of the results of this thesis

Table 4.5 shows an overview of the results presented in this chapter. They are discussed in Section 5.3.

Table 4.5: Overview of the results. The upper part of the table refers to the characterisation of the alanine dosimeter in static magnetic fields, the lower part refers to the characterisation of the alanine dosimeter in MRI. The absolute uncertainties are given with a coverage factor of $k = 1$.

Aspect under investigation	Measurable effect	Correction factor for application
Sub-millimetre air gaps	no	$k_{mag,air} = 1 \pm 0$
Static magnetic field during irradiation at the Elekta Unity™ MR Linac	no	$(K_Q \cdot k_{mag}) = 1.0011 \pm 0.0024$
Static magnetic field during irradiation at the Viewray MRIdian™ MR Linac	no	$k_{mag} = 1.0000 \pm 0.0016$
Energy dependence of the static magnetic field effect up to 15 MV	no	$k_{energy} = 1 \pm 0$
Subsequent MRI	no	$k_{subsMRI} = 1 \pm 0$
Concurring MRI	no	$k_{RF} = 0.9999 \pm 0.0019$

5 Discussion

5.1 Characterisation of the alanine dosimeter in static magnetic fields

5.1.1 Preparatory experiment regarding sub-millimetre air gaps

This preparatory experiment aimed at the investigation of the effect that sub-millimetre air gaps around the alanine detector have on the indication of the alanine dosimeter for irradiations in the presence of a static magnetic field. In the experiment, five alanine detectors were irradiated in the absence of a magnetic field in a photon beam with a nominal accelerating potential of 6 MV. These alanine detectors were located in a water phantom for the irradiations within PMMA holders. These PMMA holders provided air gap sizes of (0.0, 0.1, 0.2, 0.5, 1.0) mm around the alanine detectors. Another five alanine detectors were irradiated in the same setup in the same holders in the presence of a magnetic field with flux density 1 T. The magnetic field was generated by an electromagnet positioned in front of the linac used for the irradiation. The water phantom was placed between the pole shoes of the electromagnet for both irradiation series, see Section 3.1.1. The analysis of this preparatory experiment was splitted into two parts.
The first part (see Chapter A in the appendix) investigated the effect that sub-millimetre air gaps around the alanine detector have on the indication of the alanine dosimeter for irradiations in the absence of a magnetic field and, thus, used the data of the five alanine detectors irradiated in the absence of a magnetic field only. The results of this part of the analysis are shown in Section A.2. The ratio of correction factors for the effect of an air gap with size X around the alanine detector and for the effect of an air gap with 0.0 mm size in the absence of a magnetic field, $\frac{k_{air,X}}{k_{air,0.0mm}}$, was determined five times for $X = (0.0, 0.1, 0.2, 0.5, 1.0)$ mm. All values obtained agree well with unity within the standard uncertainty (coverage factor $k = 1$) as Figure A.1 shows. Furthermore, no trend is recognisable in the data. The optical impression can, however, be misleading since the human brain is not able to "spontaneously deal correctly with confidence margins" [Dose, 2002]. A test based on Bayesian principles whether it is more likely for the data to represent a constant or a linear model (based on Equation (207) from [Dose, 2002]) revealed that the probablity P_{const} for the constant model is 159-times higher than the probability P_{lin} for the linear model:

$$\frac{P_{lin}}{P_{const}} = 0.0063 \tag{5.1}$$

$k_{air,0.0mm}$ is constant throughout the series (and can be best assumed to equal unity). The results, thus, indicate that air gaps up to 1 mm around the alanine detector have no measurable effect on the indication of the alanine dosimeter in the absence of a magnetic field.
The second part of the analysis (see Section 3.1.1) used the data of all ten alanine test detectors from both the irradiation series in the absence and in the presence of the magnetic field. This second part of the analysis was conducted relative to the value of the test detector surrounded by the air gap with 0.0 mm size as it was done in the first part of the analysis. Different from the approach in the first part of the analysis, the second part analysis was also conducted relative to the values of the test detectors irradiated in the absence of a magnetic field in order to determine the ratio $\frac{k_{mag,air,X}}{k_{mag,air,0.0mm}}$ of correction factors for the effect of an interdependency of magnetic field and air gap for an air gap with size X around the alanine detector and for an air gap with 0.0 mm size. This effect due to the interdependency occurs in addition to the effect addressed by the correction factor $k_{air,X/0.0mm}$, which occurs in the absence and in the presence of a magnetic field alike, and which cancels out in the model equation for the second part of the analysis (see Section 3.1.1). The ratio $\frac{k_{mag,air,X}}{k_{mag,air,0.0mm}}$ was determined five times for $X = (0.0, 0.1, 0.2, 0.5, 1.0)$ mm; the results are shown in Section 4.1.1. As Figure 4.1 shows, all values up to inclusively a surrounding air gap of 0.5 mm size agree well with unity within the standard uncertainty (coverage factor $k = 1$). The value for a surrounding air gap with 1.0 mm size does scarcely not agree with unity within the standard uncertainty ($k = 1$). The optical impression of the data tends to be a down-trend, which can, however, be misleading, as mentioned above. As for the results from the first part of the analysis, the test desribed by [Dose, 2002] was applied to the data. It revealed that the probablity P_{const} for the constant model is 61-times higher than the probability P_{lin} for the linear model[1]:

$$\frac{P_{lin}}{P_{const}} = 0.0164 \tag{5.2}$$

$k_{mag,air,0.0mm}$ is constant throughout the series (and can be best assumed to equal unity) and – according to the conducted test – the data indicates no trend for increasing air gap sizes. The data, thus, disallows to verify an effect of sub-millimetre air gaps around alanine detectors on the response of the alanine dosimeter in the presence of a magnetic field[2]. The results of the two analysis parts of this preparatory experiment rather indicate that air gaps up to 1 mm around the alanine detector have no measurable effect on the indication of the alanine dosimeter in the presence of a magnetic field. It can certainly be concluded, that air gaps below 0.05 mm, as they occur in practice for the alanine system at the PTB, have a negligible effect in the presence of magnetic fields and are, hence, nothing to worry about in the

[1] The standard uncertainty with a coverage factor $k = 1$ stands for a probability of about one third that the true value can be found outside of the error bars.

[2] A trend in the data is, however, more probable than for the data in the absence of a magnetic field obtained from the first part of the analysis.

succeeding experiments of this thesis.[3]
Prior to the conduction of the experiment, there was no publication available addressing the effect of sub-millimetre air gaps around alanine detectors on the indication of the alanine dosimeter for irradiations in the presence of magnetic fields. The expectation towards the results of this experiment were, hence, formed based on the consideration of studies on air gaps around ICs, see Section 2.4.2, and the reflection of aspects of alanine dosimetry that differ from the situation in the dosimetry with ICs. The most salient difference between alanine detectors and ICs with respect to the effect of sub-millimetre air gaps in the presence of static magnetic fields is the different density of the detector material: The sensitive volume of ICs is filled with air[4], while the density of the alanine pellets which compose the alanine detectors is comparable to the density of water. Air filled ICs are, correspondingly, "electron detectors", which means that the electrons causing the measured absorbed dose originate mainly from the phantom material. Alanine dosimeters in constrast are "photon detectors" for irradiations with photon beams with nominal accelerating potentials below 10 to 15 MV[5], which means that the electrons causing the measured absorbed dose originate mainly from the detector material itself. Another probably relevant aspect is the radial distribution of the sensitivity in the resonator of the EPR spectrometer used for the readout of the irradiated alanine pellets. The detection sensitivity for radicals created in the alanine pellet due to ionising radiation decreases parabolically with increasing distance from the pellet center, see Section 2.4.3. Considering the findings of [O'Brien and Sawakuchi, 2017] (see Section 2.4.2) with these aspects of alanine dosimetry in mind leads to the expectation that air gaps around alanine detectors should have smaller effects on the indication of the alanine dosimeter in the presence of static magnetic fields than it is the case for ICs. Since small air gaps are inevitable in alanine dosimetry due to the non-waterproofness of alanine, it is, however, advisable to investigate this issue in detail, which was accomplished with the presented experiment. The obtained results are in conformity with the expectations presented above. The alanine dosimeter might be insensitive to surrounding sub-millimetre air gaps due to its density allowing for electrons originating from the detector material itself, and due to the detection sensitivity in the EPR spectrometer which is parabolically decreasing with increasing distance from the alanine pellet center.
A possible improvement for the present experiment is a change in the order of the irradiations. In the presented experiment, the order of air gap sizes surrounding the alanine test detectors for both the series in the absence and in the presence of the magnetic field was (0.0, 0.1, 0.2, 0.5, 1.0) mm. It would have been preferable to apply a "back and forth" order, e.g. (0.0, 1.0, 0.1, 0.5, 0.2) mm in order to rule out

[3] At this, it is assumed that the conclusions obtained from this experiment performed for a magnetic field with flux density 1 T are transferable to the range of magnetic flux densities common in MRgRT (0.35 T to 1.5 T).
[4] There are also liquid filled ICs. Air filled ICs are, however, the most common type.
[5] It was found, that the alanine dosimeter changes into an "electron detector" in this transient area [Anton et al., 2013].

that a drift over the day, e.g. in terms of the output of the linac or the temperature, affects the data. Such influences are, however, addressed by correction factors and included within the uncertainty budget. The presented results can, thus, be considered trustworth also for the applied order of increasing air gap sizes.
After the conduction of the experiment, [Billas et al., 2020] published their results of an investigation of air gaps around alanine detectors. In [Billas et al., 2020], the impact of air gaps on the alanine detector in the presence of static magnetic fields was investigated by means of MC simulations. It was concluded that uncertainties of up to up to 0.52 % and 0.47 % for 6 MV and 8 MV, respectively, have to be considered for a magnetic flux density of 1.5 T [Billas et al., 2020]. At this, it has to be noted, that the geometry of the alanine pellets and holders and the EPR spectrometer used at the NPL in [Billas et al., 2020] differ from the alanine dosimetry system of the PTB which was applied in this work. A profound study combining experiments and MC simulations with both alanine dosimetry systems would be required for a substantial comparison of the results in [Billas et al., 2020] with the results in this work.
In this experiment, the ratios of correction factors $\frac{k_{air,X}}{k_{air,0.0mm}}$ (first part of the analysis, see Chapter A in the appendix) and $\frac{k_{mag,air,X}}{k_{mag,air,0.0mm}}$ (second part of the analysis, see Section 3.1.1) were determined. The correction factors addressed in the first part correct for the effect of sub-millimetre air gaps around alanine detectors on the indication of the alanine dosimeter for irradiations in the absence of a magnetic field; these correction factors correct for the effect due to changes in the dose distribution by replacement of water with air. The correction factors addressed in the second part of the analysis correct for the effect of the interdependence of a magnetic field and sub-millimetre air gaps around alanine detectors, which is based on the radiation transport at intersections of materials with different densities in magnetic fields. This interdependence occurs in the presence of a magnetic field in addition to the effect corrected by $k_{air,X/0.0mm}$ which affects the indication in the absence and presence of a magnetic field alike. In the analyses performed ratios were determined relative to the values for the alanine detectors surrounded by an air gap with 0.0 mm size, which remains constant in each series. Trends in the data within one series would, thus, indicate an impact of surrounding air gaps varying with different sizes. No such trend was found for the presented data in neither analysis. For the first part investigating the situation in the absence of a magnetic field, a constant model is 159-times more likely than a linear model. For the second part investigating the situation in the presence of a magnetic field, a constant model is 61-times more likely than a linear model. An effect of sub-millimetre air gaps around alanine detectors on the indication of the alanine dosimeter is, thus, not verified by this experiment, neither for irradiations in the absence nor in the presence of a magnetic field. It can be concluded, that air gaps occuring in the practice of alanine dosimetry (below 0.05 mm) have a negligible effect on the indication of the alanine dosimeter – in the absence of a magnetic field and in the presence of a magnetic field with a flux density common in MRgRT.

5.1.2 Characterisation at the Elekta Unity™ MR Linac device

This experiment aimed at the determination of the correction factor k_{mag} at the Elekta Unity™ MR Linac device (1.5 T, 7 MV). The correction factor k_{mag} converts the standard indication of the alanine dosimeter which equals the absorbed dose-to-water in the absence of a magnetic field into the absorbed dose-to-water in the presence of the static magnetic field. Alanine detectors were irradiated at the Elekta Unity™ MR Linac at the Christie hospital in Manchester, UK and their indications were set into relation to the absorbed doses-to-water determined with Farmer-type IC transfer standards which were calibrated directly in the magnetic field of the Elekta Unity™ MR Linac. The analysis was performed in two different ways. On the one hand, the correction factor k_{mag} itself was determined. This analysis is based on an assumption about the radiation quality correction factor K_Q for the alanine dosimeter, see Section 3.1.2. In the practical application, both the correction factor k_{mag} and the correction factor K_Q have to be applied, see Equation 2.30 and e.g. Equation 3.9. Since the product $(K_Q \cdot k_{mag})$ is experimentally available without any assumption about the radiation quality correction factor K_Q which implies a smaller associated uncertainty, the product of correction factors $(K_Q \cdot k_{mag})$ was determined on the other hand in order to provide it for application. The determination of the mere correction factor k_{mag} is, however, important for the comparison with the results from literature (see below) and with the results from the other experiments within this thesis (see Sections 5.1.3 and 5.1.4).
The correction factor k_{mag} was determined to $k_{mag} = 0.9971 \pm 0.0033$ in this experiment, see Section 4.1.2, which equals unity within the standard uncertainty ($k = 1$). It can, hence, be concluded that the alanine dosimeter is not measurably affected in the setup of this experiment with a magnetic field with a flux density of 1.5 T and a radiation quality with $\mathrm{TPR}_{20,10} = 0.697 \pm 0.003$.
As mentioned above, the correction factor k_{mag} converts the standard indication of the alanine dosimeter into the actual absorbed dose-to-water at the measurement point in the presence of a static magnetic field. The correction factor k_{mag} contains only the possible change in the response of the alanine dosimeter. The change in the dose distribution due to the magnetic field is not included since the actual absorbed dose-to-water at the point of measurement is accessible by the Farmer-type IC transfer standards directly calibrated in the magnetic field. It is, however, not to be assumed that a possible change in the response of the alanine dosimeter is caused by a change in the process of the radical formation in the presence of a static magnetic field. I am not aware of any mechanism by which this would be possible. Instead, it is to be assumed that possible changes in the response of the alanine dosimeter in the presence of a static magnetic field are caused by changes in the trajectories of the secondary electrons in the alanine pellets and in the immediate surrounding of the alanine pellets. E.g. the secondary electron trajectories in the presence of magnetic fields could run to a greater or lesser extent through areas of the alanine pellets for which the EPR spectrometer shows a reduced sensitivity than in the absence of a magnetic field. The sensitivity of the EPR spectrometer decreases parabolically

with increasing distance from the pellet center in horizontal and vertical direction, see Section 2.4.3. The obtained correction factor $k_{mag} = 0.9971 \pm 0.0033$, see Section 4.1.2, implies that the standard indication of the alanine dosimeter has to be revised downwards in the presence of a magnetic field with 1.5 T flux density for irradiations with photons with a nominal accelerating potential of 7 MV, i.e. the standard indication is too high to be equivalent to the actual absorbed dose-to-water at the point of measurement in the presence of the magnetic field. The reason for this highered standard indication could be that the secondary electron trajectories run increasingly through the inner areas of the alanine pellet for which the EPR spectrometer features a higher sensitivity than for the outer areas.[6]
The immediate surrounding relevant for these changes, i.e. the PMMA holder and water, can be easily reproduced in other setups. The obtained results for the correction factor k_{mag} and the product of correction factors ($K_Q \cdot k_{mag}$) are, thus, not only valid for the setup applied in this experiment, but whenever an alanine detector consisting of alanine pellets with identical nature and arrangement as here within a PMMA holder identical to the holder applied here is irradiated in water in the presence of a magnetic field with flux density 1.5 T using a photon beam with $\mathrm{TPR}_{20,10} = 0.697 \pm 0.003$ (see Section 3.1.2).
A possible repetition of this experiment should be performed with a modified PMMA holder or another fixation system allowing for identical positioning of the alanine detectors and the transfer standards. In this way, no correction factor k_{depth}, see Section 3.1.2, would be required reducing the overall uncertainty associated with the obtained correction factor k_{mag}.
A comparison of the correction factor k_{mag} obtained in the present investigation with results from literature reveals the following: [Billas et al., 2021] found a correction factor $k^{al}_{Q_B,Q} = 0.9957 \pm 0.0059$ (corresponding to the notation k_{mag} in the present report) for Elekta Unity™ machines (Table 2 in [Billas et al., 2021]). The correction factor k_{mag} obtained in the present investigation agrees with this value within the standard uncertainties ($k = 1$). Furthermore, [Billas et al., 2020] found values of $k_{Q_B,Q} = 0.9964 \pm 0.0060$ for the irradiation of alanine detectors with a photon beam with a nominal accelerating potential of 6 MV[7] in the presence of a static magnetic field with 1.5 T flux density and $k_{Q_B,Q} = 0.9938 \pm 0.0055$ for the irradiation of alanine detectors with a photon beam with a nominal accelerating potential of 8 MV again in the presence of a static magnetic field with 1.5 T flux density (Table 1 in [Billas et al., 2020]). Please note, that the measurements for obtaining these correction factors have not been performed at the Elekta Unity™ MR Linac but in a setup with an electromagnet and a conventional linac. The correction factor k_{mag} obtained in the present investigation agrees with these values within the standard uncertainties ($k = 1$). There is also a publication by [Pojtinger et al., 2020] mentioning a correction factor $k_{al,\vec{B},Q} = 0.9989(28)$ (Sec. 3.3 in [Pojtinger et al., 2020]) based

[6] This aspect could be addressed by future work investigating the trajectories by detailed MC simulations, see Chapter 6.

[7] Unfortunately, I cannot find any information on $\mathrm{TPR}_{20,10}$ values in [Billas et al., 2020].

on measurements at the Elekta Unity™ machine in Blonay, Switzerland (Hôpital Riviera-Chablois, see Sec. 2.5 in [Pojtinger et al., 2020]). The correction factor k_{mag} obtained in the present investigation agrees with this value within the standard uncertainties ($k = 1$).
From the present experiment at the Elekta Unity™ MR Linac, it can be concluded that the alanine dosimeter is not measurably affected by a magnetic field with a flux density of 1.5 T at radiation qualities close to $\mathrm{TPR}_{20,10} = 0.697 \pm 0.003$ with microsurroundings as in the present setup (i.e. alanine pellets, PMMA holder, water). The standard indication of the alanine dosimeter for 1.5 T and $\mathrm{TPR}_{20,10} = 0.697 \pm 0.003$ has to be corrected downwards by (0.29 ± 0.33) % in order to equal the actual absorbed dose-to-water in the magnetic field. This agrees with unity within the standard uncertainty (coverage factor $k = 1$). The present experiment does not allow for direct conclusions regarding irradiations at the Viewray MRIdian™ MR Linac device since both radiation quality and magnetic flux density differ. For irradiations at the Elekta Unity™ MR Linac, this experiment allows for the conclusion that the experimentally determined product of correction factors $(K_Q \cdot k_{mag}) = 1.0011 \pm 0.0024$ should be used for converting the standard indication of the alanine dosimeter (without correction for the radiation quality K_Q) into the actual absorbed dose-to-water at the point of measurement in the 1.5 T magnetic field. As mentioned above, this product of correction factors features the advantage to be determined by pure experiment without assumptions about the radiation quality correction factor K_Q, resulting in the smallest possible associated uncertainty.

5.1.3 Characterisation in magnetic fields up to 1.4 T for 6 MV photons

As in the previously described experiment, see Section 5.1.2, the aim of the present experiment was to determine the correction factor k_{mag}. In the previously described experiment conducted at an Elekta Unity™ MR Linac, the correction factor k_{mag} required for measurements at that device (1.5 T, 7 MV) was determined. In the present investigation conducted at the conventional linac at the PTB with an electromagnet positioned in front of the accelerator head, the correction factor k_{mag} was, however, determined for the series of magnetic flux densities (0.3, 0.6, 0.9, 1.2, 1.4) T with a nominal accelerating potential of 6 MV. While the previous experiment aimed at a correction factor k_{mag} for direct application, the series of correction factors k_{mag} obtained from this experiment allows for both more information about the behaviour of the correction factor k_{mag} with increasing magnetic flux density and information about the correction factor k_{mag} required for the application at theViewRay MRIdian™ MR Linac device (0.35 T, 6 MV).
Alanine detectors were irradiated in the presence of magnetic flux densities of (0, 0, 0.3, 0.6, 0.9, 1.2, 1.4) T, a procedure which was performed in total three times. Correction factors k^*_{mag} which convert the standard indication of the alanine dosime-

ter into the hypothetic absorbed dose-to-water at the point of measurement in the absence of a magnetic field were determined from the resulting experimental data. These correction factors k^*_{mag} incorporate the field effect, i.e. the change of the dose distribution at the point of measurement due to the magnetic field, and a possible change in the response of the alanine dosimeter due to the magnetic field. As these correction factors k^*_{mag} include the field effect which depends on the respective geometry of the setup, the obtained results for the correction factors k^*_{mag} are only valid for the setup applied in this experiment.
$c_{\vec{B}}$ factors for magnetic flux densities of (0.3, 0.6, 0.9, 1.2, 1.4) T were determined for the applied setup from simulated ddcs at magnetic flux densities of (0, 0.3, 0.6, 0.9, 1.2, 1.4) T. The $c_{\vec{B}}$ factors convert the absorbed dose-to-water in the absence of a magnetic field into the absorbed dose-to-water in the presence of a magnetic field at the same point of interest. They, thus, contain information about the dose distribution in the presence of the static magnetic field in the applied setup.
The correction factors k_{mag} for magnetic flux densities of (0.3, 0.6, 0.9, 1.2, 1.4) T in the applied setup were determined by multiplying the respective $c_{\vec{B}}$ factors and correction factors k^*_{mag}, see Section 3.1.3. The correction factors k_{mag} convert the standard indication of the alanine dosimeter into the actual absorbed dose-to-water at the point of measurement in the presence of a magnetic field. They do not consider a field effect, since the actual absorbed dose-to-water at the point of measurement in the presence of a magnetic field is accessible via the $c_{\vec{B}}$ factors.[8] They contain only the possible change in the response of the alanine dosimeter.
The resulting correction factors k_{mag} were shown in Section 4.1.3 in Table 4.2 and Figure 4.2. The correction factors k_{mag} for 0.3 T, 0.6 T, and 1.2 T equal unity within the standard uncertainty (coverage factor $k = 1$). The correction factor k_{mag} for 0.9 T equals unity within the expanded uncertainty with coverage factor $k = 2$. The correction factor k_{mag} for 1.4 T is scarcely not equal to unity within the expanded uncertainty with coverage factor $k = 3$ and equals unity within the expanded uncertainty with coverage factor $k = 4$.
The obtained correction factors k_{mag} (Table 4.2 and Figure 4.2) do not significantly differ from unity for magnetic flux densities of (0.3, 0.6, 0.9, 1.2) T and these values do not show any trend, see Section D.3. This allows to draw conclusions about the correction factor k_{mag} required for a magnetic flux density of 0.35 T as it is present at the ViewRay MRIdian™ MR Linac device. It can be assumed that – using alanine detectors identical to the alanine detectors applied here in terms of nature and arrangement of the alanine pellets in a micro-surrounding (i.e. PMMA holder and water) as in the present experiment – the standard indication of the alanine dosimeter corresponds to the actual absorbed dose-to-water at the point of measurement also in a magnetic field with 0.35 T flux density. This implies that no magnetic field correction factor is required for dose determinations with the alanine dosimeter at the ViewRay MRIdian™ MR Linac device; it is sufficient to consider an uncertainty component of 0.16 % corresponding to the uncertainty associated with the obtained

[8] (The $c_{\vec{B}}$ factor in the product "removes" the field effect.)

correction factors k_{mag}, see Table 4.2. It has, however, to be noted, that the radiation quality applied in the present investigation is not the same as it is applied at the ViewRay MRIdian™ MR Linac device. But as the following experiment shows, see Section 5.1.4, no energy dependence of the correction factors k_{mag} was measurable. The results obtained for a radiation quality $TPR_{20,10} = 0.683$ can, hence, also be seen valid for the radiation quality with $TPR_{20,10} = 0.648$ at the ViewRay MRIdian™ MR Linac device.
The question can be raised whether the measured effect at a magnetic flux density of 1.4 T results from experimental difficulties as the experimental realisation at 1.4 T is the most vulnerable in the present setup. The output of the linac was found to fluctuate after changing the magnetic flux density since the beam guidance is disturbed by the stray magnetic field of the electromagnet (see Chapter B in the appendix); this was especially observed for higher flux densities. Principally, these fluctuations are not a problem since the absorbed dose-to-water was monitored by a transmission IC. However, it cannot be excluded that effects cancel out in the large measurement volume of the transmission IC used for monitoring while this is not the case for the comparably small sensitive volume of the alanine detector. It has to be considered in addition, that the point of measurenent for the alanine detector and the transmission IC is not the same. Another aspect is, that the heat generation of the electromagnet is the strongest at 1.4 T, which is the maximum magnetic flux densitiy achievable with this electromagnet. Principally, this shouldn't be a problem either since the temperature inside the water phantom is monitored by a temperature sensor and since this irradiation temperature is used for correcting the alanine indication. Each alanine detector was placed within the water phantom ten minutes prior to the irradiation in order to assure that the temperature of the alanine pellets is the same as the temperature of the water in the phantom. It is, however, imaginable, that there was a temperature rise during the irradiation of the alanine detectors in the presence of the magnetic field with flux density 1.4 T occuring that fast, that there was a temperature gradient between the measurement point of the temperature sensor and the position of the alanine detector (see Figure 3.10). In this case, the temperature value used for the calculation of the correction factor for the irradiation temperature would have been higher than the actual irradiation temperature of the alanine pellets. However, realistic possible disagreements are covered by the uncertainties associated with the irradiation temperatures ruling out an impairment of the obtained correction factors k_{mag} by the temperature developments. Furthermore, the results from the experiment addressing the energy dependence of the correction factors k_{mag} help to rule out a temperature effect, see Section 5.1.4. Generally, "back and forth" orders for the magnetic flux densities, e.g. (0, 1.4, 0.3, 1.2, 0.6, 0.9, 0) T in the irradiation runs would have been preferable, as they allow to exclude trends in the course of the irradiation runs more clearly. Here, however, the order of increasing magnetic flux densities was the best choice due to the increasing heat generation of the electromagnet with increasing flux density. It can be concluded, that an impairment of the correction factor k_{mag} for 1.4 T due to experimental challenges is not to be expected since fluctuations of the linac and

temperature changes are considered in the applied corrections and in the uncertainty budget. This is supported by the fact that the correction factor k_{mag} obtained for the situation at the Elekta Unity™ MR Linac ($k_{mag} = 0.9971 \pm 0.0033$ for 1.5 T and 7 MV, see Section 4.1.2) where the heat development is not an issue agrees with the correction factor for 1.4 T from the present investigation ($k_{mag} = 1.0058 \pm 0.0016$, see Section 4.1.3) within the expanded uncertainties with coverage factor $k = 2$. Nevertheless, it would be of interest to further look upon the situation at 1.4 T in a future investigation, e.g. by determining the correction factor k_{mag} in the applied setup for several values between 1.2 T and 1.4 T. Currently, the behaviour between 1.2 T and 1.4 T remains unclear since no trend can be deduced from the obtained data points (see Figure 4.2).

As mentioned above, the correction factors k_{mag} contain only the possible change in the response of the alanine dosimeter. As described in Section 5.1.2, this change is assumed to be caused by changes in the trajectories of the secondary electrons in the alanine pellets and in the immediate surrounding of the alanine pellets resulting in secondary electron trajectories running to a greater or lesser extent through areas of the alanine pellets for which the EPR spectrometer shows a reduced sensitivity. The following is e.g. imaginable: The obtained correction factor k_{mag} for 1.4 T implies that the standard indication of the alanine dosimeter has to be revised upwards, i.e. the standard indication is too low to be equivalent to the actual absorbed dose-to-water at the point of measurement in the presence of the 1.4 T magnetic field. The reason for this lowered standard indication could be that the secondary electron trajectories run increasingly through the outer areas of the alanine pellet for which the EPR spectrometer features a reduced sensitivity, due to the stronger bending of these trajectories in the highest magnetic flux density under investigation in this experiment. This behaviour is, however, in contrast to the conclusion drawn in the previous experiment at the Elekta Unity™ MR Linac, where the resulting correction factor k_{mag} is smaller than unity (but equals unity within the standard uncertainty with coverage factor $k = 1$), see Section 5.1.2. Further MC simulations focussing on the trajectories of the secondary electrons in and around the alanine pellets are required in order to clarify the situation.

The immediate surrounding relevant for the changes in the trajectories of the secondary electrons, i.e. the PMMA holder and water, can be easily reproduced in other setups. The obtained results for the correction factor k_{mag} can, thus, not only be seen valid for the setup applied in this experiment, but whenever an alanine detector consisting of alanine pellets with identical nature and arrangement as here within a PMMA holder identical to the holder applied here is irradiated in water in the presence of magnetic fields with flux densities of (0.3, 0.6, 0.9, 1.2, 1.4) T using a photon beam with $\mathrm{TPR}_{20,10} = 0.683$. This applies also to photon beam radiation qualities similar to the radiation quality applied in the present experiment, since no measurable energy dependence of the correction factors k_{mag} between 6 MV and 15 MV could be found, see Section 5.1.4 below.

A comparison with results from literature can be found in the following Section 5.1.4. This comparison takes into account not only the results for the correction fac-

tors k_{mag} for 6 MV but also the results for the series at 10 MV and 15 MV (see Section 3.1.4).
In this study, the correction factors k_{mag} converting the standard indication of the alanine dosimeter into the absorbed dose-to-water at the point of measurement in the presence of a magnetic field were determined for magnetic flux densities of (0.3, 0.6, 0.9, 1.2, 1.4) T. The results reveal, that there is no significant deviation of the correction factor k_{mag} from unity for flux densities of (0.3, 0.6, 0.9, 1.2) T while an effect of approximately 0.6 % was measured in the presence of a magnetic field with flux density 1.4 T. The results of this experiment allow to draw conclusions about the magnetic field correction factor k_{mag} required for dose determinations with the alanine dosimeter at the ViewRay MRIdian™ MR Linac device, which features a magnetic flux density of 0.35 T and a photon beam with a nominal accelerating potential of 6 MV ($TPR_{20,10} = 0.648$). Since no significant deviation of the correction factor k_{mag} from unity for flux densities of (0.3, 0.6, 0.9, 1.2) T was found, no magnetic field correction factor is required for dose determinations with the alanine dosimeter at the ViewRay MRIdian™ MR Linac device; it is sufficient to consider an uncertainty component of 0.16 % since this is the uncertainty associated with the obtained correction factors k_{mag}, see Table 4.2. I.e. a correction factor $k_{mag} = 1.0000 \pm 0.0016$ should be applied for the application of the alanine dosimeter at the ViewRay MRIdian™ MR Linac device.

5.1.4 Energy dependence in magnetic fields up to 1.4 T

The aim of the present experiment was to investigate the energy dependence of the correction factors k_{mag}.[9] To that end, correction factors k_{mag} were determined for an irradiation series with a nominal accelerating potential of 10 MV and a series with 15 MV in addition to the series with 6 MV described in the previous Section 5.1.3. The procedure was identical to the procedure for 6 MV, see Section 5.1.3, with the only difference that the magnetic flux densities were (0, 0, 0.7, 1.4) T and that there were four runs in the 15 MV series.
The resulting correction factors k_{mag} for 10 MV and 15 MV were shown in Section 4.1.4 in Table 4.3 and Figure 4.3. The correction factors k_{mag} in the 10 MV series show an increase with increasing magnetic flux density. The correction factor k_{mag} for 0.7 T is scarcely not equal to unity within the expanded uncertainty with coverage factor $k = 3$ and equals unity within the expanded uncertainty with coverage factor $k = 4$. The correction factor k_{mag} for 1.4 T equals unity within the expanded uncertainty with coverage factor $k = 5$. The correction factors k_{mag} in the 15 MV series for both 0.7 T and 1.4 T are larger than unity. The correction

[9] This issue is of interest since in the absence of magnetic fields a small, non-significant drop of the relative response of the alanine dosimeter for radiation qualities with nominal accelerating potential between 8 and 15 MV can be observed [Anton et al., 2013], Table 3 and Figure 2. This can be explained by the alanine dosimeter changing from a photon detector (the secondary electrons rise within the detector) to an electron detector (the secondary electrons rise outside the detector), see Section 5.1.1.

factor k_{mag} for 0.7 T is scarcely not equal to unity within the expanded uncertainty with coverage factor $k = 2$ and equals unity within the expanded uncertainty with coverage factor $k = 3$. The correction factor k_{mag} for 1.4 T equals unity within the expanded uncertainty with coverage factor $k = 2$. The uncertainties associated with the correction factors k_{mag} in the 15 MV series are larger by approximately a factor of two compared to the correction factors k_{mag} determined in the investigations using 6 MV and 10 MV photon beams. This is due to the larger uncertainty associated with the $c_{\vec{B}}$ factor due to the lacking phase space file for 15 MV photon beams (see Section E.2 in the appendix). A test based on Bayesian principles whether it is more likely for the resulting correction factors k_{mag} in the 10 MV series to represent a constant or a linear model (based on Equation (207) from [Dose, 2002]) revealed a higher probablity for a linear model than for a constant model. The details of this test are presented in Section E.3 in the appendix. The same test applied to the the correction factors k_{mag} in the 15 MV series revealed a higher probablity for a constant model than for a linear model, see also Section E.3 in the appendix.
The correction factors k_{mag} contain only the possible change in the response of the alanine dosimeter as described in Section 5.1.2. As described there in addition, this change is assumed to be caused by changes in the trajectories of the secondary electrons in the alanine pellets and in the immediate surrounding of the alanine pellets resulting in secondary electron trajectories running to a greater or lesser extent through areas of the alanine pellets for which the EPR spectrometer shows a reduced sensitivity.
The obtained correction factors k_{mag} for 0.7 T and 1.4 T in both the 10 MV and 15 MV series imply that the standard indication of the alanine dosimeter has to be revised upwards, i.e. the standard indication is too low to be equivalent to the actual absorbed dose-to-water at the point of measurement in the presence of the magnetic fields with 0.7 T and 1.4 T flux density, respectively. The reason for this lowered standard indication could be that the secondary electron trajectories run increasingly through the outer areas of the alanine pellet for which the EPR spectrometer features a reduced sensitivity. This is in agreement with the findings in the previous investigation with 6 MV photons, see Section 5.1.3. In the 10 MV series, this effect is stronger in case of 1.4 T than in the case of 0.7 T. In the 15 MV series, this effect is comparable in the case of 0.7 T and 1.4 T; the obtained correction factors k_{mag} for both 0.7 T and 1.4 T agree with each other within the standard uncertainty ($k = 1$). This agreement within the standard uncertainty is also observed in the investigation with 10 MV photon beams (see Figure 4.3). It could be assumed that the stronger effect for 1.4 T in the 10 MV series is related to a stronger bending in the presence of a higher magnetic flux density: due to the less bent trajectories in the presence of the magnetic field with 0.7 T flux density, the trajectories are more likely to run through the central areas of the alanine pellets for which the EPR spectrometer features a higher sensitivity. Anyway, such assumptions have to be handeled with caution due to the agreement of the correction factors of one series within the standard uncertainty. As mentioned in Section 5.1.3, MC simulations focussing on the trajectories of the secondary electrons in and around the alanine pellets would be

required for clarifying the cause for the observed behaviour of the alanine dosimeter. As already pointed out in Section 5.1.3, the immediate surrounding relevant for these changes, i.e. the PMMA holder and water, can be easily reproduced in other setups. The obtained results for the correction factor k_{mag} are, thus, not only valid for the setup applied in this experiment, but whenever an alanine detector consisting of alanine pellets with identical nature and arrangement as here within a PMMA holder identical to the holder applied here is irradiated in water in the presence of magnetic fields with flux densities of 0.7 T and 1.4 T using a photon beam with $\mathrm{TPR}_{20,10} = 0.733$ (10 MV) and $\mathrm{TPR}_{20,10} = 0.760$ (15 MV), respectively. The following paragraph addresses a comparison of the correction factors k_{mag} obtained in the 6 MV, 10 MV, and 15 MV series, respectively, as well as for 7 MV at the Elekta Unity™ MR Linac. The magnetic flux densities under investigation were (0.3, 0.6, 0.9, 1.2, 1.4) T for 6 MV, (0.7, 1.4) T for 10 MV and 15 MV and 1.5 T for 7 MV. This allows for the following direct comparisons: the correction factors k_{mag} for 0.7 T obtained in the 10 MV and in the 15 MV series and the correction factors k_{mag} for 1.4 T obtained in all series (6 MV, 10 MV, and 15 MV photon beam). In both cases, there is an agreement of the obtained correction factors k_{mag} within the standard uncertainty ($k = 1$) (see Figure 4.4 and 4.5). Unfortunately, no data points are available for the 10 MV and 15 MV series at (0.3, 0.6, 0.9, 1.2) T and no data point at 0.7 T is available for the 6 MV series, further are no data points available for (6, 10, 15) MV and 1.5 T and for the experiment at the MR Linac (7 MV) no further data points than at 1.5 T. This hampers more direct comparisons. Unfortunately the amount of magnetic flux densities was reduced from (0.3, 0.6, 0.9, 1.2, 1.4) T in the investigation with 6 MV photon beams to 0.7 T and 1.4 T in the investigations with 10 MV and with 15 MV photon beams due to time constraints. But the correction factors k_{mag} for 0.7 T in the 10 MV and in the 15 MV series agree with the correction factor k_{mag} for 0.9 T in the 6 MV series within the standard uncertainty ($k = 1$) and with the correction factor k_{mag} for 0.6 T in the 6 MV series within the expanded uncertainty with coverage factor $k = 2$ (see Figure 4.4 and 4.5). And the correction factor k_{mag} for 1.5 T at 7 MV agrees with the correction factors k_{mag} for 1.4 T in the 6 MV, 10 MV, and 15 MV series, respectively, within an expanded uncertainty with coverage factor $k = 2$, $k = 3$, and $k = 2$, respectively. The available data points, thus, indicate no measurable energy dependence of the correction factors k_{mag} between 6 MV and 15 MV. The above conclusion that the results for the correction factor k_{mag} are, thus, not only valid for the setup applied in this experiment, but whenever an alanine detector consisting of alanine pellets with identical nature and arrangement as here within a PMMA holder identical to the holder applied here is irradiated in water in the presence of magnetic fields with flux densities of 0.7 T and 1.4 T can, thus, be extended to photon beams close to $\mathrm{TPR}_{20,10} = 0.733$ and $\mathrm{TPR}_{20,10} = 0.760$, respectively: Close to $\mathrm{TPR}_{20,10} = 0.733$, the response of the alanine dosimeter is measurably affected by magnetic flux densities of 0.7 T and 1.4 T in irradiations providing micro-surroundings as in the present investigation (i.e. nature and arrangement of alanine pellets, PMMA holder, and water). The affectation is more pronounced in the case of 1.4 T with (0.73±0.15) % compared to (0.46±0.15) %

in the case of 0.7 T. Close to $TPR_{20,10} = 0.760$, it can be concluded, that the effect of magnetic flux densities of 0.7 T and 1.4 T on the response of the alanine dosimeter for irradiations with micro-surroundings as in this experiment (identical alanine pellets, PMMA holder, and water) is at the edge of significance: The standard indication of the alanine dosimeter has to be revised upwards by $(0.56 \pm 0.27)\,\%$ for 0.7 T in order to equal the actual absorbed dose in the magnetic field, which scarcely doesn't agree with unity within an expanded uncertainty with coverage factor $k = 2$. For 1.4 T, the standard indication has to be revised upwards by $(0.50 \pm 0.27)\,\%$, which equals unity within an expanded uncertainty with coverage factor $k = 2$.
The present investigation does not allow for direct conclusions regarding irradiations at the ViewRay MRIdian™ MR Linac device and at the Elekta Unity™ device[10] since both the radiation quality and the magnetic flux densities applied are not identical. The agreement of the data points in the 15 MV and 10 MV series with the data points in the 6 MV series underlines, however, the reliability of the 6 MV data. Furthermore, the agreement shows that the conclusions drawn from the 6 MV data are also valid in the situation at the ViewRay MRIdian™ MR Linac device although the radiation quality applied at this MR Linac differs slightly from the radiation quality in the 6 MV series.
In Section 5.1.3, it was mentioned, that the measured effect at a magnetic flux density of 1.4 T when using a 6 MV photon beam could result from experimental problems as the experimental realisation at 1.4 T was the most vulnerable in the 6 MV investigation. This was mainly due to strong temperature developments during the irradiations in the presence of a magnetic field with 1.4 T flux density. With the knowledge of the present results obtained when using a 10 MV photon beam, it can be said, that it is even more unlikely that the measured effect at 1.4 T for 6 MV photon beams was caused by temperature changes. The temperature in the present setup with 10 MV photon beams was much more stable, also due to the fact, that only four alanine irradiations were performed per run in contrast to seven irradiations in the experiment with 6 MV photon beams. Nevertheless, an effect of comparable size as in the previous experiment with 6 MV photon beams is measurable for 1.4 T with 10 MV photon beams. In that respect, the present investigation helps to better understand the results obtained in the previous investigation with 6 MV photon beams.
Prior to a possible repetition of the exeriment, a phase space file for the nominal acceleration potential of 15 MV at the applied linac should be obtained. With the usage of this phase space file for the MC simulations instead of the EGSnrc mohan spectrum, see Section E.2, the uncertainties associated with the $c_{\vec{B}}$ factors and, hence, also with the correction factors k_{mag} in the 15 MV series would be of the size as in the 10 MV series. Furthermore, more data points should be gained in the 10 MV and 15 MV series, at the same magnetic flux densities as in the 6 MV series, however, at least a data point at 0.6 T instead of 0.7 T allowing for a direct

[10] The situation at the Elekta Unity™ device is, anyway, addressed by the investigation discussed in Section 5.1.2.

comparability.
In the folllowing, a comparison of the obtained results with results available in literature is presented.
Correction factors $k_{Q_B,Q}$ obtained from alanine irradiations with an Elekta Synergy linac with a nominal accelerating potential of 6 MV and 8 MV are presented in [Billas et al., 2020] in Table 1. These correction factors $k_{Q_B,Q}$ correspond to the correction factors k_{mag} determined in my work. No TPR values are reported, but I assume that the radiation quality for 6 MV is comparable to the radiation quality in my investigation using 6 MV photon beams, and that the radiation quality for 8 MV is in between the radiation qualities of 6 MV and 10 MV used in my investigations. The correction factors $k_{Q_B,Q}$ from [Billas et al., 2020] for 6 MV and 8 MV and the correction factors k_{mag} for 6 MV, 10 MV, and 15 MV are shown together in Figure 5.1. The correction factors $k_{Q_B,Q}$ from [Billas et al., 2020] for 6 MV and 8 MV photon beams equal each other at the respective magnetic flux densities within the standard uncertainty ($k = 1$). A similar situation can be observed for my results. The correction factors k_{mag} for 6 MV, 10 MV, and 15 MV photon beams equal each other within the standard uncertainty ($k = 1$) for a magnetic flux density of 1.4 T, and the correction factors k_{mag} for 10 MV and 15 MV photon beams equal each other within the standard uncertainty ($k = 1$) for a magnetic flux density of 0.7 T. As mentioned above, there is unfortunately no direct equivalent for the data points at 0.7 T in the 10 MV and 15 MV series in the results from the investigation with 6 MV photon beams. Comparing the correction factors k_{mag} for 0.7 T from the 10 MV and the 15 MV series with the correction factor k_{mag} for 0.9 T at 6 MV reveals – as already mentioned – an agreement within the standard uncertainty ($k = 1$), while comparing the correction factors k_{mag} for 0.7 T in the 10 MV and 15 MV series with the correction factor k_{mag} for 0.6 T at 6 MV reveals an agreement within the expanded uncertainty with coverage factor $k = 2$. A direct comparison of the results in [Billas et al., 2020] with my results from the present investigation is difficult, since neither the radiation qualities nor the magnetic flux densities applied in the experiments are the same. Nevertheless, a comparison of the 8 MV data in [Billas et al., 2020] with my 15 MV data is attempted in the following. My correction factor k_{mag} for 0.7 T and 15 MV equals the correction factor $k_{Q_B,Q}$ from [Billas et al., 2020] for 0.5 T and 8 MV within the standard uncertainty ($k = 1$), and it equals the correction factor $k_{Q_B,Q}$ from [Billas et al., 2020] for 1.0 T and 8 MV within the standard uncertainty ($k = 1$). My correction factor k_{mag} for 1.4 T and 15 MV equals the correction factor $k_{Q_B,Q}$ from [Billas et al., 2020] for 1.5 T and 8 MV within the expanded uncertainty with coverage factor $k = 2$. As mentioned above, this comparison has to be taken with a grain of salt, since the magnetic flux densities and the radiation quality are not the same. Furthermore, details in the experimental setup are not identical, e.g. a different type of alanine pellets with slightly different measures and a PMMA holder with a different inner diameter are used in [Billas et al., 2020]. What can be stated clearly is, nevertheless, that the results from [Billas et al., 2020] and the results in the present investigation are close to each other and that the uncertainties associated with the correction factors k_{mag} are smaller than

the uncertainties associated with the correction factors $k_{Q_B,Q}$ presented in [Billas et al., 2020] by factors of up to four.
A correction factor $k_{al,\vec{B},Q} = 0.9989(28)$ for alanine irradiations with an Elekta Unity™ MR Linac (1.5 T) is presented in [Pojtinger et al., 2020] in Section 3.3 (see also Section 2.5). This correction factor $k_{al,\vec{B},Q}$ corresponds to the correction factors k_{mag} determined in my work. The $TPR_{20,10}$ for the Elekta Unity device is reported by [de Prez et al., 2019] as 0.701(2) while it is $TPR_{20,10} = 0.733$ (10 MV) and $TPR_{20,10} = 0.760$ (15 MV) for the linac used in the present investigation (a comparison of this literature value with the correction factor k_{mag} obtained at another Elekta Unity™ MR Linac was presented in Section 5.1.2). The correction factor $k_{al,\vec{B},Q}$ for 1.5 T agrees with the obtained correction factor k_{mag} for 1.4 T 15 MV within an expanded uncertainty with coverage factor $k = 2$. As before, this comparison is performed under the restrictions that the magnetic flux densities and the radiation quality and details in the experimental setup are not identical. The uncertainties associated with the correction factors k_{mag} for 1.4 T at 15 MV and the uncertainty associated with the correction factor $k_{al,\vec{B},Q}$ presented in [Pojtinger et al., 2020] are comparable. The correction factor $k_{al,\vec{B},Q}$ for 1.5 T agrees also with the obtained correction factor k_{mag} for 1.4 T at 6 MV and 10 MV within an expanded uncertainty with coverage factor $k = 2$. The uncertainties associated with the correction factors k_{mag} for 1.4 T at 6 MV and 10 MV are smaller than the uncertainty associated with the correction factor $k_{al,\vec{B},Q}$ presented in [Pojtinger et al., 2020] by a factor of two.
The aim of the present investigation was to determine the correction factors k_{mag} converting the standard indication of the alanine dosimeter into the actual absorbed dose-to-water at the point of measurement in the presence of a magnetic field for flux densities of 0.7 T and 1.4 T when photon beams with nominal accelerating potential of 10 MV and 15 MV, respectively, are applied, and to draw conclusions regarding the energy dependence of these correction factors k_{mag} by comparing the present results with the results obtained when applying photon beams with a nominal accelerating potential of 6 MV in the previous investigation. Altogether, the obtained results in the 6 MV, 10 MV, and 15 MV series indicate no measurable energy dependence of the correction factors k_{mag} between 6 MV and 15 MV. Since no energy dependence was measured, it is confirmed by this investigation, that the results obtained from the 6 MV series ($TPR_{20,10} = 0.683$) can be transferred to the situation at the ViewRay MRIdian™ MR Linac device ($TPR_{20,10} = 0.648$), as already stated in Section 5.1.3: Since no significant deviation of the correction factor k_{mag} from unity for flux densities of (0.3, 0.6, 0.9, 1.2) T was found in the 6 MV series, no magnetic field correction factor is required for dose determinations with the alanine dosimeter at the ViewRay MRIdian™ MR Linac device; it is sufficient to consider an uncertainty component of 0.16 % since this is the uncertainty associated with the obtained correction factors k_{mag}, see Section 5.1.3. An additional comparison of the correction factors k_{mag} using a 5 cm × 10 cm fieldsize with correction factors k_{mag} obtained using a 4 cm × 10 cm fieldsize (see Chapter E.4 in the appendix) revealed no measurable difference.

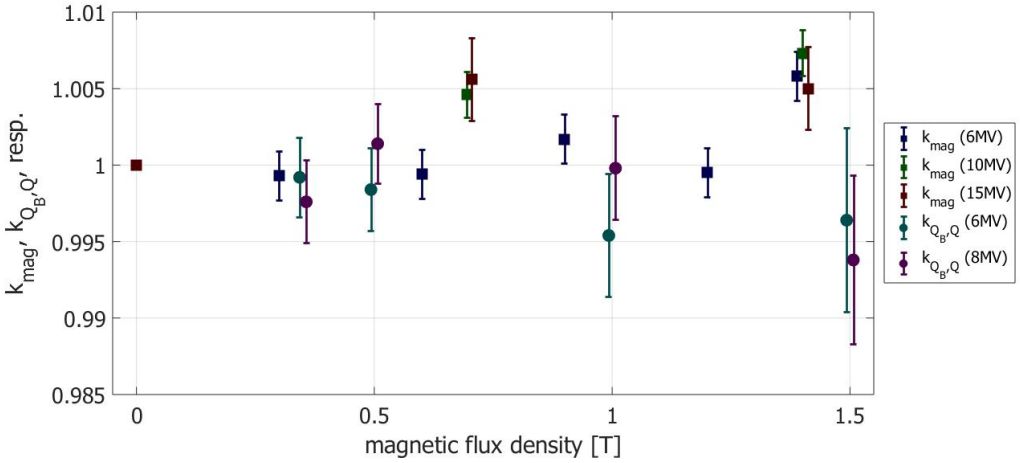

Figure 5.1: Correction factors k_{mag} obtained in the investigations with 6 MV photon beams (dark blue squares), 10 MV photon beams (green squares), and 15 MV photon beams (red squares) together with the corresponding results for the correction factors $k_{Q_B,Q}$ from [Billas et al., 2020] for 6 MV (light blue circles) and 8 MV (purple circles). (Coverage factor $k = 1$, the uncertainties given are absolute uncertainties.)

5.2 Characterisation of the alanine dosimeter in MRI

5.2.1 Effect of MRI on irradiated alanine detectors

This experiment aimed at the investigation of the effect that the exposure of already irradiated alanine pellets to an MRI system has on the indication of the alanine dosimeter, i.e. the effect that MRI has on the radicals formed in the alanine due to the impact of ionising radiation. This aspect is relevant for the application of the alanine dosimeter for end-to-end tests in MRgRT, which can involve MRI after irradiation. An MRI system is composed of three main components (see Section 2.1.1). The possible effects that these three main MR components could have on the alanine dosimeter and assumptions about possible effects are described in detail in Section 2.4.3. In the following, it is described how the present investigation allowed to verify or falsify these assumptions regarding the three MRI components.
The present investigation allowed to verify the assumption that the radicals formed by ionising radiation in the alanine dosimeter are not moved due to the Lorentz force e.g. if the patient bench on which they are placed is moved inside the static magnetic main field $\vec{B}_0$, which is generated by the superconducting magnet (see Section 2.4.3): The irradiated alanine pellets containing radicals were placed in the experimental setup on the patient bench. Then, the bench was moved into the MRI system before applying the MR sequences. The alanine pellets with the radicals were, thus, moved in the static magnetic main field $\vec{B}_0$. The static magnetic main

field $\vec{B}_0$ is always turned on (see Section 2.1.1). The elimination or even variation of this influence was, hence, not possible in this experiment.
The performed experiment also allowed to verify the assumption that the electric vortex fields induced by changes in the gradient fields do not have an effect on the amount of radicals in the alanine pellets: Alanine pellets were exposed to different MR sequences which are unavoidably accompanied by changing gradient fields (see Section 2.1.4). The influence of the gradient system on the alanine pellets can be varied by the lateral position of the alanine pellet in the MRI system. The gradient fields are zero in the isocenter of the system; their strength increases towards the periphery. In the performed experiment, alanine detectors were positioned in the isocenter (0 cm) as well as (15, 27.5, 30) cm left of the isocenter.
The SAR thresholds (see Section 2.1.7) were not exceeded in the present experiment (94 % of the threshold were reached in the MR sequence with maximum RF pulses, see Section 3.2.1). No measurable effect of an RF field induced temperature rise on the amount of radicals in the alanine pellets was, hence, expected, see Section 2.4.3. This assumption could be verified in the present experiment. The influence of the RF fields on the alanine pellets can be varied by the adjustment of the parameters of the applied MR sequence. This experiment included the exposure of irradiated alanine detectors to an MR measurement with maximum RF pulses (94 % SAR) and almost diminishing pulses (1 % SAR), see the Sections 3.2.1 and 3.2.1.
In this investigation, the correction factor $k_{subsMRI}$ was determined. It corrects for a possible effect that the exposure to an MRI system can have on already irradiated alanine detectors. At this, twelve different conditions covering the possible characteristics of the three MRI components (see Section 2.1.1) were investigated. These involved enhanced and suppressed RF pulses, minimum and maximum gradient fields, and the main field with a flux density of 2.89 T, see above. The resulting values for the correction factor $k_{subsMRI}$ are shown in Table 4.4 and Figure 4.6. All obtained values for the correction factor $k_{subsMRI}$ agree with unity within the standard uncertainty ($k = 1$) with one exception: the value for Condition C_c (min. RF impact, max. gradient impact, see Section 3.2.1) agrees with unity only within the expanded uncertainty with coverage factor $k = 2$.[11] Hence, no significant deviation from unity was found for any of the twelve values determined. It can be concluded that the exposure of irradiated alanine detectors to the three applied components of an MRI system (RF pulses, gradient fields, and static magnetic field with flux density 2.89 T) has no measurable effect on the indication of the alanine dosimeter. To my knowledge, there is no similar study in literature to which the present results could be compared.
The results of the present investigation allow to draw the conclusion that subsequent MRI has no measurable effect on the indication of the alanine dosimeter since none

[11] The uncertainties plotted in Figure 4.6 correspond to a coverage factor $k = 1$: There is a 68 % probability for the "true value" of $k_{subsMRI}$ to be within the plotted error bars; the probablity for the "true value" to fall outside the error bars is still about one third. An agreement within the expanded uncertainty with coverage factor $k = 2$' is, hence not seen as an measurable effect. However, Chapter F in the appendix presents a closer look at this value.

of the obtained correction factors $k_{subsMRI}$ shows a significant deviation from unity. This indicates that the alanine dosimeter is suited for the application in end-to-end tests in MRgRT. Neither a correction factor nor an uncertainty contribution have to be considered, if MRI follows an irradiation. The question remains, if a correction factor is required if alanine detectors are irradiated during MRI. This question is answered by the investigation addressed in the following Section 5.2.2.

5.2.2 Effect of MRI during irradiation

The aim of this investigation was to determine the correction factor k_{RF}. The correction factor k_{RF} is required if an MR sequence is applied during the irradiation of the alanie dosimeter. This situation can, with the current technical development, only be accomplished at an MR Linac device, which also involves the presence of the static magnetic base field of the MR Linac device. The correction factor k_{RF} corrects the indication of the alanine dosimeter already corrected for the presence of the static magnetic field by the application of the correction factor k_{mag} (see Section 5.1.2) if an MR sequence is applied in addition to the static magnetic base field of an MR Linac device. The correction factor k_{RF} has, hence, to be included in Equation 2.30 in addition to the correction factor k_{mag} (see Section 2.4.3) in order to obtain the actual absorbed dose-to-water at the point of measurement with the alanine dosimeter at an MR Linac device if MRI is applied during the irradiation, see Equation 3.39.

The present investigation was conducted at the same Elekta Unity™ MR Linac device as the investigation discussed in Section 5.1.2. The correction factor k_{RF} was obtained via comparison of signals of alanine detectors irradiated at the Elekta Unity™ device during the application of an MR sequence with signals of alanine detectors which were irradiated at the same device without application of MRI. The resulting correction factor k_{RF} is, as presented in Section 4.2.2: $k_{RF} = 0.9999 \pm 0.0019$. Since the obtained correction factor k_{RF} agrees with unity within the standard uncertainty ($k = 1$), it can be concluded that the application of MRI during the irradiation of alanine detectors does not have a measurable effect on the response of the alanine dosimeter. This means that the radical formation in the alanine material is not measurably impaired by the impact of the RF pulses of the MR sequences. It can be assumed that this finding is not only valid for the situation at the Elekta Unity™ device but also at other MR Linac devices, e.g. the ViewRay MRIdian™ MR Linac.

As mentioned in Section 3.2.2, the readout of all alanine detectors involved should be performed on the same measurement day in a possible repetition of the present investigation. This allows to further reduce the uncertainty associated with the correction factor k_{RF}.

To my knowledge, there is currently no other investigation of the impact of MRI exposure during irradiation on the alanine indication. Hence, no comparison with data from literature can be presented here.

This experiment allows for the conlusion that the alanine dosimeter is not measur-

ably affected by MRI during irradiation. The standard indication of the alanine dosimeter already corrected for the magnetic field by application of k_{mag} has to be corrected downwards by $(0.01 \pm 0.19)\,\%$ in order to assure that the indication corresponds to the actual absorbed dose-to-water for irradiations with concurring MRI. This agrees with unity within the standard uncertainty ($k = 1$), i.e. no measurable effect was detected.
The previous experiment (see Section 5.2.1) focussed on the effect of MRI on already irradiated alanine detectors and found that subsequent MRI has no measurable effect on the response of the alanine dosimeter. The present experiment investigated the effect of MRI during the irradiation on the alanine dosimeter and also found no measurable effect. Since there is no measurable effect of MRI on the alanine dosimeter regardless of whether the MR sequences are applied during of after the irradiations it can be concluded that the alanine dosimeter is suitable for end-to-end tests in MRgRT. Alanine pellets could for example be attached to the patients' skin (or they could be placed within a phantom [Gallas et al., 2015; Niebuhr et al., 2019]) throughout the course of the treatment. This does not only apply for MRgRT treatments at the Elekta Unity™ MR Linac, which was applied in the present investigation, but also for treatments at other MR Linacs, e.g. the Viewray MRIdian™ machine.

5.3 Summarising discussion of the results of this thesis

This section provides a summarising discussion covering the content of the Sections 5.1.1 to 5.2.2 as well as of Table 4.5 in Section 4.3, which summarises the obtained results.
The first part of this thesis addresses the alanine dosimeter in static magnetic fields. The preparatory experiment discussed in Section 5.1.1 revealed that sub-millimetre air gaps surrounding the alanine pellets within the detector holder have no measurable effect on the response of the alanine dosimeter in the presence of a static magnetic field. Hence, no correction factor regarding the air gaps had to be considered in the subsequent experiments of this thesis. The experiment performed at the Elekta Unity™ MR Linac device at the Christie hospital in Manchester, UK, which is discussed in Section 5.1.2, provided the product[12] of correction factors ($K_Q \cdot k_{mag}$) which has to be included in Equation 2.30 for the application of the alanine dosimeter at Elekta Unity™ MR Linac devices. The determined correction factor k_{mag} equals unity within the standard uncertainty corresponding to no measurable effect in the static magnetic field of the MR Linac. The investigation including a 6 MV photon beam, which is discussed in Section 5.1.3, allowed to determine the correction factor k_{mag} that has to be included in Equation 2.30 for the application of the

[12] Providing the product is advantageous compared to providing the single correction factors with regard to the associated uncertainty, see Section 5.1.2.

alanine dosimeter at Viewray MRIdian™ MR Linac devices. No measurable effect was found here either. The investigation including 10 MV and 15 MV photon beams, which is discussed in Section 5.1.4, revealed no measurable energy dependence of the correction factor k_{mag} between 6 MV and 15 MV. This finding is the rationalisation why the results obtained in the 6 MV series can be transferred to the situation at the Viewray MRIdian™ machine, which features a slightly different radiation quality.[13] The first part of the thesis, hence, provides the information required for the application of the alanine dosimeter at the currently clinically available MR Linac machines.

The second part of this thesis addresses the alanine dosimeter in MRI. The experiment discussed in Section 5.2.1 revealed that the exposure of irradiated alanine detectors to MRI has no measurable effect on the alanine dosimeter. In the experiment discussed in Section 5.2.2, the correction factor k_{RF} to be included in Equation 2.30 for irradiations of the alanine dosimeter with concurring MRI was determined. The obtained correction factor equals unity within the standard uncertainy corresponding to no measurable effect of concurring MRI on the alanine dosimeter. These two experiments confirm, hence, the suitability of the alanine dosimeter for end-to-end tests in MRgRT as stated in Section 5.2.2.

This work was started when MRgRT was about to be transferred from research to clinical application. In the meantime, five MR Linac devices have been installed for clinical application in Germany alone [Uniklinikum Dresden, 2022] and research regarding the alanine dosimeter in MRgRT was already published, see [Billas et al., 2020, 2021]. However, this work is the first profound study of the alanine dosimetry system applied at the German metrology institute PTB.[14] Further, the presented data plays the important role to provide values the already available literature data can be compared to. Last but not least, the uncertainties associated with the values presented in this work are up to a factor of four smaller than current values from literature, see e.g. Section 5.1.4.

[13] A direct investigation at a Viewray MRIdian™ MR Linac would, of course, have been preferable. However, beamtime at a Viewray MRIdian™ MR Linac could not be obtained for this work.

[14] This also implies that the present work is the first profound study in which irradiation and detector readout are performed by the same scientist, since – to my knowledge – at the NPL, where the studies [Billas et al., 2020, 2021] were conducted, the irradiated alanine detectors are transferred to the department of chemistry and a resulting value is transmitted back.

6 Conclusion and outlook

The aim of this thesis was to characterise the alanine dosimeter in magnetic fields as they occur in MRgRT. This characterisation was split into two parts: The first part addressed the characterisation of the alanine dosimeter in static magnetic fields, the second part addressed the impact of RF pulses and gradient fields of MRI in addition. This division was chosen as the static magnetic main field of an MR Linac cannot be switched off easily. Hence, the alanine dosimeter is exposed to the static magnetic main field whenever it is positioned within an MR Linac. No measurable effect of the static magnetic field on the alanine dosimeter was found in the first part of this thesis. The alanine dosimeter is, hence, an excellent choice for dose assessments in MRgRT. Correction factors to be applied at the Elekta Unity™ and at the ViewRay MRIdian™ MR Linac device ($(K_Q \cdot k_{mag}) = 1.0011 \pm 0.0024$ and $k_{mag} = 1.0000 \pm 0.0016$, respectively), which agree with unity within the standard uncertainty, are provided. No measurable effect of RF pulses and gradient fields on the alanine dosimeter was found in the second part of this thesis. The alanine dosimeter is, hence, also suited for end-to-end tests in MRgRT which can involve MRI after or during irradiation, e.g. with the alanine dosimeter positioned on or within anthropomorphic phantoms [Gallas et al., 2015; Niebuhr et al., 2019]. The correction factor to be applied when MRI takes place during the irradiation ($k_{RF} = 0.9999 \pm 0.0019$), which also agrees with unity within the standard uncertainty, is provided.
The results of the characterisation in static magnetic fields agree with current literature data, while the associated uncertainties are reduces up to a factor of four compared to the values from literature. The characterisation of the impact of RF pulses and gradient fields on the alanine dosimeter has – to my knowledge – not yet been reported in literature.
Aspects that can be improved in possible repetitions of the performed experiments are stated in the Sections 5.1.1 to 5.2.2. Of higher interest, however more theoretically than for the practical application, is a profound MC study focussing on the trajectories of the secondary electrons in and around the alanine pellets for irradiations in static magnetic fields. The findings of such a study would probably explain the results obtained in this thesis. A cooperation with the Institut für Medizinische Physik und Strahlenschutz (IMPS) in Gießen, Germany, as e.g. in [Anton et al., 2013] would be preferable for that purpose due to the established experience with MC simulations in alanine at this institute.

Appendix

A Sub-millimetre air gaps in the absence of a magnetic field

The effect of sub-millimetre air gaps around the alanine detectors on the indication of the alanine dosimeter in the presence of static magnetic fields has been studied in a preparatory experiment, see Section 3.1.1, and the results have been presented in Section 4.1.1. This preparatory experiment included the investigation of the effect of sub-millimetre air gaps around the alanine detectors on the indication of the alanine dosimeter in the absence of static magnetic fields. The conduction of the experiment is described in Section 3.1.1. The analysis and the obtained results are presented in the following sections.

A.1 Analysis

The aim was to determine $\frac{k_{air,X}}{k_{air,0.0mm}}$ which is the ratio of the correction factors k_{air} for the indication of the alanine dosimeter for an air gap of size X and for the air gap with 0.0 mm size. The correction factor k_{air} addresses the changes due to air gaps surrounding alanine detectors which are based on the alteration of the local dose distribution due to the inserted air volume (see Section 2.4.3). The ratio of the correction factors k_{air} relative to the correction factor $k_{air,0.0mm}$ was formed since this allows for a smaller overall uncertainty due to several components cancelling out in the model equation. The derivation of the model equation for $\frac{k_{air,X}}{k_{air,0.0mm}}$ is outlined in the following.

Derivation of the model equation. With the corrected dose-normalised amplitude A_D^{corr} as the indication of the alanine detectors and the applied dose-to-water D_{appl} the response R of the alanine detectors is

$$R = \frac{A_D^{corr}}{D_{appl}} \tag{A.1}$$

The corrected dose-normalised amplitude A_D^{corr} is given by Equation 2.30. No volume and sensitivity correction is required due to constant gradients in all irradiations (see Section 2.4.3), and no environment correction is required since all irradiations are performed within water phantoms (see Section 2.4.3). The expression for A_D^{corr} is, hence:

$$A_D^{corr} = \frac{A_m}{\bar{m}} \cdot \bar{m}^b \cdot D^b \cdot K_T \cdot K_Q \cdot K_F \cdot K_{air} \tag{A.2}$$

The ratio of two alanine response values R equals unity in the case of entirely corrected response values:

$$1 = \frac{R_X}{R_{0.0mm}} \tag{A.3}$$

Combining the Equations A.1, A.2, and A.3 eventually results in

$$\frac{k_{air,X}}{k_{air,0.0mm}} = \frac{Q_X}{\frac{A_{m,X}}{\bar{m}_X} \cdot k_{T,X}} \cdot \frac{\frac{A_{m,0.0mm}}{\bar{m}_{0.0mm}} \cdot k_{T,0.0mm}}{Q_{0.0mm}} \tag{A.4}$$

The masses of the base pellets, the absorbed doses-to-water applied to the base pellets, the radiation quality correction and the fading correction cancel out as described in Section 3.1.1. In that section, it is also described why the factors k_i can be used instead of the factors K_i, and why the charge Q_i can be used instead of the applied dose-to-water $D_{appl,i}$.
The values of $A_{m,X}$ and $A_{m,0.0mm}$ are obtained from the EPR measurement of the alanine detectors irradiated in the absence of a static magnetic field, and the masses $\bar{m}_X$ and $\bar{m}_{0.0mm}$ are obtained from the weighting process (see Section 3.1.1).

A.1.1 Uncertainty

In the following, it is discussed how the uncertainty budget for $\frac{k_{air,X}}{k_{air,0.0mm}}$ is set up. The symbol u is used for absolute uncertainties, u_r for relative uncertainties. All uncertainties are given for a coverage factor $k = 1$ and are, thus, corresponding to a confidence probability of approximately 68 % (see Section 2.6).

Contribution due to the amplitude. The uncertainty associated with the amplitude values $A_{m,X/0.0mm}$ has two contributions. One is due to the reproducibility of the amplitude measurement and the other one is due to the homogeneity of the detector material. Both contributions affect test and base pellets. In this analysis, the contributions due to reproducibility and homogeneity for the base pellets ($u_r(A_{base}^{repro})$ and $u_r(A_{base}^{hom})$) cancel out since the quantity of interest is the ratio of values which were obtained on the same EPR measurement day using the same base. The contribution due to reproducibility of the test pellets $u_r(A_{test}^{repro})$ has to be considered two times, for the test detector surrounded by the air gap with size X and for the test detector surrounded by the gap with 0.0 mm size. The contribution due to homogeneity of the test pellets $u_r(A_{test}^{hom})$ has to be considered two times as well, again for the test detector surrounded by the air gap with size X and for the test detector surrounded by the gap with 0.0 mm size. Both components $u_r(A_{test}^{repro})$ and $u_r(A_{test}^{hom})$ have, however, to be considered only once for the value $\frac{k_{air,0.0mm}}{k_{air,0.0mm}}$.
The uncertainty components $u_r(A_{test}^{repro})$ are calculated according to Equation 3.6 as described in Section 3.1.1. The uncertainty components $u_r(A_{test}^{hom})$ are calculated according to Equation 3.7 as described in Section 3.1.1.

Contribution due to the mass. In addition to the contribution from the amplitude, there is the contribution from the pellet masses as it is described in Section 3.1.1. The component $u_r(\bar{m})$ has to be considered two times, for the test detector surrounded by the air gap with size X and for the test detector surrounded by the gap with 0.0 mm size. The component has to be considered only once for the value $\frac{k_{air,0.0mm}}{k_{air,0.0mm}}$. No contribution due to the mass of the base pellets is needed, since all values were obtained on the same EPR measurement day, ruling out a contribution due to changes in the mass by additional handlings.

Contribution due to the irradiation temperature. The uncertainty for the correction factor addressing the irradiation temperature is calculated according to Equation 2.33 as described in Section 2.4.3. The component $u_r(k_T)$ has to be considered two times, for the test detector surrounded by the air gap with size X and for the test detector surrounded by the gap with 0.0 mm size. The component has to be considered only once for the value $\frac{k_{air,0.0mm}}{k_{air,0.0mm}}$.

Contribution due to the applied dose. The uncertainty contribution due to the applied dose D_{appl} or rather due to the charge Q indicated by the external transmission IC is composed of the components listed in Section 3.1.1, resulting analogously as there in $u_r(Q) = 0.09\,\%$. This component $u_r(Q)$ has to be considered two times, for the test detector surrounded by the air gap with size X and for the test detector surrounded by the gap with 0.0 mm size. The component has to be considered only once for the value $\frac{k_{air,0.0mm}}{k_{air,0.0mm}}$.

Summary. The uncertainty budget is summarised in Table A.1. The total relative uncertainty associated with $\frac{k_{air,X}}{k_{air,0.0mm}}$, $u_r\left(\frac{k_{air,X}}{k_{air,0.0mm}}\right)$, is obtained from the listed uncertainty contributions according to:

$$u_r\left(\frac{k_{air,X}}{k_{air,0.0mm}}\right) = \sqrt{\sum_i \left(u_{r,i}{}^2\right)} \tag{A.5}$$

The single components and the total uncertainty are rounded according to the rules in [Beringer et al., 2012]. The total uncertainty is calculated using the non-rounded values for the single components. The dominant uncertainty contribution is due to the alanine amplitude determination.

A.2 Results

The respective results for the ratio $\frac{k_{air,X}}{k_{air,0.0mm}}$ are presented in the following. It was found, that sub-millimetre air gaps around the alanine detectors have no measurable effect on the indication of the alanine dosimeter in the absence of static magnetic fields. Table A.2 and Figure A.1 show the experimental results leading to this

Table A.1: Uncertainty budget for the ratio $\frac{k_{air,X}}{k_{air,0.0mm}}$. The total uncertainty was calculated using the non-rounded single components. All uncertainties are given for a coverage factor $k = 1$. The values in brackets are for the data point at 0.0 mm, where several components cancel out (see text).

Contribution	due to ...	u_r in %
$u_r(A^{repro}_{test,X})$	reproducibility of the amplitude determination (test pellets, air gap X)	0.18 (–)
$u_r(A^{repro}_{test,0.0mm})$	reproducibility of the amplitude determination (test pellets, 0.0 mm air gap)	0.18 (0.18)
$u_r(A^{hom}_{test,X})$	homogeneity of the alanine pellet composition (test pellets, air gap X)	0.15 (–)
$u_r(A^{hom}_{test,0.0mm})$	homogeneity of the alanine pellet composition (test pellets, 0.0 mm air gap)	0.15 (0.15)
$u_r(\bar{m}_X)$	mass of test pellets (air gap X)	0.04 (–)
$u_r(\bar{m}_{0.0mm})$	mass of test pellets (0.0 mm air gap)	0.04 (0.04)
$u_r(k_{T,X})$	correction for irradiation temperature (test pellets, air gap X)	0.020 (–)
$u_r(k_{T,0.0mm})$	correction for irradiation temperature (test pellets, 0.0 mm air gap)	0.020 (0.020)
$u_r(Q_X)$	sum of charge readings of the external transmission chamber (monitor 2) for test pellets (air gap X)	0.09 (–)
$u_r(Q_{0.0mm})$	sum of charge readings of the external transmission chamber (monitor 2) for test pellets (0.0 mm air gap)	0.09 (0.09)
Total:	$u_r\left(\frac{k_{air,X}}{k_{air,0.0mm}}\right) = 0.4\ (0.26)$	

Table A.2: Experimentally obtained values for the ratio of correction factors $\frac{k_{air,X}}{k_{air,0.0mm}}$ which correct the indication of the alanine dosimeter for the possible impact of air gaps around the alanine detector during irradiations in the absence of a static magnetic field. (Coverage factor $k = 1$, the uncertainties given are absolute uncertainties.)

Quantity	experimentally obtained value with absolute uncertainty
$\frac{k_{air,0.1mm}}{k_{air,0.0mm}}$	0.998 ± 0.004
$\frac{k_{air,0.2mm}}{k_{air,0.0mm}}$	0.999 ± 0.004
$\frac{k_{air,0.5mm}}{k_{air,0.0mm}}$	0.997 ± 0.004
$\frac{k_{air,1.0mm}}{k_{air,0.0mm}}$	0.998 ± 0.004
$\frac{k_{air,0.0mm}}{k_{air,0.0mm}}$	1.0000 ± 0.0026

conclusion. The ordinate in the graph shows the values for the ratio $\frac{k_{air,X}}{k_{air,0.0mm}}$ while the abscissa shows the size of the air gap surrounding the alanine detector associated with the correction factor $k_{air,X}$ in the numerator of the determined ratio. $\frac{k_{air,X}}{k_{air,0.0mm}}$ is the ratio of correction factors for a possible effect of the surrounding air gaps for an air gap of (0.1, 0.2, 0.5, 1.0) mm size and 0.0 mm size in the absence of a magnetic field.
The results are discussed together with the results from the analysis considering also the irradiation series in the presence of a magnetic field in Section 5.1.1.

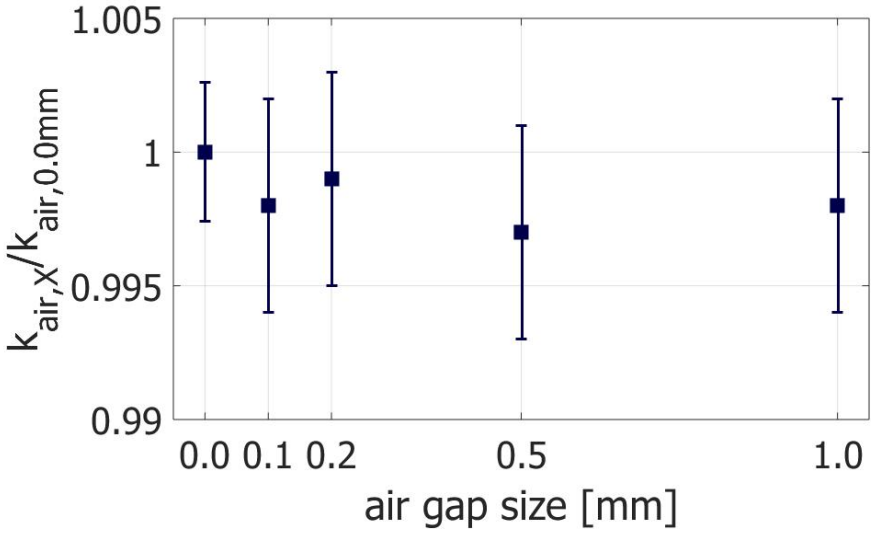

Figure A.1: Experimentally obtained values for the ratio of correction factors $\frac{k_{air,X}}{k_{air,0.0mm}}$ which correct the indication of the alanine dosimeter for the possible impact of air gaps around the alanine detector during irradiations in the absence of a static magnetic field (Coverage factor $k = 1$, $X = (0.0, 0.1, 0.2, 0.5, 1.0)$ mm).

B Effect of the stray magnetic field on the monitoring ICs

Many of the irradiations in this thesis were performed with the electromagnet ER073W (Bruker) in front of the conventional linac at the PTB (see Sections 3.1.1, 3.1.3, and 3.1.4). The alanine detectors were positioned in a water phantom between the pole shoes of this electromagnet while they were irradiated with the photon beams generated by the linac. Prior to the experiments it was expected that the reponse of the alanine dosimeter is – if at all – scarcely affected by the presence of a static magnetic field. Thus, any possible impairment of the data obtained from the experiments had to be considered with care and particular attention had to be directed to the determination of the experimental uncertainties.
The determination of the alanine response requires a monitoring of the output of the linear accelerator (see Section 3.1.1). Two monitoring options are available at the linac at the PTB: an internal transmission IC is installed within the accelerator head and an external transmission IC is mounted directly in front of the accelerator head. In the setup with the electromagnet in front of the linac, it has to be considered that the stray magnetic field accompanying the static magnetic field generated between the pole shoes of the electromagnet might impair the signal of these transmission ICs[1]. In respect of this impairment, it is advisable to increase the distance between the electromagnet and the accelerator head, in order to position the transmission ICs as far outside the stray magnetic field as possible since the stray magnetic field decreases rapidly with distance from the center of the electromagnet. Increasing the distance is, however, limited by the tolerable deviation from the SSD of 100 cm recommended in reference protocols for dosimetry as [Andreo et al., 2000] or [Deutsches Institut für Normung e.V., 2008]. For the setup with the electromagnet in front of the linac, an SSD of 110 cm was chosen, i.e. the electromagnet was positioned such, that the surface of the water phantom located centrally between its pole shoes for alanine irradiations is in a distance of 110 cm from the source. This SSD of 110 cm is – for this work – a neglectable deviation from the reference SSD while the impact of the stray magnetic field on the transmission ICs is reduced. The SSD of 110 cm implies a distance of 120 cm between the source and the center of the pole shoes. A stray field in the order of the terrestrial magnetic field can, however, not be excluded at the location of the transmission ICs in this setup. As mentioned above, it is expected that the reponse of the alanine dosimeter is – if at all – scarcely affected by the presence of a static magnetic field. Thus, the

[1] The impairment of the external transmission IC is expected to be more pronounced than the impairment of the internal transmission IC due to its closer distance to the electromagnet.

impairment of the signal of the transmission ICs due to this stray magnetic field has to be considered for the analysis of the experiments. This is accomplished by determining correction factors and their associated uncertainties. This chapter of the appendix presents the determination of these correction factors addressing the impact of the stray magnetic field on the transmission ICs. They are to be used for the correction of the monitor signals in irradiations of the alanine dosimeter in the presence of static magnetic fields up to 1.4 T generated by the electromagnet in front of the linac at the PTB. Please note, that these correction factors are only valid in the described setup with the electromagnet in front of the linac at the PTB with a distance of 120 cm between the center of the pole shoes and the source. The correction factors have to be redetermined as soon as the electromagnet is relocated with respect to the transmission ICs or if the electromagnet is replaced by another electromagnet.

B.1 Materials and methods

This section addresses the applied devices, the performed experiment, and its analysis. Descriptions of the electromagnet and the linac at the PTB applied in this experiment can be found in Section 3.1.1. The aim of this experiment is to determine correction factors for the internal transmission IC defaultly installed within the accelerator head of the linac and the PTB-built external transmission IC mounted directly in front of the accelerator head. Since these monitors are under investigation themselves, an additional monitoring option for the output of the linac is required in this experiment. This superordinated monitoring option is realised by a Farmer-type IC located well outside the stray magnetic field. The following sections describe the three monitors applied in this investigation.

B.1.1 Farmer-type IC (Monitor 1)

The Farmer-type IC FC65G-3069 – referred to as "Monitor 1" in the following – equipped with a build-up cap was positioned in air in 4 m distance from the source (see Figure B.1). The distance of 4 m is the largest possible distance due to the limits of the irradiation room. The IC was aligned to the center of the photon beam using the room lasers. The desired property of the signal of this Monitor 1 is its complete indepedence of the static magnetic field generated by the electromagnet since this IC is positioned well outside the stray magnetic field. This signal is needed in the present experiment in order to remove the drift of the output of the linac from the data.
Special attention was required in the experiment with regard to the following issue: The photon beam passes the interspace between the pole shoes of the electromagnet but the photons reach Monitor 1 unaffected by any magnetic field due to their zero charge. Test measurements revealed, however, a dependence of the signal of this monitor on the magnetic flux density generated by the electromagnet. This

behaviour is explained by electrons "contaminating" the photon beam. These electrons arise when the photons interact with the matter of the accelerator head and the external transmission IC (and negligibly with air). In the absence of a magnetic field, these "contamination electrons" reach Monitor 1 and contribute to the signal indicated by this IC. But the contamination electrons do not contribute to the signal indicated by Monitor 1 if a magnetic field is generated by the electromagnet. The electrons are strongly deflected due to the Lorentz force even for small magnetic flux densities preventing them from reaching the sensitive volume of Monitor 1. These contamination electrons, hence, hamper the independence of the signal of Monitor 1 from the magnetic flux density generated by the electromagnet. This problem was solved by placing a water phantom with 7 cm thickness and 30 cm width and height immediately in front of Monitor 1, see Figure B.1. This water phantom filters out the contamination electrons which would otherwise contribute to the signal in the absence of a magnetic field. Further electrons arise, however, from the interaction of the photons with this water phantom but this process is independent of the magnetic flux density generated by the electromagnet. Positioning the water phantom in front of Monitor 1 assures, hence, the independence of its signal from the magnetic flux density generated by the electromagnet.

B.1.2 External transmission IC (Monitor 2)

The PTB-built external transmission IC – referred to as "Monitor 2" in the following – has been described in Section 3.1.1 (including Figure 3.6). This transmission IC is generally recommended for monitoring the output of the linac at the PTB – instead of the internal transmission IC which is defaultly installed within the head of the linac. This recommendation is based on the experience of the group that the external transmission IC provides signals of higher stability. This Monitor 2 is composed of two independent compartments ("Monitor 2a" and "Monitor 2b", see Figure 3.7). Correction factors addressing the impairment of the two compartments Monitor 2a and 2b by the stray magnetic field in the setup with the electromagnet in front of the linac are to be determined in the presented experiment.

B.1.3 Internal transmission IC (Monitor 3)

Besides Monitor 2, the internal transmission IC – referred to as "Monitor 3" in the following – installed within the head of the linac by default is available for monitoring the output of the linac at the PTB. This Monitor 3 has been described in Section 3.1.3 (including Figure 2.16). It is generally not used for monitoring in irradiations performed by the group, since Monitor 2 (see Section B.1.2) was found to provide signals of higher stability. For monitoring irradiations in the presence of magnetic fields performed in the setup with the electromagnet in front of the linac, the signal of this Monitor 2 is, however, of higher interest: Installed within the accelerator head, it is positioned in a larger distance from the electromagnet than Monitor 2, hence, experiencing a weaker stray magnetic field. Correction factors

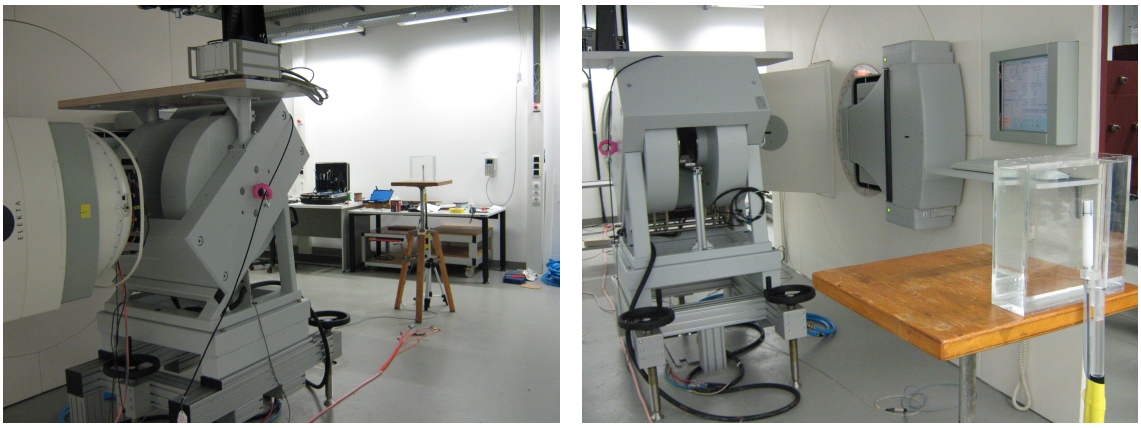

(a) (b)

Figure B.1: The experimental setup applied in the present experiment from two perspectives. In (a), the view is in beam direction. The accelerator head with the electromagnet in front of it is shown on the left. The water phantom with the Farmer-type IC (Monitor 1) behind in 4 m distance from the source can be seen on the wooden platform on the right. In (b), the view is opposite to the beam direction. The electromagnet with the accelerator head behind is shown on the left. The Farmer-type IC (Monitor 1) equipped with a build-up cap (white) in front of the water phantom can be seen on the right.

addressing the impairment of Monitor 3 by the stray magnetic field in the setup with the electromagnet in front of the linac are to be determined in the presented experiment.

B.1.4 Irradiation with the Elekta precise treatment system™ linac at the PTB

For the determination of the correction factors addressing the impairment of the monitoring transmission ICs (Monitor 2 and 3) by the stray magnetic field the electromagnet was positioned in front of the linac as described in Section 3.1.1. However, there were no alanine irradiations included in this experiment and, hence, there was no water phantom between the pole shoes of the electromagnet in the present setup.

The idea for this experiment was as follows: The signal of Monitor 2 and 3 in the presence of a photon beam generated by the linac was measured both in the absence of a static magnetic field at the electromagnet and in the presence of a static magnetic field with flux density j generated between the pole shoes of the electromagnet. In addition, the signal of Monitor 1 which is unaffected by the changes of the magnetic fields generated by the electromagnet was measured, since this allows to remove the drift of the output of the linac (see Section 3.1.1) from the

data prior to determining the desired correction factors, see Section B.2.
The order of the magnetic flux densities generated by the electromagnet in the present experiment was (0, 0.35, 0, 0, 1.0, 0, 0, 1.4, 0, 0, 0.7, 0) T. The chosen values cover the total range of magnetic flux densities that can be generated by the electromagnet employed. As indicated above, the switching between 0 T and j (with $j = \{0.35, 1.0, 1.4, 0.7\}$ T) allows to relate the measured signals at the magnetic flux density j to the measured signals at 0 T (see Section B.2). The to-and-fro order was chosen in order to assure that the finally obtained results are unaffected by any drift. The signals of Monitor 1, 2a/b, and 3 were averaged and recorded every ten seconds. At least 20 measurement points were taken for each magnetic flux density setting, since this is a solid tradeoff between measurement time and prevention of distortion of the final results by statictical fluctuations according to the experience of the group. Table B.1 shows an overview of the measurement points taken for each magnetic flux density setting at the electromagnet. As described in the Sections B.1.1 to B.1.3, Monitor 1 was positioned in 4 m distance from the source behind a water phantom, while Monitor 2a and 2b were positioned approximately 13 cm in front of the accelerator head, and Monitor 3 was fixed in its default position within the accelerator head. The dose rate of the linac was set to 275 MU per minute with a pulse rate frequency of 200 Hz, since test measurements revealed stable signals of the Monitors 1, 2a/b, and 3 for this setting. A voltage of $U = +250$ V was applied to Monitor 1 ("hochgelegt"). The voltage for Monitor 2a/b was $U = +300$ V. The default settings (set by Elekta) were applied for Monitor 3. These are the standard voltage settings used in the group. The air temperature used for the air density correction of the signal of Monitor 2 was measured within the transmission IC, while the temperatures used for the correction of the signals of Monitor 1 and 3 were measured outside but near to these ICs. The air pressure used for the air density correction of the signal of Monitor 1 and 2 was measured at the same height as these ICs within the irradiation room, the pressure used for the correction of the signal of Monitor 3 was measured in the so called "pressureboard" within the accelerator head.[2] For a magnetic flux density of 1.4 T generated between the pole shoes of the electromagnet, a correction of the "2T error" of the linac was required. This issue is explained in the following. The electron beam generated by the linac is guided through several magnets inside the accelerator before its "conversion" into a photon beam by hitting the Bremsstrahlung target ("source") in the accelerator head. This guidance is sensitive to additional magnetic fields. An error occurs as soon as the source is no longer hit centrally by the electron beam. In standard clinical use of the linac, this error can occur due to changes of the terrestrial magnetic field experienced by the accelerator head when it is rotated to different positions corresponding to different heights of the accelerator head above the floor. In the present experiment, the "2T error" is triggered by the stray magnetic field accompanying the magnetic

[2] The information regarding Monitor 3 was obtained from personal communication with an Elekta service engineer.

Table B.1: Overview of the measurement points taken with Monitor 1, 2a/b, and 3 for each magnetic flux density setting at the electromagnet. The first column gives the identifier used for each situation in the following. The magnetic flux densities given in the third column are achieved between the pole shoes of the electromagnet by setting the current given in the forth column.

Situation	Measurement points	Magnetic flux density [T]	Current [A]
A_{before}	1 to 26	0	0
A	28 to 50	0.35	10.5
A_{after}	54 to 76	0	0
B_{before}	112 to 143	0	0
B	155 to 176	1.0	31.5
B_{after}	182 to 206	0	0
C_{before}	270 to 291	0	0
C	310 to 331	1.4	57.45
C_{after}	344 to 380	0	0
D_{before}	444 to 465	0	0
D	472 to 492	0.7	21.3
D_{after}	499 to 520	0	0

field generated by the electromagnet[3]. The "2T error" was corrected manually after switching on the magnetic field with 1.4 T flux density, i.e. the flux densities at the magnets used for beam guidance within the accelerator head were adapted such that the source was hit centrally again. This adaptation was revoked after switching the electromagnet off. The following section describes how the correction factors addessing the impairment of Monitor 2 and 3 by the stray magnetic field were determined based on the data taken in the present experiment.

[3] This error is not triggered during the generation of magnetic fields up to 1.2 T due to the weaker accompanying stray fields.

B.2 Analysis

The aim of this analysis is the determination of the correction factors $c_{strayB,monX,j}$ addressing the impact of the stray magnetic field accompanying a magnetic field with flux density j generated by the electromagnet in front of the linac on the signals of Monitor 2 and 3. The necessary steps in order to obtain $c_{strayB,monX,j}$ are described in the following sections. All uncertainties given in the following are given for a coverage factor $k = 1$. Please note, that absolute uncertainties are indicated with u, while relative uncertainties are indicated with u_r.

B.2.1 Underlying type B uncertainty budget associated with a single measurement of the different monitors

In this section, the type B uncertainties of the monitor signals for a single measurement point (see Table B.1) are given for Monitor 1, 2a/b, and 3. These uncertainties are required for the determination of the uncertainty associated with the mean signal $S_{monX,sitY}$ in Section B.2.2.
For the signal of Monitor 1 at a single measurement point, contributions of 0.05 % for the current measurement, of $\frac{0.1\,\%}{\sqrt{3}}$ for random variation drift[4], of $\frac{0.01\,\%}{\sqrt{3}}$ for non-consideration of the leakage current, of $\frac{0.0341\,\%}{\sqrt{3}}$ for the deviation of the measured temperature from the temperature in the IC, and of 0.1 % for the influence of temperature variation on the measurement system are considered. Quadratic adding of these contributions results in a total type B uncertainty of 0.13 % associated with the signal of Monitor 1 at a single measurement point ($u_r^B(S_{(mon1,sitY),i}) = 0.13\,\%$, see Section B.2.2). The contributions due to changes of the air pressure and the temperature during one measurement, and due to deviation of the measured pressure from the pressure in the IC are negligible. The contributions due to the uncertainty due to the barometer and the thermometer calibration, and the contributions due to deviations from the reference conditions cancel out since each single measurement is affected in the same manner.
For Monitor 2a/b, the uncertainty budget is almost the same as the budget presented for Monitor 1 above. However, a larger contribution of 0.1 % is considered for the deviation of the measured temperature from the temperature in the IC, due to the larger temperature gradient in the larger sensitive volume of this IC. Quadratic adding of the contributions results, thus, in a total type B uncertainty of 0.16 % associated with the signal of Monitor 2a/b at a single measurement point ($u_r^B(S_{(mon2a/b,sitY),i}) = 0.16\,\%$, see Section B.2.2). Please note, that this applies to both Monitor 2a and 2b.
According to the experience in the group, the signal of Monitor 3 shows larger variations than the signal of Monitor 2a/b (see Section 3.1.3). Larger contributions are, thus, considered in the uncertrainty budget for the signal of Monitor 3 at a single

[4] The division by $\sqrt{3}$ here and below is due to the underlying uniform probabilty density function.

measurement point. The considered contributions are 0.1 % for the current measurement, $\frac{0.2\,\%}{\sqrt{3}}$ for random variation drift, $\frac{0.01\,\%}{\sqrt{3}}$ for non-consideration of the leakage current, $\frac{0.1\,\%}{\sqrt{3}}$ for the deviation of the measured pressure from the pressure in the IC, $\frac{0.2\,\%}{\sqrt{3}}$ for the deviation of the measured temperature from the temperature in the IC, and 0.1 % for the influence of temperature variation on the measurement system. Quadratic adding of these contributions results in a total type B uncertainty of 0.22 % associated with the signal of Monitor 3 at a single measurement point ($u_r^B(S_{(mon3,sitY),i}) = 0.22\,\%$, see Section B.2.2). As for Monitor 1, the contributions due to changes of the air pressure and the temperature during one measurement are negligible, and the contributions due to the uncertainty of the barometer and the thermometer calibration cancel out since each single measurement is affected in the same manner.

B.2.2 Obtaining the mean signal $S_{monX,sitY}$ for Monitor X and Situation Y

During the continuous irradiation (see Section B.1.4), the signals of Monitor 1, 2a/b, and 3 were automatically averaged every ten seconds and these averaged signals were recorded in a log file. The magnetic flux density setting at the electromagnet was changed such, that at least 20 measurement points of Monitor 1, 2a/b, and 3 per magnetic flux density setting were obtained. The mean signal $S_{monX,sitY}$ is calculated from these n (with $n \geq 20$) recorded values $S_{(monX,sitY),i}$ for Monitor X (with $X = \{1, 2a, 2b, 3\}$) and Situation Y (with $Y = \{A_{before}, A, ..., D, D_{after}\}$, see Table B.1 for the identifiers of the situations) according to

$$S_{monX,sitY} = \frac{1}{n} \cdot \sum_{i=1}^{n} S_{(monX,sitY),i} \tag{B.1}$$

The type A uncertainty associated with this mean signal $S_{monX,sitY}$, i.e. the standard deviation of the mean values, is calculated according to

$$\begin{aligned} u^A(S_{monX,sitY}) &= \sqrt{\frac{1}{n \cdot (n-1)} \cdot \sum_{i=1}^{n} \left(S_{(monX,sitY),i} - S_{monX,sitY}\right)^2} \\ u_r^A(S_{monX,sitY}) &= \frac{u^A(S_{monX,sitY})}{S_{monX,sitY}} \end{aligned} \tag{B.2}$$

In addition to the type A uncertainty, there is a type B uncertainty associated with $S_{monX,sitY}$. It is obtained from error propagation starting with the underlying type B uncertainties associated with $S_{(monX,sitY),i}$, which were presented in Section B.2.1. These type B uncertainties associated with the signals of the single

measurement points for Monitor 1, 2a/b, and 3 are:

$$\begin{aligned} u_r^B(S_{(mon1,sitY),i}) &= 0.13\,\% \\ u_r^B(S_{(mon2a/b,sitY),i}) &= 0.16\,\% \\ u_r^B(S_{(mon3,sitY),i}) &= 0.22\,\% \end{aligned} \tag{B.3}$$

According to error propagation, the uncertainties associated with the mean signal $S_{monX,sitY}$ are obtained as

$$u^B(S_{monX,sitY}) = \frac{1}{n} \cdot \sqrt{\sum_{i=1}^{n} (u^B(S_{(monX,sitY),i}))^2} \tag{B.4}$$

The total uncertainty associated with the mean signal $S_{monX,sitY}$ is obtained by quadratic adding of the type A and the type B contribution:

$$u_r^{tot}(S_{monX,sitY}) = \sqrt{u_r^A(S_{monX,sitY})^2 + u_r^B(S_{monX,sitY})^2} \tag{B.5}$$

The obtained mean signals $S_{monX,sitY}$ for Monitor 1, 2a/b, and 3 for the situations listed in Table B.1 are shown in Figure B.2. The mean signals $S_{monX,sitY}$ in these graphs are normalised to $S_{monX,sitCbefore}$[5]. The normalisation was performed by dividing the original values and their associated uncertainties by the rounded values for $S_{monX,sitCbefore}$.

B.2.3 Obtaining the normalised ratio $R^N_{monX,sitY}$ in order to remove the drift of the linac from the data

As visible in Figure B.2, the data $S_{monX,sitY}$ features an upward trend which is ascribed to the drift of the output of the linac in the course of the irradiation day (see Section 3.1.1). This drift – and the jumps due to the changes of the magnetic flux density setting at the electromagnet – are removed from the data by forming the ratio $R_{monX,sitY}$ of $S_{monX,sitY}$ and $S_{mon1,sitY}$ according to

$$R_{monX,sitY} = \frac{S_{monX,sitY}}{S_{mon1,sitY}} \tag{B.6}$$

The uncertainties associated with $R_{monX,sitY}$ are obtained as

$$u_r(R_{monX,sitY}) = \sqrt{u_r(S_{monX,sitY})^2 + u_r(S_{mon1,sitY})^2} \tag{B.7}$$

In order to obtain better comparability of the data, the values $R_{monX,sitY}$ are normalised to the rounded value of $R_{monX,sitCbefore}$ (see the previous section), i.e. values and uncertainties are divided by the rounded value of $R_{monX,sitCbefore}$:

$$R^N_{monX,sitY} = \frac{R_{monX,sitY}}{R_{monX,sitCbefore}} \tag{B.8}$$

[5] Signal $S_{monX,sitCbefore}$ was chosen for normalisation since it is the closest to the mean of the smallest ($S_{mon1,sitAbefore}$) and the largest obtained value ($S_{mon1,sitDbefore}$) for Monitor 1.

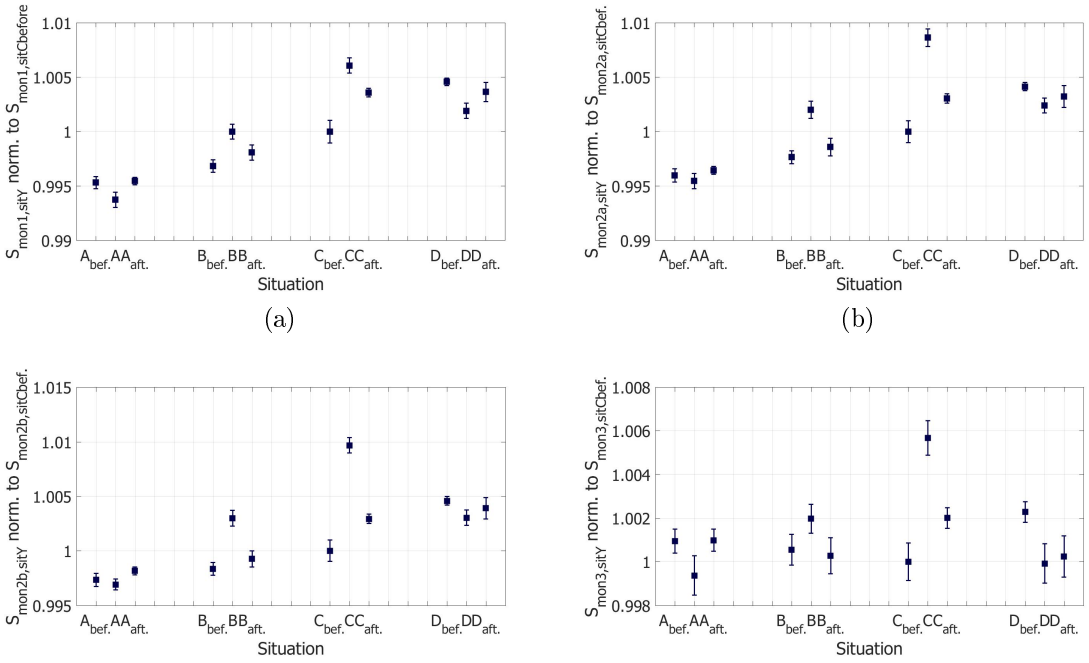

Figure B.2: Mean signals $S_{monX,sitY}$ normalised to the respective signal $S_{monX,sitCbefore}$, see text, for Monitor 1, 2a/b, and 3. An upward trend is apparent in the course of the irradiation day especially for Monitors 1 and 2a/b, which is largely ascribed to the drift in the output of the linac (see Section 3.1.1). It can also be seen, that the apparent jumps in the data of Monitor 1 are less pronounced than in the data of Monitor 2a/b and 3. This is according to the expectation since Monitor 1 is not affected by the stray magnetic field (but the signal it detects is affected by the impact of the stray magnetic field on the output of the linac, see Section B.1.4). All uncertainties shown refer to a coverage factor $k = 1$.

with

$$u_r(R^N_{monX,sitY}) = \frac{u(R^N_{monX,sitY})}{R^N_{monX,sitY}} \tag{B.9}$$

The obtained values $R^N_{monX,sitY}$ for Monitor 2a/b and 3 for the situations listed in Table B.1 are shown in Figure B.3.

B.2.4 Obtaining the correction factors $C_{monX,j}$ for the experimentally investigated magnetic flux density settings at the electromagnet

In this section it is described how the correction factor $C_{monX,j}$ was obtained. The correction factor $C_{monX,j}$ addresses the impact on Monitor X caused by a stray magnetic field accompanying a field with flux density j generated with the electromagnet in the setup with the electromagnet in front of the linac. The correction factor $C_{monX,j}$ was determined for the four experimentally investigated magnetic flux densities $j = (0.35, 0.7, 1.0, 1.4)$ T.
In a first step, the mean of $R^N_{monX,sitYbefore}$ and $R^N_{monX,sitYafter}$ was formed in order to enhedge the analysis against remaining drifts in the data (see the caption of Figure B.3):

$$R^N_{monX,sitY,0T} = \frac{1}{2} \cdot (R^N_{monX,sitYbefore} + R^N_{monX,sitYafter}) \tag{B.10}$$

The uncertainty associated with $R^N_{monX,sitY,0T}$ is obtained by

$$u(R^N_{monX,sitY,0T}) = \frac{1}{2} \cdot \sqrt{u(R^N_{monX,sitYbefore})^2 + u(R^N_{monX,sitYafter})^2} \tag{B.11}$$

Please note that "0T" was added to the index, replacing the differentiation of Situation Y_{before}, Y, and Y_{after}. The values previously denoted as $R^N_{monX,sitY}$ are from now on denoted as $R^N_{monX,sitY,j}$. For more clarity, the respective values in the updated

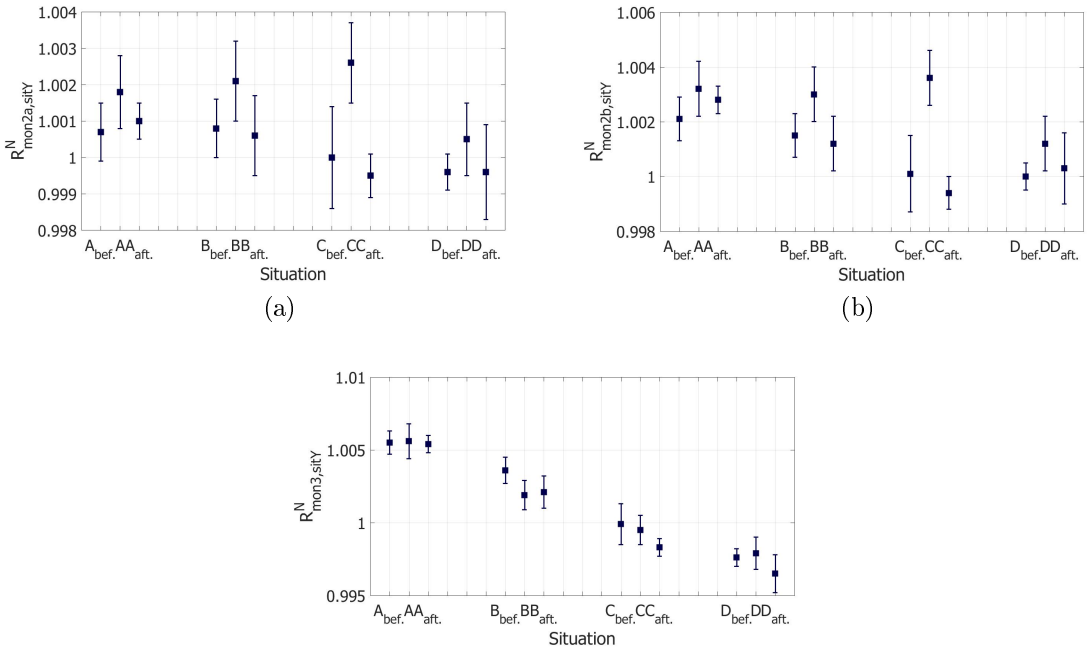

Figure B.3: Values $R^N_{monX,sitY}$ normalised to the respective signal $R_{monX,sitCbefore}$, see text. All uncertainties shown refer to a coverage factor $k = 1$. Apparently, the upward trend ascribed to the drift of the linac (see Figure B.2) is removed from the data. However, a slight overcompensation can be assumed for Monitor 2a and 2b which might origin in an additional drift of Monitor 1 in the course of the irradiation day. By forming the ratio $R^{(N)}_{mon3,sitY}$ a downward trend was imposed to the data of Monitor 3. This is due to the fact, that $S_{mon3,sitY}$ shows no apparent upward trend, which might be explained by the fact that this monitor is located within the accelerator head, which could lead to a similar drift of the output of the linac and the signal of Monitor 3 due to a similar warming experience. However, neither the overcompensation for Monitor 2a and 2b, nor the downward trend imposed to Monitor 3 are problematic in the following analysis since mean values of the data points of Situation Y_{before} and Y_{after} will be used, see Section B.2.4.

notation are listed below for Monitor 2a/b and 3.

$$
\begin{aligned}
R^N_{mon2a,sitA,0T} &= 1.0009 \pm 0.0005 \\
R^N_{mon2a,sitB,0T} &= 1.0007 \pm 0.0007 \\
R^N_{mon2a,sitC,0T} &= 0.9998 \pm 0.0008 \\
R^N_{mon2a,sitD,0T} &= 0.9996 \pm 0.0007
\end{aligned}
$$

$$
\begin{aligned}
R^N_{mon2a,sitA,0.35T} &= 1.0018 \pm 0.00010 \\
R^N_{mon2a,sitB,1.0T} &= 1.0021 \pm 0.00011 \\
R^N_{mon2a,sitC,1.4T} &= 1.0026 \pm 0.00011 \\
R^N_{mon2a,sitD,0.7T} &= 1.0005 \pm 0.00010
\end{aligned}
$$

$$
\begin{aligned}
R^N_{mon2b,sitA,0T} &= 1.0024 \pm 0.0005 \\
R^N_{mon2b,sitB,0T} &= 1.0014 \pm 0.0007 \\
R^N_{mon2b,sitC,0T} &= 0.9997 \pm 0.0008 \\
R^N_{mon2b,sitD,0T} &= 1.0002 \pm 0.0007
\end{aligned}
\tag{B.12}
$$

$$
\begin{aligned}
R^N_{mon2b,sitA,0.35T} &= 1.0032 \pm 0.00010 \\
R^N_{mon2b,sitB,1.0T} &= 1.0030 \pm 0.00010 \\
R^N_{mon2b,sitC,1.4T} &= 1.0036 \pm 0.00010 \\
R^N_{mon2b,sitD,0.7T} &= 1.0012 \pm 0.00010
\end{aligned}
$$

$$
\begin{aligned}
R^N_{mon3,sitA,0T} &= 1.0055 \pm 0.0005 \\
R^N_{mon3,sitB,0T} &= 1.0028 \pm 0.0007 \\
R^N_{mon3,sitC,0T} &= 0.9991 \pm 0.0007 \\
R^N_{mon3,sitD,0T} &= 0.9971 \pm 0.0007
\end{aligned}
$$

$$
\begin{aligned}
R^N_{mon3,sitA,0.35T} &= 1.0056 \pm 0.00012 \\
R^N_{mon3,sitB,1.0T} &= 1.0019 \pm 0.00010 \\
R^N_{mon3,sitC,1.4T} &= 0.9995 \pm 0.00010 \\
R^N_{mon3,sitD,0.7T} &= 0.9979 \pm 0.00011
\end{aligned}
$$

In the second step, the correction factor $C_{monX,j}$ was introduced as the factor correcting $R^N_{monX,sitY,j}$ (calculated by Equations B.6 and B.8, and re-written in the

updated notation as described above) to the value $R^N_{monX,sitY,0T}$ (calculated according to Equation B.10) which is unaffected by the stray magnetic field accompanying the magnetic field with flux density j generated by the electromagnet:

$$R^N_{monX,sitY,j} \cdot C_{monX,j} = R^N_{monX,sitY,0T} \tag{B.13}$$

The correction factor $C_{monX,j}$ is, thus, obtained from

$$C_{monX,j} = \frac{R^N_{monX,sitY,0T}}{R^N_{monX,sitY,j}} \tag{B.14}$$

with the associated uncertainty

$$u_r(C_{monX,j}) = \sqrt{u_r(R^N_{monX,sitY,0T})^2 + u_r(R^N_{monX,sitY,j})^2} \tag{B.15}$$

The results for the correction factor $C_{monX,j}$ for the Monitors 2a, 2b, and 3 for the magnetic flux densities $j = (0.35, 0.7, 1.0, 1.4)$ T generated by the electromagnet are listed in Table B.2 and shown in Figure B.4. The correction factors $C_{mon2a,j}$ and $C_{mon2b,j}$ obtained for the two chambers of Monitor 2 agree well with each other within the standard uncertainty ($k = 1$). The correction factors $C_{mon2b,j}$ for $j = (1.0, 1.4)$ T agree with the correction factors $C_{mon3,j}$ within the expanded uncertainty with coverage factor $k = 2$. The correction factors $C_{mon3,j}$ equal unity within the standard uncertainty for all magnetic flux densities investigated while the correction factors $C_{mon2a/b,j}$ seem to follow a down trend for increasing magnetic flux density. The optical impression can, however, be misleading since the human brain is not able to "spontaneously deal correctly with confidence margins" [Dose, 2002]. A test based on Bayesian principles whether it is more likely for the data to represent a constant or a linear model (based on Equation (207) from [Dose, 2002]) was, thus, performed for the correction factors $C_{monX,j}$ obtained for Monitor 2a, 2b, and 3. The test was performed twice for the correction factors $C_{monX,j}$ obtained for each monitor. In one case, a data point for the situation without a magnetic field (0 T) was included as unity with vanishing uncertainty, i.e. $C_{monX,0T} = 1 \pm 1 \times 10^{-8}$. In the other case, no data point at 0 T was included and only the four experimentally determined values shown in Figure B.4 were considered. The results of these tests are summarised in Table B.3.

B.2.5 Obtaining the final correction factors $c_{strayB,monX,j}$ from the experimental data by least squares fitting

The presented experiment allowed to determine the correction factors $C_{monX,j}$ for the impact that a stray magnetic field accompanying a field with flux density $j = (0.35, 0.7, 1.0, 1.4)$ T generated by the electromagnet has on the Monitors 2a, 2b, and 3. This section describes how the final correction factors $c_{strayB,monX,j}$ for any magnetic flux density between 0 T and 1.4 T can be derived from the experimental

Table B.2: Results for the correction factor $C_{monX,j}$ addressing the impact that the stray magnetic field accompanying a magnetic field with flux densitiy $j = (0.35, 0.7, 1.0, 1.4)$ T generated by the electromagnet has on the Monitors $X = \{2a, 2b, 3\}$. All uncertainties given refer to a coverage factor $k = 1$.

Magnetic flux density j [T]	Monitor 2a	Monitor 2b	Monitor 3
0.35	0.9991 ± 0.0011	0.9992 ± 0.0011	0.9999 ± 0.0012
1.0	0.9986 ± 0.0013	0.9984 ± 0.0012	1.0010 ± 0.0012
1.4	0.9972 ± 0.0013	0.9961 ± 0.0012	0.9996 ± 0.0013
0.7	0.9991 ± 0.0012	0.9990 ± 0.0012	0.9991 ± 0.0013

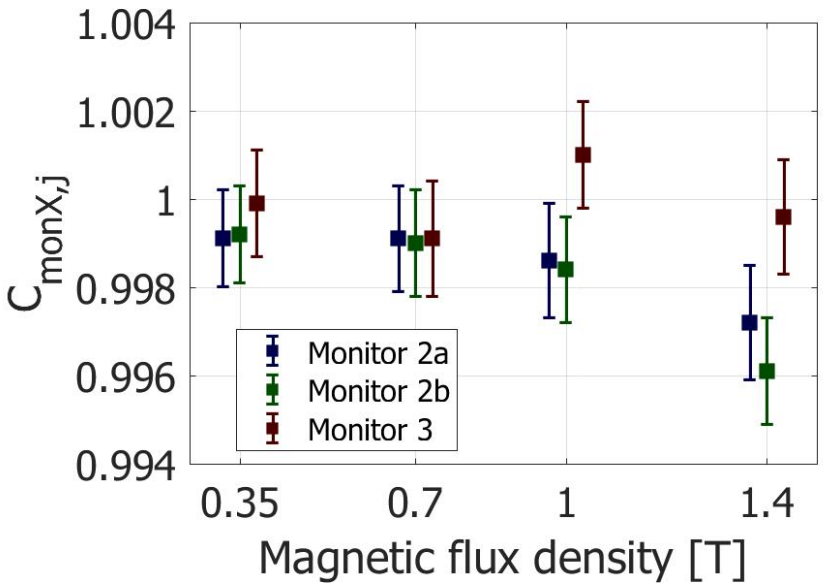

Figure B.4: Results for the correction factor $C_{monX,j}$ addressing the impact that the stray magnetic field accompanying a magnetic field with flux densitiy $j = (0.35, 0.7, 1.0, 1.4)$ T generated by the electromagnet has on the Monitors $X = \{2a, 2b, 3\}$. All uncertainties shown refer to a coverage factor $k = 1$. Please note that all values for all monitors were obtained for the same flux densities $j = (0.35, 0.7, 1.0, 1.4)$ T, however, their position respective to the abscissa was straightened out in order to improve the visual perceptibility.

Table B.3: Results of the tests based on Bayesian principles ([Dose, 2002], see text) whether it is more likely for the obtained data points for $C_{monX,j}$ to represent a constant or a linear model. Given is the ratio of probabilities $\frac{P_{lin}}{P_{const}}$ for a linear and a constant model and in brackets how many times more likely a constant model is, e.g. for Monitor 2a not considering a data point at 0 T, a constant model is 270-times more likely than a linear model. Please see the text for an explanation regarding the two versions of the test with respect to the data point $C_{monX,0T}$.

$C_{monX,0T}$	Monitor 2a	Monitor 2b	Monitor 3
$1 \pm 1 \times 10^{-8}$	$\frac{P_{lin}}{P_{const}} = 0.0247$; (40)	$\frac{P_{lin}}{P_{const}} = 0.4443$; (2.3)	$\frac{P_{lin}}{P_{const}} = 8.3967 \times 10^{-4}$; (1200)
–	$\frac{P_{lin}}{P_{const}} = 0.0037$; (270)	$\frac{P_{lin}}{P_{const}} = 0.0116$; (86)	$\frac{P_{lin}}{P_{const}} = 0.0020$; (500)

data. The approach was developed considering the results from the Bayesian test of linearity or constancy in the data, whose results are summarised in Table B.3. The situation for the correction factors $C_{mon2a,j}$ of Monitor 2a is ambiguous. Constancy in the data, and thus, a vanishing dependence on the magnetic flux density, appears probable. It is, hence, advisable to pragmatically determine a single correction factor $c_{strayB,mon2a,p}$ for all magnetic flux densities in the interval $(0\,T; 1.4\,T]$ by averaging the four experimentally determined correction factors $C_{monX,j}$. The situation for the correction factors $C_{mon2b,j}$ of Monitor 2b is different. Taking into account a data point at unity for 0 T, constancy is only twice as probable as a linear down trend. It is, hence, advisable in this case to perform a linear least squares fit to the data with fixed ordinate intercept at unity. The final correction factors $c_{strayB,mon2a,j}$ for any magnetic flux density j in the interval $(0\,T; 1.4\,T]$ can then by determined based on the resulting linear equation. The situation for the correction factors $C_{mon3,j}$ reveals again another scenario. Constancy is clearly more probable than for Monitor 2a and 2b, suggesting that an effect of the stray magnetic field on Monitor 3 is not measurable, which is in accordance with the expectation due to the larger distance between the electromagnet and Monitor 3. With the situation of Monitor 3 in mind and considering the fact that Monitor 2a and 2b are two chambers of the same transmission IC what makes a similar impairment by the stray magnetic field consequential it was decided that a linear fit is the method of choice for determining the final correction factors $c_{strayB,mon2a,j}$ for any magnetic flux density j in the interval $(0\,T; 1.4\,T]$.
In the following, the determination of the final correction factors $c_{strayB,monX,j}$ via the linear equation obtained from a least squares fit to the experimentally determined data points $C_{monX,j}$ is presented. The results are given for the stray magnetic fields

accompanying fields with flux densities of $j = (0.3, 0.6, 0.7, 0.9, 1.0, 1.2, 1.4)\,\mathrm{T}$ generated by the electromagnet, since these are the magnetic flux densities applied in the experiments of this thesis with the electromagnet in front of the linac (see Sections 3.1.1, 3.1.3, and 3.1.4). For each Monitor X, a linear function was fitted to the four respective data points $C_{monX,j}$ with a fixed ordinate intercept at unity, as no magnetic field implies a correction factor equaling unity. The least squares fits were performed using Origin 2018b. For Monitor 2a, the linear equation obtained from the least squares fit was

$$c_{strayB,mon2a,j} = 1 - 0.00175 \cdot j \tag{B.16}$$

for any magnetic flux density j in the interval $(0\,T; 1.4\,T]$. For Monitor 2b, the linear equation obtained from the least squares fit was

$$c_{strayB,mon2b,j} = 1 - 0.00225 \cdot j \tag{B.17}$$

for any magnetic flux density j in the interval $(0\,T; 1.4\,T]$. For Monitor 3, the linear equation obtained from the least squares fit was

$$c_{strayB,mon2b,j} = 1 - 0 \cdot j \tag{B.18}$$

for any magnetic flux density j in the interval $(0\,T; 1.4\,T]$. The relative uncertainty associated with $c_{strayB,monX,j}$ was set to one and a half times the mean relative uncertainty $u_r^{mean}(C_{monX,j})$ associated with the values $C_{monX,j}$ used for the linear fit:

$$u_r(c_{strayB,monX,j}) = \frac{3}{2} \cdot u_r^{mean}(C_{monX,j}) \tag{B.19}$$

with $u_r^{mean}(C_{mon2a,j}) = u_r^{mean}(C_{mon2b,j}) = 0.0012$ and $u_r^{mean}(C_{mon3,j}) = 0.0013$. Table B.4 shows an overview of the final correction factors $c_{strayB,monX,j}$ determined for the magnetic flux densities $j = (0.3, 0.6, 0.7, 0.9, 1.0, 1.2, 1.4)\,\mathrm{T}$, which are relevant in this thesis. Figure B.5 shows these correction factors $c_{strayB,monX,j}$ together with the experimentally determined data points $C_{monX,j}$ and the linear fit to these data points for Monitor 2a, 2b, and 3.

B.3 Results

The magnetic fields of interest in the experiments with the electromagnet in front of the linac performed in this thesis are $j = (0.3, 0.6, 0.7, 0.9, 1.0, 1.2, 1.4)\,\mathrm{T}$. In the following, the correction factors to be used for these flux densities for Monitor 2a, 2b, and 3 are summarised. Please note, that unity is to be used in the absence of a magnetic field independent of the monitor. Further, it was decided to directly use the experimentally available correction factors $C_{monX,j}$ for the magnetic flux densities 0.7 T and 1.4 T. For all other magnetic flux densities of interest, the correction factors $c_{strayB,monX,j}$ determined via a linear fit to the data points $C_{monX,j}$ are to

Table B.4: Final correction factors $c_{strayB,monX,j}$ determined for the impact of a stray magnetic field accompanying the magnetic flux densities $j = (0.3, 0.6, 0.7, 0.9, 1.0, 1.2, 1.4)$ T generated by the electromagnet in the experiments with the electromagnet in front of the linac on the Monitor X. Please note that the correction factor $c_{strayB,monX,0T}$ is set to unity since there is no impact without a magnetic field, and that the experimentally determined values $C_{monX,j}$ are used as $c_{strayB,monX,0.7T/1.4T}$ for 0.7 T and 1.4 T. All uncertainties given refer to a coverage factor $k = 1$.

j in [T]	Monitor 2a	Monitor 2b	Monitor 3
0.0	1	1	1
0.3	0.9995 ± 0.0018	0.9993 ± 0.0018	1.0000 ± 0.0020
0.6	0.9990 ± 0.0018	0.9987 ± 0.0018	1.0000 ± 0.0020
0.7	0.9991 ± 0.0012	0.9990 ± 0.0012	0.9991 ± 0.0013
0.9	0.9984 ± 0.0018	0.9980 ± 0.0018	1.0000 ± 0.0020
1.2	0.9979 ± 0.0018	0.9973 ± 0.0018	1.0000 ± 0.0020
1.4	0.9972 ± 0.0013	0.9961 ± 0.0012	0.9996 ± 0.0013

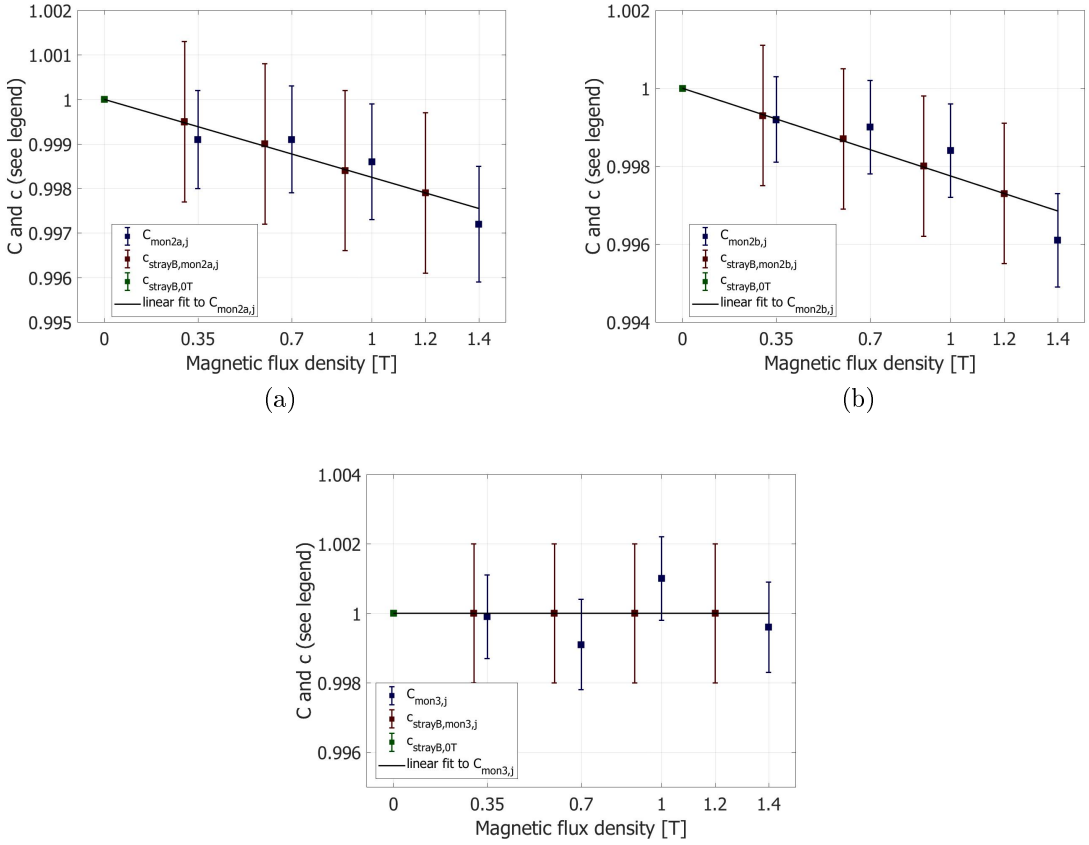

Figure B.5: Final correction factors $c_{strayB,monX,j}$ (red) for Monitor 2a (a), 2b (b), and 3 (c) determined for the magnetic flux densities $j = (0.3, 0.6, 0.7, 0.9, 1.0, 1.2, 1.4)$ T applied in the experiments with the electromagnet in front of the linac together with the experimentally determined data points $C_{monX,j}$ (blue) and the linear fit (black) to these data points. All uncertainties shown refer to a coverage factor $k = 1$.

be used. In the following, the relevant correction factors are listed ordered by the monitor they apply to. A graphic impression can be obtained from Figure B.5.

Monitor 2a:

$$\begin{aligned} c_{strayB,0T} &= 1 \\ c_{strayB,mon2a,0.3T} &= 0.9995 \pm 0.0018 \\ c_{strayB,mon2a,0.6T} &= 0.9990 \pm 0.0018 \\ c_{strayB,mon2a,0.7T} = C_{mon2a,0.7T} &= 0.9991 \pm 0.0012 \\ c_{strayB,mon2a,0.9T} &= 0.9984 \pm 0.0018 \\ c_{strayB,mon2a,1.2T} &= 0.9979 \pm 0.0018 \\ c_{strayB,mon2a,1.4T} = C_{mon2a,1.4T} &= 0.9972 \pm 0.0013 \end{aligned} \tag{B.20}$$

Monitor 2b:

$$\begin{aligned} c_{strayB,0T} &= 1 \\ c_{strayB,mon2b,0.3T} &= 0.9993 \pm 0.0018 \\ c_{strayB,mon2b,0.6T} &= 0.9987 \pm 0.0018 \\ c_{strayB,mon2b,0.7T} = C_{mon2b,0.7T} &= 0.9990 \pm 0.0012 \\ c_{strayB,mon2b,0.9T} &= 0.9980 \pm 0.0018 \\ c_{strayB,mon2b,1.2T} &= 0.9973 \pm 0.0018 \\ c_{strayB,mon2b,1.4T} = C_{mon2b,1.4T} &= 0.9961 \pm 0.0012 \end{aligned} \tag{B.21}$$

Monitor 3: Since the experimental values do not indicate an impairment of Monitor 3 by the stray magnetic field and since the linear fit to this experimental data reveals a linear equation with zero slope, $c_{strayB,mon3} = 1$ can be used for all magnetic flux densities in the intervall [0 T; 1.4 T].

B.4 Discussion and Conclusion

The aim of the present experiment was the investigation of the impact of the stray magnetic field on the monitoring transmission ICs in the experiments with the electromagnet in front of the linac (see Sections 3.1.1, 3.1.3, and 3.1.4). Correction factors, adressing the effect of the respective stray magnetic field were determined in the presented analysis.
Experiment and analysis were performed such that the drift of the output of the linac throughout the irradiation day does not impair the final results: (1) The raw data for the data points $C_{monX,j}$ was determined in the to and fro order 0.35 T – 1.0 T – 1.4 T – 0.7 T, (2) the mean signals of Monitor 2a, 2b, and 3 for these flux densities were divided by the signal of Monitor 1, a Farmer-type IC positioned well outside the stray magnetic field whose signal is affected by the drift of the linac in the

same manner as the signals of Monitor 2a/b and 3[6], and (3) the data points $C_{monX,j}$ were determined relative to mean signals of the respective monitor in the absence of a magnetic field measured immediately prior and after the measurement at the magnetic flux density j. These three measures ensure that the final results are not impaired by any drift (due to the linac or another aspect within the experiment).
The decision on how to determine correction factors for magnetic flux densities not directly measured in the experiment was made according to the results of a test applying Bayesian principles whether it is more likely for the obtained data to be described by a constant or by a linear model. According to the findings of the test, it was decided to determine the correction factors for any magnetic flux density j in the interval $(0\,T; 1.4\,T]$ based on a linear least squares fit to the data points $C_{monX,j}$.
The final correction factors are summarised in Section B.3. The chosen method of analysis reveals no measurable effect of the stray magnetic field on Monitor 3. This is according to the expectation based on the ample distance between Monitor 3 and the electromagnet and, thus, serves as a proof of consistency for the performed analysis.
The presented experiment was performed with a photon beam with a nominal accelerating potential of 6 MV. However, it can be assumed that the determined correction factors apply for irradiations with 10 MV and 15 MV as well. The correction factors can, thus, be used in the analysis of all experiments within this thesis with the electromagnet in front of the linac. Please note, however, that these correction factors are only valid for the setup with the electromagnet in front of the linac with the positioning as described in Section 3.1.1. The correction factors have to be redetermined, as soon as the electromagnet is replaced by another electromagnet or relocated with respect to the transmission ICs.

[6] This measure does not only remove the drift from the data but also the jumps in the output of the linac during restabilisation after changes in the magnetic flux density setting at the electromagnet.

C Supplement to the characterisation at the Elekta Unity™ MR Linac device

The magnetic field correction factor k_{mag} and the product of correction factors ($K_Q \cdot k_{mag}$) were determined from the experiment described in Section 3.1.2. The resulting values were presented in Section 4.1.2. These values are mean values obtained from the single values of five alanine detectors. The mean values – as presented in Section 4.1.2 – together with the single values are shown in Table C.1 and Figure C.1 and in Table C.2 and Figure C.2, respectively. The ordinates in the graphs show the correction factor k_{mag} and the product of correction factors ($K_Q \cdot k_{mag}$), respectively, while the abscissae indicate whether it is a single value or a mean value.

Table C.1: Obtained values for the single correction factors k_{mag} for irradiations with the Elekta Unity™ MR Linac (7 MV, 1.5 T) and their mean, which is the final result. This correction factor k_{mag} converts the standard indication of the alanine dosimeter irradiated in the presence of a static magnetic field into the actual absorbed dose-to-water at the point of measurement in the presence of this magnetic field. (Coverage factor $k = 1$, the uncertainties given are absolute uncertainties.)

k_{mag}	
single values	mean value
0.999 ± 0.008	
0.996 ± 0.008	
1.000 ± 0.007	0.9971 ± 0.0033
0.993 ± 0.007	
0.998 ± 0.007	

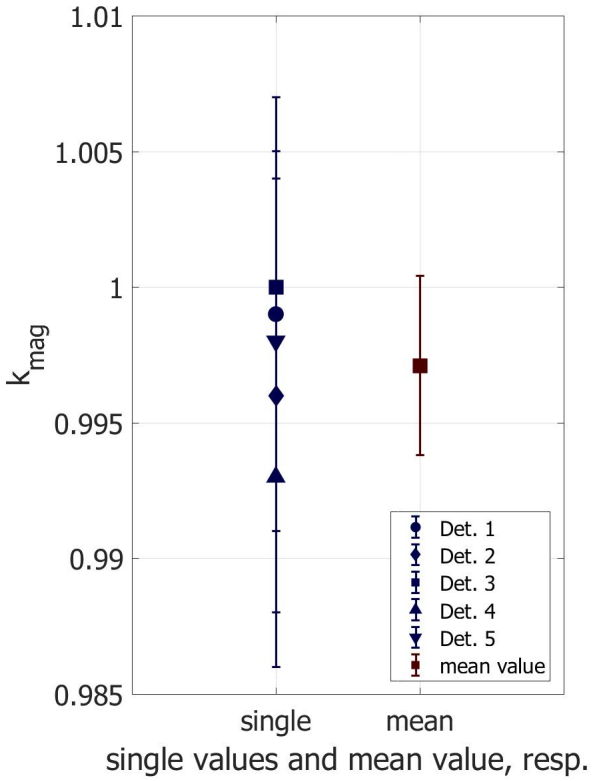

Figure C.1: Obtained values for the single correction factors k_{mag} (blue) for irradiations with the Elekta Unity™ MR Linac (7 MV, 1.5 T) and their mean (red), which is the final result. This correction factor k_{mag} converts the standard indication of the alanine dosimeter irradiated in the presence of a static magnetic field into the actual absorbed dose-to-water at the point of measurement in the presence of this magnetic field. (Coverage factor $k = 1$, the uncertainties given are absolute uncertainties.)

Table C.2: Values for the product of correction factors ($K_Q \cdot k_{mag}$) obtained from the individual alanine detectors for irradiations with the Elekta Unity™ MR Linac (7 MV, 1.5 T) and their mean, which is the final result. This product of correction factors ($K_Q \cdot k_{mag}$) converts the standard indication of the alanine dosimeter – without the radiation quality correction factor K_Q – irradiated in the presence of a static magnetic field into the actual absorbed dose-to-water at the point of measurement in the presence of this magnetic field. (Coverage factor $k = 1$, the uncertainties given are absolute uncertainties.)

$(K_Q \cdot k_{mag})$	
single values	mean value
1.003 ± 0.006	
1.000 ± 0.006	
1.004 ± 0.005	1.0011 ± 0.0024
0.997 ± 0.005	
1.002 ± 0.005	

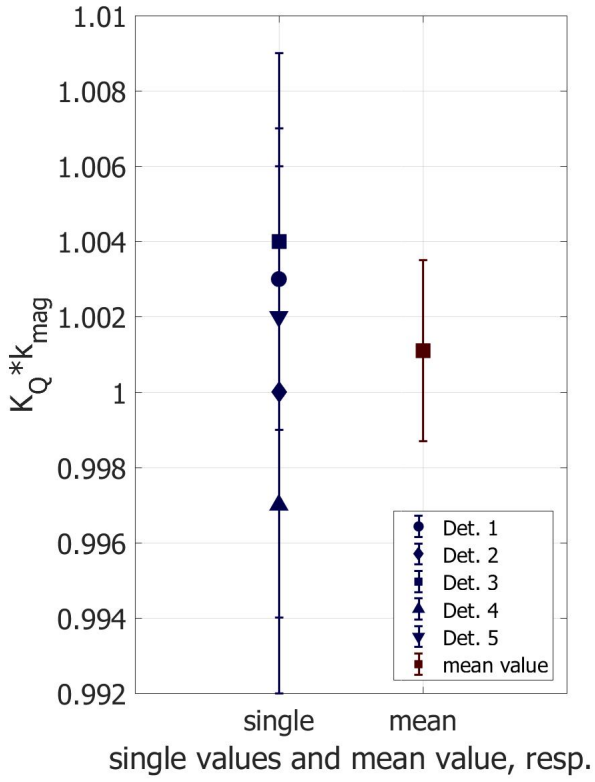

Figure C.2: Values for the product of correction factors ($K_Q \cdot k_{mag}$) obtained from the individual alanine detectors (blue) for irradiations with the Elekta Unity™ MR Linac (7 MV, 1.5 T) and their mean (red), which is the final result. This product of correction factors ($K_Q \cdot k_{mag}$) converts the standard indication of the alanine dosimeter – without the radiation quality correction factor K_Q – irradiated in the presence of a static magnetic field into the actual absorbed dose-to-water at the point of measurement in the presence of this magnetic field. (Coverage factor $k = 1$, the uncertainties given are absolute uncertainties.)

D Supplement to the characterisation in magnetic fields up to 1.4 T for 6 MV photons

D.1 Results for the correction factors k^*_{mag} and the $c_{\vec{B}}$ factors

The magnetic field correction factors k_{mag} for 6 MV photons in magnetic fields with flux densities of (0.3, 0.6, 0.9, 1.2, 1.4) T have been determined from the correction factors k^*_{mag} directly obtained from the experiment described in Section 3.1.3 and from the $c_{\vec{B}}$ factors obtained from the MC simulations in the geometry of this experiment (see Section 3.1.3). The correction factors k^*_{mag} convert the standard indication of the alanine dosimeter irradiated in the presence of a static magnetic field into the absorbed dose-to-water at the point of measurement in the absence of a magnetic field; the $c_{\vec{B}}$ factors convert the absorbed dose-to-water D in the absence of a static magnetic field at a point of interest into the absorbed dose-to-water $D^{\vec{B}}$ in the presence of the static magnetic field $\vec{B}$ (see Section 2.5). The resulting values for the correction factors k_{mag}, which convert the standard indication of the alanine dosimeter irradiated in the presence of a static magnetic field into the actual absorbed dose-to-water at the point of measurement in the presence of this magnetic field, have been presented in Section 4.1.3. The underlying correction factors k^*_{mag} and $c_{\vec{B}}$ factors are shown in this section in Table D.1 and Figure D.1 and in Table D.2 and Figure D.2, respectively. The ordinates in these graphs show the correction factors k^*_{mag} and the $c_{\vec{B}}$ factors, respectively, while the abscissae in these graphs show the flux density of the static magnetic field in Tesla. Figure D.3 shows the correction factors k_{mag}, k^*_{mag}, and $c_{\vec{B}}$ in a single graph. The ordinate in the graph shows the respective correction factor while the abscissa shows the flux density of the static magnetic field in Tesla.

The correction factors k^*_{mag} have been obtained from the experiment by averaging over the two individual irradiations in the absence of a magnetic field performed and by averaging over the the three irradiation runs performed. The results for the correction factors k^*_{mag} before averaging over the two individual irradiations in the absence of a magnetic field and before averaging over the three irradiation runs are also shown in this section.
The analysis of this experiment is based on the ratio of the alanine indication in the presence and in the absence of a static magnetic field (see Chapter 3.1.3). Two

alanine detectors were irradiated in the absence of a static magnetic field in each irradiation run. Thus, ratios of the alanine indications in the presence of (0.3, 0.6, 0.9, 1.2, 1.4) T were formed for the calculation of the correction factors k^*_{mag} once to the first alanine indication obtained in the absence of a magnetic field, and once to the second alanine indication obtained in the absence of a magnetic field. The mean of these two ratios was then taken for each of the flux densities (0.3, 0.6, 0.9, 1.2, 1.4) T. This mean was further used to calculate the correction factors k_{mag}. Figure D.4 shows the correction factors k^*_{mag} based on the single indications in the absence of a magnetic field before taking the mean together with the mean of these two correction factors. The correction factors are shown on the ordinate, the abscissa shows the magnetic flux density in Tesla. The figure shows that the correction factors k^*_{mag} based on the single indications in the absence of a magnetic field run in parallel in each irradiation run. The ratios obtained with the second indication in the absence of a magnetic field are larger in the first irradiation run while the ratios obtained with the first indication in the absence of a magnetic field are larger in the second and third irradiation run. The correction factors k^*_{mag} based on the single indications in the absence of a magnetic field agree with each other within the standard uncertainty ($k = 1$) in all cases.
The results obtained for the correction factors k^*_{mag} before averaging over the three individual irradiation runs I, II, and III, are shown in Figure D.5. The values shown here are the mean of the correction factors k^*_{mag} obtained using the single indications in the absence of a magnetic field (see above). The correction factors are shown on the ordinate, the abscissa shows the magnetic flux density in Tesla. The obtained values for the three runs agree within the standard uncertainty (coverage factor $k = 1$) for (0.3, 0.6, 0.9, 1.2) T. But they are spread for the flux density of 1.4 T. For 1.4 T, the agreement between the value for Run I and Run III and between Run II and Run III, respectively, is within the expanded uncertainty with coverage factor $k = 2$, the agreement between Run I and Run II is only within the expanded uncertainty with coverage factor $k = 3$. Figure D.6 shows these correction factors k^*_{mag} for the individual runs together with the mean values for the correction factors k^*_{mag} which are obtained by averaging over the three individual correction factors at the respective magnetic flux density. Again, the correction factors are shown on the ordinate, and the abscissa shows the magnetic flux density in Tesla. The averaging over the individual values for the three runs could only be questioned for the magnetic flux density of 1.4 T. Since it is, however, not clear which of the three values of the three individual irradiation runs is the most or the least reliable, it was decided to include all three values for averaging. Issues that could explain the spread of the data points at 1.4 T are discussed in Section 5.1.3.

D.2 Further investigations regarding the $c_{\vec{B}}$ factors

The general procedure for obtaining the $c_{\vec{B}}$ factors from MC simulations is described in Section 3.1.3. As mentioned there, the behaviour of the resulting $c_{\vec{B}}$ factors (see

Table D.1: Experimentally obtained values for the correction factors k^*_{mag} (6 MV). This correction factor converts the standard indication of the alanine dosimeter irradiated in the presence of a static magnetic field into the absorbed dose-to-water at the point of measurement in the absence of a magnetic field. (Coverage factor $k = 1$, the uncertainties given are absolute uncertainties.)

Magnetic flux density	k^*_{mag}
0 T	1 ± 0
0.3 T	0.9976 ± 0.0015
0.6 T	0.9976 ± 0.0015
0.9 T	0.9998 ± 0.0015
1.2 T	0.9991 ± 0.0015
1.4 T	1.0050 ± 0.0015

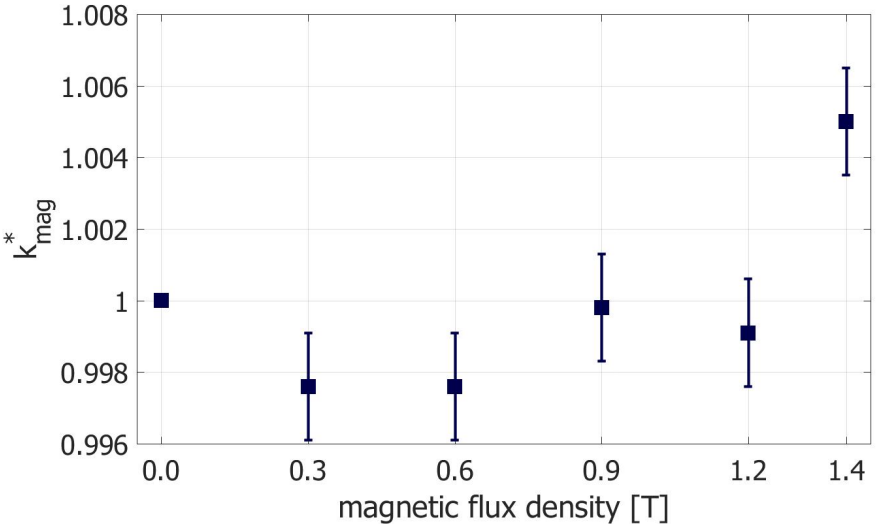

Figure D.1: Experimentally obtained values for the correction factors k^*_{mag} (6 MV). This correction factor converts the standard indication of the alanine dosimeter irradiated in the presence of a static magnetic field into the absorbed dose-to-water at the point of measurement in the absence of a magnetic field. (Coverage factor $k = 1$, the uncertainties given are absolute uncertainties.)

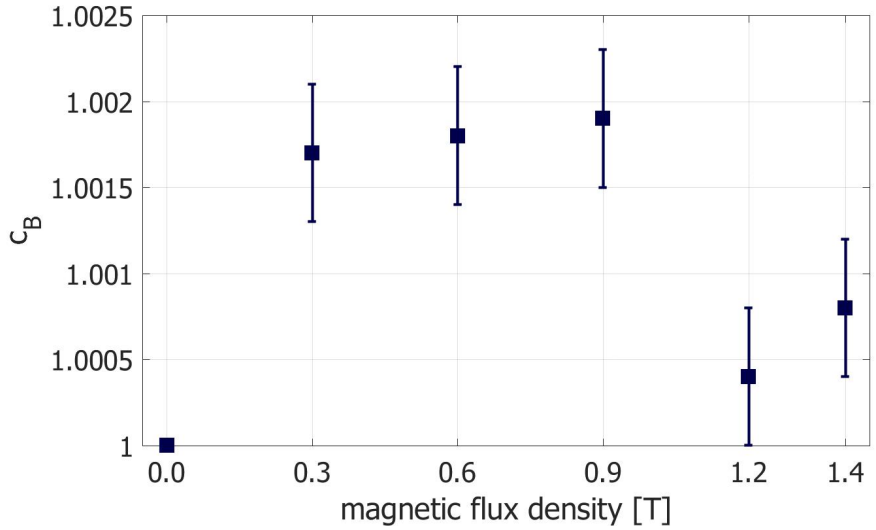

Figure D.2: $c_{\vec{B}}$ factors obtained from MC simulations (6 MV). This factor converts the absorbed dose-to-water D in the absence of a static magnetic field at a point of interest into the absorbed dose-to-water $D^{\vec{B}}$ in the presence of the static magnetic field $\vec{B}$. (Coverage factor $k = 1$, the uncertainties given are absolute uncertainties.)

Table D.2: $c_{\vec{B}}$ factors obtained from MC simulations (6 MV). This factor converts the absorbed dose-to-water D in the absence of a static magnetic field at a point of interest into the absorbed dose-to-water $D^{\vec{B}}$ in the presence of the static magnetic field $\vec{B}$. (Coverage factor $k = 1$, the uncertainties given are absolute uncertainties.)

Magnetic flux density	$c_{\vec{B}}$
0 T	1 ± 0
0.3 T	1.0017 ± 0.0004
0.6 T	1.0018 ± 0.0004
0.9 T	1.0019 ± 0.0004
1.2 T	1.0004 ± 0.0004
1.4 T	1.0008 ± 0.0004

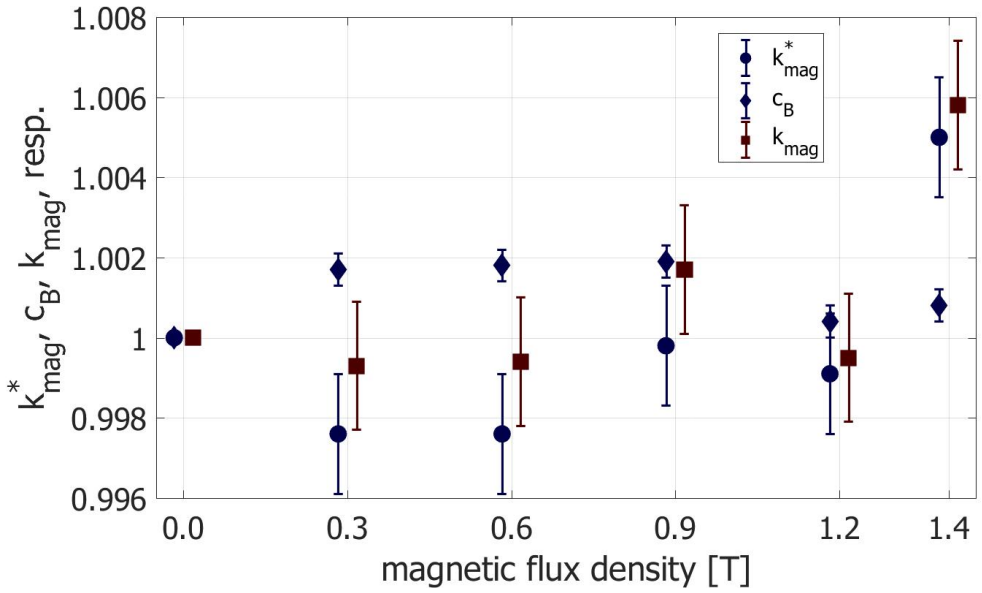

Figure D.3: Obtained correction factors k_{mag}, k^*_{mag}, and $c_{\vec{B}}$ in a single graph (6 MV). The correction factors k_{mag} are indicated by the red squares, the correction factors k^*_{mag} by the blue diamonds, and the $c_{\vec{B}}$ factors by the blue circles. Please note that the values for k_{mag}, k^*_{mag}, and $c_{\vec{B}}$ are plotted in a straightened way in order to improve the distinguishability; nevertheless, they refer to the same magnetic flux density each time. (Coverage factor $k = 1$, the uncertainties given are absolute uncertainties.)

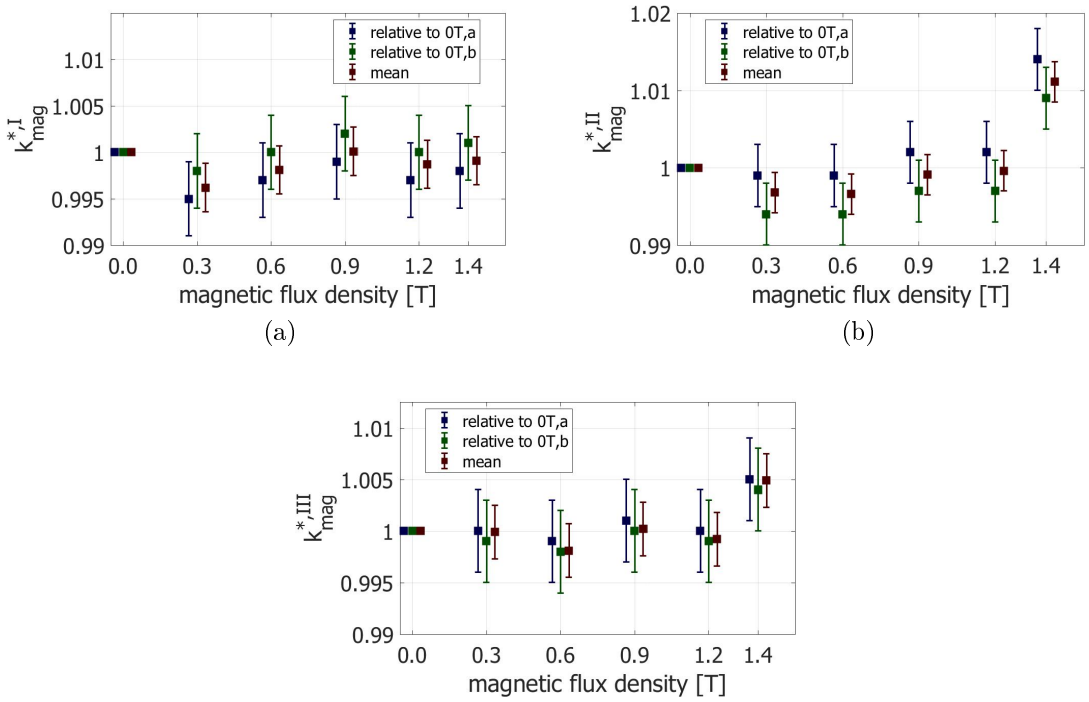

Figure D.4: The correction factors k^*_{mag} obtained using the single indications in the absence of a magnetic field and their mean for all three irradiation runs. (a) shows the results for irradiation run I, (b) for Run II, and (c) for Run III. The results obtained using the first indication in the absence of a magnetic field in each irradiation run ("relative to 0T,a") are displayed by blue symbols, the results obtained using the second indication in the absence of a magnetic field in each irradiation run ("relative to 0T,b") are displayed by green symbols. The mean of these two data points, which is used for calculating the final correction factors k_{mag}, is displayed by red symbols. Please note, that the shown data points correspond to the same magnetic flux density each time. They are presented in a straightened way in order to improve the distinguishability. (Coverage factor $k = 1$, the uncertainties given are absolute uncertainties.)

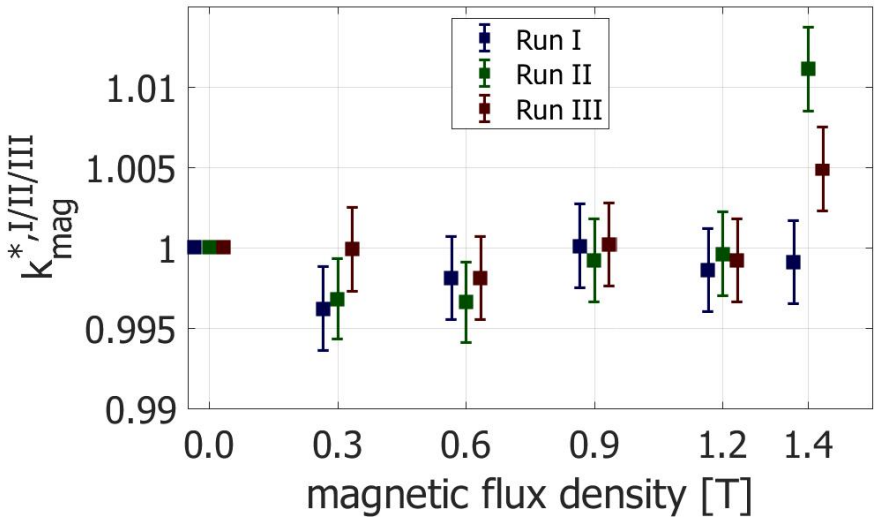

Figure D.5: Correction factors k^*_{mag} obtained by pure experiment after averaging over the two irradiations in the absence of a magnetic field. The results of the first irradiation run are shown in blue, the results of the second run in green, and of the third run in red. Please note, that the shown data points correspond to the same magnetic flux density each time. They are presented in a straightened way in order to improve the distinguishability. (Coverage factor $k = 1$, the uncertainties given are absolute uncertainties.)

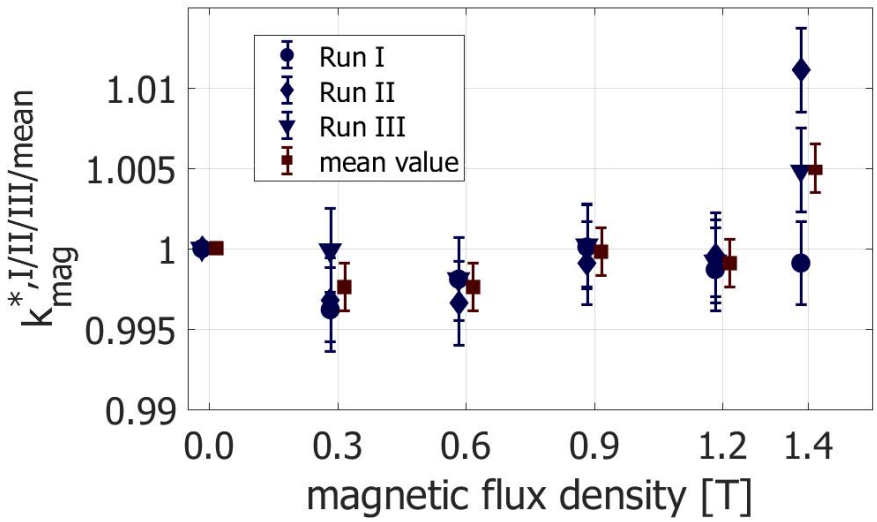

Figure D.6: Correction factors k^*_{mag} obtained by pure experiment. The mean values are shown in red, the results for the individual runs are shown in blue. (Coverage factor $k = 1$, the uncertainties given are absolute uncertainties.)

Table D.2 and Figure D.2 in Section D.1) was unexpected. The expectation was, that the $c_{\vec{B}}$ factors are smaller than unity and decrease linearly with increasing magnetic flux density. In order to better understand the reason for the different behaviour of the $c_{\vec{B}}$ factors in the experimentally applied setup, $c_{\vec{B}}$ factors were additionally determined for modified simulation geometries. All four simulation geometries are described in the following.

Setup D ("RealSetup") which was used for obtaining the $c_{\vec{B}}$ factors in the experimentally applied setup, is described in detail in Section 3.1.3. It should only be mentioned here, that this setup involves a water phantom with 7 cm width, 20 cm length, and 20 cm height, a photon field with 5 cm width and 10 cm height, and the pole shoes of the electromagnet. For this setup, the $c_{\vec{B}}$ factors for (0.3, 0.6, 0.9, 1.2, 1.4) T were determined, since these are the experimentally applied magnetic flux densities.

Setup C ("SetupWoElmag") consists of the same water phantom as in Setup D, and the same photon field as in Setup D is applied as well. However, the pole shoes of the electromagnet are not included in this setup. This setup was chosen since the first assumtion was, that the unexpected behaviour of the $c_{\vec{B}}$ factors in the experimentally applied setup could be due to backscattering from the pole shoes. For this setup, the $c_{\vec{B}}$ factors for (0.3, 0.9, 1.5, 3.0) T were determined, since this offers overlaps with the experimentally applied range of magnetic flux densities and with the range of magnetic flux densities applied in [van Asselen et al., 2018] (see below).

Setup B ("LikeAsselen") uses a setup more similar to the simulation geometry described in [van Asselen et al., 2018]. A water phantom with 40 cm width, 40 cm height, and 20 cm length[1] was used. The photon field was applied as in Setup D and C, and the pole shoes were not included as in Setup C. This setup – and the following Setup A – were chosen in order to be able to better compare the obtained $c_{\vec{B}}$ factors with the results given in [van Asselen et al., 2018]. For this setup, $c_{\vec{B}}$ factors for (0.9, 1.5, 3.0) T were determined, since this offers overlaps with the range of magnetic flux densities applied for Setup C and in [van Asselen et al., 2018].

Setup A ("LikeAsselen10x10") is the same as Setup B except of the fact, that a photon field with 10 cm width and 10 cm height is applied. As for Setup B, the $c_{\vec{B}}$ factors for (0.9, 1.5, 3.0) T were determined.

The resulting $c_{\vec{B}}$ factors for all four setups are shown in Figure D.7. The $c_{\vec{B}}$ factors are shown on the ordinate, the abscissa shows the magnetic flux density in Tesla. This compilation allows for the following observations: The $c_{\vec{B}}$ factors obtained with the Setups A and B show the expected behaviour: they are smaller than unity and decrease with increasing magnetic flux density. Under consideration that the beam quality used by [van Asselen et al., 2018] and in this work is not the same[2], the

[1] The water phantom used in [van Asselen et al., 2018] is cubic with a length of 40 cm. It was, however, decided to keep the length as in Setup D and C, since I preferred not to make any changes in the simulation code affecting the dose scoring in order to ensure the comparability of all results.

[2] The $TPR_{20,10}$ for the photon beam used in this work is 0.683 (without magnetic field, see Section 3.1.3), while [van Asselen et al., 2018] states a $TPR_{20,10}$ of 0.700.

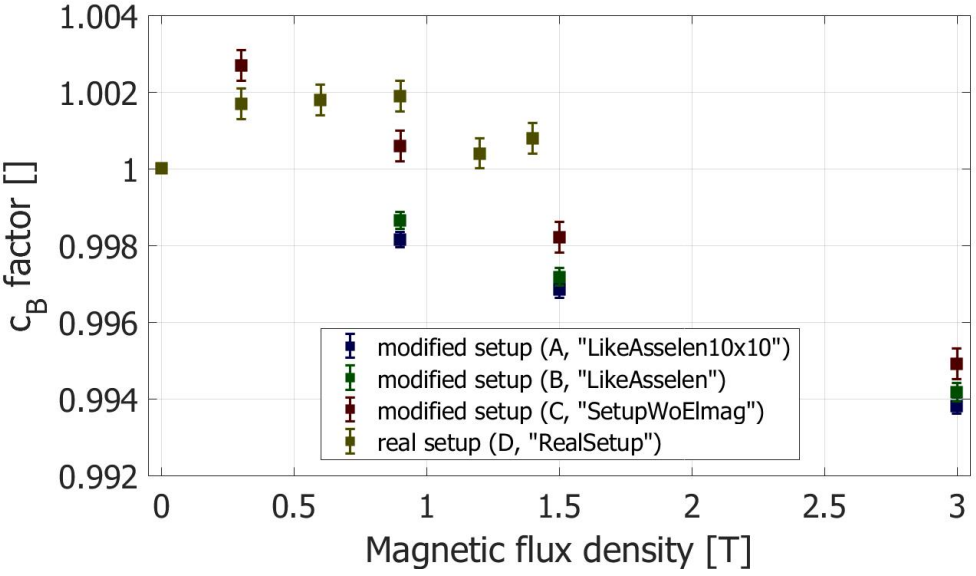

Figure D.7: $c_{\vec{B}}$ factors obtained from MC simulations with four different simulation geometries (see text). The yellow symbols show the $c_{\vec{B}}$ factors obtained for the experimentally applied setup (Setup D), and are also shown in Figure D.2. The $c_{\vec{B}}$ factors obtained for Setup A are shown in blue, the results for Setup B are shown in green, and for Setup C, they are shown in red. (Coverage factor $k = 1$, the uncertainties given are absolute uncertainties.)

resulting $c_{\vec{B}}$ factors obtained in this work agree well with the $c_{\vec{B}}$ factors presented in [van Asselen et al., 2018]. The $c_{\vec{B}}$ factors obtained with Setup C are according to the expectations for magnetic flux densities of 1.5 T and 3.0 T. The $c_{\vec{B}}$ factors obtained for magnetic flux densities of 0.3 T and 0.9 T in this setup, are, however, larger than unity. All $c_{\vec{B}}$ factors obtained with Setup D, which is the experimentally applied setup, are larger than unity.

It can, thus, be concluded that the reason for the unexpected behaviour of the $c_{\vec{B}}$ factors determined for the experimentally applied setup (i.e. that they are larger than unity and do not linearly decrease with increasing magnetic flux density) lies in the interplay of the measures of the water phantom and the electron trajectories in the presence of the respective magnetic flux density. The comparison of the results for Setup C and D shows, that backscattering from the pole shoes plays – if any – only a minor role.

D.3 Test based on Bayesian principles regarding the model representing the obtained correction factors k_{mag}

A test based on Bayesian principles whether it is more likely for the resulting correction factors k_{mag} (see Section 4.1.3) to represent a constant or a linear model (based on Equation (207) from [Dose, 2002]) revealed, that the probabilty P_{const} for a constant model is about 50-times higher than the probability P_{lin} for a linear model. The exact probability ratio depends on how the data point for 0 T is considered. Four versions of the test were performed: (1) The correction factor k_{mag} for 0 T was considered as $k_{mag,0T} = 1.0000 \pm 0.0016$, i.e. the uncertainty was set as for the other data points. (2) The correction factor k_{mag} for 0 T was considered as $k_{mag,0T} = 1.0000 \pm 1E-8$, i.e. the uncertainty was set to be vanishing. (3) The correction factor k_{mag} for 0 T was considered as $k_{mag,0T} = 1.0000 \pm 1E-80$, i.e. the uncertainty was decreased even further than in (2). (4) The correction factor k_{mag} for 0 T was not considered, i.e. the test considered only the data points from 0.3 T to 1.4 T. The results obtained in these four versions of the test are summarised in Table D.3. All versions of the test reveal a higher probability for a constant model, i.e. the test based on Bayesian principles seems to interpret the data point at 1.4 T as an outlier. Version (4) of the test is to be discarded, since it is an important information for the test that the data point at 0 T is expected to be unity. It has to be considered, too, that the knowledge about this data point at 0 T is higher than for the experimentally obtained data points. An about 50-times higher probablity for a constant model can, hence, be concluded. It is, however, important to keep in mind, that the performed test does only compare a constant model and a linear model. It is indeed possible, that the model to describe the obtained correction factors k_{mag} is not linear. The meaningfulness of the test is, thus, restricted for the 6 MV series. Nevertheless, the test was performed in order to be able to compare its results to the results of the test applied for the correction factors k_{mag} determined in the 10 MV and 15 MV series (see Section E.3).

Table D.3: Results of the test based on Bayesian principles described in [Dose, 2002] whether it is more likely for the obtained correction factors k_{mag} in the 6 MV series to represent a constant or a linear model. Given is the ratio of probabilities $\frac{P_{lin}}{P_{const}}$ for a linear and a constant model and in brackets how many times more likely a constant model is, e.g. in version (1) of the test, the constant model is 48-times more likely than a linear model.

Consideration of data point at 0 T	$\frac{P_{lin}}{P_{const}}$
(1): $k_{mag,0T} = 1.0000 \pm 0.0016$	0.0207 (48)
(2): $k_{mag,0T} = 1.0000 \pm 1E-8$	0.0189 (53)
(3): $k_{mag,0T} = 1.0000 \pm 1E-80$	0.0189 (53)
(4): $k_{mag,0T} = -$	0.0439 (23)

E Supplement to the investigation of the energy dependence in magnetic fields up to 1.4 T

E.1 Results for the correction factors k^*_{mag} and the $c_{\vec{B}}$ factors

The magnetic field correction factors k_{mag} for 10 MV and 15 MV photons in magnetic fields with flux densities of (0.7, 1.4) T have been determined in order to investigate the energy dependence of the correction factors k_{mag}. The correction factors k_{mag} are calculated from the correction factors k^*_{mag} which are directly obtained from the experiments described in Section 3.1.4 and from the $c_{\vec{B}}$ factors which are obtained from the MC simulations in the geometry of these experiments (see Section 3.1.4).[1] The resulting values for the correction factors k_{mag} are presented in Section 4.1.4. The underlying correction factors k^*_{mag} and the $c_{\vec{B}}$ factors are shown in this section in Table E.1 and Figure E.1 and in Table E.2 and Figure E.2, respectively. The ordinates in these graphs show the correction factors k^*_{mag} and the $c_{\vec{B}}$ factors, respectively, while the abscissae in these graphs show the flux density of the static magnetic field in Tesla. Figure E.3 shows the correction factors k_{mag}, k^*_{mag}, and $c_{\vec{B}}$ for 10 MV and 15 MV, respectively, in a single graph. The ordinates show the respective correction factor while the abscissae show the flux density of the static magnetic field in Tesla.

The correction factors k^*_{mag} for the 10 MV series show an increase with increasing magnetic flux density. The correction factor k^*_{mag} for 0.7 T equals unity within an expanded uncertainty with coverage factor $k = 2$, the correction factor k^*_{mag} for 1.4 T equals unity only within an expanded uncertainty with coverage factor $k = 6$. The correction factors k^*_{mag} for the 15 MV series also show an increase with increasing magnetic flux density. The correction factor k^*_{mag} for 0.7 T equals unity within an expanded uncertainty with coverage factor $k = 3$, the correction factor k^*_{mag} for 1.4 T equals unity only within an expanded uncertainty with coverage factor $k = 8$. The $c_{\vec{B}}$ factor in the 10 MV series for 0.7 T is larger than unity and equals unity only within an expanded uncertainty with coverage factor $k = 7$, the $c_{\vec{B}}$ factor for 1.4 T in the 10 MV series is smaller than unity and equals unity within an expanded uncertainty with coverage factor $k = 5$. The $c_{\vec{B}}$ factor for 0.7 T in the 15 MV series equals unity within the standard uncertainty ($k = 1$), the $c_{\vec{B}}$ factor for 1.4 T is smaller than

[1] A short description of the correction factors k^*_{mag} and the $c_{\vec{B}}$ factors is given in Section D.1.

unity and equals unity only within an expanded uncertainty with coverage factor $k = 3$. According to the results presented in Section D.2, these behaviours can be ascribed to the interplay of the measures of the water phantom and the electron trajectories in the presence of the respective magnetic flux density. The uncertainties associated with the $c_{\vec{B}}$ factors in the 15 MV series are larger by approximately a factor of two compared to the $c_{\vec{B}}$ factors determined in the investigations using 6 MV and 10 MV photon beams. This is due to an additional uncertainty component taking into account that a mohan spectrum had to be used since no phase space file for 15 MV photon beams was available for the applied linac (see Section E.2 below).
The correction factors k^*_{mag} have been obtained from the experiments by averaging over the two individual irradiations in the absence of a magnetic field performed and by averaging over the the three (four) irradiation runs performed in the irradiations with 10 MV (15 MV) photons. The results for the correction factors k^*_{mag} before averaging over the two individual irradiations in the absence of a magnetic field and before averaging over the three (four) irradiation runs are also shown in this section. The procedure for obtaining the correction factors k^*_{mag} is the same as described in Section D.1 for the 6 MV series with the only difference, that the magnetic flux densities in the 10 MV and 15 MV series are (0.7, 1.4) T and that there are four irradiation runs in the 15 MV series.
Figures E.4 and E.5 show the correction factors k^*_{mag} based on the single indications in the absence of a magnetic field before taking the mean, together with the mean of these two correction factors for 10 MV and 15 MV, respectively. The correction factors are shown on the ordinate, the abscissa shows the magnetic flux density in Tesla.
The figures show that the correction factors k^*_{mag} for both 10 MV and 15 MV based on the single indications in the absence of a magnetic field run in parallel in each irradiation run. The rounded values of the ratios obtained with the two indications in the absence of a magnetic field for 10 MV are the same in the first irradiation run while the ratios obtained with the second indication in the absence of a magnetic field are slightly larger in the second and third irradiation run. The ratios obtained with the first indication in the absence of a magnetic field for 15 MV are larger in the first and second irradiation run, while they are smaller in the third and fourth irradiation run. The correction factors k^*_{mag} based on the single indications in the absence of a magnetic field agree with each other within the standard uncertainty ($k = 1$) in all cases.
The results obtained for the correction factors k^*_{mag} for 10 MV before averaging over the three individual irradiation runs I, II, and III, are shown in Figure E.6, and the results obtained for the correction factors k^*_{mag} for 15 MV before averaging over the four individual irradiation runs I, II, III, and IV are shown in Figure E.7. The values shown in these figures are the mean of the correction factors k^*_{mag} obtained using the single indications in the absence of a magnetic field (see above). The correction factors are shown on the ordinates, the abscissae show the magnetic flux density in Tesla. The obtained values for 10 MV for the three runs agree within the standard uncertainty ($k = 1$) for both 0.7 T and 1.4 T. For 15 MV, the obtained values for

Table E.1: Experimentally obtained values for the correction factors k^*_{mag} (10 MV and 15 MV). This correction factor converts the standard indication of the alanine dosimeter irradiated in the presence of a static magnetic field into the absorbed dose-to-water at the point of measurement in the absence of a magnetic field. (Coverage factor $k = 1$, the uncertainties given are absolute uncertainties.)

Magnetic flux density	k^*_{mag} for 10 MV	k^*_{mag} for 15 MV
0 T	1 ± 0	1 ± 0
0.7 T	1.0025 ± 0.0015	1.0037 ± 0.0013
1.4 T	1.0089 ± 0.0015	1.0099 ± 0.0013

the four runs agree within the expanded uncertainty with coverage factor $k = 2$ for both 0.7 T and 1.4 T.
The Figures E.8 and E.9 show these correction factors k^*_{mag} for the individual runs together with the mean values for the correction factors k^*_{mag} which are obtained by averaging over the three (four) individual correction factors at the respective magnetic flux density. Again, the correction factors are shown on the ordinates, and the abscissae show the magnetic flux density in Tesla. The distribution of the values shows that averaging over the individual values for the three (four) runs is reasonable.
Please note that the order of magnetic flux densities in the experiments was (0, 0, 0.7, 1.4) T for all irradiation runs with 10 MV but (0, 0, 0.7, 1.4) T in Run I to III with 15 MV, and (0, 0.7, 1.4, 0) T in Run IV for 15 MV. There is no significant deviation between the correction factors k^*_{mag} from Run I to III and from Run IV at 15 MV. It can, hence, be concluded, that both orders are equally reliable.

E.2 Determination of the correction factor k_{mohan} required due to the lacking phase space file

As mentioned in Section 3.1.4, the ddcs for determining the $c_{\vec{B}}$ factors required for the investigation of the response of the alanine dosimeter to 15 MV photon beams in magnetic fields with flux densities of 0.7 T and 1.4 T were obtained using a mohan spectrum whereas the $c_{\vec{B}}$ factors for the investigations in 6 MV and 10 MV photon beams were obtained using phase space files. The mohan spectrum for 15 MV was applied since no phase space file was available for the linac at the nominal acceler-

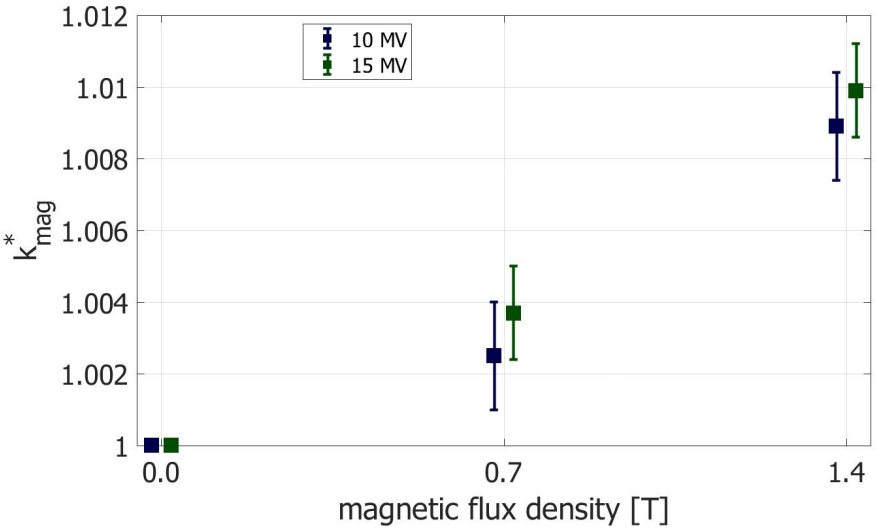

Figure E.1: Experimentally obtained values for the correction factors k^*_{mag} for 10 MV (blue) and 15 MV (green). This correction factor converts the standard indication of the alanine dosimeter irradiated in the presence of a static magnetic field into the absorbed dose-to-water at the point of measurement in the absence of a magnetic field. (Coverage factor $k = 1$, the uncertainties given are absolute uncertainties.)

Table E.2: $c_{\vec{B}}$ factors obtained from MC simulations (10 MV and 15 MV). This factor converts the absorbed dose-to-water D in the absence of a static magnetic field at a point of interest into the absorbed dose-to-water $D^{\vec{B}}$ in the presence of the static magnetic field $\vec{B}$. (Coverage factor $k = 1$, the uncertainties given are absolute uncertainties.) Please note that the higher associated uncertainty for 15 MV results from the correction factor k_{mohan} which is additionally required for that radiation quality since no phase space file was available, see Section E.2.

Magnetic flux density	$c_{\vec{B}}$ for 10 MV	$c_{\vec{B}}$ for 15 MV
0 T	1 ± 0	1 ± 0
0.7 T	1.00214 ± 0.00033	1.0019 ± 0.0023
1.4 T	0.99839 ± 0.00035	0.9951 ± 0.0023

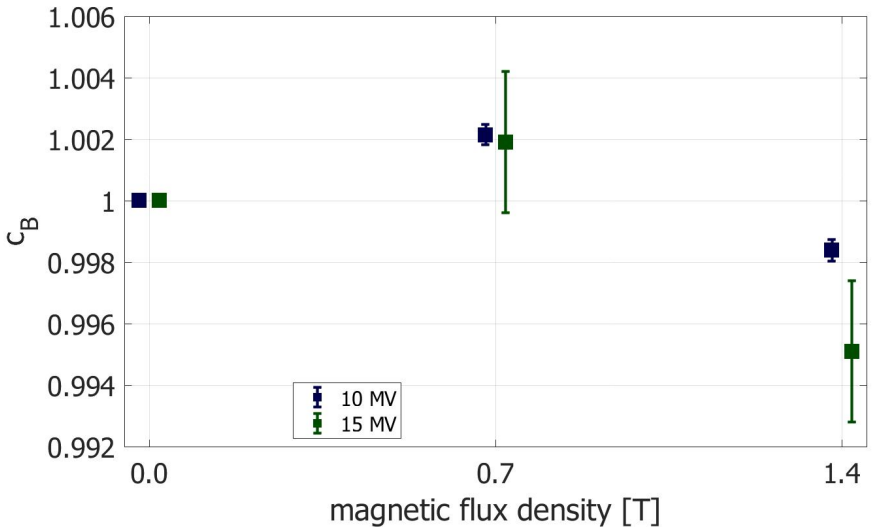

Figure E.2: $c_{\vec{B}}$ factors obtained from MC simulations for 10 MV (blue) and 15 MV (green). This factor converts the absorbed dose-to-water D in the absence of a static magnetic field at a point of interest into the absorbed dose-to-water $D^{\vec{B}}$ in the presence of the static magnetic field $\vec{B}$. (Coverage factor $k = 1$, the uncertainties given are absolute uncertainties.) Please note that the higher associated uncertainty for 15 MV results from the correction factor k_{mohan} which is additionally required for that radiation quality since no phase space file was available, see Section E.2.

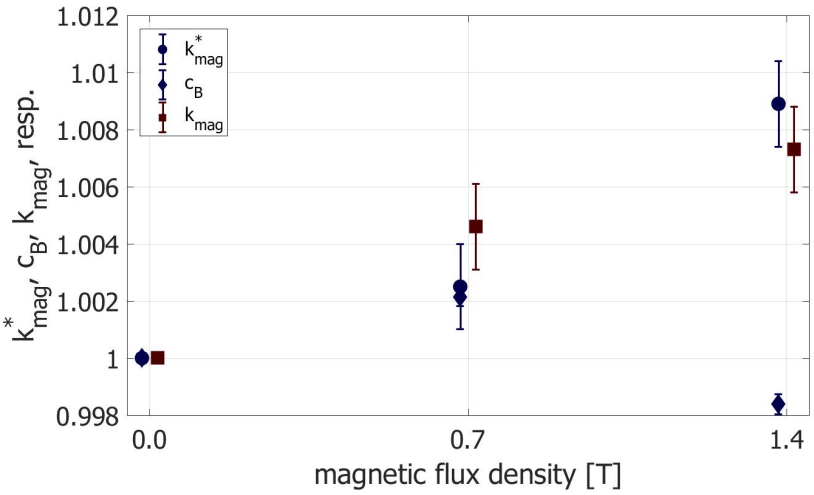

(a)

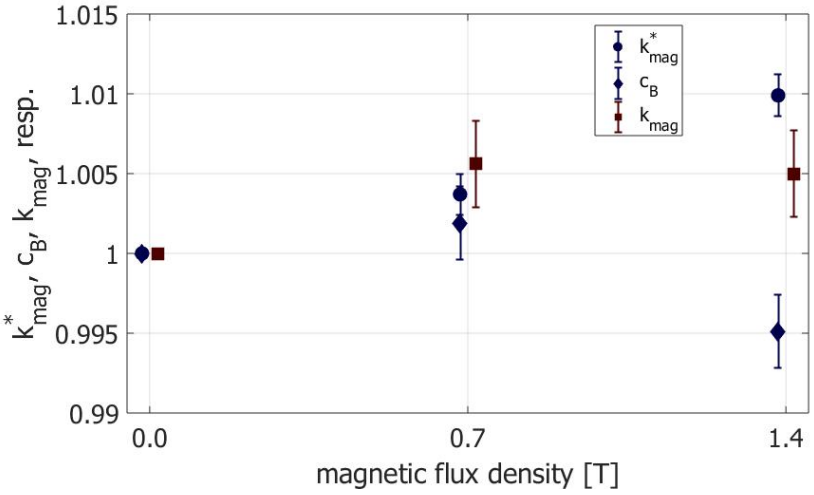

(b)

Figure E.3: Obtained correction factors k_{mag}, k^*_{mag}, and $c_{\vec{B}}$ in a single graph. (a) shows the respective factors for 10 MV and (b) for 15 MV. The correction factors k_{mag} are indicated by the red squares, the correction factors k^*_{mag} by the blue diamonds, and the $c_{\vec{B}}$ factors by the blue circles. Please note that the values for k_{mag}, k^*_{mag}, and $c_{\vec{B}}$ are plotted in a straightened way in order to improve the distinguishability; nevertheless, they refer to the same magnetic flux density each time. (Coverage factor $k = 1$, the uncertainties given are absolute uncertainties.)

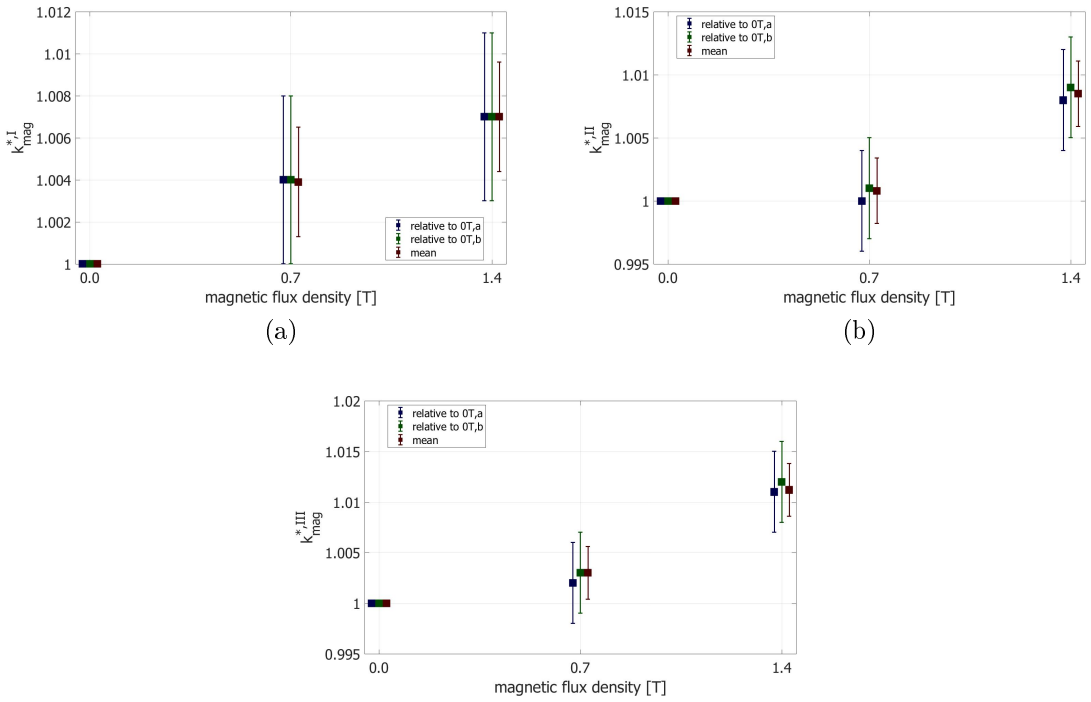

Figure E.4: The correction factors k^*_{mag} obtained using the single indications in the absence of a magnetic field and their mean for all three irradiation runs with 10 MV photons. (a) shows the results for the first irradiation run, (b) for the second, and (c) for the third. The results obtained using the first indication in the absence of a magnetic field in each irradiation run ("relative to 0T,a") are displayed by blue symbols, the results obtained using the second indication in the absence of a magnetic field in each irradiation run ("relative to 0T,b") are displayed by green symbols. The mean of these two data points, which is used for calculating the final correction factors k_{mag}, is displayed by red symbols. Please note, that the shown data points correspond to the same magnetic flux density each time. They are presented in a straightened way in order to improve the distinguishability. (Coverage factor $k = 1$, the uncertainties given are absolute uncertainties.)

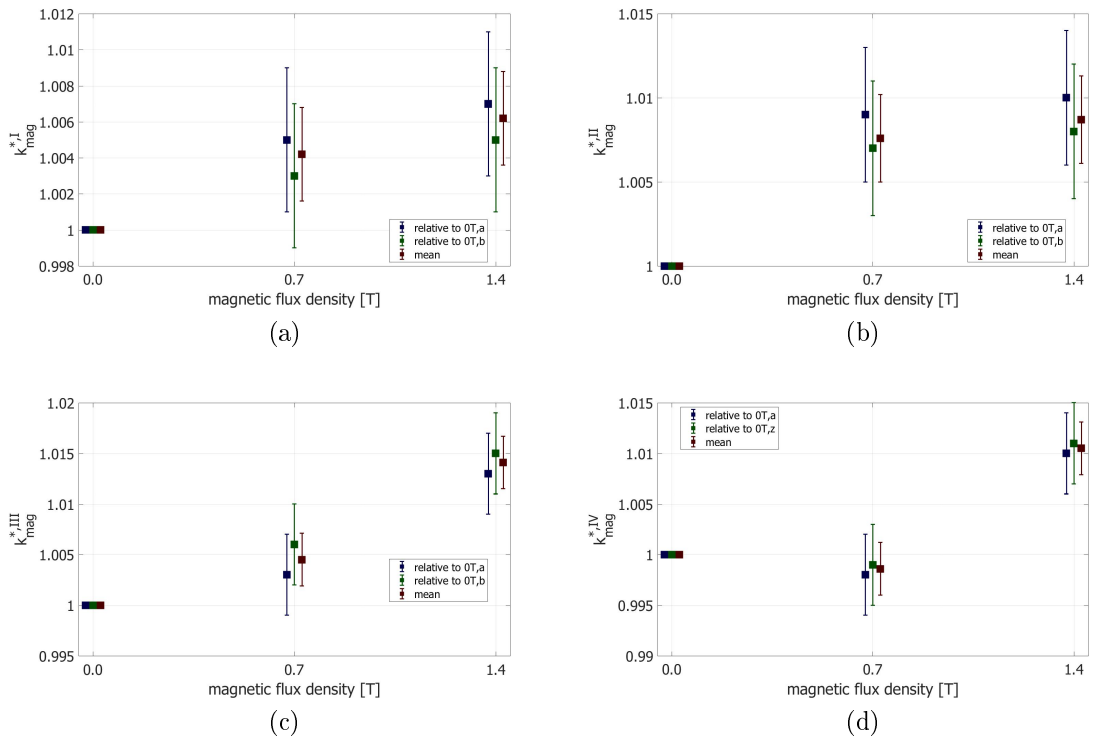

Figure E.5: The correction factors k^*_{mag} obtained using the single indications in the absence of a magnetic field and their mean for all four irradiation runs with 15 MV photons. (a) shows the results for the first irradiation run, (b) for the second, (c) for the third, and (d) for the fourth. The results obtained using the first indication in the absence of a magnetic field in each irradiation run ("relative to 0T,a") are displayed by blue symbols, the results obtained using the second indication in the absence of a magnetic field in each irradiation run ("relative to 0T,b/z") are displayed by green symbols. The mean of these two data points, which is used for calculating the final correction factors k_{mag}, is displayed by red symbols. Please note, that the shown data points correspond to the same magnetic flux density each time. They are presented in a straightened way in order to improve the distinguishability. (Coverage factor $k = 1$, the uncertainties given are absolute uncertainties. Please note, that the second irradiation in the absence of a magnetic field is labeled "0T,z" for the fourth run, since the order of irradiations was varied in this run, see the last paragraph in Section E.1.)

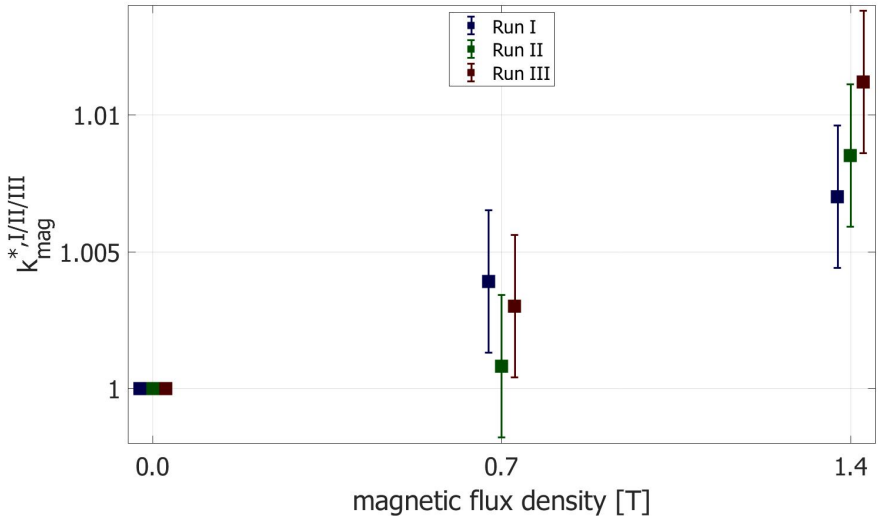

Figure E.6: Correction factors k^*_{mag} obtained by pure experiment after averaging over the two irradiations in the absence of a magnetic field (10 MV). The results for the first irradiation run are shown in blue, the results for the second run in green, and for the third run in red. Please note, that the shown data points correspond to the same magnetic flux density each time. They are presented in a straightened way in order to improve the distinguishability. (Coverage factor $k = 1$, the uncertainties given are absolute uncertainties.)

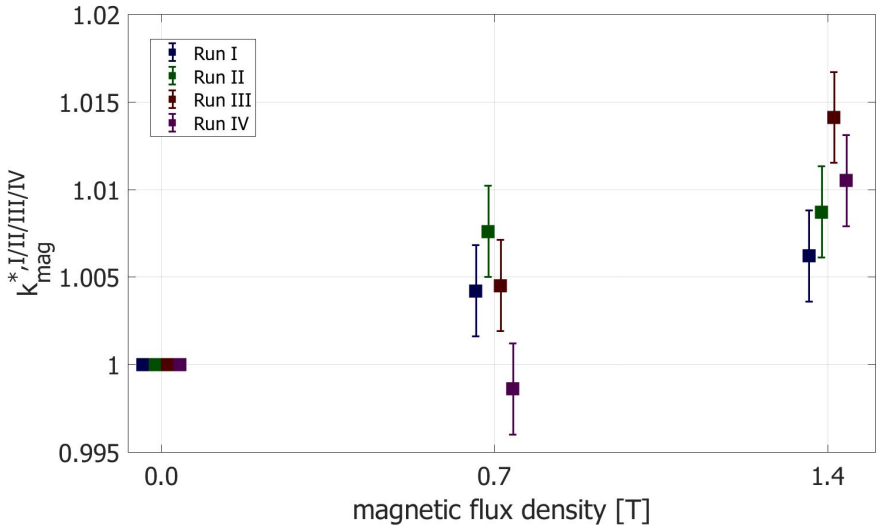

Figure E.7: Correction factors k^*_{mag} obtained by pure experiment after averaging over the two irradiations in the absence of a magnetic field (15 MV). The results for the first irradiation run are shown in blue, the results for the second run in green, for the third run in red, and for the fourth run in purple. Please note, that the shown data points correspond to the same magnetic flux density each time. They are presented in a straightened way in order to improve the distinguishability. (Coverage factor $k = 1$, the uncertainties given are absolute uncertainties.)

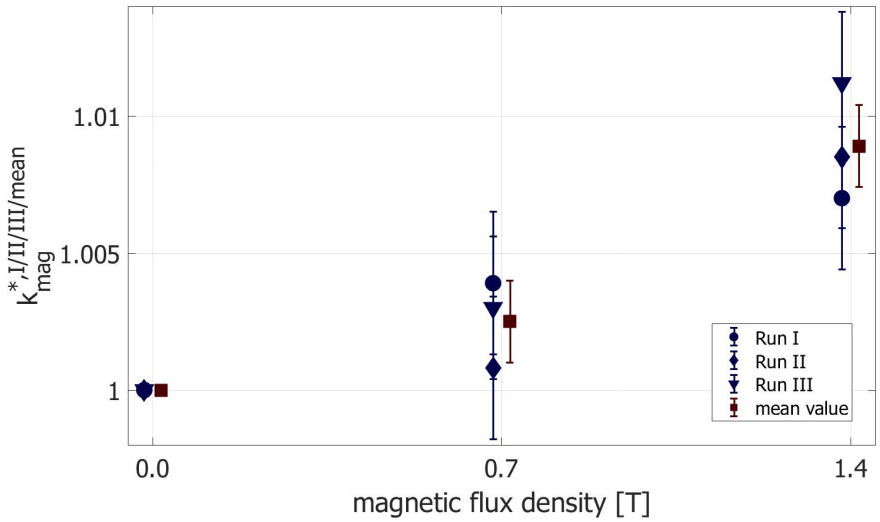

Figure E.8: Correction factors k^*_{mag} obtained by pure experiment after averaging over the two irradiations in the absence of a magnetic field (10 MV). The mean values are shown in red, the results for the individual runs are shown in blue. Please note, that the shown data points correspond to the same magnetic flux density each time. They are presented in a straightened way in order to improve the distinguishability. (Coverage factor $k = 1$, the uncertainties given are absolute uncertainties.)

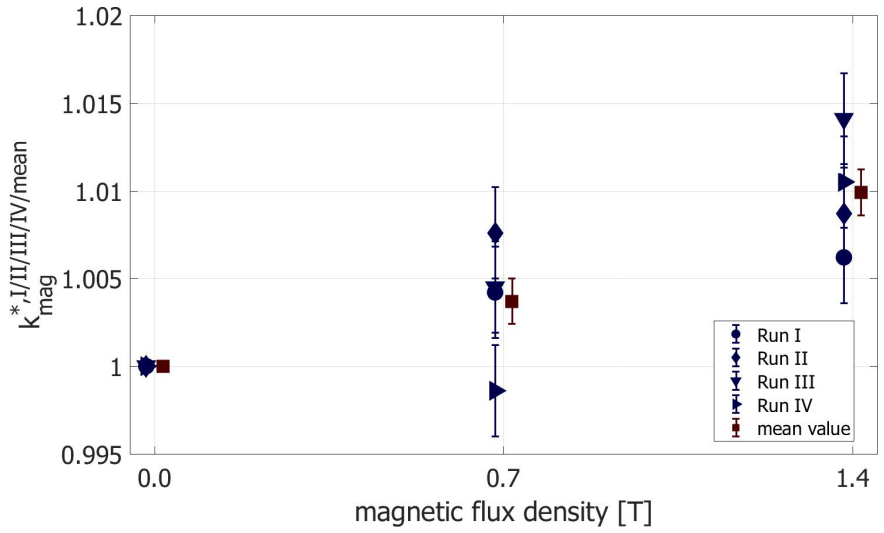

Figure E.9: Correction factors k^*_{mag} obtained by pure experiment after averaging over the two irradiations in the absence of a magnetic field (15 MV). The mean values are shown in red, the results for the individual runs are shown in blue. Please note, that the shown data points correspond to the same magnetic flux density each time. They are presented in a straightened way in order to improve the distinguishability. (Coverage factor $k = 1$, the uncertainties given are absolute uncertainties.)

ating potential of 15 MV.

The file "mohan15.spectrum" available with EGSnrc was used for defining the radiation source for the MC calculations of the ddcs. It was defined as a collimated source with a field size of 5 cm width and 10 cm height. However, it has to be considered in the analysis, that the mohan spectrum is not identical with the experimentally applied photon spectrum. Figure E.10 shows the comparison of the ddcs obtained with the mohan spectrum and the phase space file exemplarily for 0 T and 1.4 T at 10 MV. Hence, the $c_{\vec{B}}$ factors determined with the mohan spectrum do not describe the actual experimental situation, and they are, thus, called $\tilde{c}_{\vec{B}}$ factors in the following for differentiation. The correction factor k_{mohan} for converting the $\tilde{c}_{\vec{B}}$ factors obtained with the mohan15.spectrum into the $c_{\vec{B}}$ factors for the real setup with the 15 MV photon beam and the uncertainty associated with this correction factor k_{mohan} were determined based on the comparison of the $c_{\vec{B}}$ factors obtained with the mohan spectra and the phase space files for the 6 MV and the 10 MV photon beam.

$c_{\vec{B}}$ factors were determined with the mohan6.spectrum available with EGSnrc for (0.6, 0.9, 1.4) T and with the mohan10.spectrum for (0.7, 1.4) T, and they were compared to the $c_{\vec{B}}$ factors determined with the available phase space files for 6 MV and 10 MV. The $c_{\vec{B}}$ factors obtained with the mohan spectra and the phase space files are listed in Table E.3 and shown in Figure E.11, where the abscissa shows the magnetic flux density in Tesla and the ordinate the respective $c_{\vec{B}}$ factors. Table E.3 also lists the deviation of the $c_{\vec{B}}$ factors determined with the mohan spectra from the $c_{\vec{B}}$ factors determined with the phase space files. All $c_{\vec{B}}$ factors determined with the mohan spectra are smaller than the respective $c_{\vec{B}}$ factors determined with the phase space files with a mean deviation of 0.37 %. Table E.3 and Figure E.11 show in addition, that the deviation decreases with decreasing magnetic flux density.

The difference of the $c_{\vec{B}}$ factors determined with the mohan spectrum and the phase space file is not randomly scattered but systematic. It was, thus, decided to correct the $\tilde{c}_{\vec{B}}$ factors obtained with the 15 MV mohan spectrum upwards by 0.4 %. The uncertainty of this correction was conservatively set to $\frac{0.4\,\%}{\sqrt{3}}$, i.e. a uniform distribution with 0.4 % half width. The correction factor k_{mohan} results, thus, as

$$k_{mohan} = 1.0040 \pm 0.0023 \tag{E.1}$$

The $\tilde{c}_{\vec{B}}$ factors obtained with the 15 MV mohan spectrum are listed in Table E.4. Please note, that this table contains also the $\tilde{c}_{\vec{B}}$ factors for the additional irradiation run with reduced field size, see Section E.4. The $\tilde{c}_{\vec{B}}$ factors were converted into the $c_{\vec{B}}$ factors corresponding to the real setup via multiplication with the correction factor k_{mohan}:

$$c_{\vec{B}} = \tilde{c}_{\vec{B}} \cdot k_{mohan} \tag{E.2}$$

The uncertainty associated with the $c_{\vec{B}}$ factors is obtained via

$$\begin{aligned} u_r(c_{\vec{B}}) &= \sqrt{u_r(\tilde{c}_{\vec{B}})^2 + u_r(k_{mohan})^2} \\ &= \sqrt{\left(\frac{u(\tilde{c}_{\vec{B}})}{\tilde{c}_{\vec{B}}}\right)^2 + \left(\frac{u(k_{mohan})}{k_{mohan}}\right)^2} \end{aligned} \tag{E.3}$$

and

$$u(c_{\vec{B}}) = u_r(c_{\vec{B}}) \cdot c_{\vec{B}} \tag{E.4}$$

The resulting $c_{\vec{B}}$ factors with their associated uncertainties are listed in Table E.4 as well as in Table E.2 in Section E.1. The contribution due to the k_{mohan} correction is dominant. The uncertainties for the $c_{\vec{B}}$ factors for 15 MV are, hence, about six to seven times as large as for 6 MV and 10 MV. This affects the uncertainty associated with the finally determined correction factors k_{mag}, as described in Chapter 5. Figure E.12 shows the $\tilde{c}_{\vec{B}}$ and $c_{\vec{B}}$ factors for 15 MV for $5 \times 10\,\mathrm{cm}^2$ field size and for $4 \times 10\,\mathrm{cm}^2$ field size together with the $c_{\vec{B}}$ factors for 6 MV and 10 MV determined with phase space files and mohan spectra, respectively. The magnetic flux density in Tesla is shown on the abscissa, the ordinate shows the respetive factors.

Table E.4 and Figure E.12 show that the resulting $c_{\vec{B}}$ factors for 15 MV for a field size of 5 cm×10 cm and for a field size of 4 cm×10 cm agree with each other within the standard uncertainty ($k = 1$). They also show that the uncertainties associated with the $c_{\vec{B}}$ factors are about 14-times larger than the uncertainties associated with the $\tilde{c}_{\vec{B}}$ factors. Figure E.12 shows that the $c_{\vec{B}}$ and the $\tilde{c}_{\vec{B}}$ factors for 15 MV assimilate with the $c_{\vec{B}}$ factors obtained for 6 MV and 10 MV with phase space files and mohan spectra, respectively; only the large uncertainties associated with the $c_{\vec{B}}$ factors for 15 MV stand out. This shows, that the correction factor k_{mohan} was chosen reasonably. The $c_{\vec{B}}$ factors for 0.6 T and 0.7 T, respectively, agree with each other within the standard uncertainty ($k = 1$) for 6 MV, 10 MV, and 15 MV. At 1.4 T, the $c_{\vec{B}}$ factor for 15 MV (5 cm×10 cm field size) agrees with the $c_{\vec{B}}$ factor for 10 MV within an expanded uncertainty with coverage factor $k = 2$, and it agrees with the $c_{\vec{B}}$ factor for 6 MV within an expanded uncertainty with coverage factor $k = 3$.

E.3 Test based on Bayesian principles regarding the model representing the obtained correction factors k_{mag}

A test based on Bayesian principles (based on Equation (207) from [Dose, 2002]) was performed in order to find out whether it is more likely for the correction factors k_{mag} obtained in the 10 MV and 15 MV series to represent a constant or a linear model.

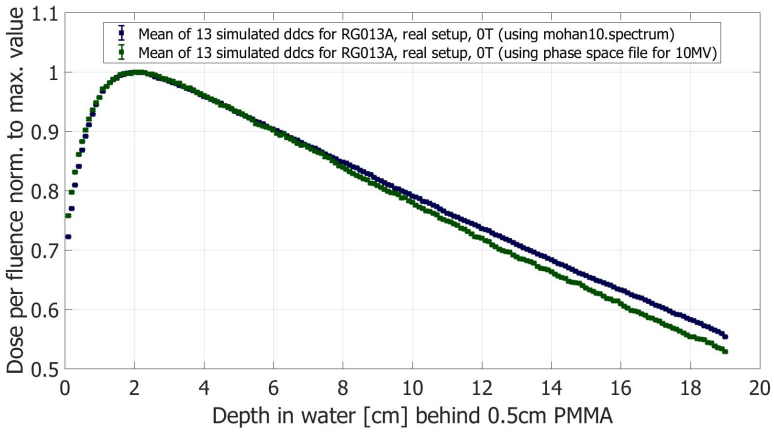

(a)

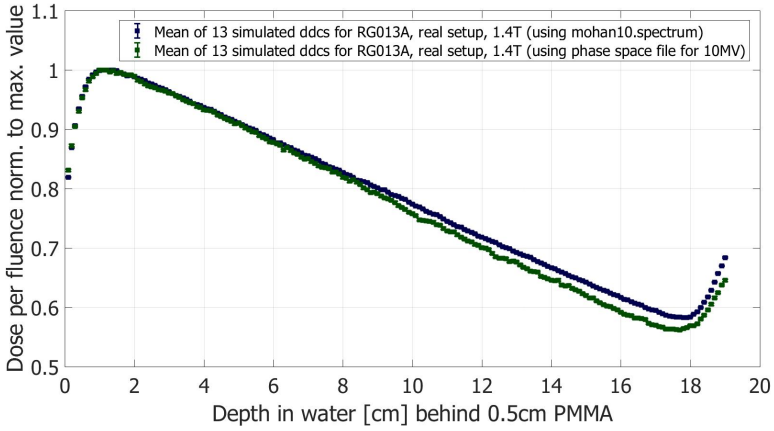

(b)

Figure E.10: Comparison of the ddcs obtained with the mohan spectrum (blue) and the phase space file (green) for 10 MV and (a) 0 T and (b) 1.4 T. The abscissa shows the depth in water in cm behind 0.5 cm PMMA and the ordinate shows the respective dose values per fluence, which are normalised to the maximum value.

Table E.3: $c_{\vec{B}}$ factors obtained with the mohan spectra and the phase space files for 6 MV and 10 MV and their deviations. (Coverage factor $k = 1$, the uncertainties given are absolute uncertainties.)

Photon energy	Magnetic flux density	$c_{\vec{B}}^{mohan}$ factor with mohan spectrum	$c_{\vec{B}}^{phsp}$ factor phase space file	Deviation of $c_{\vec{B}}^{mohan}$ from $c_{\vec{B}}^{phsp}$
6 MV	0.6 T	0.99917 ± 0.00021	1.0018 ± 0.0004	-0.26 %
	0.9 T	0.99830 ± 0.00021	1.0019 ± 0.0004	-0.36 %
	1.4 T	0.99637 ± 0.00021	1.0008 ± 0.0004	-0.44 %
10 MV	0.7 T	0.99843 ± 0.00019	1.00214 ± 0.00033	-0.37 %
	1.4 T	0.99414 ± 0.00020	0.99839 ± 0.00035	-0.43 %
			Mean deviation:	-0.37 %

Table E.4: $\tilde{c}_{\vec{B}}$ factors obtained with the mohan15.spectrum and $c_{\vec{B}}$ factors for 15 MV obtained as a product of the $\tilde{c}_{\vec{B}}$ factors and the correction factor k_{mohan}. The values are shown for the field size used in the experiment regarding the energy dependence (5 cm×10 cm) as well as for the additional irradiation run with reduced field size (4 cm×10 cm, see Section E.4). The uncertainties given are absolute uncertainties with coverage factor $k = 1$.

Field size	Magnetic flux density	$\tilde{c}_{\vec{B}}$ factor	$c_{\vec{B}}$ factor
5 cm×10 cm	0.7 T	0.99787 ± 0.00016	1.0019 ± 0.0023
	1.4 T	0.99114 ± 0.00017	0.9951 ± 0.0023
4 cm×10 cm	0.7 T	0.99766 ± 0.00016	1.0017 ± 0.0023
	1.4 T	0.99242 ± 0.00017	0.9964 ± 0.0023

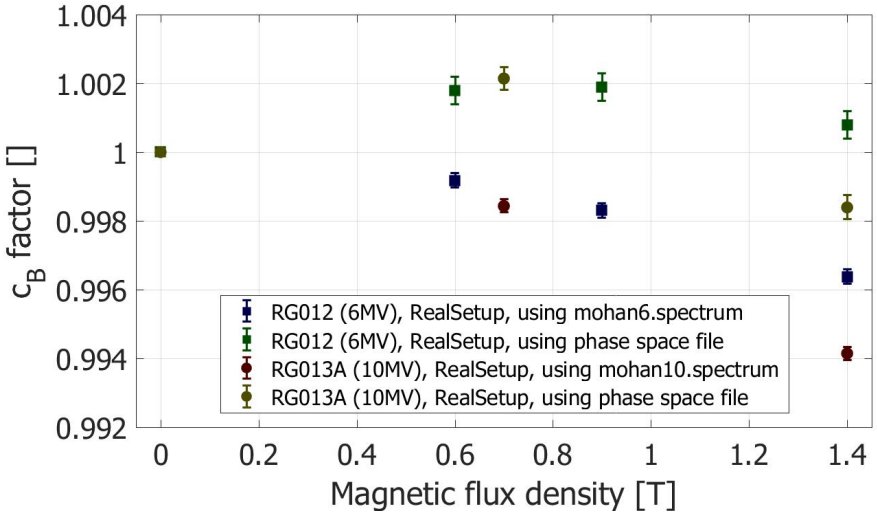

Figure E.11: $c_{\vec{B}}$ factors obtained with the mohan spectra and the phase space files for 6 MV and 10 MV. The $c_{\vec{B}}$ factors for 6 MV obtained with the mohan spectrum are shown by blue squares, the $c_{\vec{B}}$ factors for 6 MV obtained with the phase space file are shown by green squares. The $c_{\vec{B}}$ factors for 10 MV obtained with the mohan spectrum are shown by red circles, the $c_{\vec{B}}$ factors for 10 MV obtained with the phase space file are shown by yellow circles. (Coverage factor $k = 1$, the uncertainties given are absolute uncertainties.)

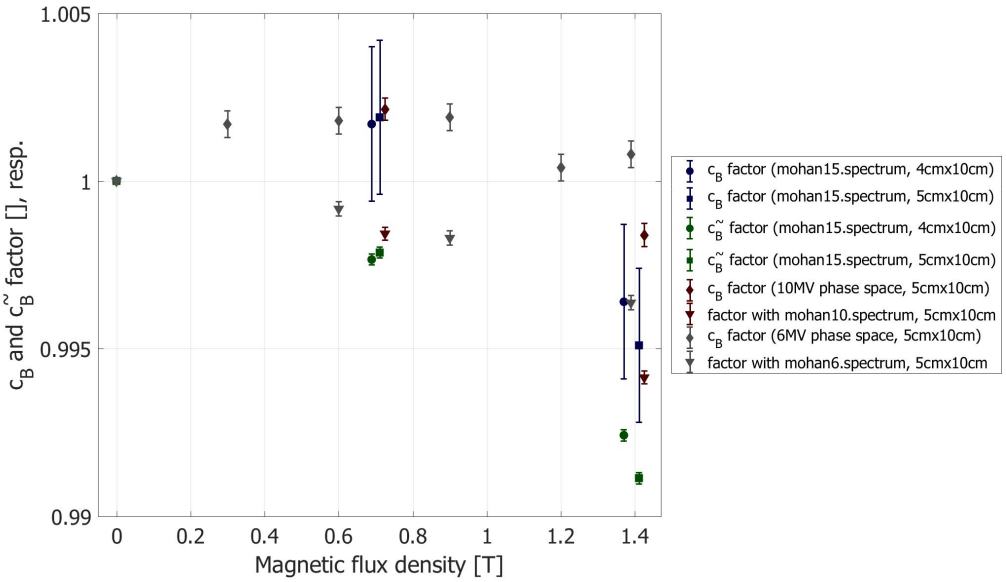

Figure E.12: $\tilde{c}_{\vec{B}}$ (green) and $c_{\vec{B}}$ factors (blue) for 15 MV for $5 \times 10\,\mathrm{cm}^2$ field size (squares) and for $4 \times 10\,\mathrm{cm}^2$ field size (circles) together with the $c_{\vec{B}}$ factors for 6 MV (grey) and 10 MV (red) determined with phase space files (diamonds) and mohan spectra (triangles), respectively. (Coverage factor $k = 1$, the uncertainties given are absolute uncertainties.)

For the correction factors k_{mag} obtained in 10 MV photon beams, the test revealed that the probabilty P_{lin} for a linear model is higher than the probability P_{const} for a constant model. For the correction factors k_{mag} obtained in 15 MV photon beams, the test revealed that the probability P_{const} for a constant model is higher than the probability P_{lin} for a linear model.
The exact probability ratios depend on how the data point for 0 T is considered. Four versions of the test were performed as described in Section D.3. The results obtained in these four versions of the test are summarised in Table E.5 for the 10 MV and 15 MV series, respectively.
Version (4) of the test, which only consideres the data points at 0.7 T and 1.4 T without any data point at 0 T is – as described in Section D.3 – to be discarded, since it is an important information for the test that the data point at 0 T is expected to be unity. It has to be considered, too, that the knowledge about this data point at 0 T is higher than for the experimentally obtained data points. It can, thus, be concluded from the tests, that the probability for a linear model is significantly higher than for a constant model in the 10 MV series and that the probability for a constant model is slightly higher than for a linear model in the 15 MV series.
The application of this test to the data obtained in the investigation using 6 MV photon beams (see Section D.3) revealed a higher probability for a constant model, i.e. the test based on Bayesian principles seems to interpret the data point at 1.4 T

Table E.5: Results of the test based on Bayesian principles described in [Dose, 2002] whether it is more likely for the correction factors k_{mag} obtained from the 10 MV and 15 MV series to represent a constant or a linear model. Given is the ratio of probabilities $\frac{P_{lin}}{P_{const}}$ for a linear and a constant model.

Consideration of data point at 0 T	10 MV series $\frac{P_{lin}}{P_{const}}$	15 MV series $\frac{P_{lin}}{P_{const}}$
(1): $k_{mag,0T} = 1.0000 \pm 0.0016$	0.7025	0.0080
(2): $k_{mag,0T} = 1.0000 \pm 1E-8$	15541	0.0605
(3): $k_{mag,0T} = 1.0000 \pm 1E-80$	15541	0.0605
(4): $k_{mag,0T} = -$	0.0085	0.0069

in the 6 MV series as an outlier. It is, however, important to keep in mind, that the performed test does only compare a constant model and a linear model. It is indeed possible, that the model to describe the correction factors k_{mag} in the 6 MV series is not linear. The meaningfulness of the test is, thus, restricted in the case of the 6 MV series. The comparison of linear and constant models only seems to be justified for the data obtained from the 10 MV and 15 MV series according to the visual impression. The visual impression can, however, be misleading, and it has to be considered, that the trend of the data is less clear due to the reduced amount of data points. The meaningfulness of the test could be as restricted as in the case of the 6 MV series.

E.4 Additional irradiation run with varied field size at 15 MV

The irradiation series of alanine detectors in the presence of static magnetic fields with various flux densities using 6 MV, 10 MV, and 15 MV photon beams were performed with a photon field size of 5 cm width and 10 cm height. The width was reduced compared to the reference field size of 10 cm width in order to spare the pole shoes of the electromagnet, see Section 3.1.3.
In an additional irradiation run, alanine detectors were irradiated with a 15 MV photon beam in the presence of magentic fields with flux densities of (0, 0.7, 1.4, 0) T, while the field size was reduced to 4 cm width. The height of 10 cm was not

changed. This additional irradiation was performed in order to meet the objective that stray radiation from the pole shoes could affect the resulting correction factors k_{mag}. Such an impairment was not to be expected: The stray radiation contains more low-energetic electrons than the direct radiation. Farmer IC are sensitive to these low-energetic electrons while the alanine dosimeter is less sensitive for low-energetic electrons. If a Farmer IC was used as a monitor, the stray radiation might have had an effect on the results. A transmission IC (see Section 3.1.4) was, however, applied in the experiment with 15 MV photons as well as in the 6 MV and 10 MV series. This monitor is completely insensitive against the stray radiation since the stray radiation occurs between the pole shoes and not at the point of measurement of the transmission IC. It was, hence, expected, that the reduced field size has no significant effect on the resulting correction factors k_{mag}.
This additional experiment with the $(4 \times 10)\,\mathrm{cm}^2$ field size and the required MC simulations of the ddcs, the analysis, and the obtained results are described in the following.

E.4.1 Experiment and Analysis

The experiment was conducted as described in Section 3.1.4 for 15 MV photons with the only difference that the width of the field size was not 5 cm but 4 cm. The height of 10 cm remained unchanged. The dose rate was 225 MU/min and the pulse rate frequency was 98 Hz. The base detectors were the same as for Run IV in the 15 MV series (see Section 3.1.4). The MC simulations of the respective ddcs were performed as described in Section 3.1.4 for the 15 MV series with the only difference that the width of the photon field was reduced to 4 cm.
The analysis was conducted as described in Section 3.1.4 for the 15 MV series with the only difference, that there was no averaging over several irradiation runs. The final correction factor k^*_{mag} for this additional experiment is the mean of the two factors determined relative to the two irradiations in the absence of a magnetic field.

E.4.2 Results and Conclusion

The correction factors k^*_{mag} resulting from the experiment are shown in Table E.6 and the $c_{\vec{B}}$ factors obtained from the MC simulations are shown in Table E.7. The correction factors k_{mag} obtained as the product of $c_{\vec{B}}$ and k^*_{mag}, see Equation 3.30, are shown in Table E.8. Figure E.13 shows the correction factors k_{mag} obtained for this additional run with the $(4 \times 10)\,\mathrm{cm}^2$ field size together with the correction factors k_{mag} obtained in the four runs of the irradiation series with 15 MV photons with the $(5 \times 10)\,\mathrm{cm}^2$ field size. The ordinate in the graph shows the correction factors k_{mag}, while the abscissa shows the flux density of the static magnetic field in Tesla.
The correction factors k_{mag} obtained from the additional run with the field size of $(4 \times 10\,\mathrm{cm})^2$ agree with each of the correction factors k_{mag} obtained from the four runs with the field size of $(5 \times 10\,\mathrm{cm})^2$ within the standard uncertainty ($k = 1$).

Table E.6: Experimentally obtained values for the correction factors k^*_{mag} for the additional run with a field size of $(4 \times 10\,\mathrm{cm})^2$. (Coverage factor $k = 1$, the uncertainties given are absolute uncertainties.)

Magnetic flux density	k^*_{mag}
0 T	1 ± 0
0.7 T	1.0011 ± 0.0026
1.4 T	1.0104 ± 0.0026

Table E.7: $c_{\vec{B}}$ factors obtained from MC simulations for the setup in the additional run with a field size of $(4 \times 10\,\mathrm{cm})^2$. (Coverage factor $k = 1$, the uncertainties given are absolute uncertainties.)

Magnetic flux density	$c_{\vec{B}}$
0 T	1 ± 0
0.7 T	1.0017 ± 0.0023
1.4 T	0.9964 ± 0.0023

There is, hence, no reason for assuming that the correction factors k_{mag} obtained in the irradiation series with 6 MV, 10 MV, and 15 MV photons are impaired by stray radiation from the pole shoes of the electromagnet.

Table E.8: Values for the correction factors k_{mag} obtained for the additional experiment with a field size of $(4 \times 10\,\mathrm{cm})^2$. (Coverage factor $k = 1$, the uncertainties given are absolute uncertainties.)

Magnetic flux density	k_{mag}
0 T	1 ± 0
0.7 T	1.0028 ± 0.0035
1.4 T	1.0068 ± 0.0035

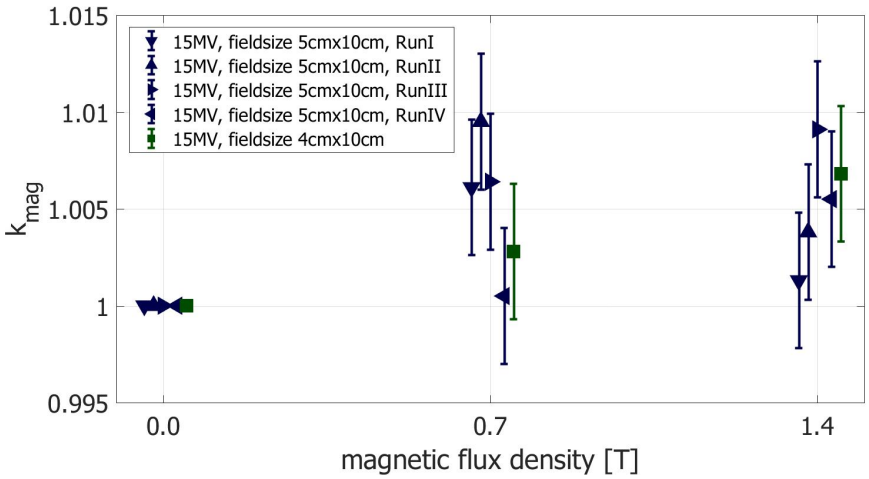

Figure E.13: Obtained correction factors k_{mag} for the four runs with a field size of $(5 \times 10)\,\mathrm{cm}^2$ (blue triangles) and the additional run with a field size of $(4 \times 10)\,\mathrm{cm}^2$ (green square). Please note that the values for k_{mag} are plotted in a straightened way in order to improve the distinguishability; nevertheless, they refer to the same magnetic flux density each time. (Coverage factor $k = 1$, the uncertainties given are absolute uncertainties.)

F Supplement to the investigation of the effect of MRI on irradiated alanine detectors

F.1 Condition C_c – a closer look

As delineated in the discussion in Section 5.2.1, the correction factor $k_{subsMRI}$ determined for Condition C_c does not significantly differ from unity. However, it is the value with the largest "deviation". This was the occasion for having a closer look on this situation in order to ensure that the reason for the deviation was not a mistake in the analysis. Each alanine detector in this experiment consisted of four alanine pellets and so did detector hm27-a6...d6 used for Condition C_c. In the analysis (see Section 3.2.1), the mass-related mean amplitude of the four pellets A_m was used. For Condition C_c, the individual amplitudes of the single pellets were analysed as well. This led to the conclusion, that only the amplitude of a single alanine pellet (hm27-d6) causes the "deviation" from unity. The mass-related mean amplitude of the other three pellets hm27-a6...c6 was, thus, calculated for the EPR measurement before and after the exposure to MRI. The correction factor $k_{subsMRI}$ obtained using these mean amplitudes based on the three alanine pellets hm27-a6...c6 is

$$k_{subsMRI} = 0.9995 \pm 0.0019 \tag{F.1}$$

Figure F.1 shows the results for all conditions as already presented in Section 4.2.1 with this value for hm27-a6...c6 (green) in addition. This additional analysis offers no new finding compared to the general analysis in Section 3.2.1, which revealed no significant effect itself. However, as this additional analysis was performed anyway in order to ensure that the correction factor $k_{subsMRI}$ for situation C_c was determined correctly, it is mentioned in this appendix.

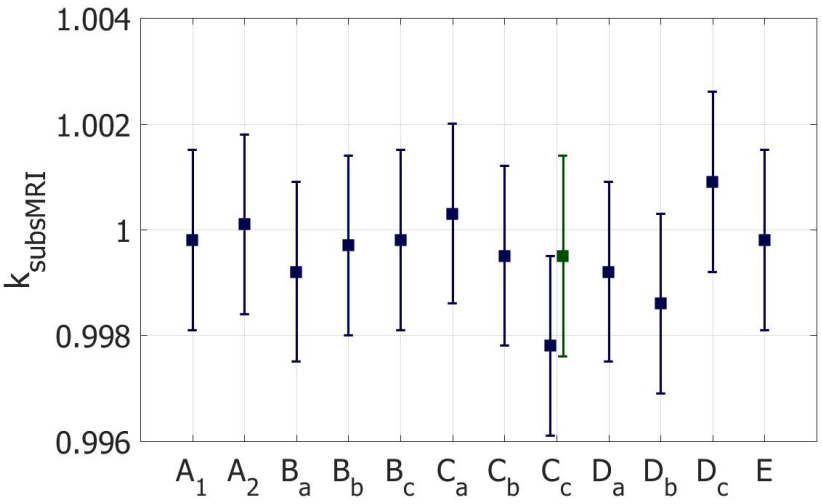

Figure F.1: Experimentally obtained values for correction factor $k_{subsMRI}$, which is correcting the indication of an alanine dosimeter exposed to an MRI system subsequent to irradiation. For the explanations of the Conditions A_1 to E, please see Tables 3.5 and 4.4. In addition to Figure 4.6, the value for Condition C_c based on the alanine detector hm27-a6...c6 ($n = 3$) is given in green. (Coverage factor $k = 1$.)

Abstracts and conference contributions

R. R. Gallas and others. Towards alanine/ESR as a secondary standard for dosimetry in magnetic fields. Contribution to the *5th MR in RT Symposium* in Sydney, Australia, June 20-23, 2017.

R. R. Gallas, T. Hackel, A. Fillmer and R.-P. Kapsch. Session 37: Young investigator forum. Towards alanine/ESR as a secondary standard for dosimetry in magnetic fields. *Biomedical Engineering/Biomedizinische Technik*, 62 s1, p. 298-300, 2017. https://doi.org/10.1515/bmt-2017-5058.

R. R. Gallas and others. Dosimetry with alanine/ESR in magnetic fields. Contribution to *The Joint International Symposium on EPR dosimetry and dating (EPR) and the International Conference on Biological Dosimetry (BioDose)* in Munich, Germany, June 11-15, 2018.

R. R. Gallas and others. Alanine/EPR dosimetry in magnetic fields. Contribution to the *EPRBioDose 2022 online*, March 28-30, 2022.

Bibliography

S. Acharya, B. W. Fischer-Valuck, R. Kashani, P. Parikh, D. Yang, T. Zhao, O. Green, O. Wooten, H. H. Li, Y. Hu, et al. Online magnetic resonance image guided adaptive radiation therapy: first clinical applications. *International Journal of Radiation Oncology* Biology* Physics*, 94(2):394–403, 2016.

J. Agnew, F. O'Grady, R. Young, S. Duane, and G. J. Budgell. Quantification of static magnetic field effects on radiotherapy ionization chambers. *Physics in Medicine & Biology*, 62(5):1731, 2017.

S. Agostinelli, J. Allison, K. al Amako, J. Apostolakis, H. Araujo, P. Arce, M. Asai, D. Axen, S. Banerjee, G. J. N. I. Barrand, et al. GEANT4 – a simulation toolkit. *Nuclear instruments and methods in physics research section A: Accelerators, Spectrometers, Detectors and Associated Equipment*, 506(3):250–303, 2003.

P. Andreo, D. T. Burns, K. Hohlfeld, M. S. Huq, T. Kanai, F. Laitano, V. Smyth, and S. Vynckier. IAEA Technical Report Series #398 – Absorbed Dose Determination in External Beam Radiotherapy: An International Code of Practice for Dosimetry based on Standards of Absorbed Dose to Water. *International Atomic Energy Agency*, 2000.

M. Anton. Development of a secondary standard for the absorbed dose to water based on the alanine EPR dosimetry system. *Applied radiation and isotopes*, 62 (5):779–795, 2005.

M. Anton. Uncertainties in alanine/ESR dosimetry at the Physikalisch-Technische Bundesanstalt. *Physics in medicine and biology*, 51(21):5419, 2006.

M. Anton and L. Büermann. Relative response of the alanine dosimeter to medium energy x-rays. *Physics in Medicine & Biology*, 60(15):6113, 2015.

M. Anton, R.-P. Kapsch, M. Krystek, and F. Renner. Response of the alanine/ESR dosimetry system to MV x-rays relative to ^{60}Co radiation. *Physics in Medicine & Biology*, 53(10):2753, 2008.

M. Anton, R.-P. Kapsch, and T. Hackel. Is there an influence of the surrounding material on the response of the alanine dosimetry system? *Physics in medicine and biology*, 54(7):2029, 2009.

M. Anton, R.-P. Kapsch, A. Krauss, P. von Voigts-Rhetz, K. Zink, and M. McEwen. Difference in the relative response of the alanine dosimeter to megavoltage x-ray and electron beams. *Physics in medicine and biology*, 58(10):3259, 2013.

J. M. Arber and P. H. G. Sharpe. Fading characteristics of irradiated alanine pellets: the importance of pre-irradiation conditioning. *Applied Radiation and Isotopes*, 44(1-2):19–22, 1993.

G.P. Arrighini, M. Maestro, and R. Moccia. Magnetic properties of polyatomic molecules: Magnetic susceptibility of H_2O, NH_3, CH_4, H_2O_2. *The Journal of chemical physics*, 49(2):882–889, 1968.

A. Arslan and B. Sengul. Comparison of radiotherapy techniques with flattening filter and flattening filter-free in lung radiotherapy according to the treatment volume size. *Scientific Reports*, 10(1):1–8, 2020.

P. Bachert. Lecture "Medical Physics 2". *Ruprecht-Karls-Universität Heidelberg*, 2014.

M. Bangert and P. Ziegenhein. Bestrahlungsplanung. In W. Schlegel, C.P. Karger, and O. Jäkel, editors, *Medizinische Physik*, pages 485–514. Springer, 2018.

A. Bartolotta, P. Fattibene, S. Onori, M. Pantaloni, and E. Petetti. Sources of uncertainty in therapy level alanine dosimetry. *Applied Radiation and Isotopes*, 44(1-2):13–17, 1993.

R. Baskar, K.A. Lee, R. Yeo, and K.-W. Yeoh. Cancer and radiation therapy: current advances and future directions. *International journal of medical sciences*, 9(3):193, 2012.

M. Berger and M. Breithaupt. HF-Pulse, Pulssequenzen und Kontraste, Triggerung. In W. Schlegel, C.P. Karger, and O. Jäkel, editors, *Medizinische Physik*, pages 221–234. Springer, 2018.

E.S. Bergstrand, K.R. Shortt, C.K. Ross, and E.O. Hole. An investigation of the photon energy dependence of the EPR alanine dosimetry system. *Physics in Medicine & Biology*, 48(12):1753, 2003.

J. Beringer, J.F. Arguin, R.M. Barnett, K. Copic, O. Dahl, D.E. Groom, C.J. Lin, J. Lys, H. Murayama, C.G. Wohl, et al. Review of particle physics. *Physical Review D-Particles, Fields, Gravitation and Cosmology*, 86(1):010001, 2012.

H. Bichsel, D.H. Pierson, J.W. Boring, A. Green, M. Inokuti, and G. Hurst. ICRU report 31: Average energy required to produce an ion pair. *J. ICRU*, pages 1–52, 1979.

A. Bielajew, H. Hirayama, W.R. Nelson, D.W.O. Rogers, et al. History, overview and recent improvement of EGS4. *KEK Internal 94-4/NRCC-PIRS-0436*, 1994.

I. Billas, H. Bouchard, U. Oelfke, D. Shipley, C. Gouldstone, and S. Duane. Alanine dosimetry in strong magnetic fields: use as a transfer standard in MRI-guided radiotherapy. *Physics in Medicine & Biology*, 65(11):115001, 2020.

I. Billas, H. Bouchard, U. Oelfke, and S. Duane. Traceable reference dosimetry in MRI guided radiotherapy using alanine: calibration and magnetic field correction factors of ionisation chambers. *Physics in Medicine & Biology*, 66(16):165006, 2021.

F. Bloch. Nuclear induction. *Physical review*, 70(7-8):460, 1946.

T. Bostel, A. Pfaffenberger, S. Delorme, C. Dreher, G. Echner, P. Haering, C. Lang, M. Splinter, F. Laun, M. Müller, et al. Prospective feasibility analysis of a novel off-line approach for MR-guided radiotherapy. *Strahlentherapie und Onkologie*, 194(5):425–434, 2018.

W. W. Bradshaw, D. G. Cadena Jr, G. W. Crawford, and H. A. W. Spetzler. The use of alanine as a solid dosimeter. *Radiation research*, 17(1):11–21, 1962.

G. Budgell, J. Berresford, M. Trainer, E. Bradshaw, P. Sharpe, and P. Williams. A national dosimetric audit of IMRT. *Radiotherapy and Oncology*, 99(2):246–252, 2011.

National Research Council Canada. EGSnrc: software tool to model radiation transport. URL https://nrc.canada.ca/en/research-development/products-services/software-applications/egsnrc-software-tool-model-radiation-transport. Accessed: 2021-09-21.

I. D. Cavin, P. M. Glover, R. W. Bowtell, and P. A. Gowland. Thresholds for perceiving metallic taste at high magnetic field. *Journal of Magnetic Resonance Imaging: An Official Journal of the International Society for Magnetic Resonance in Medicine*, 26(5):1357–1361, 2007.

S. Chin, C. L. Eccles, A. McWilliam, R. Chuter, E. Walker, P. Whitehurst, J. Berresford, M. Van Herk, P. J. Hoskin, and A. Choudhury. Magnetic resonance-guided radiation therapy: a review. *Journal of medical imaging and radiation oncology*, 64(1):163–177, 2020.

B. Ciesielski, K. Schultka, A. Kobierska, R. Nowak, and Z. Peimel-Stuglik. In vivo alanine/EPR dosimetry in daily clinical practice: a feasibility study. *International Journal of Radiation Oncology* Biology* Physics*, 56(3):899–905, 2003.

B. Ciesielski, K. Schultka, M. Penkowski, and E. Sagstuen. EPR study of light illumination effects on radicals in gamma-irradiated L-alanine. *Spectrochimica Acta Part A: Molecular and Biomolecular Spectroscopy*, 60(6):1327–1333, 2004.

T. C. Cosmus and M. Parizh. Advances in whole-body MRI magnets. *IEEE Transactions on applied superconductivity*, 21(3):2104–2109, 2010.

C. De Angelis, P. Fattibene, S. Onori, E. Petetti, A. Bartolotta, and A. S. Santamaria. Transferability of ASTM/NIST alanine–polyethylene recipe at ISS. *Applied Radiation and Isotopes*, 52(5):1197–1201, 2000.

J. A. de Pooter, I. Billas, L. A. de Prez, S. Duane, R.-P. Kapsch, C. Karger, B. van Asselen, and J. W. H. Wolthaus. Reference dosimetry in MRI-linacs: evaluation of available protocols and data to establish a code of practice. *Physics in Medicine & Biology*, 2020.

L. de Prez, S. Woodings, J. de Pooter, B. van Asselen, J. Wolthaus, B. Jansen, and B. Raaymakers. Direct measurement of ion chamber correction factors, k_Q and k_B, in a 7 MV MRI-linac. *Physics in Medicine & Biology*, 64(10):105025, 2019.

L. A. de Prez. *A new water calorimeter for modern radiotherapy.* Dissertation, Utrecht University, 2019.

K. Derikum. Allgemeine Korrektionen bei der Ionisationsdosimetrie. In K. Hohlfeld and M. Roos, editors, *Dosismeßverfahren für Photonen- und Elektronenstrahlung hoher Energie. PTB-Bericht PTB-Dos-21.* 1992.

Deutsches Institut für Normung e.V. Dosismessverfahren nach der Sondenmethode für Photonen- und Elektronenstrahlung - Teil 2: Dosimetrie hochenergetischer Photonen- und Elektronenstrahlung mit Ionisationskammern. *DIN 6800-2:2008-03, Beuth Verlag, Berlin*, 2008.

DIN-Normenausschuss Radiologie (NAR). Dosismessverfahren nach der Sondenmethode für Protonen- und Ionenstrahlung—Teil 1: Ionisationskammern. *DIN 6801-1:2019-09, DIN Deutsches Institut für Normung e. V.*, 2016.

J. M. Dolo and V. Feaugas. Analysis of parameters that influence the amplitude of the ESR/alanine signal after irradiation. *Applied radiation and isotopes*, 62(2): 273–279, 2005.

V. Dose. Bayes in five days. *CIPS, MPI für Plasmaphysik, Garching, Germany, Reprint*, 83, 2002.

K. V. Ettinger. Free radical dosimetry techniques and their suitability for precise and accurate measurements of radiation. *International Journal of Radiation Applications and Instrumentation. Part A. Applied Radiation and Isotopes*, 40(10-12): 865–870, 1989.

B. G. Fallone. The rotating biplanar linac–magnetic resonance imaging system. In *Seminars in radiation oncology*, volume 24, pages 200–202. Elsevier, 2014.

B. G. Fallone, B. Murray, S. Rathee, T. Stanescu, S. Steciw, S. Vidakovic, E. Blosser, and D. Tymofichuk. First MR images obtained during megavoltage photon irradiation from a prototype integrated linac-MR system. *Medical physics*, 36(6): 2084–2088, 2009.

H. Fujita. New horizons in MR technology: RF coil designs and trends. *Magnetic Resonance in Medical Sciences*, 6(1):29–42, 2007.

R.R. Gallas, N. Hünemohr, A. Runz, N.I. Niebuhr, O. Jäkel, and S. Greilich. An anthropomorphic multimodality (CT/MRI) head phantom prototype for end-to-end tests in ion radiotherapy. *Zeitschrift fuer Medizinische Physik*, 25(4):391–399, 2015.

T. Garcia, T. Lacornerie, R. Popoff, V. Lourenço, and J.-M. Bordy. Dose verification and calibration of the Cyberknife® by EPR/alanine dosimetry. *Radiation Measurements*, 46(9):952–957, 2011.

S. Greilich and J.-M. Osinga-Blättermann. Strahlenphysik. In W. Schlegel, C.P. Karger, and O. Jäkel, editors, *Medizinische Physik*, pages 3–35. Springer, 2018.

T. Hackel. Dosimetrie mit Alanin/Elektronen-Spin-Resonanz. Positionierung von Dosimetersonde und Referenzsubstanz. *PTB-Bericht PTB-DOS-52*, 2006.

S.L. Hackett, B. Van Asselen, J.W.H. Wolthaus, J.G.M. Kok, S.J. Woodings, J.J.W. Lagendijk, and B.W. Raaymakers. Consequences of air around an ionization chamber: Are existing solid phantoms suitable for reference dosimetry on an MR-linac? *Medical Physics*, 43(7):3961–3968, 2016.

J.W. Hansen, K.J. Olsen, and M. Wille. The alanine radiation detector for high and low-LET dosimetry. *Radiation protection dosimetry*, 19(1):43–47, 1987.

G.H. Hartmann. Dosimetrie. In W. Schlegel, C.P. Karger, and O. Jäkel, editors, *Medizinische Physik*, pages 425–450. Springer, 2018.

M.Z. Heydari, E. Malinen, E.O. Hole, and E. Sagstuen. Alanine radicals. 2. The composite polycrystalline alanine EPR spectrum studied by ENDOR, thermal annealing, and spectrum simulations. *The Journal of Physical Chemistry A*, 106 (38):8971–8977, 2002.

S.S. Hidalgo-Tobon. Theory of gradient coil design methods for magnetic resonance imaging. *Concepts in Magnetic Resonance Part A*, 36(4):223–242, 2010.

IAEA. IAEA-TECDOC-1585. Measurement uncertainty: A practical guide for secondary standards dosimetry laboratories. *IAEA, Vienna*, 2008.

International Electrotechnical Commission IEC. IEC 60601-2-33/AMD 2:2010 Amendmend 2 – Medical electrical equipment-Part 2-33 (ed.3): Particular requirements for the safety of magnetic resonance equipment for medical diagnosis. 2015.

O. Jäkel. Bestrahlungsplanung. In W. Schlegel, C.P. Karger, and O. Jäkel, editors, *Medizinische Physik*, pages 473–484. Springer, 2018.

Joint Committee for Guides in Metrology (JCGM). Evaluation of measurement data – Guide to the expression of uncertainty in measurement, 2008. URL https://www.bipm.org/en/committees/jc/jcgm/publications. Accessed: 2022-10-19.

C. P. Karger. Klinische Strahlenbiologie. In W. Schlegel, C. P. Karger, and O. Jäkel, editors, *Medizinische Physik*, pages 451–472. Springer, 2018a.

C. P. Karger. Der Strahlentherapie-Prozess. In W. Schlegel, C. P. Karger, and O. Jäkel, editors, *Medizinische Physik*, pages 399–404. Springer, 2018b.

I. Kawrakow, D. W. O. Rogers, E. Mainegra-Hing, F. Tessier, R. W. Townson, and B. R. B. Walters. EGSnrc toolkit for Monte Carlo simulation of ionizing radiation transport. 2000. doi: 10.4224/40001303.

A. Krauss. The PTB water calorimeter for the absolute determination of absorbed dose to water in ^{60}Co radiation. *Metrologia*, 43(3):259, 2006.

A. Krauss and R.-P. Kapsch. Experimental determination of k_Q factors for cylindrical ionization chambers in 10 cm× 10 cm and 3 cm× 3 cm photon beams from 4 MV to 25 MV. *Physics in Medicine & Biology*, 59(15):4227, 2014.

M. Krystek and M. Anton. A least-squares algorithm for fitting data points with mutually correlated coordinates to a straight line. *Measurement science and technology*, 22(3):035101, 2011.

F. Kuntz, J. Y. Pabst, J. P. Delpech, J. P. Wagner, and E. Marchioni. Alanine-ESR in vivo dosimetry: a feasibility study and possible applications. *Applied radiation and isotopes*, 47(11-12):1183–1188, 1996.

M. E. Ladd. High-field-strength magnetic resonance: potential and limits. *Topics in Magnetic Resonance Imaging*, 18(2):139–152, 2007.

M. E. Ladd et al. Magnetresonanztomographie und -spektroskopie. In W. Schlegel, C. P. Karger, and O. Jäkel, editors, *Medizinische Physik*, pages 205–283. Springer, 2018.

J. J. W. Lagendijk, B. W. Raaymakers, A. J. E. Raaijmakers, J. Overweg, K. J. Brown, E. M. Kerkhof, R. W. van der Put, B. Hårdemark, M. van Vulpen, and U. A. van der Heide. MRI/linac integration. *Radiotherapy and Oncology*, 86(1): 25–29, 2008.

J. J. W. Lagendijk, B. W. Raaymakers, C. A. T. Van den Berg, M. A. Moerland, M. E. Philippens, and M. van Vulpen. MR guidance in radiotherapy. *Physics in medicine and biology*, 59(21):R349, 2014.

S. C. Leu, Z. Huang, and Z. Lin. Generation of pseudo-CT using high-degree polynomial regression on dual-contrast pelvic MRI data. *Scientific reports*, 10(1):1–11, 2020.

G. P. Liney and M. A. Moerland. Magnetic resonance imaging acquisition techniques for radiotherapy planning. In *Seminars in radiation oncology*, volume 24, pages 160–168. Elsevier, 2014.

G. P. Liney, B. Dong, J. Begg, P. Vial, K. Zhang, F. Lee, A. Walker, R. Rai, T. Causer, S. J. Alnaghy, et al. Experimental results from a prototype high-field inline MRI-linac. *Medical physics*, 43(9):5188–5194, 2016.

E. Malinen, M. Z. Heydari, E. Sagstuen, and E. O. Hole. Alanine radicals, part 3: Properties of the components contributing to the EPR spectrum of X-irradiated alanine dosimeters. *Radiation research*, 159(1):23–32, 2003a.

E. Malinen, E. A. Hult, E. O. Hole, and E. Sagstuen. Alanine radicals, Part 4: Relative amounts of radical species in alanine dosimeters after exposure to 6-19 MeV electrons and 10 kV-15 MV photons. *Radiation research*, 159(2):149–153, 2003b.

V. N. Malkov and D. W. O. Rogers. Electric and Magnetic field macros in EGSnrc. URL https://github.com/nrc-cnrc/EGSnrc/files/704931/EMFMacrosInEGSnrcReport.pdf. Accessed: 2021-08-16.

V. N. Malkov and D. W. O. Rogers. Charged particle transport in magnetic fields in EGSnrc. *Medical Physics*, 43(7):4447–4458, 2016.

M. Marrale, A. Longo, M. Spano, A. Bartolotta, M. C. D'Oca, and M. Brai. Sensitivity of alanine dosimeters with gadolinium exposed to 6 MV photons at clinical doses. *Radiation research*, 176(6):821–826, 2011.

M. Marrale, A. Carlino, S. Gallo, A. Longo, S. Panzeca, A. Bolsi, J. Hrbacek, and T. Lomax. EPR/alanine dosimetry for two therapeutic proton beams. *Nuclear Instruments and Methods in Physics Research Section B: Beam Interactions with Materials and Atoms*, 368:96–102, 2016.

M. R. McEwen and J. Taank. Examining the influence of humidity on reference ionization chamber performance. *Medical Physics*, 44(2):694–702, 2017.

D. W. McRobbie, E. A. Moore, M. J. Graves, and M. R. Prince. *MRI from Picture to Proton*. Cambridge University Press, 2017.

P. Metcalfe, G. P. Liney, L. Holloway, A. Walker, M. Barton, G. P. Delaney, S. Vinod, and W. Tome. The potential for an enhanced role for MRI in radiation-therapy treatment planning. *Technology in cancer research & treatment*, 12(5):429–446, 2013.

S. Mutic and J.F. Dempsey. The ViewRay system: magnetic resonance–guided and controlled radiotherapy. In *Seminars in radiation oncology*, volume 24, pages 196–199. Elsevier, 2014.

V. Nagy. Accuracy considerations in EPR dosimetry. *Applied Radiation and isotopes*, 52(5):1039–1050, 2000.

V. Nagy, J.M. Puhl, and M.F. Desrosiers. Advancements in accuracy of the alanine dosimetry system. Part 2. The influence of the irradiation temperature. *Radiation Physics and Chemistry*, 57(1):1–9, 2000a.

V. Nagy, O.F. Sleptchonok, M.F. Desrosiers, R.T. Weber, and A.H. Heiss. Advancements in accuracy of the alanine EPR dosimetry system: Part III: usefulness of an adjacent reference sample. *Radiation Physics and Chemistry*, 59(4):429–441, 2000b.

V. Nagy, S.V. Sholom, V.V. Chumak, and M.F. Desrosiers. Uncertainties in alanine dosimetry in the therapeutic dose range. *Applied radiation and isotopes*, 56(6): 917–929, 2002.

N.I. Niebuhr, W. Johnen, G. Echner, A. Runz, M. Bach, M. Stoll, K. Giske, S. Greilich, and A. Pfaffenberger. The ADAM-pelvis phantom – an anthropomorphic, deformable and multimodal phantom for MRgRT. *Physics in Medicine & Biology*, 64(4):04NT05, 2019.

NIST. Proton gyromagnetic ratio., a. URL https://physics.nist.gov/cgi-bin/cuu/Value?gammap. Accessed: 2020-07-07.

NIST. Proton gyromagnetic ratio., b. URL https://physics.nist.gov/cgi-bin/cuu/Value?gammapbar. Accessed: 2020-07-07.

D.J. O'Brien and G.O. Sawakuchi. Monte Carlo study of the chamber-phantom air gap effect in a magnetic field. *Medical physics*, 44(7):3830–3838, 2017.

D.J. O'Brien, D.A. Roberts, G.S. Ibbott, and G.O. Sawakuchi. Reference dosimetry in magnetic fields: formalism and ionization chamber correction factors. *Medical Physics*, 43(8):4915–4927, 2016.

D.J. O'Brien, N. Schupp, S. Pencea, J. Dolan, and G.O. Sawakuchi. Dosimetry in the presence of strong magnetic fields. *J Phys*, 847:012055, 2017.

K.J. Olsen, J.W. Hansen, and M. Wille. Response of the alanine radiation dosemeter to high-energy photon and electron beams. *Physics in Medicine & Biology*, 35(1): 43, 1990.

S. Olsson, E.S. Bergstrand, Å.K. Carlsson, E.O. Hole, and E. Lund. Radiation dose measurements with alanine/agarose gel and thin alanine films around a ^{192}Ir brachytherapy source, using ESR spectroscopy. *Physics in Medicine & Biology*, 47(8):1333, 2002.

J.-M. Osinga-Blättermann. *Determination of absorbed dose to water in a clinical carbon ion beam by means of fluorescent nuclear track detectors, ionization chambers, and water calorimetry.* Dissertation, Universität Heidelberg, 2017.

H. Palmans, P. Andreo, M. S. Huq, J. Seuntjens, and K. Christaki. Dosimetry of small static fields used in external beam radiotherapy: an IAEA-AAPM international code of practice for reference and relative dose determination. *Vienna: International Atomic Energy Agency*, 2017.

S. Panzeca, S. Savoca, G. Iacoviello, V. Caputo, F. Cuccia, N. Luca, S. Gallo, M. Brai, A. Panese, and M. Marrale. Dosimetric verification of stereotactic head treatments performed with Helical Tomotherapy using alanine dosimeters and gafchromic films. *Physica Medica*, 56:157, 2018.

T. Pawlicki, D. J. Scanderbeg, and G. Starkschall. *Hendee's radiation therapy physics.* John Wiley & Sons, 2016.

N. Perichon, T. Garcia, P. François, V. Lourenço, C. Lesven, and J.-M. Bordy. Calibration of helical tomotherapy machine using EPR/alanine dosimetry. *Medical physics*, 38(3):1168–1177, 2011.

E. B. Podgorsak et al. *Radiation oncology physics.* IAEA Vienna, 2005.

S. Pojtinger, M. Nachbar, S. Ghandour, O. Pisaturo, M. Pachoud, R.-P. Kapsch, and D. Thorwarth. Experimental determination of magnetic field correction factors for ionization chambers in parallel and perpendicular orientations. *Physics in Medicine & Biology*, 65(24):245044, 2020.

J. M. Pollard, Z. Wen, R. Sadagopan, J. Wang, and G. S. Ibbott. The future of image-guided radiotherapy will be MR guided. *The British journal of radiology*, 90(1073):20160667, 2017.

PTB. *The Earth's magnetic field at PTB.* 2022. URL https://www.ptb.de/cms/nc/en/ptb/fachabteilungen/abt2/fb-25/ag-251/live-data-earths-magnetic-field.html. Accessed: 2022-07-18.

PTW-Freiburg. Illustration of an ionisation chamber. URL https://www.ptwdosimetry.com/products/farmer-ionization-chamber-30013-waterproof/?L=0. Accessed: 2022-08-11.

A. J. E. Raaijmakers, B. W. Raaymakers, and J. J. W. Lagendijk. Integrating a MRI scanner with a 6 MV radiotherapy accelerator: dose increase at tissue–air interfaces in a lateral magnetic field due to returning electrons. *Physics in medicine and biology*, 50(7):1363, 2005.

A. J. E. Raaijmakers, B. W. Raaymakers, and J. J. W. Lagendijk. Experimental verification of magnetic field dose effects for the MRI-accelerator. *Physics in Medicine & Biology*, 52(14):4283, 2007a.

A. J. E. Raaijmakers, B. W. Raaymakers, S. Van der Meer, and J. J. W. Lagendijk. Integrating a MRI scanner with a 6 MV radiotherapy accelerator: impact of the surface orientation on the entrance and exit dose due to the transverse magnetic field. *Physics in medicine and biology*, 52(4):929, 2007b.

A. J. E. Raaijmakers, B. W. Raaymakers, and J. J. W. Lagendijk. Magnetic-field-induced dose effects in MR-guided radiotherapy systems: dependence on the magnetic field strength. *Physics in medicine and biology*, 53(4):909, 2008.

B. W. Raaymakers, A. J. E. Raaijmakers, A. N. T. J. Kotte, D. Jette, and J. J. W. Lagendijk. Integrating a MRI scanner with a 6 MV radiotherapy accelerator: dose deposition in a transverse magnetic field. *Physics in medicine and biology*, 49(17):4109, 2004.

B. W. Raaymakers, I. M. Jürgenliemk-Schulz, G. H. Bol, M. Glitzner, A. N. T. J. Kotte, B. Van Asselen, J. C. J. De Boer, J. J. Bluemink, S. L. Hackett, M. A. Moerland, et al. First patients treated with a 1.5 T MRI-Linac: clinical proof of concept of a high-precision, high-field MRI guided radiotherapy treatment. *Physics in Medicine & Biology*, 62(23):L41, 2017.

R. Rai, S. Kumar, V. Batumalai, D. Elwadia, L. Ohanessian, E. Juresic, L. Cassapi, S. K. Vinod, L. Holloway, P. J. Keall, et al. The integration of MRI in radiation therapy: collaboration of radiographers and radiation therapists. *Journal of Medical Radiation Sciences*, 64(1):61–68, 2017.

C. M. Rank, C. Tremmel, N. Hünemohr, A. M. Nagel, O. Jäkel, and S. Greilich. MRI-based treatment plan simulation and adaptation for ion radiotherapy using a classification-based approach. *Radiation Oncology*, 8(1):1–13, 2013.

K. J. Ray, N. R. Sibson, and A. E. Kiltie. Treatment of breast and prostate cancer by hypofractionated radiotherapy: potential risks and benefits. *Clinical oncology*, 27(7):420–426, 2015.

D. F. Regulla. EPR dosimetry-present and future. Technical report, 1999.

D. F. Regulla and U. Deffner. Dosimetry by ESR spectroscopy of alanine. *The International Journal of Applied Radiation and Isotopes*, 33(11):1101–1114, 1982.

H. Reich and U. Burmester. *Dosimetrie ionisierender Strahlung: Grundlagen und Anwendungen*. Teubner, 1990.

D. W. O. Rogers. Fifty years of Monte Carlo simulations for medical physics. *Physics in Medicine & Biology*, 51(13):R287, 2006.

E. Sagstuen, E. O. Hole, S. R. Haugedal, and W. H. Nelson. Alanine radicals: structure determination by EPR and ENDOR of single crystals X-irradiated at 295 K. *The Journal of Physical Chemistry A*, 101(50):9763–9772, 1997.

F. Salvat, J. M. Fernández-Varea, J. Sempau, et al. PENELOPE-2008: A code system for Monte Carlo simulation of electron and photon transport. In *Workshop Proceedings, Barcelona, Spain*, volume 30, 2008.

J. F. Schenck. Physical interactions of static magnetic fields with living tissues. *Progress in biophysics and molecular biology*, 87(2-3):185–204, 2005.

W. Schlegel. Bestrahlungsgeräte der Teletherapie. In W. Schlegel, C. P. Karger, and O. Jäkel, editors, *Medizinische Physik*, pages 405–424. Springer, 2018.

W. Schlegel, C. Thieke, O. Jäkel, M. Fast, and A.-C. Knopf. Bestrahlungsverfahren. In W. Schlegel, C. P. Karger, and O. Jäkel, editors, *Medizinische Physik*, pages 525–577. Springer, 2018.

M. K. H. Schneider, M. Krystek, and C. C. J. Schneider. Dosimetry of electron and gamma radiation with alanine/ESR spectroscopy. In *High-dose dosimetry*. 1985.

S. Shan, G. P. Liney, F. Tang, M. Li, Y. Wang, H. Ma, E. Weber, A. Walker, L. Holloway, Q. Wang, et al. Geometric distortion characterization and correction for the 1.0 T Australian MRI-linac system using an inverse electromagnetic method. *Medical Physics*, 47(3):1126–1138, 2020.

P. H. G. Sharpe and J. P. Sephton. Alanine dosimetry at NPL – The development of a mailed reference dosimetry service at radiotherapy dose levels. Technical report, 1998.

P. H. G. Sharpe, K. Rajendran, and J. P. Sephton. Progress towards an alanine/ESR therapy level reference dosimetry service at NPL. *Applied radiation and isotopes*, 47(11):1171–1175, 1996.

Siemens. Receiving head coil in an MRI system. URL https://www.healthcare.siemens.com/siemens_hwem-hwem_ssxa_websites-context-root/wcm/idc/groups/public/@global/@imaging/@mri/documents/image/mdaw/mtu4/~edisp/02_8_ch_head_coil_mood-00035389/~renditions/02_8_ch_head_coil_mood-00035389~8.jpg. Accessed: 2020-07-03.

O. F. Sleptchonok, V. Nagy, and M. F. Desrosiers. Advancements in accuracy of the alanine dosimetry system. Part 1. The effects of environmental humidity. *Radiation Physics and Chemistry*, 57(2):115–133, 2000.

K.-D. Sommer and B. R. L Siebert. Praxisgerechtes Bestimmen der Messunsicherheit nach GUM (Practical Determination of the Measurement Uncertainty under GUM). *tm–Technisches Messen/Sensoren, Geräte, Systeme*, 71(2/2004):52–66, 2004.

K. H. Spruijt, M. Dahele, J. P. Cuijpers, M. Jeulink, D. Rietveld, B. J. Slotman, and W. F. A. R. Verbakel. Flattening filter free vs flattened beams for breast

irradiation. *International Journal of Radiation Oncology* Biology* Physics*, 85 (2):506–513, 2013.

C. Stengl. Simulation of a realistic and reproducible diaphragmic breathing model for an anthropomorphic abdomen phantom for image-guided radiotherapy. Master's thesis, German Cancer Research Center (DKFZ), 2020.

J. C. Swift, D. M. Pajerowski, and M. W. Meisel. Magnetic susceptibility of L-amino acids in solid state at high magnetic fields, 2008.

H. Szymanowski, W. Y. Baek, R. Neungang-Nganwa, H. Nettelbeck, and H. Rabus. MRI-Linac: Effect of the magnetic field on the interaction cross sections. *Radiotherapy and Oncology*, 115:S431, 2015.

S. J. Thomas, M. M. Aspradakis, J. P. Byrne, G. Chalmers, S. Duane, J. Rogers, R. A. S. Thomas, G. S. J. Tudor, and N. Twyman. Reference dosimetry on TomoTherapy: an addendum to the 1990 UK MV dosimetry code of practice. *Physics in Medicine & Biology*, 59(6):1339, 2014.

D. Thwaites. Accuracy required and achievable in radiotherapy dosimetry: have modern technology and techniques changed our views? In *Journal of Physics: Conference Series*, volume 444, page 012006. IOP Publishing, 2013.

Uniklinikum Dresden. Neues Großgerät ermöglicht innovative Krebstherapie am Uniklinikum, 2022. URL https://www.uniklinikum-dresden.de/de/presse/aktuelle-medien-informationen/neues-grossgeraet-ermoeglicht-innovative-krebstherapie-am-uniklinikum. Accessed: 2023-09-14.

B. van Asselen, S. J. Woodings, S. L. Hackett, T. L. van Soest, J. G. M. Kok, B. W. Raaymakers, and J. W. H. Wolthaus. A formalism for reference dosimetry in photon beams in the presence of a magnetic field. *Physics in Medicine & Biology*, 63 (12):125008, 2018.

VTK. Orientations in an MRI system. URL https://vtk.org/Wiki/images/thumb/d/d9/DICOM-OrientationDiagram-LPS.png/800px-DICOM-OrientationDiagram-LPS.png. Accessed: 2020-07-03.

R. T. Weber, J. Jiang, and D. P. Barr. EMX user's manual. *Bruker Instruments, Billerica*, 1998.

E. Weiss, J. C. Ford, K. M. Olsen, K. Karki, S. Saraiya, R. Groves, and G. D. Hugo. Apparent diffusion coefficient (ADC) change on repeated diffusion-weighted magnetic resonance imaging during radiochemotherapy for non-small cell lung cancer: A pilot study. *Lung cancer*, 96:113–119, 2016.

Y. Xiao, S.F. Kry, R. Popple, E. Yorke, N. Papanikolaou, S. Stathakis, P. Xia, S. Huq, J. Bayouth, J. Galvin, et al. Flattening filter-free accelerators: a report from the AAPM Therapy Emerging Technology Assessment Work Group. *Journal of applied clinical medical physics*, 16(3):12–29, 2015.

G.G. Zeng, M.R. McEwen, D.W.O. Rogers, and N.V. Klassen. An experimental and Monte Carlo investigation of the energy dependence of alanine/EPR dosimetry: I. Clinical x-ray beams. *Physics in medicine and biology*, 49(2):257, 2004.

Y. Zhou, J. Yuan, O.L. Wong, W.W.Ki. Fung, K.F. Cheng, K.Y. Cheung, and S.K. Yu. Assessment of positional reproducibility in the head and neck on a 1.5-T MR simulator for an offline MR-guided radiotherapy solution. *Quantitative imaging in medicine and surgery*, 8(9):925, 2018.

W. Zou, L. Dong, and B.-K.K. Teo. Current state of image guidance in radiation oncology: implications for PTV margin expansion and adaptive therapy. In *Seminars in radiation oncology*, volume 28, pages 238–247. Elsevier, 2018.

Acknowledgements

Diese Arbeit wurde an der PTB Braunschweig in Dr. Ralf-Peter Kapschs Arbeitsgruppe "Dosimetrie für die Strahlentherapie" im Fachbereich "Dosimetrie für Strahlentherapie und Röntgendiagnostik" unter Dr. Ulrike Ankerhold begonnen. Zwischenzeitlich war Dr. Andreas Zimbal vom Fachbereich "Neutronenstrahlung" mein Vorgesetzter.
Grundlage für diese Dissertation war die sorgfältige Arbeit von Dr. Mathias Anton, der das Alanindosimetriesystem an der PTB aufgebaut hatte. In der Anfangszeit dieser Arbeit stand Dr. Steffen Greilich beratend zur Seite, ebenso Dr. Franziska Renner, die nicht wie zunächst vorgesehen die Betreuung der Arbeit übernehmen konnte. Dr. Ariane Fillmer unterstützte die Durchführung des Experiments am MR-Scanner an der PTB Berlin. Der Austausch mit Dr. Ilias Billas, Dr. Leon de Prez und Joe Berresford war wertvoll für die Auswertung des Experiments am MR Linac in Manchester, ebenso die Unterstützung von Thomas Hackel bei der Durchführung aller Experimente. Die Hinweise von Dr. Lucas Burigo und Dr. Rolf Behrens waren sehr hilfreich für die Durchführung der Monte-Carlo Simulationen mit EGSnrc.

Eigenständigkeitserklärung

Hiermit erkläre ich, dass ich die vorliegende Dissertation selbst verfasst habe ohne unzulässige Hilfe Dritter und alle verwendeten Quellen als solche gekennzeichnet sind.

_____

Ort, Datum

_____

Unterschrift